Studying Si-H Mode Sensitivity to Internal and External Perturbations through Vibrational Spectroscopy

A DISSERTATION SUBMITTED TO THE FACULTY OF THE GRADUATE SCHOOL OF THE UNIVERSITY OF MINNESOTA BY

Christopher Jerald Huber

IN PARTIAL FULFILLMENT OF THE REQUIREMENTS DOCTOR OF PHILOSOPHY

Aaron, M. Massari, advisor

August 2015

Acknowledgements

I want start off by thanking the people who always had my best interests in mind and kept my morale and spirits up throughout my career, especially graduate school. Thank you Laura for keeping me positive even when research was not going well. It is no coincidence that my trajectory changed, for the better, when I met you. Thank you Mom and Dad for providing me the work ethic and sense of values that I use on an everyday basis. Thank you Ali, Ryan, Landon, Owen, Matt, Emily, Brantley, Quinn, and Avery for keeping me grounded and reaffirming the idea of family above everything else. Thank you to all my friends in Prescott, La Crosse, Minneapolis, and across the country. There are too many of you to thank individually but you know who you are. My friends have constantly reminded me that it is important to enjoy life and taught me the value of levity in my life.

Thank you to all of my teachers back in Prescott, WI, especially Mr. Peterson and Mr. Brazalle. Without the foundation that you all provided, college would have been drastically different. Thank you to the chemistry program at University of Wisconsin-La Crosse for inspiring me to pursue chemistry. Specifically I would like to thank Dr. Rolfhus and Dr. Kirsch for teaching me how to be a research scientist and Dr. Loh for challenging me day in and day out. Without your quantum mechanics course I would have never pursued graduate school. Thank you to everyone in the Chemistry and Materials lab at Trane Co.

Thank you Dr. Blank, Dr. Doreen Leopold, and Dr. Frontiera for your insight and guidance throughout my career. Thank you to the Laser Spectroscopy Group members for constantly raising the bar and providing useful feedback on my research. Thank you to the Massarians, past and present, for all of the help throughout my time in grad school. Thank you to Audrey and Brynna for showing me how to tame the 2D-IR experiment. Thank you Dan and Tim for the countless times I asked you questions and you still answered them. Thank you Ivan for constantly challenging me and pushing me. Thank you Zahra, Patrick, and Courtney for all of the morale building talks that we have had over the years. Thank you RiAnna for your help on my projects and helping me become a better mentor. Thank you everyone who has helped me down the path of academia, especially everyone at Augsburg College. Finally, thank you Aaron for never losing faith in me and inspiring me to be a better scientist everyday. I could not have asked for a better advisor.

Abstract:

Over the course of this thesis, I hope to display an understanding of how a vibrational mode's sensitivity is dictated by inter- and intramolecular structure and composition. In the following chapters, a new vibrational ultrafast spectroscopic probe was used to study solvatochromism, confined solvent structure and dynamics, and structural dynamics of solid state materials, subsequently gaining knowledge of the probe's inherent sensitivity and limitations in the process. First Chapter 2 provides a comprehensive background on 2D-IR spectroscopy, including the theory behind the technique and subsequent data analysis. Chapter 3 presents a solvatochromic study on a carbonyl vibration highlighting the analyses that will be used to extract molecular information from FTIR measurements of the same mode in different solvents. Chapter 4 utilizes some of the analyses from Chapter 3 to characterize a new Si-H probe intrinsically bound in a nanoporous silica sol-gel solid state sample. Chapter 4 also provides an introductory description of this novel mode's sensitivity to solvent through solvatochromic analyses and ultrafast spectroscopy. Chapter 5 investigates a surface bound Si-H probe's ability to measure interfacial solvent structure and dynamics inside mesoporous silica nanoparticles. Finally, Chapter 6 is a comprehensive study of the sensitivity of an Si-H mode to the structural and compositional evolution during a silica sol-gel formation and subsequent aging.

Table of Contents

List of Figures

List of Tables

Chapter 1: Introduction

1.1 Motivation

Since the first 2D-IR study published in 1998[1], over 400 2D-IR papers have been published, yet the technique is still in its infancy with many new systems yet to be investigated. To push the technique in new directions, some have focused on new technologies, such as pulse shaping, and new applications, such as 2D-IR microscopy.[2, 3] Others are interested in developing models that aid in spectral analysis[4, 5], while still others try to apply 2D-IR to novel systems.[6, 7] The work described herein contributes in this final category by introducing the silane vibrational mode to the 2D-IR repertoire. This thesis is a collective effort to characterize this vibrational mode's sensitivity to inter- and intramolecular structure and dynamics in solution and immobilized at the surface of silica. The following pages of this chapter give a general description of solvation effects, solvent dynamics, and silica sol-gel syntheses.

1.2 Solvation

The phenomenon of solvent molecules favorably interacting with another molecule, often referred to as solvation, plays a significant role in countless processes that we see everyday. Solvation of ionic compounds stabilizes the separated ions permitting dissolution.[8] Solvation can provide pathways for energy relaxation of an excited vibration through energy transfer mechanisms.[9-11] Solvent effects have been widely studied in the field of catalysis.[12-14] Transition State Theory (TST) states that the reactivity of a catalyst is primarily influenced by the energy of the initial and transition states of a reaction.[15, 16]

Thus, the stabilization or destabilization of either state will influence the reaction rate. For example, Ladanyi and coworkers found through simulations that the inclusion of condensed Ar and Xe gases improved H exchange between methane and methyl radicals through what they term a static caging effect.[17]

In essence, solvation is nothing more than the intermolecular interactions between a molecule of interest, presumably a solute molecule, and the surrounding solvent. These electrostatic interactions between solute and solvent molecules perturb the properties of the solute. For example, hydrogen bonding, dipole-dipole, and Van der Waals forces all have had well documented influences on solute observables.[18-23] Distinguishing each force's respective influence on a particular observable can be difficult for complex solute and solvent molecules. One empirical approach developed by Kamlet and Taft is to use linear solvation energy relations (LSER) [22] in which an observable, such as a vibrational frequency, measured in a range of solvents is fit with a linear combination of solvent properties referred to as the solvent parameter (S).

$$S = S_0 + \mathrm{a}\alpha + \mathrm{b}\beta + \mathrm{c}(\pi^* + \mathrm{d}\delta) \tag{1.1}$$

Tabulated values for solvent hydrogen bond donating (α) and accepting (β) strengths, polarizabilities (π^*) and polarizability corrections (δ) are available in the literature.[19, 23-25] The value of each parameter's coefficient determines the relative influence of the respective parameter, and thus the corresponding intermolecular force, on that observable, assuming that the model is able to find a correlation with S. For instance, a large value for c would indicate that Van der Waals forces are significant, whereas the values of a or b indicate whether or not the solvent hydrogen bonds with the solute and ultimately, whether this impacts the observable.

Our understanding of solvent interactions is constantly evolving as new systems are studied and new correlations are determined and analyzed. Despite the growing knowledge of solvation there remains a lot to discover. The observables that are subjected to LSER analyses are often obtained by spectroscopy. While NMR[26] and electronic spectroscopies[27] can provide unique insight into solvation, the focus of this thesis will be vibrational spectroscopy, specifically FTIR and 2D-IR spectroscopies. Vibrational spectroscopy can be used to study a vast array of phenomena but only with a proper understanding of the probe vibration in use. A mode's average vibrational frequency is influenced by solvation, or rather, the interaction of the surrounding electric field. From a physical point of view, a solution is nothing more than a collection of dipoles and point charges combining to form a net electric field. The surrounding electric field instantaneously interacts with the electric dipole of the vibrating bond, influencing the mode's vibrational frequency. This phenomenon is referred to as the vibrational Stark effect (VSE).[28, 29] Assuming a variety of chemical environments, the VSE ensures that any vibrational mode will vibrate with a spectrum of frequencies. Using FTIR spectroscopy, scientists can measure a bond's center frequency and peak width, providing insight into the type and number of solvent interactions, respectively. 2D-IR spectroscopy expands on the information provided by FTIR spectroscopy, determining the underlying effects solvent dynamics have on the peak width. As discussed in the motivation, 2D-IR spectroscopy provides insight into solvent dynamics occurring on the time scale of tens of femtoseconds to hundreds of picoseconds.

1.3 Solvent Dynamics

As chemists we are exposed to the concept of static solvation in many upper level chemistry or physics courses. In reality, the solute and solvent molecules are constantly moving, which means that the net electric field experienced by a vibrational mode is continuously changing. Predicting molecular motions of solvent molecules can be difficult, let alone the effect these motions have on the system. Solvent dynamics can affect a variety of systems from protein interactions[30-33] to catalytic reactivity.[12, 34] In general, solvent dynamics should impact any process requiring movement of a substance through a solution.

Focusing once again on catalytic reactivity, we discussed how static solvent effects fit into TST. While TST dictates that the rate coefficient depends on the energy of the reactants and the transition state, the rate of the reaction is still influenced by the diffusion of the reactants.[16, 35] TST breaks down in some dilute solutions, as reactions can become diffusion limited if the solution dynamics make it difficult for reactants (products) to diffuse to (way from) a catalyst. Under these conditions the local concentration of reactants around a catalyst does not reflect the solution concentration and the rate is slowed. A complete picture of the solvation effects on the reaction rate begins to emerge. Static solvation of the system, described in Section 1.2, may influence the reaction coefficient for a given reaction and the solvent dynamics may influence the effective concentration of reactants further shaping the reactivity of the system.

Solution dynamics have been studied through both theoretical modeling, via extensive MD calculations[36-40] or experimentally, via ultrafast spectroscopy.[41-44] The latter has the capability of measuring solvent dynamics on the scale of hundreds of femtoseconds.

A variety of techniques can be used to measure solvent dynamics either through the perspective of the solvent molecule or a solute molecule. Optical Kerr Effect spectroscopy and anisotropy techniques can measure rotations, librations, and translations of solvent molecules.[45-49] Transient absorption spectroscopy measures the lifetime of excited states, which can indicate how solvation affects relaxation pathways. Vibrational Echo Spectroscopy (VES) can measure the solvent dynamics surrounding a particular vibrational mode.[50-54] One common VES experiment, 2D-IR spectroscopy, provides a more complete description of the dynamics with a 100 fold gain in sensitivity. A much deeper description of 2D-IR spectroscopy will be found in Chapter 2.

1.4 Interfacial Solvation

The solvation of a surface has an underlying importance for many aspects of chemistry used every day. Solvent-surface interactions are responsible for the separation used in many liquid chromatography techniques. [20, 55, 56] The interaction of a reactant, solvent, and a heterogeneous catalyst determines the reactivity of system and possibly the selectivity of the reaction. [57-61] Solvent-surface interactions are one of the major factors that dictate how a solution flows in microfluidic systems.[62] All of the systems above require an understanding of not only the types of solvent-surface interactions but also how these interactions influence the dynamics of the solvent near the surface.

Monte Carlo simulations show that solvent molecules near a surface will organize in a dense, lamellar-like macrostructure. [63-68] The extent of the ordering depends on the strength of the solvent interactions with the surface and also other solvent molecules. Typically, the stronger both interactions are, the further the ordering will extend. Due to

resource constraints, many simulations calculate the diffusion of molecules using trajectory calculations rather than explicit dynamic motions. The models often predict a correlation between the density of the solvent layers and the time constants of diffusion with slower diffusion occurring near the surface. [63-68] The calculated time constants of diffusion are qualitatively meaningful but not simply related to the time constants of the underlying dynamics.

The time scales of the interfacial dynamics can be found through a select number of experimental techniques. Many experimental studies employ confined volumes to increase the surface area, adding significantly more solvent-surface interactions. These confined volume systems typically have diameters on the scale of a few to tens of nanometers. For years, the common description of these systems was the "core-shell model", which separated the solvent into two discrete regions. The "shell" is comprised of solvent molecules near the surface whose properties are perturbed by the existence of the interface. Conversely, the "core" contains solvent molecules that behave independently of the interface. In other words, the core contains bulk-like solvent molecules. The shell region is said to typically extend 1-3 nm from the surface depending on the solvent and surface chemistries.[68, 69]

Many different porous materials have been used as confined volume systems, including reverse micelles,[69-73] porous silica,[47, 74, 75] zeolites,[76] and metal organic frameworks.[77] Piletic and coworkers used reverse micelles to measure the vibrational relaxation and solvent dynamics of water within the micelles of varying sizes via IR transient absorption and 2D-IR spectroscopies.[69] Fourkas and coworkers have conducted extensive ultrafast OKE measurements on various solvents within silica sol-gels.[47, 78-80]

Chapters 4-5 detail two different confined dynamic studies of solvents within silica sol-gel pores using covalently bonded Si-H modes as the probe.

1.5 Silica Sol-gels

Sol-gel syntheses have revolutionized the field of synthetic-materials[81] and spawned numerous papers utilizing the synthesis to create a variety of metal oxide networks and particles. These materials can be made from relatively cheap reactants and without the extreme conditions that other syntheses require, making sol-gel syntheses a greener alternative. Because this synthetic technique is highly customizable, the resulting metal oxide, most often silica,[82, 83] can range widely in both particle size and in pore diameter.[81, 84] These materials can be utilized in a variety of ways, from industrial coatings to potential drug delivery systems. [85-88]

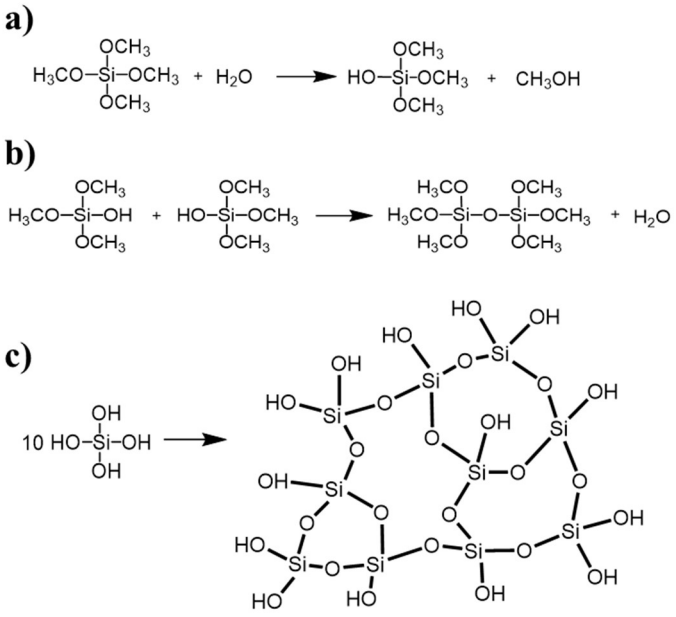

Figure 1.1 The reaction schemes for the a) hydrolysis of tetramethoxy silane (TMOS) precursors, b) the condensation of silanol groups, and c) the cross linking or polymerization of multiple monomers

Figure 1.1 depicts the reaction scheme for a typical sol-gel synthesis using a tetramethoxy silane (TMOS) precursor. In the first step, water hydrolyzes the alkoxy side chain of the precursor, creating a more reactive species called a silanol (Figure 1.1a). In the second step, these silanols react with one another creating a more condensed structure (Figure 1.1b). These steps occur very quickly and are energetically favorable. As the Si-O-Si network continues to grow, branch, and cross-link, eventually suspended silica aggregates are formed and the mixture is termed a "sol". As the polymer growth and aggregation progresses, the solution becomes more viscous and eventually gels. In this discussion, a gel is defined as a material which behaves more solid-like than liquid-like but still exhibits properties of both. Gelation is typically verified by analyzing the viscoelastic properties through rheology, as will be demonstrated in Chapter 6.

The kinetics of silica sol-gel syntheses have been analyzed via various analytical techniques. The pH dependence of the hydrolysis and subsequent condensation reactions is possibly the most studied variable of the sol-gel kinetics.[81, 89-91] Depending on the application of the material, acid or base initiators are used to catalyze the reaction. The two reactions are not kinetically optimized at the same pH as hydrolysis and condensation are faster in acidic and basic conditions, respectively.[81] As a result, the mechanism of polymerization is pH dependent. Acid initiators favor hydrolysis over condensation promoting linear polymer growth whereas base initiators favor condensation leading to branch-like polymer growth. The silica growth mechanism affects the mechanical properties of the product and ultimately the applications of the material. [81, 92-94]

Regardless of the growth mechanism, pockets of alcohol and water byproducts form providing the construct for the aforementioned pores in the gelled product.[89, 91] The porosity of the sample can be varied by adjusting the water to precursor ratio, although even with optimal ratios the pore diameters are limited. [95] While microporous materials work for some applications, others such as drug delivery require larger pores. [86-88] Through advances in surfactant technology and templating methods, silica particles can be synthesized as small as 50 nm but still house 10 nm pores. [96, 97]

The mechanical properties of the material change over the course of the reaction. Prior to gelation the reaction mixture behaves like a fluid solution. As gel formation is occurring the viscosity of the solution increases until the system reaches the gel point at which the sample behaves equally like a solid and a liquid.[81] After the gel is formed the system continues to condense through a process called gel aging.[93] During gel aging it is assumed that the pores of the gel are still filled with the alcohol and water byproducts and the material is accordingly referred to as an alcogel. Once the alcohol and water mixture begins to evaporate through a process called gel drying, the sample can either become a xerogel or an aerogel depending on the drying process. Xerogels are created through passive evaporation, where the leaving solvent collapses the pores creating a dense material. Conversely, aerogels are created through super critical drying, where the intercolated solvent is replaced by super critical CO_2.[98] In the super critical state, CO_2 has neglible surface tension, leaving the pores mostly intact upon removal. [98] The highly porous, completely dry aerogels have unique thermal insulation properties.

Over the course of this thesis, I hope to display an understanding of how a vibrational mode's sensitivity is dictated by inter- and intramolecular structure and

composition. In the following chapters, a new vibrational ultrafast spectroscopic probe was used to study solvatochromism, confined solvent structure and dynamics, and structural dynamics of solid state materials, subsequently gaining knowledge of the probe's inherent sensitivity and limitations in the process. First Chapter 2 provides a comprehensive background on 2D-IR spectroscopy, including the theory behind the technique and subsequent data analysis. Chapter 3 presents a solvatochromic study on a carbonyl vibration highlighting the analyses that will be used to extract molecular information from FTIR measurements of the same mode in different solvents. Chapter 4 utilizes some of the analyses from Chapter 3 to characterize a new Si-H probe intrinsically bound in a nanoporous silica sol-gel solid state sample. Chapter 4 also provides an introductory description of this novel mode's sensitivity to solvent through solvatochromism analyses and ultrafast spectroscopy. Chapter 5 investigates a surface bound Si-H probe's ability to measure interfacial solvent structure and dynamics inside mesoporous silica nanoparticles. Finally Chapter 6 is a comprehensive study of the sensitivity of an Si-H mode to the structural and compositional evolution during a silica sol-gel formation and subsequent aging.

Chapter 2: Background for Two-dimensional Infrared Spectroscopy

2.1: Why 2D-IR?

Vibrational echo experiments are ultrafast non-linear techniques that provide chemical insight into processes that occur on the timescale of hundreds of femtoseconds to hundreds of picoseconds. Vibrational Echo Spectroscopy (VES), first observed in 1993 and later resolved in 1995 by Fayer and coworkers, was the first technique to use infrared light to investigate the dynamics lying beneath the surface of a linear spectrum.[50, 99] From VES, came two-dimensional infrared (2D-IR) spectroscopy. In 1998, Hamm, Hochstrasser, and coworkers published the first 2D-IR paper measuring the protein dynamics using carbonyl modes.[1] Since then 2D-IR has been used to study chemical exchange between two moieties,[100] energy coupling between intramolecular vibrations[101], and perhaps the most impactful and certainly most common use for 2D-IR spectroscopy, studying structural or solvent dynamics in the condensed phase.

Author's note: Moving from linear spectroscopy i.e. FTIR, to non-linear spectroscopy comes with drastic increases in cost, complexity, and difficulty. If the same information can be gleaned from either non-linear or linear spectroscopy, it is advisable to use the linear technique. However, typically the novel information gained by non-linear techniques, like 2D-IR, wholly surpasses the information uncovered from linear spectroscopy, providing more than enough motivation to take up the challenge.

Before we discuss the utility of 2D-IR spectroscopy we must first discuss the limitations of linear spectroscopy. Linear spectroscopy implies a linear relationship between the incoming electric field and the induced polarization of the oscillators. Conversely, non-linear spectroscopy requires multiple electric field interactions to produce the non-linear polarization. The multiple electric fields can come from a single pulse or more ideally, multiple pulses. The scope of this work is vibrational spectroscopy, as such, the term linear spectroscopy will imply the use of Fourier Transform Infrared (FTIR) spectroscopy. We start this discussion by imagining the FTIR spectrum of an ideal diatomic gas with the understanding that we will work our way towards interesting condensed phase systems, introducing steps in complexity along the way. In an ideal gas, there are no molecular interactions, ensuring that each gas molecule will vibrate with the exact same frequency. If we assume that this gas has an infinite vibrational lifetime, the peak width would be infinitely narrow. Moving towards a more realistic system, we introduce a finite vibrational lifetime causing the line spectrum to homogeneously broaden due to Heisenberg's uncertainty principle.

Once again, we will take a step up in complexity and introduce intermolecular interactions. Even with the diffuse nature of gases, molecules will commonly collide, the force of which is dictated by the kinetic energy of the molecules and their electrostatic interactions. The addition of intermolecular interactions gives rise to additional spectral broadening, via the vibrational Stark effect.[29] The vibrational Stark effect explains how an applied electric field will perturb the Hamiltonian of any molecule in the field. The vibrational frequency is thus dependent on the electric field or, in the case of molecules, the chemical environment. For the duration of the collision, the gas molecule experiences

an applied electric field that quickly diminishes as the two molecules recoil away from each other. It is during this time period that the molecule exhibits a change in frequency and the peak broadens. Unlike gas systems, the molecules within a condensed phase system are constantly interacting with other molecules, thus emphasizing the role intermolecular forces play in the linear peak shape. We will once again work up our description of linear spectroscopy by increasing the level of complexity incrementally.

Imagine that there is a low concentration of some solute dissolved in isopropanol. Each solute molecule has a carbonyl stretching mode that will be monitored via FTIR spectroscopy. Starting with a completely static system, that is a system in which the molecules do not move, the solute molecules will be found to have a variety of interactions with isopropanol. Focusing on the extremes, some of the carbonyl modes may be solvated by alcohol groups while others will be solvated by alkyl groups. Based on the vibrational Stark effect, we would expect the modes in these specific environments to vibrate at slightly different frequencies. This distribution of chemical environments will be referred to as static inhomogeneity. We will group the probe molecules with similar chemical environments, thus the same vibrational frequencies, into a singular statistical mechanical subensemble. In reality, condensed phase systems will have a continuum of environments involving numerous molecules, each described by a homogeneously broadened subensemble, that combine to form the full ensemble of chemical environments. Each chemical environment will have a corresponding homogeneously broadened peak, with the same homogeneous linewidth (Figure 2.1a). The ensemble of the homogeneous linewidths from each subensemble gives the FTIR line shape. Understanding static contributions is very important in vibrational spectroscopy, however a completely static solution is

unrealistic. In order to move towards a real solution system, molecular motions or dynamics must be introduced.

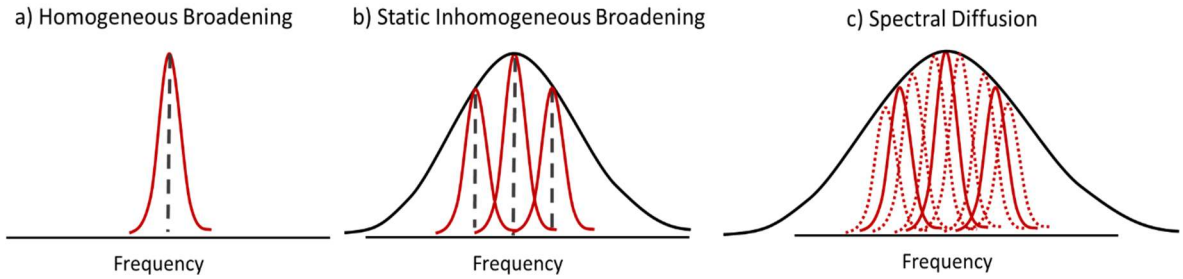

Figure 2.1 Illustrations of a) homogeneous and b-c) inhomogeneous spectral broadening due to both static (2.1b) and dynamic (2.1a & 2.1c) phenomena.

Using the same solution system as above, we will discuss the effect that dynamics have on the linear peak shape. At this point, there is a static distribution of subensembles with different frequencies contributing to an inhomogeneously broadened peak (Figure 2.1b). Let's say that the solvent/solute molecules are now allowed to move freely through the solution. We would imagine that the chemical environment surrounding a given mode on a given molecule would change over time, therefore creating a time dependent vibrational frequency. The timescales and the extent of molecular motions determine the broadening effect on the spectrum. Some motions are independent of the specific chemical environment resulting in the further homogeneous broadening. (Figure 2.1a). While other motions are deemed to cause exchange within the subensemble populations, a process referred to as dynamic inhomogeneous broadening or spectral diffusion (Figure 2.1c). Typically the motions responsible for spectral diffusion are slower and more drastic than the homogeneous broadening motions, but this not always the case. Both the spectral diffusion and additional homogeneous broadening contribute to additional spectral

broadening of the linear lineshape. Unfortunately, linear spectroscopy is unable to discern between the broadening from static inhomogeneity and dynamic contributions. The insufficiency of linear spectroscopy to investigate molecular dynamics provides the proper motivation for implementing non-linear spectroscopy.

2.2: Response Functions

In order to understand the information elucidated from 2D-IR spectroscopy, we must examine the quantum mechanical processes involved in the experiment. To start, picture ideal gas molecules, any of which can be described by a time dependent wave function $|\psi\rangle = \sum_n c_n e^{-\frac{iE_n t}{\hbar}} |n\rangle$ where $|n\rangle$ is an eigenstate for the Hamiltonian and c_n is a weighting coefficient or population of state n. Prior to any excitation ($t = -\infty$), c_n is time independent, however, as the oscillating electric field begins to interact with the molecules, c_n couples with the oscillating field and becomes time dependent:

$$\frac{\partial}{\partial t} c_n(t) = -\frac{i}{\hbar} c_n(t) e^{-i\omega_{mn} t} \langle n|\hat{\mu}|m\rangle \tag{2.1}$$

In Equation 2.1, ω_{mn} is the frequency of the transition between E_m and E_n and $\langle m|\hat{\mu}|n\rangle$ is the transition dipole moment

$$\langle m|\hat{\mu}|n\rangle = \frac{d\mu}{dx} \langle m|\hat{x}|n\rangle \tag{2.2}$$

where x is a coordinate of the vibrating bond and μ is the static electric dipole of the molecule. Essentially, the transition dipole moment is the change in the electric dipole as the bond coordinate changes during the vibration. After the laser pulse, the coefficient becomes time independent once again, leaving the system in a superposition between

states. For simplicity, we will focus on a two level system, where $|0\rangle$ and $|1\rangle$ represent the ground and first excited vibrational states, respectively.

$$|\psi\rangle = c_0 e^{-\frac{iE_0 t}{\hbar}} |0\rangle + ic_1 e^{-\frac{iE_1 t}{\hbar}} |1\rangle \tag{2.3}$$

The wave functions in Equation 2.3 have the typical time dependence, $-\frac{iE_n t}{\hbar}$, derived from solving the time dependent Schrodinger equation. We know that, prior to any excitation, a molecule at room temperature is most likely found in the vibrational ground state, so we can assume that $c_1 \ll c_0$ and $c_0 \approx 1$. The time evolution of the superposition in Equation 2.3 is aptly described by a molecular response function, $R(t)$. Keeping in mind our system consists of many molecules we will define a new term, macroscopic polarization, $P(t)$, as the sum of the molecular response functions.

Drawing comparisons to classical systems, $P(t)$ is found to be related to the expectation value of the dipole moment for the $|0\rangle$ to $|1\rangle$ transition.

$$P(t) = \langle \mu \rangle = c_0 c_1 \langle 0|\mu|1\rangle \sin(\omega_{01} t) + c_0^2 \langle 0|\mu|0\rangle + c_1^2 \langle 1|\mu|1\rangle \tag{2.4}$$

The first term in $P(t)$ describes the time dependent coherence of the molecular response functions and the second and third terms describe the static electric dipoles for the ground and first excited states. Equation 2.4 assumes a single vibrational frequency, although we know that this is not realistic in a condensed phase system. Figure 2.2 illustrates the effect that changing the frequency of $R(t)$ will have on $P(t)$. A monochromatic vibration (Figure 2.2a) ensures that the phase of each oscillator never destructively interferes producing a purely coherent system, that is, a system that will never lose its coherence assuming an infinite vibrational lifetime (Figure 2.2c). However once a distribution of frequencies is

introduced, the originally coherent oscillators quickly lose their phase relationship with one another (Figure 2.2b). The result is a Free Induction Decay (FID) of the macroscopic polarization shown in Figure 2.2d. This dephasing of the molecular response functions is exaggerated once the intermolecular interactions are allowed to evolve, as is the case in solvent or structural dynamics.

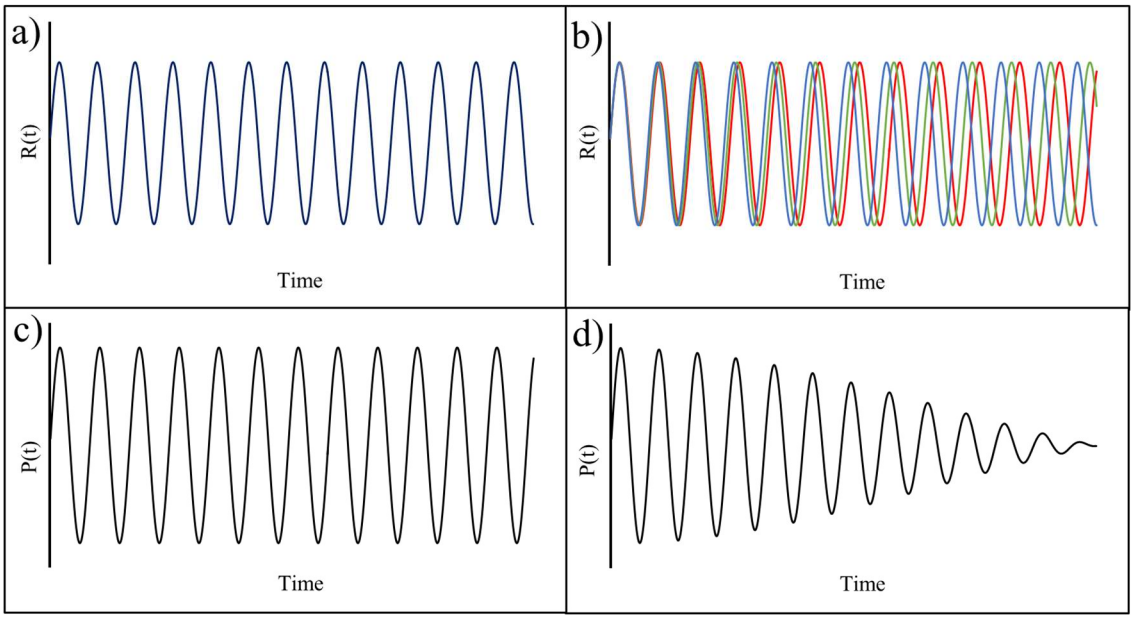

Figure 2.2 Illustrations of the molecular response functions and macroscopic polarizations for a monochromatic ideal gas (2.2a and 2.2b respectively) and a real gas (2.2c and 2.2d respectively).

This description of the quantum superposition is not fundamentally useful for describing the interaction of a laser pulse with a sample in the condensed phase. A spectroscopic measurement of condensed phase systems must be considered at some scale to be an ensemble average of the billions upon billions of molecules within the spot size of the laser beam(s). Condensed phase systems also exhibit a wide variety of chemical environments, resulting in a wide variety of transitional energies needed to excite to higher energy levels. The ensemble breaks down into subensembles of molecules in different environments. Any formalism used to describe these convoluted systems must have the

flexibility to describe transitions with variable energy but also must satisfy the statistical mechanics of a condensed phase. Density matrix formalism satisfies the conditions needed to effectively describe mixed states, in this case condensed phase systems. Descript backgrounds on density matrices can be found elsewhere, in this thesis the formalism will be used at a complexity just high enough to effectively describe the quantum mechanical fundamentals of the 2D-IR pulse sequence.

2.3: Density Matrix Formalism

A two by two density matrix will be used to describe a two level system. In these matrices, the diagonal terms describe the populations of the two states and the off diagonal terms describe the time dependent coherences between the two states. All terms will at minimum have a time dependence as described by the time dependent Schrodinger equation plus any additional terms such as vibrational relaxation and/or dynamics. After each interaction involving a high energy electric field, the density matrix is multiplied by a transition dipole matrix, $\mu(t)$, made up of only off diagonal terms. The structure of the transition dipole matrix forces the system to either be in a coherence state or population state depending on the density matrix prior to the interaction with an electric field. Initially, the density matrix has only non-zero terms along the diagonal representing a system with populations of both the ground and first excited states. The first interaction, at $t = 0$, puts the density matrix in a coherent state as indicated by the only non-zero terms residing in the off diagonal. The second photon interaction at, $t = t_1$, results in non-zeros along the diagonal signifying a population state. The system after the second interaction is described by a first order molecular response function, $R^1(t_1)$.

$$R^{(1)}(t_1) \propto i\langle \mu_1, [\mu_0, \rho(-\infty)] \rangle \tag{2.5}$$

The interaction of light with the wave function, described by the manipulation of the density matrix by the transition dipole operator, will dictate which of the two terms in $R^1(t_1)$ is favored, which will be explained later. The final excitation occurs at $t = t_1 + t_2$, pushing the system back into a coherence state. Finally at $t = t_1 + t_2 + t_3$, the system emits an electric field, referred to as an echo. The third order response function, $R^3(t_1)$ is defined as the density matrix after the interaction of the three incoming electric fields and the emission of the echo.

$$R^{(3)}(t_3, t_2, t_1) \alpha\, i\langle \mu_3 \left[\mu_2, \left[\mu_1, [\mu_0, \rho(-\infty)]\right]\right] \rangle \tag{2.6}$$

The idea of the macroscopic polarization was introduced earlier as a way to set the stage for an in depth discussion of its involvement in the echo process. In the end, it is the macroscopic polarization that is responsible for the emission of the echo. As such, it is important to consider $P(t)$ throughout this description of the pulse sequence. After the first field interaction, the system enters a coherence period in which the oscillators start to dephase due to the static inhomogeneity in the sample. What was left out of the earlier discussion is the effect that structural dynamics have on $P(t)$.

Recall that structural dynamics cause spectral broadening via VSE. By the same mechanisms, these frequency fluctuations cause additional dephasing during the first coherence period. As previously discussed, homogeneous broadening is the combination of both fast molecular motions, called pure dephasing, and broadening from the Fourier transform of the vibrational lifetime. These terms are typically combined into one dephasing term, called homogeneous dephasing time (T_2).

$$\frac{1}{T_2} = \frac{1}{2T_1} + \frac{1}{T_2^*} \tag{2.7}$$

In the equation above, T_1 is the vibrational lifetime and $T_2^\star$ is the pure dephasing time constant. Typically, the timescale of pure dephasing ranges from tens to hundreds of femtoseconds whereas the vibrational lifetime can range from picoseconds to hundreds of picoseconds. Thus, the homogeneous dephasing is limited to no more than twice the vibrational lifetime. Spectral diffusion or dynamic inhomogeneous broadening also results in oscillator dephasing through the mechanisms described earlier. Both static and dynamic dephasing mechanisms can occur at any point in the pulse sequence. It is only through experimental design that 2D-IR can deconvolute each process.

After the second pulse, the system leaves the coherent state and enters what is referred to as a population state. Upon the interaction, the oscillators will either enter the first excited state via stimulated absorption or relax to the ground state through stimulated emission. Either way, the system is no longer oscillating in a superposition. As such, the dephasing due to the static distribution of frequencies (static inhomogeneity) pauses for the time being, leaving homogeneous dephasing and spectral diffusion as the only dephasing mechanisms. Vibrational relaxation will continue to occur, but will not have an impact on the phase relationships between oscillators. When the third pulse interacts with the sample, the system enters a second and final coherence state. In a two level system, there are two coherent states of interest. The first is the original coherence state prior to population, which results in the continuation of the dephasing processes until all phase relationships are lost. The second coherence state is the conjugate of the original coherence state prior to population which causes the molecular response functions to evolve in the opposite direction, rebuilding the phase relationships lost due to static inhomogeneity. Both the

higher and lower frequency modes oscillate in the opposite direction with the same frequency. So the lag in phase that developed during the first coherence period between slower and faster modes, now acts as a head start for the lower frequency modes. Ultimately if the frequencies remain static, the frequency differences remain constant and the oscillators will regain a maximum macroscopic polarization after some time, $t_3 \approx t_1$. This process of rebuilding the phase relationship is referred to as rephasing.

What are left out of this description are the dephasing effects due to dynamics. The rephasing process only maximizes $P(t)$ if the relative frequency difference of the oscillators does not change. Any frequency changes perturb the phase relationships and prevent effective rephasing. If molecular dynamics cause a frequency fluctuation for a particular mode, that mode will oscillate at a different frequency during the coherence periods. Regardless of when the frequency jump occurs, the natural phase relationship is now perturbed. Rephasing cannot recover the perturbed phase relationship as the mode's new frequency does not match the lag produced by the previous frequency. The dynamic motion has effectively stunted the macroscopic polarization. Thus, the rephasing process removes only the dephasing due to static inhomogeneous broadening, ultimately providing the dynamical sensitivity to this nonlinear spectroscopic technique. When $P(t)$ reaches its maximum, the echo is emitted. The intensity of the echo signal is directly proportional to the square of the macroscopic polarization,

$$I_{echo} \propto \left(P(t)^{(3)}\right)^2 \tag{2.8}$$

Thus, the echo signal via a rephasing pathway is dependent on the dephasing due to dynamic motions.

Up to this point we have defined macroscopic polarization as the sum of individual third order molecular response functions through the lens of density matrices. We also now understand, qualitatively, how dynamic motions affect the macroscopic polarization. In order to ascertain quantitative information on the dynamics, we must consider a more sophisticated density matrix by adding dephasing terms to each of the elements in the density matrices. Each element of the density matrix holds information on either the population or coherence of the state. The time dependence of these elements was previously defined by solving the time dependent Schrodinger wave equation, however, we now know that quantum processes affect both the population and coherence states. The population of any excited state is affected by vibrational relaxation and a coherence state is affected by both dynamic motions and vibrational relaxation. The density matrix for a given system should reflect these dependences. To account for the vibrational relaxation, the excited state diagonal element was multiplied by a decaying exponential of the form $e^{-\frac{t}{T_1}}$. The ground state population was assumed to be largely unaffected by the relaxation due to the relative disparity of the populations at room temperature. The off diagonal elements of the density matrix were multiplied by decays with time constants for homogeneous dephasing and spectral diffusion, $e^{-\frac{t}{T_2}} \cdot \prod_n^k e^{-\frac{t}{\tau_n}}$. This new time dependent term contains a decay term with the homogeneous dephasing time constant, T_2, encompassing both the dynamic pure dephasing, population relaxation, and also the product of decay terms for the various time scales, τ_n, of spectral diffusion. While it is important to explicitly understand the origins of the time dependence for the density matrices, the matrices and the response functions typically encompass all of these terms within the time frames of the pulse sequence, i.e. t_1, t_2, t_3.

The expression for the response function in Equation 2.6 leaves some ambiguity in how the transition dipole operators interact with the wave function, or in other words how the light interacts with a molecule. As a matter of fact, there are eight different combinations of the operations, called pathways, in which the sequence progresses. Each pathway represents a unique sequence of light interactions and has a unique third order molecular response function, $R(t)^{(3)}$, signified by R_n. The explicit expressions for each R_n can be found in various references and will not be discussed here, instead each pathway will be discussed through the use of two sided Feynman diagrams.[102, 103]

Figure 2.3 exhibits two sided Feynman diagrams for the eight pathways. Double sided Feynman diagrams are set up with the following formalism. The middle of the diagram represents a density matrix in the $|n\rangle\langle m|$ state, indicating that the left side of the diagram represents the ket vector and the right side represents the bra vector. When $n = m$ the molecule is in a population state and when $n \neq m$ the molecule is in a coherence state. The vertical bars in a diagram represent a time axis, with the bottom of the bars representing $t = -\infty$. Arrows in the diagram represent incoming photons or wave vectors. By convention, arrows that point from left to right represent negative wave vectors and arrows that point from right to left represent positive wave vectors. Wave vectors that point towards the density matrix represent stimulated absorption whereas wave vectors pointing away from the density matrix represent stimulated emission. The dashed arrow at the top of each diagram represents the emission of the echo pulse.

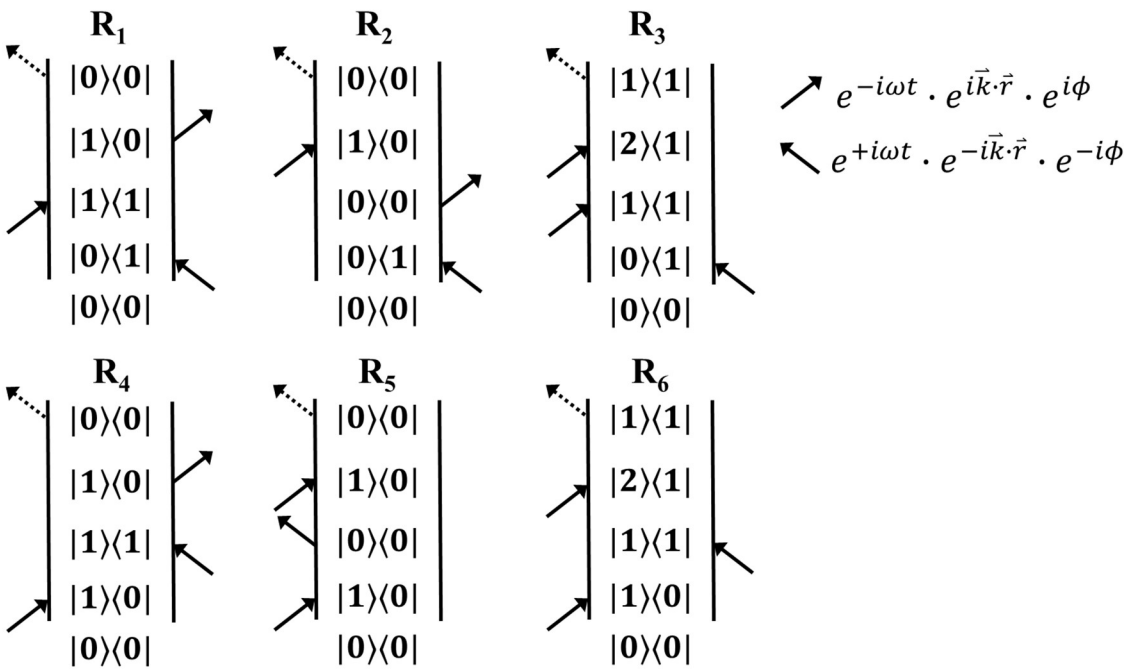

Figure 2.3 Feynman diagrams representing both rephasing (R1-3) and non-rephasing (R4-6) pathways

At first glance, some things become clear from the Feynman diagrams shown in Figure 2.3. First, each diagram represents a pathway where a molecule interacts with three temporally separated photons and the eventual emission of an echo photon. How the molecule interacts with a photon depends on the sign of the wave vector and whether the photon interacts with the bra or ket vector. For example, a negative wave vector will cause stimulated absorption when interacting with a ket vector but causes stimulated emission when interacting with a bra vector. Note that it is actually the sign of the frequency associated with the wave vector that explicitly influences the type of interaction but this is a level of sophistication that will not be covered in this description. In each response function, R_n, the first interaction, at $t = 0$, is an excitation into a coherence state, either $|1\rangle\langle 0|$ or $|0\rangle\langle 1|$. The second interaction, at $t = t_1$, puts the system into a population state, either $|0\rangle\langle 0|$ or $|1\rangle\langle 1|$. The third interaction, at $t = t_1 + t_2$, puts the system into its final

coherence state, either $|1\rangle\langle 0|$ or $|0\rangle\langle 1|$ for a two level system. Note that if the system is expanded to a more realistic three levels, the system can be excited into a coherence between the first and second excited states,$|2\rangle\langle 1|$, as seen in R_3 and R_6. The Feynman diagrams are nice visual models to distinguish between the rephasing, $R_1 - R_3$, and non-rephasing, $R_4 - R_6$, pathways. Note that a molecular response function can neither be rephasing or non-rephasing as phase necessitates a reference to another molecule. However, the Feynman diagrams illustrate possible response function pathways that lead to rephasing or non-rephasing of the macroscopic polarization. The Feynman diagrams for the rephasing pathways in Figure 2.3 illustrate that the final coherence state, $|1\rangle\langle 0|$, is the conjugate of the initial coherence, $|0\rangle\langle 1|$, whereas the non-rephasing pathways have the same coherence state, $|1\rangle\langle 0|$, after the first and third pulses. Once again, it is the phase relationship between the coherence states that dictates the information held within the signal.

2.4: Laser Setup

To understand the significance of a measurement one must understand the intricacies of the instrument used. This section provides an in depth description of the laser setup used in the experiments presented in later chapters.

A Ti:Sapphire crystal inside a prebuilt oscillator (KMLabs) is pumped with 4 W of 532 nm CW light from a Nd:YAG laser (SpectraPhysics Millenia) generating a 200 mW, 800 nm seed pulse. The generated seed pulse has a pulse duration of 25 fs and a bandwidth of ~45 nm at the FWHM. The seed pulse is aligned into the Regenerative Amplifier where it is stretched in time by diffraction gratings preventing optic damage before entering the amplifier cavity. Inside the cavity, the 800 nm seed is overlapped in a Ti:Sapphire crystal with 8 W of 527 nm pulsed light from a Nd:YLF pump laser (SpectraPhysics Empower). Two birefrigent Pockels cells control the buildup within the cavity and ultimately release a 1.5 W, 800 nm pulse. The pulse is recompressed using diffraction gratings resulting in 40 fs pulses at a frequency of 1 kHz with 1 W of average power. The output power is split equally between the 2D-IR experiment and the adjacent vibrational Sum Frequency Generation experiment.

The 500 mW laser beam is sent into an optical parametric amplifier where it is immediately split into three different portions. Four percent of the beam is sent through a 5 mm sapphire crystal to produce broadband white light. The white light is overlapped with fourteen percent of the incoming 800 nm light in a β-barium borate (BBO) crystal generating signal and idler beams. The signal and idler beams are overlapped with the remaining 82% of the 800 nm light in a different spot of the same BBO crystal, amplifying

both the signal and idler beams. The idea of parametric amplification is that the 800 nm pump beam is down converted to the signal and idler beams. The frequencies of the beams are dependent on the angle of the crystal. The two near IR beams are sent out of the OPA into a $AgGaS_2$ crystal where difference frequency generation produces mid-IR light. At this point, the tunable μJ pulses are near the transform limit with a pulse duration of approximately 90 fs and a bandwidth of 200 cm^{-1}. The laser is centered on the vibration of interest. This vibration will serve as the probe for the dynamics as described earlier. Not every probe measures the same dynamics, in fact some vibrations are more sensitive to hydrogen bonding solvents than others. The light at this point is collimated and is sent into either the pump probe or 2D-IR setups. From this point, the experiments are significantly different, as such separate descriptions of the experiments are provided.

2.4.1: 2D-IR Spectroscopy Experiment Setup

The collimated light is sent into three beam splitters producing three near-equal power beams (A, B, and C) and a significantly weaker local oscillator. The pulses for each beam are temporally separated through the use of delay stages. Beams A, B, and C are spatially overlapped in a BOXCARS geometry. This geometry will be discussed in great detail later. The emitted echo is coaligned with a local oscillator reference pulse (0.3-0.5 nJ per pulse, approximately 100 × larger than the signal), spectrally resolved in a 0.32 meter monochromator with a 75 line/mm grating, and detected with a liquid N_2 cooled 64-element mercury cadmium telluride (MCT) linear array detector (Infrared Associates, Inc). The spectral resolution of this specific setup is 4 cm^{-1}. The scatter from the solid-state

samples in Chapter 5 was reduced through a fibrillation method developed in the Massari Lab by Spector and coworkers.[104]

The theory behind each of the quantum pathways and the technical 2D-IR laser setup were previously discussed, however it is important to discuss at large how a typical 2D-IR experiment is executed. In order to do this, we will introduce a new timing convention. While parts of this description are admittedly redundant, the subtle differences in the timing description is critical. Once more 2D-IR spectroscopy is a three pulse technique, where the pulses are typically overlapped spatially but temporally delayed. Like before, the first pulse arrives at $t = 0$ however, the timing between the first and second pulses and the second and third pulses will be now referred to as τ and the waiting time, T_w, respectively. To reiterate, $t_1 = \tau$ and $t_2 = T_w$. The timing between the third pulse and the emitted echo will still be referred to as t_3. The echo is heterodyned with weak local oscillator beam producing an interferogram. A 2D-IR spectrum is taken by scanning τ from negative values (explained later) to positive values at a given T_w. This process is repeated 2-3 times for 15-25 T_ws, with a higher density of scans at shorter T_ws.

2.4.2: BOXCARS Geometry

As indicated the in the Feynman diagrams for R_1-R_3, the rephasing process requires the interaction of a negative wave vector and subsequent interactions with two positive wave vectors, resulting in echo fields emanating in the $-k_1+k_2+k_3$ phase matched direction. Conversely, the non-rephasing process requires the interaction of a positive wave vector, and subsequent interactions with a negative wave vector and then another positive wave vector, with the signal emanating in the $k_1-k_2+k_3$ phase matched direction. For reasons that

will be covered later, both the non-rephasing and rephasing signals must be collected in order to retrieve the phase information contained within a 2D-IR spectrum. This becomes difficult as the signals point in wildly different directions. Fortunately, using a BOXCARS geometry and experimental tricks, both the rephasing and non-rephasing signals can be collected in the same phase matched direction. Figure 2.4 exhibits one adaptation of the BOXCARS geometry used for 2D-IR spectroscopy. In this geometry, three infrared beams are overlapped spatially onto a sample. The beams will be designated A, B, and C so as to avoid confusion with the order of the pulse sequence.

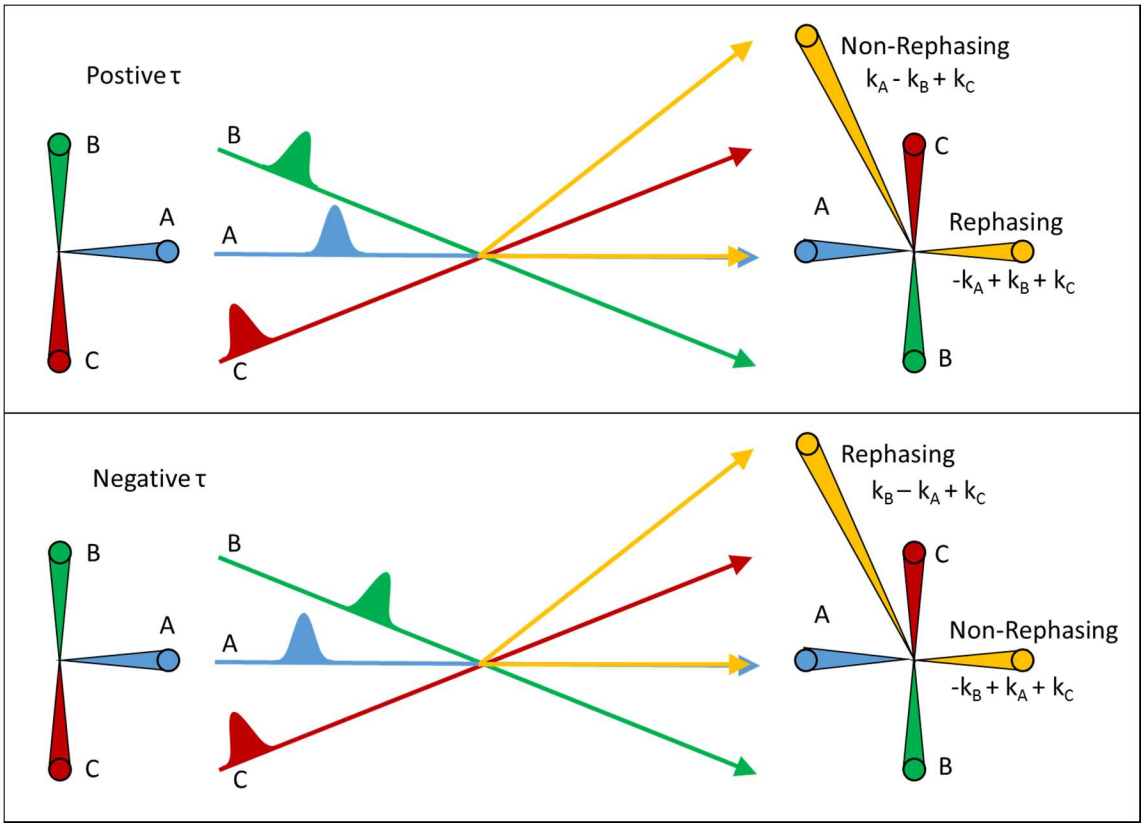

Figure 2.4 A diagram of the BOXCARS beam geometry for both positive and negative values of τ. The rephasing and non-rephasing signals are emitted in the same phase matched direction when the order of the first two pulses are switched.

The pulses of beams A and B can be controlled temporally through the use of delay stages providing the ability to manipulate the order of the pulse sequence. When the pulse

sequence proceeds as A, B, then C, the rephasing signal emanates in the $-k_A+k_B+k_C$ direction and the non-rephasing signal emanates in the $k_A-k_B+k_C$ direction as shown in top frame of Figure 2.4. When the order of A and B are then switched, suddenly the rephasing and non-rephasing signals can be collected in the $-k_B+k_A+k_C$ (same as $k_A-k_B+k_C$) and $k_B-k_A+k_C$ (same as $-k_A+k_B+k_C$) directions, respectively. By only changing timing, the rephasing and non rephasing signals can both be collected in the $-k_A+k_B+k_C$ phase matched direction. Note that both signals could also be collected in the other direction but is less convenient with the BOXCARS setup.

In the BOXCARS geometry, the beams are aligned to be three corners of a diamond, providing a convenient location for the echo signal. Since the order of the pulses dictates the origins of the echo, keeping a reference for the timing between the first and second pulses, τ, is critical. By convention, τ is said to be positive when pulse A is the first pulse (rephasing) and is negative when pulse B is the first pulse (non-rephasing).

2.4.3: Pump Probe Experiment Setup

The collimated light is sent into a beam splitter separating a small fraction (~7%) from the parent beam which will be used as the probe. The remaining 93% of the parent beam was chopped and used as the pump. Once again, the pulses for each beam are temporally separated through the use of delay stages. The pump and probe beams are overlapped in the sample with the transmitted probe being aligned into the monochromator and onto the MCT array. The scatter from the solid-state samples in Chapter 5 was reduced through a fibrillation method developed in the Massari Lab by Spector and coworkers.[104]

2.5: 2D-IR Design and Results

The rephasing and non-rephasing regions of the interferogram of a scan at a given T_w are separately Fourier transformed. The original time axis, τ, is now a frequency axis, ω_τ, and is used as the x-axis for the 2D-IR plots. Each Fourier transformed slice is plotted as a function of monochromator frequency, ω_m, thus providing the y-axis of the 2D plot. Both the rephasing and non-rephasing data are transformed into 2D plots. It is at this point that the two plots are added together resulting in the purely absorptive 2D-IR plot. The mathematical derivation of the purely absorptive 2D-IR signal can be found in numerous comprehensive reviews and books,[102, 103] as such we will only discuss the significance of the outcomes.

The vibrational echo signal is measured by heterodyned detection on a solid state detector. Heterodyne detection is the result of interference between the echo signal and a stronger local oscillator (LO) field. The signal from the detector is the square of the echo and the LO electric fields.

$$S(t) = \left|E_{sig} + E_{LO}\right|^2 = E_{LO}^2 + 2E_{sig}E_{LO} + E_{sig}^2 \tag{2.9}$$

The signal from the local oscillator is removed by subtracting off a reference spectrum, which is the laser spectrum of the local oscillator on the detector when the echo is not being emitted. The signals remaining are the cross term and the echo signal. Experimentally, the local oscillator electric field is optimized to be a few orders of magnitude stronger than the echo field so that the cross term dominates the signal in Equation 2.9. As a result, the

phase information contained in the echo electric field is preserved. The emitted echo signal is complex with both the real and imaginary terms containing a combination of the absorptive and dispersive lineshapes. In the end, the purely absorptive lineshape is optimal, as it offers a significant improvement in spectral resolution, enhancing the technique's ability to distinguish between peaks and to measure dynamics. Although the echo is complex, the heterodyne signal contains only real components, so any idea of separating the signals through post processing is not viable. To solve this problem we must step back to our previous discussion of the rephasing and non-rephasing pathways.

The rephasing pathways are distinguished from the non-rephasing pathways by the flipping of the coherence after interacting with the third pulse. Conveniently, the conjugation of the coherences results in equal but opposite dispersive components for the rephasing and non-rephasing signals. The dispersive components simply cancel out when the rephasing and non-rephasing signals are added, leaving purely absorptive lineshapes. Collecting both the rephasing and nonrephasing signals is covered in Section 2.5.1.

Experimentally, the plot is typically not ready for analysis at this point as phase errors have distorted the data. Phase corrections can be applied to account for these errors. The application and optimization of these corrections is often referred to as phasing. The equations used during phasing are listed below.[105]

$$S_{2DIR}(\omega_m, \omega_\tau) = S_R(\omega_m, \omega_\tau)\Phi_R(\omega_m, \omega_\tau) + S_{NR}(\omega_m, \omega_\tau)\Phi_{NR}(\omega_m, \omega_\tau) \tag{2.10a}$$

$$\Phi_R(\omega_m, \omega_\tau) = \exp[i(\omega_m\Delta_{3,LO} + \omega_\tau\Delta_{1,2} + Q_1\omega_m^2 + Q_2\omega_m\omega_\tau)] \tag{2.10b}$$

$$\Phi_{NR}(\omega_m, \omega_\tau) = \exp[i(\omega_m\Delta_{3,LO} - \omega_\tau\Delta_{1,2} + Q_1\omega_m^2 + Q_2\omega_m\omega_\tau)] \tag{2.10c}$$

Both the rephasing and non-rephasing signals are multiplied by separate phase corrections prior to their addition. The phasing parameters are manually floated to optimize the spectrum following both external and internal constraints. $\Delta_{1,2}$ and $\Delta_{3,LO}$ are phase errors associated with the timing between the first and second pulses and the third pulse and local oscillator respectively. Q_1 and Q_2 are phasing errors associated with the chirp of each beam. Setting up the experiment, the number of optics each beam travels through is carefully thought out as to not introduce more chirp in one beam compared to others, but the number of beam splitters needed to set up the experiment makes matching the chirp difficult.

Phasing of the data can be a nebulous process, so it is important to apply as many constraints as possible. First the projection of the 2D-IR plot onto the ω_m axis should overlap with the pump probe spectrum of the same sample.[106] The pump probe projection method is widely accepted as the most important metric of well phased data. Although the technique is typically taught through an easier physical interpretation, pump-probe spectroscopy is a third order self-heterodyned technique. Since the first two photons come from the pump and the third pulse and local oscillator come from the probe, the $\Delta_{1,2}$ and $\Delta_{3,LO}$ phase errors are zero. While it is not clear how much error is associated with chirp of the two beams, a pump-probe spectrum is assumed to be free of phase errors.[106] Phasing the 2D-IR projection so that it matches the phase perfect pump-probe lowers the error in the correction. The projection is especially sensitive to the values of the $\Delta_{3,LO}$ and chirp phasing parameters but has less sensitivity for the $\Delta_{1,2}$ parameter. The application of additional phasing constraints, along with pump-probe projection, is often necessary. Another common approach is to compare the purely absorptive spectrum to the absolute

value spectrum, that is, the addition of the absolute values of the rephasing and non-rephasing signals. This method is primarily sensitive to the $\Delta_{1,2}$ parameter, providing a second constraint to the phasing process. In addition to these constraints, it is important to check the quality of the phasing using the following metrics: Are the 0-1 and 1-2 peaks centered vertically over one another? This can be checked by projecting the spectrum onto the ω_τ axis. Are the peaks symmetrical? The peaks should only be symmetrical *if* there is only a single ensemble/population and the bond has a sufficient anharmonicity. Interference between two close peaks will appear as asymmetry.

Correctly phased spectra can be seen in the bottom of Figure 2.5. Understanding the intricacies of a 2D-IR plot can take some time but a basic description of how to interpret a 2D-IR plot follows. Each plot will have two axes, ω_τ and ω_m, the origins of which were previously described. The ω_τ and ω_m axes can be thought of as the excitation and emission axes, respectively. In other words, ω_τ is the frequency of light that originally excites the oscillators into the initial coherence state and ω_m is the frequency of the emitted echo. A 2D-IR spectrum is therefore a correlation plot between the frequencies of light absorbed and emitted during the pulse sequence. Each plot will have at least two peaks, by convention, a positive going 0-1 peak that lies on the diagonal and a negative going 1-2 peak that lies below the 0-1 peak. The anharmonicity of the bond is the distance between the maxima of the two peaks parallel to the monochromator axis. If we take a step back and think about the origins of these two peaks, the general layout of a 2D-IR plot makes sense. At modest temperatures, the population of the 1-2 peak is negligible and so the first excitation is into the 0-1 coherence state at a frequency, ω_{01}. The pulse sequence occurs and some oscillators will emit from the 0-1 coherence at a frequency, ω_{01}, while others are

excited into the 1-2 coherence where they emit an echo at a frequency, ω_{12}, where $\omega_{12} = \omega_{01} - 2\omega\chi$. So the 0-1 peak is found where the excitation and emission involve only the 0-1 transition ($\omega_\tau = \omega_m = \omega_{01}$) and the 1-2 peak is found where the system is first excited into the 0-1 transition but emits the echo from the 1-2 transition ($\omega_\tau = \omega_{01}, \omega_m = \omega_{12}$). Many 2D-IR studies involve multiple excited modes, which result in interesting 2D-IR spectra where peaks can lie off-diagonally whenever the peaks are anharmonically or chemically coupled. The scope of this thesis does not require further knowledge of these crosspeaks, however detailed descriptions of these phenomena can be found elsewhere.[100-102]

All the dynamical information accessible to 2D-IR spectroscopy lies within the shape of the 0-1 or 1-2 peaks. While both peaks often provide equivalent information,[102, 103] the 0-1 peak will be used to study the dynamics. The two-dimensional peak shape holds information about correlation between an oscillator's original frequency and its frequency after the course of the pulse sequence. Depending on the system, a probe vibration may experience a frequency shift due to oxidation or reduction, chemical reaction, or molecular dynamics. The systems that were studied during the course of this thesis were chemically inert on the ultrafast time scales of this experiment. Any frequency shifts during the window of the pulse sequence are thus assumed to be the evolution of the oscillator's chemical environment via molecular dynamics. Highly correlated frequencies indicate that the chemical environment has not significantly changed on the time scale of the pulse sequence and result in narrow peaks along the diagonal. Highly uncorrelated frequencies indicate that the chemical environment changed significantly through a previously discussed dynamic broadening mechanism and result in very round, almost circular peaks.

It is important to remember that each 2D-IR spectrum is for a specific T_w. Just because a peak is highly correlated at short T_w's does not mean it will be correlated at longer T_w's.

Figure 2.5 illustrates this concept of frequency correlation and the role broadening mechanisms play in the peak shape. The first example is an inhomogeneously broadened system where the dynamics are significantly slower than the vibrational lifetime of the mode. Regardless of the length of the pulse window, the peak remains highly correlated and the motions are deemed static. Many solid state systems, such as silica glasses, fall into this category. In these static systems, the antidiagonal width of the 2D peak comes from the homogeneous broadening of the subensembles. The second system has a similar inhomogeneity as the first system but has dynamics with timescales within the window of the pulse sequence. At early T_w's, the peaks are still highly correlated because the molecules have not had enough time to evolve. However at later T_w's, the molecular motions allow the oscillators to sample other subensembles and the peak broadens. The second system exemplifies why multiple T_w's are taken of a sample. While an individual 2D-IR spectrum will indicate whether or not dynamics have occurred over the course of the experiment, it is not until 2D-IR spectra at varying T_w's are compared that our understanding of the dynamics really develops.

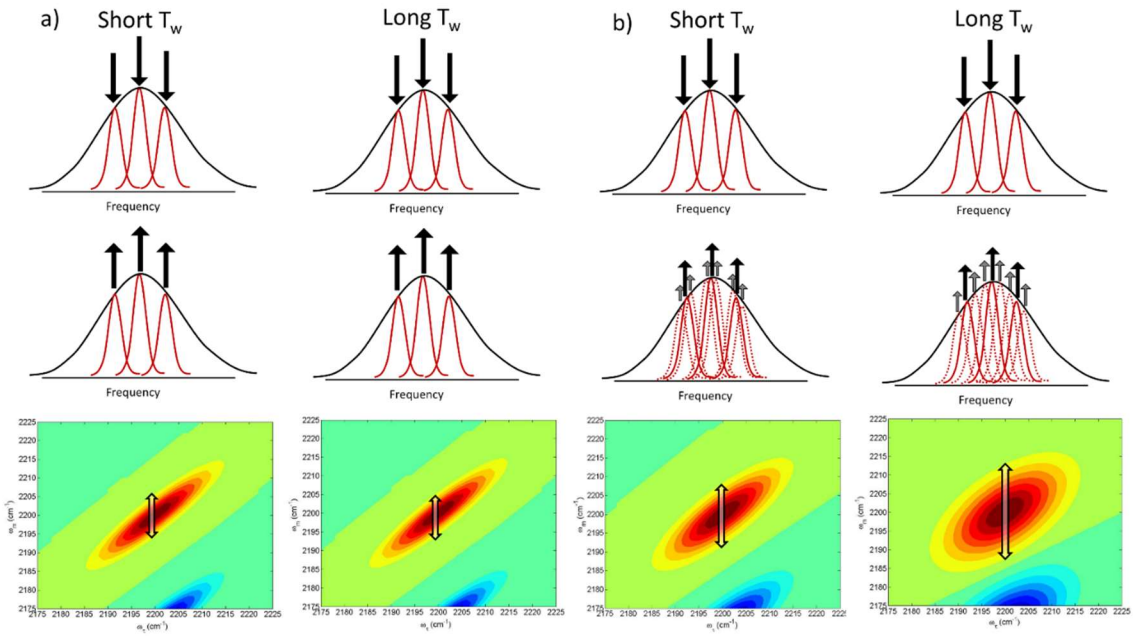

Figure 2.5 Illustration of spectral diffusion for a "static" system (2.5a) and a system with slow yet resolvable dynamics (2.5b). Both examples include 2D spectra at short and long T_w's.

2.6: Quantifying 2D-IR Data

Quantifying the peak shapes in 2D-IR spectra is imperative for retrieving dynamical information. We will start this 2D-IR discussion with the broad scope of vibrational echo spectroscopy (VES). The first VES experiments prompted the discovery of a phenomenological link between the time constants captured by vibrational ultrafast spectroscopy and dynamic motions within the sample. Fayer and coworkers were the first to find this link which they termed the Frequency-Frequency Correlation Function, FFCF or $C(t)$. [5] Empirically, $C(t)$ fits to a multi-exponential decay of the following form.

$$C(t) = \frac{\delta(t)}{T_2} + \sum_i {\Delta_i}^2 \exp\left(\frac{-t}{\tau_i}\right) \tag{2.11}$$

Equation 2.11 is the sum of i exponential decays, each of which have a specific time constant, τ_i, and amplitude, Δ_i^2, for the specific dynamic motion i. The number of decays

needed is dependent on the complexity of the sample. In the case of solid-state materials, it is common to need a static term where $\tau_{static} = \infty$. The Δ_i values are interpreted as the magnitudes of frequency fluctuations induced by the surroundings, and, when squared as in Equation 2.11, effectively weight the motion's contribution to the dephasing.

The FFCF details the contribution of both the homogeneous and inhomogeneous broadening to dephasing. The exponential decays encapsulate only the time constants for dynamics involved in spectral diffusion. The additional term at the beginning of Equation 2.11 captures the homogeneous dephasing and thus the homogeneous linewidth. As discussed previously, heterodyned 2D-IR spectroscopy provides significantly more information than previous homodyned VES experiments with shorter acquisition time. The amount of data provided by 2D-IR necessitates a more efficient method of ascertaining the FFCF. Understanding that both broadening sensed by the 2D-IR peak shape and the dephasing of the macroscopic polarization sensed by the time dependent echo signal are described by the same mechanism, it is evident that there must be a connection between peak shape and the FFCF, used previously for VES experiments. The most successful peak shape analysis methods have been able to relate their respective metric to the FFCF.

Eccentricity,[107] nodal slope,[108] and inhomogeneity index[109] methods have been implemented with varying success, but by far the two most common methods are the Center Line Slope (CLS) and Ellipticity methods. Both the CLS and Ellitpticity methods have been used to fit the data presented in Chapters 3-5 and will be the focus of this section. Starting with the CLS method, it was first developed by Kwak and coworkers in 2007 and quickly became popular due to its direct relationship to the normalized frequency-frequency correlation function, $\overline{C_n}(t)$.[5] The CLS method analyzes the 0-1 peakshape by

taking slices through the peak along the ω_τ axis, parallel to the ω_m axis. These slices are fit with a Gaussian and the centers of each Gaussian is plotted as a function of ω_τ and fit with a linear function. The slope of this line, called the center line slope, can vary from zero to one depending on whether the 0-1 peak is uncorrelated or highly correlated. When the peak is highly correlated, it is elongated along the diagonal and the maxima are centered along the diagonal as well, resulting in a CLS of one. When the peaks are uncorrelated, the antidiagonal width is the same as the diagonal width and the maxima are centered at the same frequency, resulting in a CLS of zero. The decay of the CLS as a function of T_w is directly proportional to the $\overline{C_n}(t)$.

$$CLS(T_w) = \overline{C_n}(t) = \sum_i {\Delta_i}^2 \exp\left(\frac{-t}{\tau_i}\right) \tag{2.12}$$

Like the Equation 2.11, the normalized FFCF succeeds in capturing the time constants of the dynamics contributing to spectral diffusion, but it fails to obtain any information about the homogeneous dephasing. Furthermore, the amplitudes in Equation 2.12 do not hold any physical meaning, used only to weight the specific decays based on the dynamic's contribution to dephasing. In their seminal work, Kwak and coworkers derived a method of solving for the full FFCF using $\overline{C_n}(t)$ and the linear peak shape provided by FTIR.[5]

The Ellipticity method for peak shape analysis was first published by Lazonder and coworkers in 2006 and was adapted for use in 2D-IR experiments by Andrei Tokmakoff.[4, 110] As opposed to CLS, ellipticity directly compares the diagonal and antidiagonal widths of the 0-1 peak.

$$E = \frac{\left(\Delta\omega_{diag}\right)^2 - \left(\Delta\omega_{antidiag}\right)^2}{\left(\Delta\omega_{diag}\right)^2 + \left(\Delta\omega_{antidiag}\right)^2} \tag{2.13}$$

The widths, $\Delta\omega$, can be defined as the diagonal and antidiagonal full widths at half max (FWHM) for a given peak. It is worth noting that as long as the same metric is used for both the diagonal and antidiagonal widths, any width (i.e. 1/e) could be used to calculate E. Like CLS, the ellipticity decay as a function of T_w is directly proportional to $\overline{C_n}(t)$.

$$E(T_w) = \overline{C_n}(t) = \sum_i \Delta_i{}^2 \exp\left(\frac{-t}{\tau_i}\right) \tag{2.14}$$

Even though the Kwak method of converting $\overline{C_n}(t)$ to $C_n(t)$ was meant for the CLS method, it is equally viable for the Ellipticity method.

From Equation 2.13 and Equation 2.14, it follows that the two methods are mathematically equivalent. Whether or not the two methods are equally sensitive to the peak shape is up for debate. Kwak showed that the CLS method was insensitive to apodization of the interferogram, permitting the artificial reduction of noise in the spectrum.[5] Roy and coworkers showed that multiple methods as well as anti-diagonal width analysis captured 2D-IR peak shapes with equal validity.[111] Huber and coworkers have suggested that the ellipticity method is better suited to characterize very heterogeneous systems such as solvent enriched silica sol-gels.[7] In these silica matrix systems, the CLS method was found to be noisier and also less sensitive to the dynamics of the intercolated solvent than the Ellipticity method.

2.7: Analyzing Pump-Probe Spectra

In vibrational pump-probe experiments, a sample is irradiated with a chopped pump beam followed by a much weaker probe beam. The probe beam is sent into the detector

and a difference spectrum between when the pump is on and off is produced. For the work presented here, spectra with the pump off is subtracted from spectra with the pump on.

$$I_{pump\ probe} = I_{pump\ on} - I_{pump\ off} \tag{2.15}$$

Note that the sign convention used here is opposite of the typical transient absorbance experiment. The pump-probe signal given by Equation 2.15 is positive when the pump is on, whether through increased transmission or the emission of photons.

Thorough descriptions of the pump probe processes can be found elsewhere, but brief description follows.[112, 113] Before the arrival of either the pump or probe pulses, the system is assumed to be primarily in the ground state at room temperature. Since the pump and probe beams are split from the same beam, they necessarily have the same bandwidth and center frequency, typically tuned to the vibration of interest. When the pump pulse interacts with the sample, a small portion of the oscillators are excited into the first excited state. Now after some time delay, T_w, the probe pulse is sent through the sample. With some population in both the ground and first excited states, the probe pulse can interact with the sample in three different ways. Some photons will excite oscillators from the ground state to the first excited state, while other photons will initiate stimulated emission in excited oscillators resulting in the relaxation of the oscillators and the emission of a photon of the same energy. Finally, since the probe pulse has a ~200 cm^{-1} band width, another portion of the photons will excite oscillators from the first excited state to the second excited state. In contrast, when the pump is blocked, all of the oscillators are assumed to be in the ground state, limiting the interactions to only 0-1 excitation.

When the pump is on, the ground state is less populated and more of the probe at ω_{01} is transmitted, while at the same time stimulated emission of photons at ω_{01} and excited state absorption at ω_{12} can occur. The increased transmittance, called the ground state bleach, and the stimulated emission result in positive I_{pp} at ω_{01}. Conversely, the excited state absorption results in negative I_{pp} at ω_{12}. Even though two processes contribute to the signal at ω_{01} and only one contributes to the signal at ω_{12}, their signals have the same magnitude. Figure B6a illustrates generated pump probe spectra for different T_w's. This figure shows that as the time between the pump and probe pulses increases, I_{pp} decreases due to the relaxation of the excited state. In the limit of an infinite delay, every excited state would relax and the system would no longer have any "memory" of the pump excitation, behaving as if the pump is off. Since I_{pp} is a function of the excited state population, pump probe experiments are often used to determine the lifetime of the excited state. Figure 2.6b is a pump-probe decay where, I_{pp} is plotted at a specific frequency as a function T_w. To find the vibrational lifetime, T_1, the decay in Figure 2.6b is fit with an exponential decay.

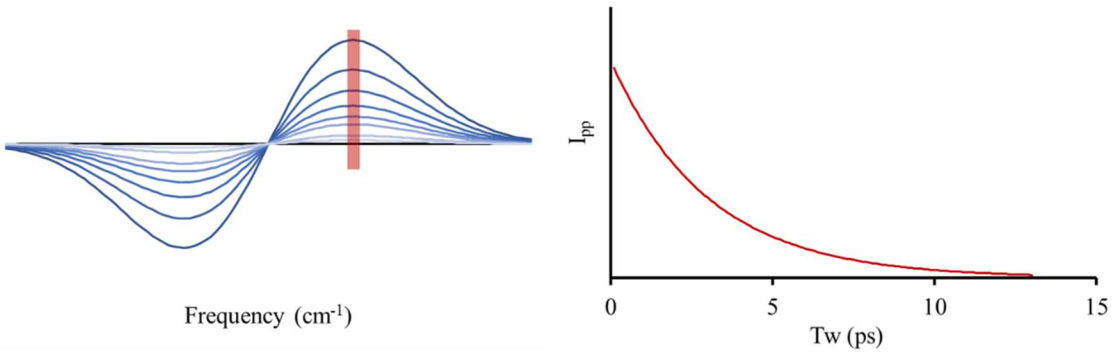

Figure 2.6 Simulations of both a) pump-probe spectra as a function of T_w and b) a pump-probe decay at a selected frequency.

Chapter 3: Vibrational Solvatochromism in Vaska's Complex Adducts

ABSTRACT: The vibrational solvatochromism of bis(triphenylphosphine) iridium(I) carbonyl chloride (Vaska's complex, VC) was investigated by FTIR spectroscopy. The carbonyl stretching frequency (ν_{CO}) was measured in 16 different organic solvents with a wide range of Lewis acidities for VC and its dioxygen (VC-O_2), hydride (VC-H_2), iodide (VC-I_2), bromide (VC-Br_2), and sulfide (VC-S_X) adducts. The ν_{CO} of the VC-O_2 complex was sensitive to the solvent electrophilicity, whereas minimal correlation was found for VC and the other adducts. The stretching frequency of the trans O_2 ligand on VC-O_2 was measured to be anticorrelated with ν_{CO}, supporting a model in which this ligand indirectly affects the carbonyl frequency by modulating the extent of metal-to-CO backbonding. The ν_{CO} values obtained from DFT calculations on VC adducts with solvent continua and explicit hydrogen bonds were used to aid the interpretations of the experimental results. The O_2 ligand is more susceptible to stronger specific solvent interactions and it binds in a fundamentally different mode from the monatomic ligands, providing a more direct communication channel with those metal d-orbitals that have the appropriate symmetry to backbond into the carbonyl π* orbital.

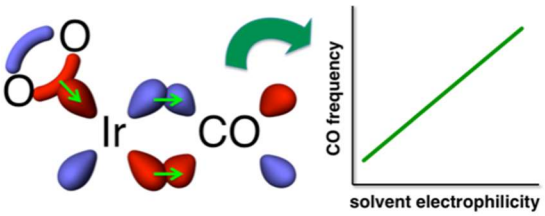

3.1: Introduction

Static and dynamic solvent-solute interactions have been implicated as key variables in some of the most important reaction types, from electron transfer to catalysis.[42, 114, 115] Developing a basic understanding of these interactions can often be achieved by monitoring chromatographic mobilities[21, 25, 116] or spectroscopic features, such as solvatochromic shifts of electronic absorption and emission spectra,[27, 117, 118] NMR chemical shifts,[24, 26, 119, 120] and vibrational frequencies[121-128] across a range of solvent types. Using these approaches, the characteristics of the solvation environment can be correlated with a systematic change in a spectral feature to provide some insight into the origins of chemical reactivity in different solvents. Yet, the collective influence of a solvent on the solute is complex, with each solvent having its own unique combination of properties (polarizability, electrophilicity, nucleophilicity, etc.). Often there is no single physical property or solvent parameter that can account for the given solvent dependence of a spectral feature. As a result, a number of empirical solvent parameter scales have been defined.[119, 120, 129-131] While the properties that these systems characterize are sometimes interrelated, they are not perfectly correlated, with each capturing a unique subset of the total intermolecular interactions.[22]

In some cases, combinations of parameters, termed linear solvation energy relations (LSER), have been utilized in an effort to capture the spectroscopic observations. For example, the LSER approach developed by Kamlet and Taft has been useful in correlating spectral features with a solvent parameter that is defined as a weighted sum of the solvent polarizability (π^*), Lewis acidity or normalized acceptor number (AN^N), and Lewis basicity or normalized donor number (DN^N).[23] By optimizing the weighting coefficients for these

terms, the relative importance of their contributions to the solvation process can be assessed. In other cases, a single solvent parameter has been shown to be sufficient to properly correlate measured values. For example, molecular vibrational frequencies have been shown in several studies to have a strong correlation with the Lewis acceptor number (AN), a scale that was developed by Gutmann from ^{31}P-NMR chemical shifts of triethylphosphine oxide in a broad range of solvents.[119, 120] Symons and coworkers reported that the carbonyl stretching vibration on acetone had a strong correlation with AN, with the C=O frequency shifting to lower wavenumbers with increasing AN.[125] The authors noted that the sensitivity to this parameter when other solvation metrics showed no correlation was due to the electron rich oxygen being particularly perturbed by the electrophilicity of the solvent. Several other groups have demonstrated a similar red-shifting of carbonyl frequencies for organic molecules as a function of the solvent AN.[121, 122, 124] On the other hand, Bacelon and coworkers reported a linear blue shifting of the CN stretching vibration for the thiocyanate ion with solvent AN, indicating that the solvent electrophilicity was experienced by the sulfur atom thereby strengthening the CN bond.[121]

The vibrational frequencies of organometallic complex ligands have also shown strong correlation with AN values, although the through-metal interactions can lead to more complex behavior. For example, Estrin and coworkers showed that the stretching frequency of a nitrosyl ligand on the pentacyanonitrosylferrate(II) ion, $[Fe(CN)_5NO]^{2-}$, actually blue shifted with increasing solvent electrophilicity.[126] On the basis of steric arguments, the authors asserted that the solvation shell interacted primarily with the nitrogens on the CN ligands and the oxygen on the NO ligand, but that there was preferential interaction of the electrophilic solvents with the cyanide groups. DFT

calculations confirmed that greater electron density resided on the cyanide nitrogens and that increasing the AN of the solvent drew electron density away from the metal and out of the NO antibonding π* orbital leading to the observed blue shift. Interestingly, the calculations also showed that the electron density in equatorial cyanide orbitals was not significantly perturbed by the electrophilicity of the solvent, whereas the axial cyanide showed complementary changes to the trans nitrosyl ligand.[126] This example highlights the fact that solvatochromic effects in organometallic complexes depend upon the balance of forces between ligands in the coordination sphere that share orbital symmetry.

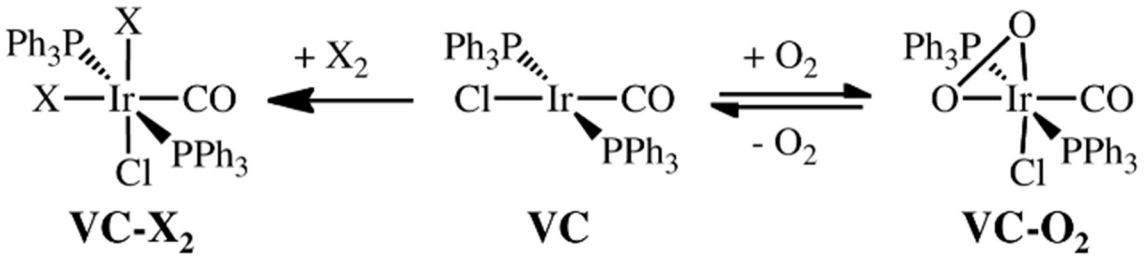

Scheme 3.1. VC and VC adduct structures, X = H, Br, I, S_X.

We recently reported that the vibrational frequency of a carbonyl ligand (ν_{CO}) on bis(triphenylphosphine) iridium(I) carbonyl chloride, also known as Vaska's complex (VC, Scheme 3.1), was independent of the solvent type whereas the ν_{CO} of the oxygen adduct (VC-O_2, Scheme 3.1) showed solvatochromic shifts for a limited set of solvents (benzene, chloroform, and *N,N*-dimethylformamide (DMF)).[42] The ν_{CO} on organometallic complexes is well documented to be a reporter of the degree of backbonding from the metal d_π orbitals into the π* antibonding orbital on the CO.[132, 133] When binding to a metal ion, the lone pair of electrons on the carbon atom of a carbonmonoxide ligand adds into a metal d-orbital of appropriate symmetry, such as the d_{z2} or d_{x2-y2} orbitals in an octahedral complex

(Figure 3.1), forming a σ-bond. In turn, the metal ion pushes electron density back out into the antibonding π* orbital on the CO, thereby strengthening the metal-ligand interaction through a π-bond, and weakening the carbon-oxygen bond. As the degree of backbonding is increased, the CO bond is weakened and its vibrational frequency is lowered; VC is commonly cited as a textbook example of this effect.[132, 133] However, a systematic study of the influence of the surrounding solvent on the ν_{CO} has not been reported. Based on previous reports of solvatochromism for organic carbonyls and metal-bound CO and NO ligands, it was unexpected that the CO frequency on VC was found in our study to be nearly insensitive to the nature of the solvent.[42] Even more surprising, the ν_{CO} for the on VC-O_2 adduct was blue shifted as the solvent electrophilicity increased.[42] We hypothesized that the absence of vibrational solvatochromism in VC and its presence for VC-O_2 was the result of the trans dioxygen ligand having a specific stronger interaction with the surrounding solvent than the other four ligands on the complex. In this way, the O_2 ligand serves as an antenna to the electrophilicity of the solvent, changing the electron density on the metal center and indirectly shifting the ν_{CO} by changing the extent of backbonding.

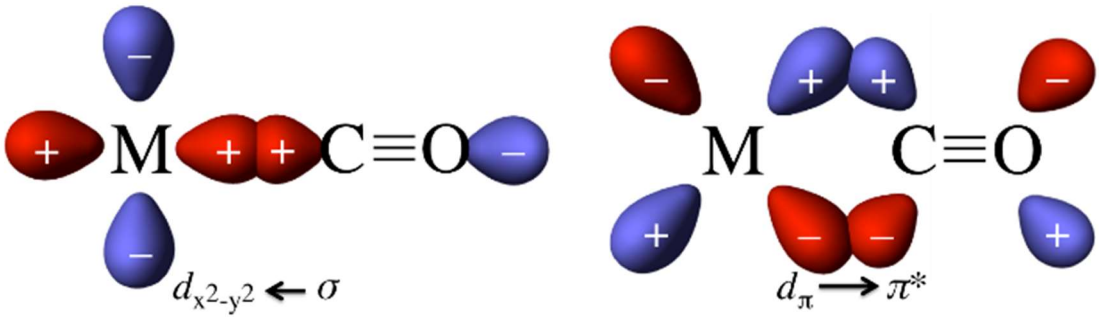

Figure 3.1. Bonding mechanism of a carbonyl to a metal ion showing σ-donation into a d-orbital with appropriate symmetry (d_{x2-y2} shown) and π-bond formation by back bonding from a d_{π} orbital to the π* antibonding orbital on the ligand.

In the current study, we have greatly expanded on the vibrational spectroscopic studies of VC, measuring the ν_{CO} across 16 solvents for VC and its oxygen (VC-O_2), hydrogen (VC-H_2), bromide (VC-Br_2), iodine (VC-I_2), and sulfide (VC-S_X) adducts. We have also carried out detailed density functional theory (DFT) calculations of two VC adducts with and without solvent continuum models, as well as explicit hydrogen bonding interactions, to aid in the interpretation of the experimental results. The experimental and computational data support our previous assertion of solvatochromism for the dioxygen adduct, but also reveal a new perspective on the effectiveness of a *trans* ligand in perturbing the ν_{CO} for an organometallic compound. The observed trends (or lack thereof) are explained in the context of ligand field theory.

3.2: Experimental and Theoretical Methods

Experiment

Bis(triphenylphosphine)iridium(I) carbonyl chloride (Vaska's complex, VC, 99.99% purity), bromine (99.5+%), and sulfur (pestanal) were used as received from Sigma Aldrich. Iodine was used as received from Fisher. Acetone and N,N-dimethylformamide (DMF) were used as received from Mallinckrodt Chemicals. Benzene, benzyl alcohol, chlorobenzene, chloroform, dichlorobenzene, dichloromethane, dimethylsulfoxide (DMSO), pyridine, and toluene were used as received from Sigma-Aldrich. Acetonitrile was used as received from J.T. Baker and tetrahydrofuran (THF) was used as received from EMD chemicals. Solutions of VC were prepared by adding 1.0 mL of solvent to ~5 mg of VC. The majority of the oxygenated VC samples (VC-O_2) were prepared by allowing

deoxygenated VC solutions in each solvent to equilibrate with air under ambient conditions for >24 hours. Identical spectra were obtained in less time (6-10 hours) by purging the headspace over the solutions with pure oxygen, hence some VC-O_2 samples were prepared using this method. Solutions of the iodide adduct of VC (VC-I_2) were prepared by dissolving ~3.5 mg of solid iodine along with ~5 mg of VC into each solvent. Solutions of the hydride adduct of VC (VC-H_2) were prepared by bubbling hydrogen gas through a freshly made VC solution (~5 mg of VC in 2.0 mL of solvent) for approximately 30 minutes. Solutions of the bromide adduct (VC-Br_2) were prepared by dissolving 5 mg of VC with 0.7 μL bromine in 1.0 mL of each solvent. Solutions of the sulfide adduct (VC-S_X) were prepared by dissolving 5 mg of VC in 1.0 mL of each solvent with 1 mg of sulfur. All solutions were prepared and studied at room temperature. The AN values for toluene, chlorobenzene, dichlorobenzene, and trichlorobenzene were not available in the literature, but were determined experimentally by monitoring the carbonyl stretching frequency of acetone.[125] A small aliquot of acetone was added to each solvent (~0.135 M solutions), and the FTIR spectra were collected following the procedure below. The toluene, chlorobenzene, and *o*-dichlorobenzene ANs were determined to be 10, 9, and 14.1, respectively.

The liquid sample cells were prepared by sandwiching each VC solution between two 3 mm CaF_2 windows with a 50 micron Teflon spacer. Due to the low solubility of VC in some of the solvents, a 200 micron Teflon spacer was used in some cases to increase the pathlength. The FTIR spectra were collected on a Nicolet 6700 FTIR spectrometer (Thermo Scientific) with an average of 64 scans and a resolution of 2 cm^{-1}. Spectra were collected for the neat solvents using the same experimental parameters and subtracted from

the corresponding VC spectra without scaling. The carbonyl peaks were fit with a Gaussian lineshape with the center of the Gaussian reported as the center frequency in Table 3.1. The FTIR spectra of the O-O vibrations were collected in a similar manner, but required the use of NaCl windows on the sample cell.

Theory

Gas-phase structures for VC-O_2 and VC-Br_2 were fully optimized at the M06-L level of theory[134] employing the 6-31G(d) basis set[135] for non-metal atoms and the (8s7p6d2f)/[6s5p3d2f] basis set and relativistic pseudopotential of Martin and coworkers[136] for iridium. To probe the influence of changes in the electronegativity of substituents *trans* or *cis* to the carbonyl group, structures were re-optimized with Br or O nuclear charges adjusted by ± 0.04 a.u.

Uncharged structures were also re-optimized including continuum solvation effects using the SMD solvent model.[137] Benzene and benzyl alcohol were chosen as solvents. In addition to "pure" continuum solvation, microsolvated structures were optimized containing one benzyl alcohol molecule coordinated more or less to substituents either *trans* or *cis* to the carbonyl, with the supermolecule still embedded in a SMD benzyl alcohol continuum. For all minima, analytic harmonic frequencies were computed. All calculations made use of the *Gaussian09* suite of electronic structure programs.[138]

3.3: Results and Discussion

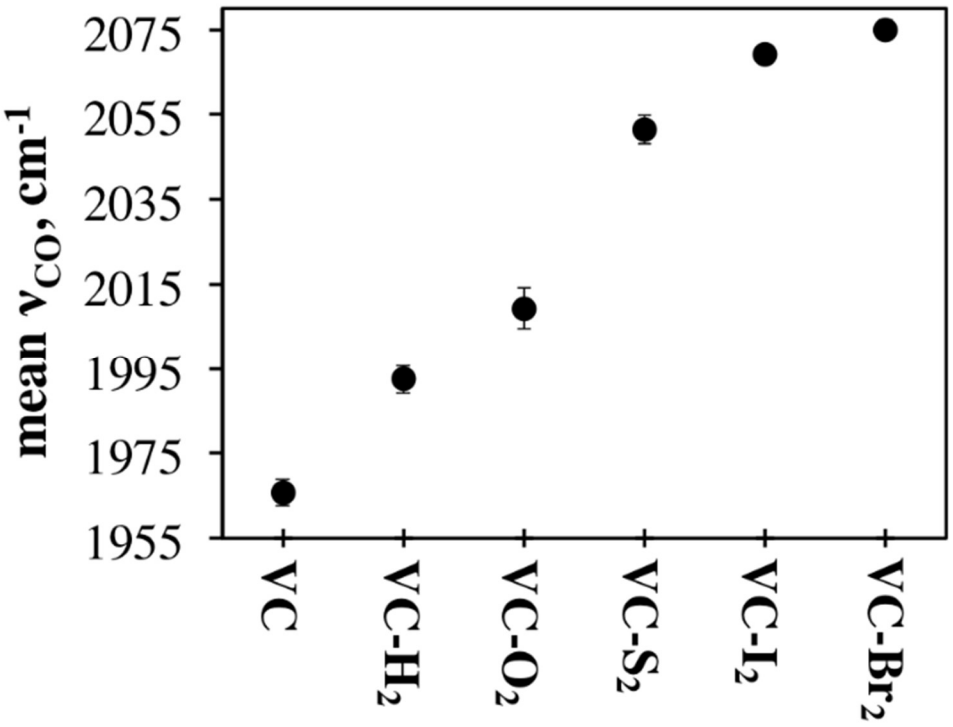

Figure 3.2. Mean ν_{CO} values for VC, VC-O_2, and VC-I_2 in 16 different solvents, and VC-H_2, VC-S_X, and VC-Br_2 in 15 different solvents. Error bars indicate the standard deviations from the mean across all solvents measured.

The vibrational frequency of the iridium-bound carbonyl (ν_{CO}) on VC is sensitive to the ligand environment around the metal.[132, 133] This is apparent in Figure 3.2, which compares the mean ν_{CO} measured for each of the adducts in all 16 solvent systems used in this study. The ν_{CO} for VC exhibits the lowest frequency at 1965.7 cm^{-1} and oxidative addition of any of the studied ligands results in a shift to higher frequency. The increased oxidation number of the iridium from 1+ to 3+ leaves less electron density available for metal-to-ligand backbonding, thereby blue shifting the ν_{CO}. This plot shows that the oxidizing effect of these ligands bound to VC increases in the order Br^- > I^- > S_X > O_2 > H-, which tracks their Mulliken electron affinities of 3.37 > 3.06 > 2.08 > 1.46 > 0.75 eV,

respectively.[139, 140] The error bars on each mean value reflect the smaller deviations that were exhibited for a given complex across many different solvents (discussed in detail below), but it is clear from this figure that the identity of the trans ligand has a much larger effect on the ν_{CO} than the surrounding solvation shell.

It was previously noted that the ν_{CO} for VC was independent of the solvent when comparing only benzene, DMF, and chloroform.[42] Figure 3.3 shows ν_{CO} measured for VC in 16 different solvents (see Table 3.1 for all numerical values) as a function of AN. The baselined and normalized FTIR spectra showing the ν_{CO} peak for VC and all adducts in all solvents are provided in Section 3.5 at the end of this chapter. In the following discussion, we plot the ν_{CO} against AN based on literature precedent noted above for correlation between this parameter and vibrational frequencies. Attempts to correlate the ν_{CO} for VC (as well as all other adducts) with the donor number (DN), polarizability (π^*), polarity index (P'), and Reichardt's $E_T(30)$ are displayed in Section 3.6 at the end of this chapter, but resulted in no meaningful correlations for any of the complexes studied. Figure 3.3 shows that the ν_{CO} values for VC measured in the majority of these solvents do not vary by more than a few wavenumbers; 13 of the 16 solvents resulted in ν_{CO} values that were within one standard deviation of the mean, and the values are randomly distributed around the mean as a function of AN. The coefficient of the correlation squared (R^2) for the entire dataset is only 0.47, showing weak correlation between the AN and ν_{CO}. However, there are a few notable changes that can be identified. In particular, the most electrophilic solvents demonstrated a gradual blue-shift in the ν_{CO}. Empirically, we found it useful to categorize the solvents as hydrogen bond donating (blue triangles), chlorinated solvents (red squares), and all other solvents (black circles) in the following discussion.

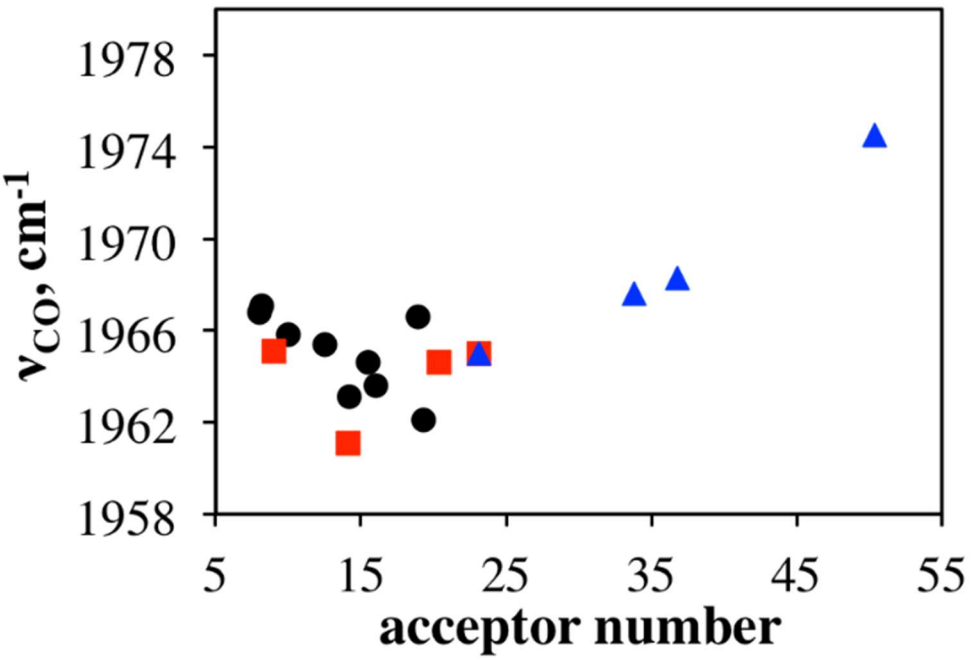

Figure 3.3. Measured ν_{CO} values for VC as a function of AN in hydrogen bond donating (blue triangles), chlorinated (red squares), and other (black circles) solvents

In Figure 3.3, it is clear that the only solvents that have even a minor influence on the ν_{CO} are the most electrophilic, the hydrogen bond donating solvents. This might be interpreted as arising from a weak hydrogen bond with the lone pairs on the carbonyl oxygen,[141] but this seems unlikely to be the case since a hydrogen bond would red-shift the ν_{CO}. Furthermore, as will be shown below, some of the adducts of VC do not show this frequency shift in these solvents. An alternate explanation of the monotonic ν_{CO} shift for the hydrogen bond donating solvents is that these solvents interact directly with the iridium, which is possible in VC's square planar geometry. Yet, aside from this subset of solvents, the ν_{CO} on VC is fairly insensitive to the surrounding solvent. This suggests that the iridium-bound CO ligand by itself is not readily perturbed by direct interactions with the solvent, nor by the indirect influence of the solvent on the chloride and triphenylphosphine ligands.

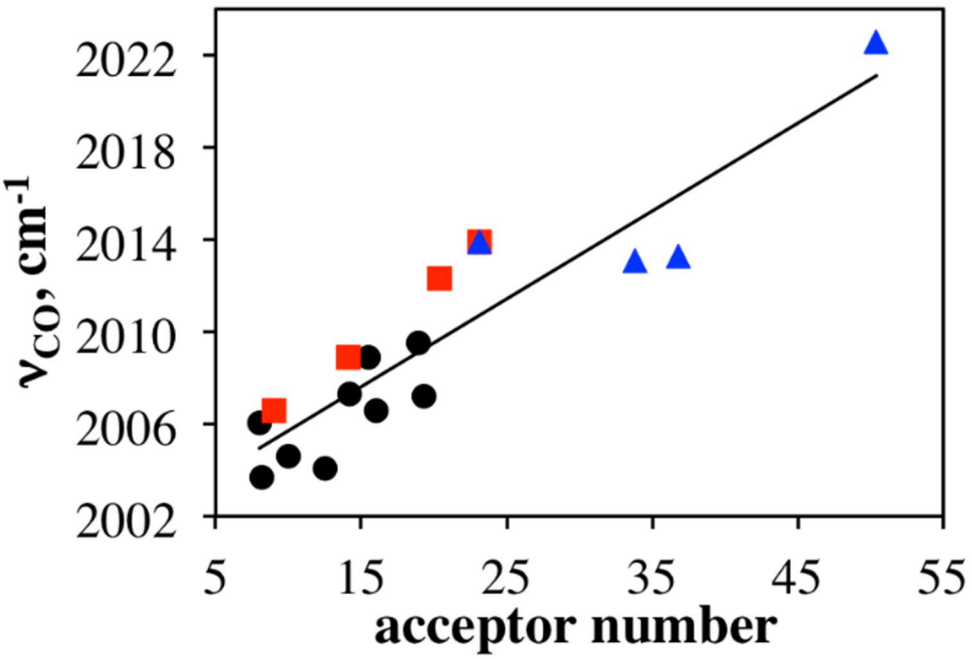

Figure 3.4. Measured ν_{CO} values for VC-O_2 as a function of AN in hydrogen bond donating (blue triangles), chlorinated (red squares), and other (black circles) solvents.

In contrast, Figure 3.4 shows that the ν_{CO} on the VC-O_2 adduct clearly displays vibrational solvatochromism for the 16 solvents studied. The dioxygen ligand is unique among those studied here in that it retains the diatomic nature of an O_2 molecule upon addition to VC, which has led to a great deal of interest in this species as a model for oxygen carrying organometallic systems.[142-144] As such, the geometry of the VC-O_2 adduct is not as ideally octahedral about iridium as in the other cases. Table 3.1 demonstrates that for VC-O_2 the ν_{CO} shifts by nearly 19 cm^{-1} across the range of solvent studied. Even within each of the sub-categories defined above, the hydrogen bond donors (blue triangles), the chlorinated solvents (red squares), and the remaining organic solvents (black circles), there is a clear blue-shift with solvent AN. The R^2 value for linear regression across the full dataset is 0.85, which indicates that 85% of the variation in ν_{CO} can be considered to be linearly correlated with the solvent AN. An LSER treatment was employed in an attempt to improve the correlation, but resulted in coefficients that put nearly all of the weight on

the AN^N variable (not shown). The linear regression shown in Figure 3.3 indicates a blue-shift of 0.38 cm^{-1} per AN unit. Taken together with the lack of solvatochromism for VC (Figure 3.3), this is further support for our hypothesis that the dioxygen ligand imparts a sensitivity to the surrounding solvent.[42] Consistent with the work by Bacelon and coworkers in which the nitrosyl frequency was modulated by the trans cyanide ligand,[121] the dioxygen on VC-O_2 is an electron rich ligand that is readily influenced by the electrophilicity of the surrounding solvent. Thus, the solvatochromism of the ν_{CO} is an inductive effect whereby the electrophilicity of the solvent polarizes the electron density on the O_2 ligand, which thereby draws electron density off of the iridium and out of the π^* CO orbital.

Table 3.1. Compilation of AN, and measured ν_{CO}, ν_{OO}, $\nu_{Ir\text{-}H}$ values for all 16 solvents.

solvent	acceptor number, AN [a]	ν_{CO} (cm^{-1})						ν_{OO} (cm^{-1})	$\nu_{Ir\text{-}H}$ (cm^{-1})
		VC	VC-H_2	VC-O_2	VC-S_X	VC-I_2	VC-Br_2	VC-O_2	VC-H_2
THF	8	1966.8	1991.4	2006.1	2049.5	2069.2	2075.5	--[c]	2094.9
benzene	8.2	1967.1	1991.8	2003.7	2053.4	2068.8	2075.9	862.5	2091.5
chlorobenzene	9 [b]	1965.1	1990.1	2006.6	2051.4	2068.7	2075.9	861.6	2095.8
toluene	10 [b]	1965.8	1990.4	2004.6	2054.1	2069.1	2075.4	862.6	2092
acetone	12.5	1965.4	1991.9	2004.1	2048.6	2070.5	2074.2	--[c]	2095.7
o-dichlorobenzene	14.1 [b]	1961.1	1991.7	2008.9	2046.2	2068.8	2075.7	861.0	2089.8
pyridine	14.2	1963.1	1989.6	2007.3	2058.1	2067.9	2076.6	--[c]	2090.5
benzonitrile	15.5	1964.6	1990.3	2008.9	2053.8	2068.3	2074.1	--[c]	2095.7
DMF	16	1963.6	1989.9	2006.6	2047.7	2069.4	2076.5	--[c]	2093.8
acetonitrile	18.9	1966.6	1991.6	2009.5	2046.7	2068.6	2075.9	859.2	--[c]
DMSO	19.3	1962.1	1989.6	2007.2	2049.9	2068.2	2067.7	--[c]	2091.1
dichloromethane	20.4	1964.6	1994.2	2012.3	2054.2	2068.6	2073.5	860.1	2096
chloroform	23.1	1965	1996.7	2013.9	2051.7	2070.1	2076	858.5	2097.7
phenylethanol	33.8	1967.6	--[c]	2013.1	2053.1	2069.3	2076.4	--[c]	--[c]
benzyl alcohol	36.8	1968.3	1996.1	2013.3	2053.2	2069.1	2076.4	853.6	2098
m-cresol	50.4	1974.5	2001.4	2022.6	--[c]	2072.2	--[c]	852.2	2099.4
mean ν		1965.7	1992.4	2009.3	2051.4	2069.2	2075.0	859.0	2094.3
standard dev.		3.1	3.3	4.8	3.3	1.0	2.2	3.8	2.9

a. Acceptor numbers obtained from refs [24, 120] (below) unless otherwise noted.

b. Values obtained from the frequency of acetone carbonyl in this solvent.[125]

c. Peak not observed.

If a redistribution of electron density were occurring, it would be expected that the vibrational frequency of the oxygen-oxygen (ν_{OO}) vibration would also be perturbed. Figure 3.5 shows that this is indeed the case as the ν_{OO} red-shifts with solvent AN. The spectral congestion from the solvent and weak absorptivity of this mode precluded collection in all 16 solvents, but it can be seen that more than half of the solvents showed the expected correlation. The anticorrelation of ν_{OO} with ν_{CO} as the AN is varied suggests that the interactions of the solvent with VC-O_2 shift electron density out of the CO π^* orbital and into the O_2 π^* ligand orbital. However, it has been reported that the ν_{OO} is not always well correlated with O-O bond length as the other iridium-bound ligands are varied, and that this vibrational mode is more complex and involves the motions of the metal center.[145] Nonetheless, the data in Figures 3.4 and 3.5 show that there is a change in the ν_{OO} that mirrors the change in ν_{CO} in support of the inductive influence of the trans dioxygen ligand on VC-O_2.

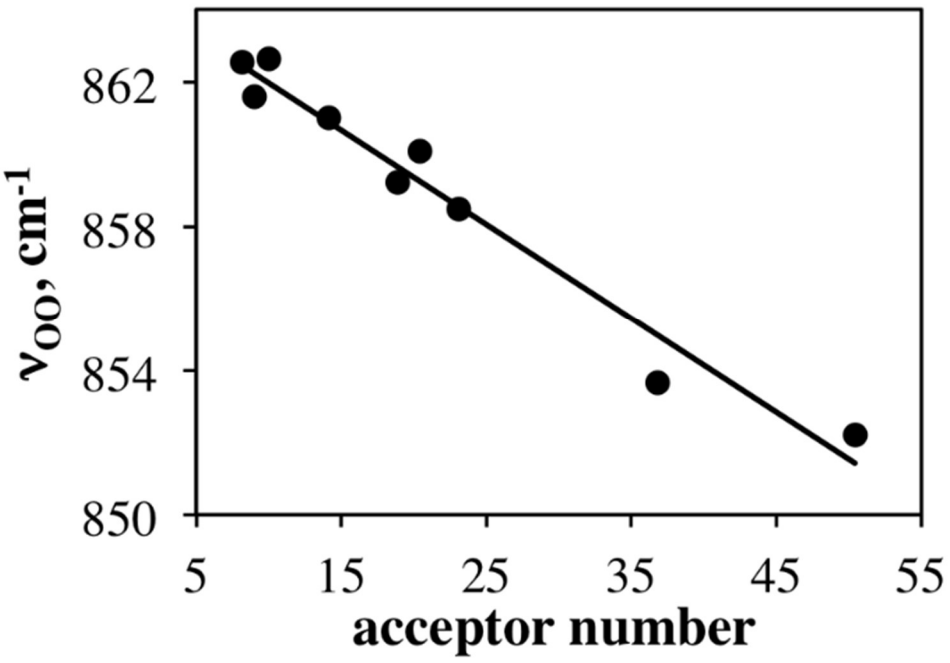

Figure 3.5. Measured ν_{OO} values for VC-O_2 as a function of AN in 9 of the 16 solvents used in this work.

In order to test whether the dioxygen ligand is unique in its ability to influence ν_{CO}, we measured ν_{CO} values for VC-H_2 in the same series of solvents. Unlike the dioxygen ligand, dihydrogen lyses upon oxidative addition leaving it nearly irreversibly bound in VC-H_2 (see Scheme 3.1),[142, 146] although it has been shown that the reductive elimination can be driven photochemically.[147] The complex is octahedral like VC-O_2, but contains two hydrides in place of the O_2 ligand, which coordinate only as σ-donors whereas dioxygen is both a sigma donor and a π-acceptor. The mean ν_{CO} is intermediate to those of VC and VC-O_2 (Figure 3.1). The measured ν_{CO} values are shown in Figure 3.6a and Table 3.1. The y-axis scale is again 22 cm^{-1} for direct comparison to previous figures. Across the entire range of ANs, the ν_{CO} shifts by about 12 cm^{-1}, though the correlation of the entire dataset to a linear regression (not shown) was not overly strong ($R^2 = 0.75$). The ν_{CO} values for VC-H_2 in the non-chlorinated, non-hydrogen bonding solvents (black circles) are insensitive to the nature of the solvent. The same can be said of the hydrogen bonding

solvents (blue triangles), which have slightly higher ν_{CO} values but show a flat response to AN. The ν_{CO} does appear to show a distinct solvent sensitivity in chlorinated solvents (red squares), while the hydrogen bonding solvents (blue triangles) have higher ν_{CO} values on average. Attempts to correlate any of the variations with other solvent parameters were not successful (see Section 3.6). If the influence of the hydride ligand on ν_{CO} were achieved in the same inductive manner as the dioxygen ligand, one would expect that the blue-shift shift in ν_{CO} might be mirrored in the strength of the iridium-hydrogen bond. To this end, the $\nu_{Ir\text{-}H}$ is plotted in Figure 3.6b (values in Table 3.1) and shows that the non-chlorinated and chlorinated solvents have no significant impact on the iridium-hydrogen frequency, and that all of the hydrogen bond donating solvents result in slightly higher $\nu_{Ir\text{-}H}$ values. We conclude that the most electrophilic solvents studied may draw some electron density toward the hydride ligand, thereby strengthening the Ir-H bond and decreasing the extent of metal-to-ligand backbonding onto the CO. However, the effects are small compared to those of the VC-O_2 adduct and the correlation with AN is weak.

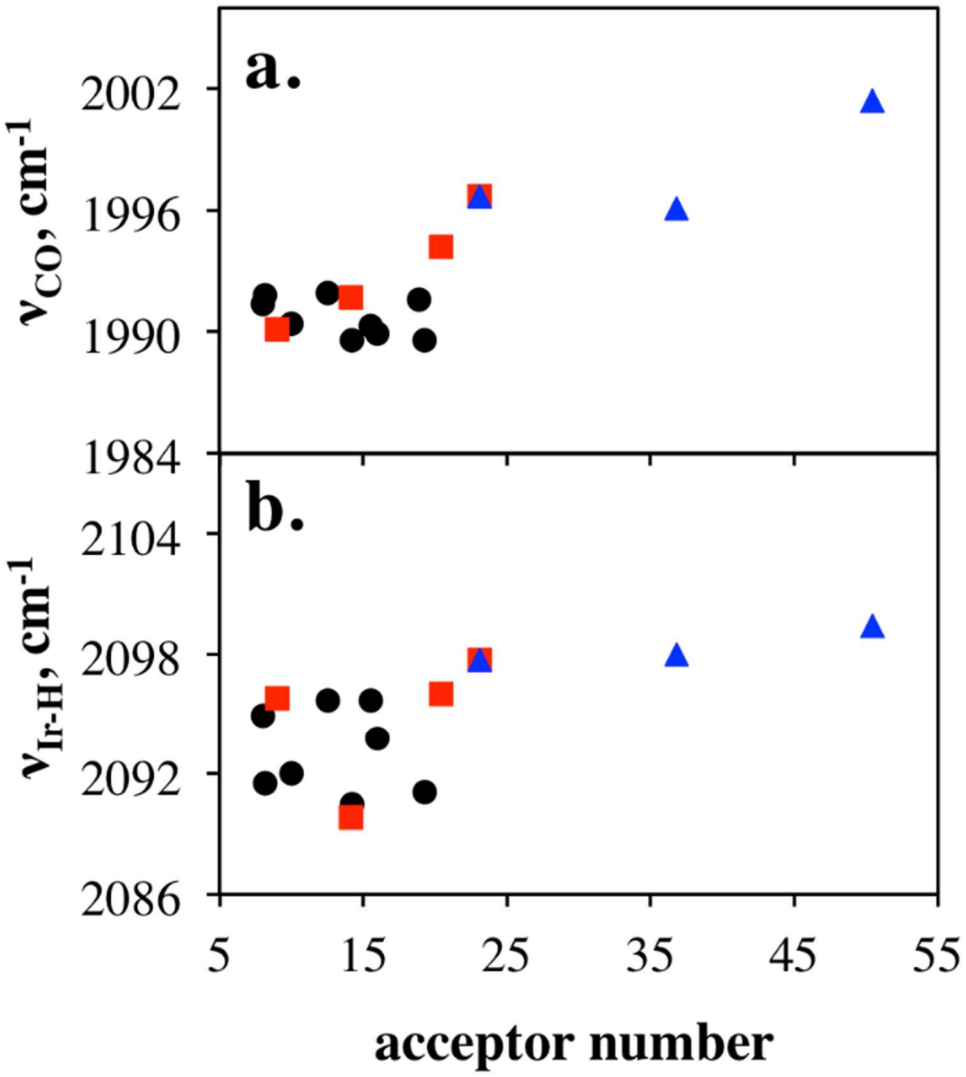

Figure 3.6. a) ν_{CO} values and b) ν_{Ir-H} values for VC-H_2 as a function of AN in hydrogen bond donating (blue triangles), chlorinated (red squares), and other (black circles) solvents

Since the VC-H_2 mean ν_{CO} was intermediate to VC and VC-O_2 (Figure 3.1) and exhibited mild solvatochromism compared to VC-O_2, we decided to explore the possibility that stronger electron withdrawing trans ligands might offer an even more dramatic solvatochromic influence on ν_{CO}. Halide ligands satisfy this requirement and their adducts of VC have been reported previously.[148, 149] Figures 3.7a and 7b show the ν_{CO} for two halogen adducts, VC-I_2 and VC-Br_2, as a function of solvent AN. The hydrogen bond

donating, chlorinated, and remaining solvents are again color coded as blue triangles, red squares, and black circles, respectively, and the y-axis on these plots displays a range of 22 cm^{-1} for direct comparison to the VC-O_2 data in Figure 3.4. It can be seen from Figure 3.7a and Table 3.1 that the ν_{CO} values for VC-I_2 do not shift by more than 1.5 cm^{-1} from the mean frequency in 15 of the 16 solvents studied; the solvent that induced the largest shift, m-cresol, resulted in a ν_{CO} that was only 3 cm^{-1} from the mean. The ν_{CO} in VC-Br_2 in Figure 3.7b shows a similar insensitivity of to the nature of the solvent, although there is one outlier (DMSO) and we were not successful in identifying the peak in m-cresol. The lack of solvent sensitivity of these halide adducts is intriguing. It provides further support for the notion that the iridium-bound CO ligand by itself is not sensitive to the solvation environment. In addition, it demonstrates that the not all electron rich trans ligands have the same solvatochromic influence on ν_{CO} and that the O_2 ligand apparently has a unique channel to modulate the ν_{CO} (Figure 3.4).

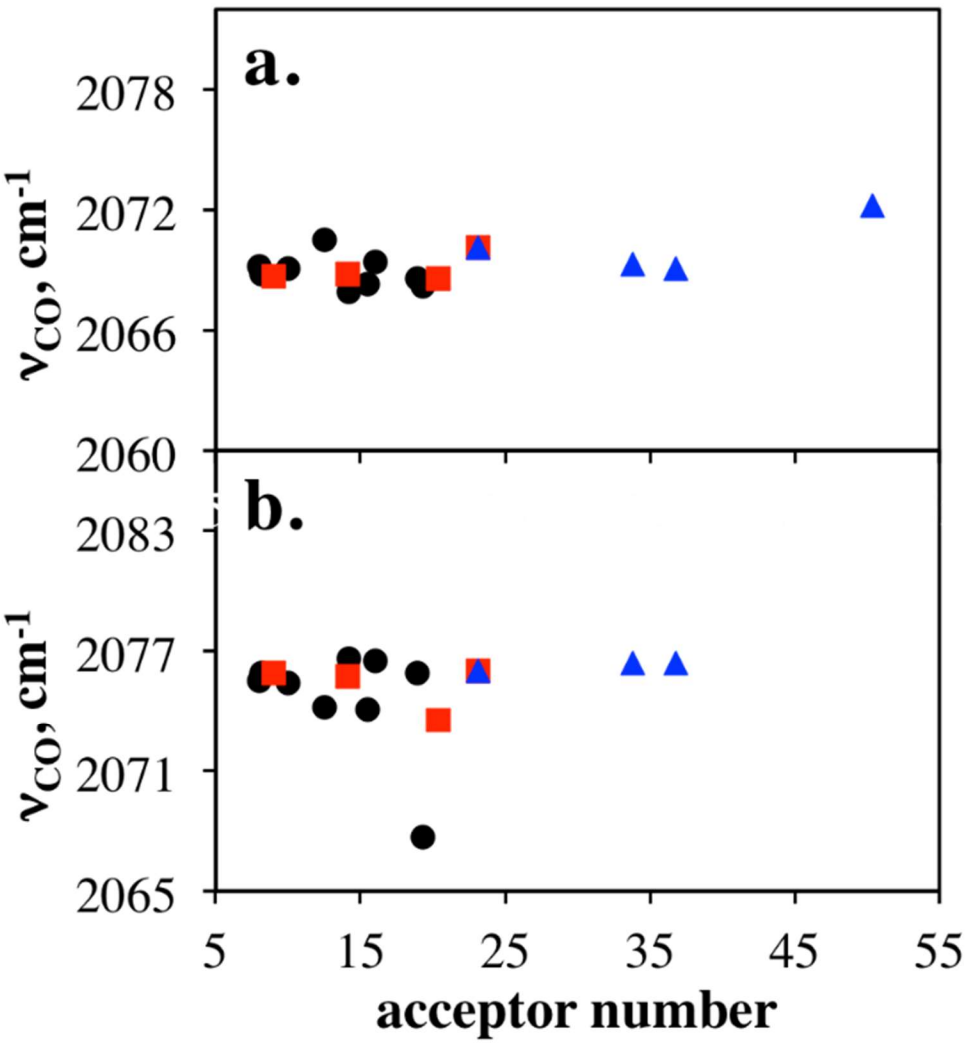

Figure 3.7. Measured ν_{CO} values for a) VC-I_2 and b) VC-Br_2 as a function of AN in hydrogen bond donating (blue triangles), chlorinated (red squares), and other (black circles) solvents.

DFT calculations were carried out on VC-O_2 and VC-Br_2 in order to gain a deeper insight into the possible influence of the surrounding solvent shell on the ν_{CO}. Table 3.2 compiles the experimental and calculated ν_{CO} values from this portion of the study. The calculated ν_{CO} for the adducts in vacuum show the expected trend in that the Br_2 adduct has the higher ν_{CO} by about 41 cm^{-1}, though the experimental ν_{CO} splitting for the adducts is 72 and 63 cm^{-1} for benzene and BA, respectively. To probe the sensitivity of ν_{CO} to

changes in electron withdrawing strength that might be induced by the solvation shell near the O_2 or Br_2 ligands, the electronegativity of each O and Br atom was varied by 0.04 a.u. Table 3.2 shows that these variations indicate that the CO frequency is nearly indifferent to which O atom is modulated. This is probably due to the fact that the O_2 ligand binds in a side-on fashion, forming a sigma bond by donation of the ligand π bond into a d-orbital of appropriate symmetry. A change in either atom results in a change in the electron density in this bonding orbital. In contrast, VC-Br_2 shows that only modulation of the trans Br atom has a significant effect on ν_{CO}, with a 2.8 cm^{-1} average shift after a ±0.04 variation in the electronegativity. It is also important to point out that the magnitude of this frequency shift is comparable to the shifts calculated after the same modulation of either O atom on VC-O_2. Therefore, with equal perturbation of *both* O or Br atoms by the solvation shell, it would be expected that the O_2 ligand could impart a more significant change in the oxidation state of the iridium.

Table 3.2. Comparison of experimental and DFT calculated ν_{CO} values.

adduct	experimental ν_{CO} (cm^{-1})		calculated ν_{CO} (cm^{-1})				
	benzene	BA	vacuum	Δq = ±0.04 a.u.	benzene ∞	BA ∞	BA ∞ + $BnOH_{H\text{-bond}}$
VC-O_2	2003.7	2013.3	2070.7	± 2.4 *cis* ± 3.1 *trans*	2063.5	2045.6	2047.0 *cis* 2052.8 *trans*
VC-Br_2	2075.9	2076.4	2111.3	± 0.5 *cis* ± 2.8 *trans*	2108.1	2088.3	2091.0 *cis* 2088.5 *trans*

Benzene and benzyl alcohol solvent continua (benzene∞ and BA∞, in Table 3.2, repectively) were included in the DFT calculations on the neutral molecules and resulted

in a red-shifting of all ν_{CO} values, moving them closer to the experimental frequencies but maintaining a ~44 cm^{-1} differential between VC-O_2 and VC-Br_2 in either solvent (see Table 3.2). From a solvatochromic perspective, it is intriguing that the calculations predict that there should be an approximately 20 cm^{-1} red-shift for the ν_{CO} on either adduct when going from benzene (low AN) to BA (high AN). Yet, we find that experimentally the ν_{CO} for VC-O_2 exhibits a 10 cm^{-1} blue-shift while VC-Br_2 is insensitive to this solvent change. Clearly, the complexity of solvation is not fully captured by the solvent continua alone (note the extent *explicit* solvent molecules introduce a confining potential associated with exchange repulsion between the solute and solvent molecules, this would be expected to introduce a counteracting *blue* shift, and this may explain the absence of any net shift observed experimentally). In order to improve on these models, calculations were performed for both adducts using the BA continuum but also including an explicit benzyl alcohol molecule oriented so as to make a hydrogen bond to the O_2 or Br ligands. All four fully optimized structures are provided in Figure 3.8.

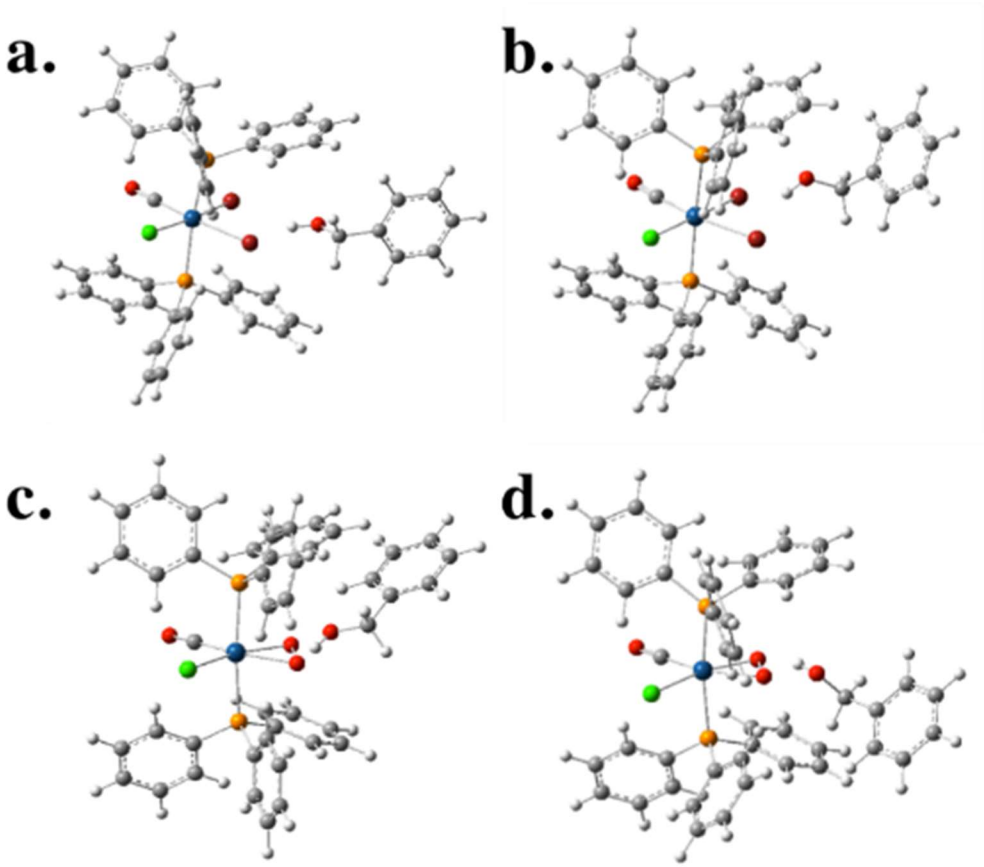

Figure 3.8. DFT optimized structures of a) and b) VC-Br_2 adducts and c) and d) VC-O_2 adducts microsolvated with one benzyl alcohol (BnOH) molecule. Microsolvation was initiated with BnOH with a hydrogen bonding geometry to the *cis* (a and c) and *trans* (b and d) Br/O atoms. Note that attempts to generate a microsolvate for the Br complex analogous to the *cis* coordinated species of the O_2 complex smoothly optimized to the structure shown at upper left, which has weak interactions with both *cis* and *trans* Br atoms.

Hydrogen bonding was imposed at either the *cis* or *trans* atoms in both cases for comparison, however, in the *cis* Br case, the BA molecule smoothly moved around the equator of the metal complex until the hydroxyl hydrogen was roughly midway between the two Br atoms. Table 3.2 shows that all four calculations resulted in a blue-shift in ν_{CO}, but the largest perturbation was calculated for hydrogen bonding to the trans O atom. This shows that the iridium-bound CO on VC-O_2 can be quite sensitive to modulation of the electron withdrawing nature of the O_2 ligand induced by specific solvent interactions, such as hydrogen bonds to the dioxygen lone pairs, and, as for the nuclear charge variation, the

sensitivity is greatest when the *trans* oxygen atom is involved. Such strong interactions, especially in the presence of multiple hydrogen bonds, would be expected to lead to a blue-shifting of the ν_{CO} for the adduct. Likewise, the formation of a strong hydrogen bond to the Br atoms on VC-Br_2 could lead to a smaller blue-shifted frequency, but the optimized structure reveals that this interaction is exceedingly weak with a hydrogen bond length of 2.46 Å in the case of the *trans* H-bonded complex, and 2.6–2.7 Å in the nominally *cis* bonded complex. Thus, despite the shortcomings of the solvent continua, these calculations predict that specific strong interactions are expected at the dioxygen ligand of VC-O_2 leading to a blue-shift of the ν_{CO}. Only weak hydrogen bonding interactions are predicted for VC-Br_2, which begins to explain the insensitivity of its ν_{CO} to the surrounding solvent.

Returning to the solvatochromic trend for ν_{CO} for VC-O_2, we note that the chlorinated and aromatic solvents in Figure 3.4 also follow the blue-shift trend of the hydrogen bonding solvents. In order to understand the vibrational solvatochromism in VC-O_2, and general lack thereof in the other adducts, we consider the bonding orbital interactions for each ligand type. Figure 3.9 shows a graphical representation of the relevant in-plane ligands for the VC adducts, excluding the chlorides in the plane and the triphenylphosphines above and below the plane of the image. Figure 3.9a shows the expected bonding interactions for the dioxygen ligand, in which the π-bond adds into a metal d-orbital to form a sigma bond. Because of the side-on binding mode of this ligand, the orbital into which the oxygen donates electrons is the same symmetry as that which backbonds into the antibonding π* orbital of the CO ligand (d_π).[132, 143, 145] Likewise, the sigma bond donation from the CO ligand pushes electron density into the orbital that has the appropriate symmetry to backbond into the π* orbital of the O_2 ligand (d_{x2-y2}).[132, 143, 145]

(Figure 3.9b). In contrast, the halide and hydride interactions with the metal arise via sigma donation from an s-p hybridized orbital into a d-orbital with the same symmetry as the sigma bond formation with the CO, as shown schematically in Figure 3.9d.[150] For the halides, π-donation can also occur, but is progressively weaker moving down the group, leaving minimal interaction of the halide ligands and no interaction of the hydride ligands with the d_π orbitals that contribute to back bonding to the CO (Figure 3.9c).[150] We rationalize that the solvatochromic behavior of VC-O_2 has its origins in the fact that the dioxygen ligand, by virtue of its side-on ligation, donates electron density into a metal d-orbital that has the appropriate symmetry to back bond into the CO π* antibonding orbital. Any displacement of electron density between the metal and the dioxygen ligand is communicated through the same d_π-orbitals that back bond onto the carbonyl. In contrast, the primary mode of interaction for the halides and the only mode of interaction between the hydrides and the metal is through a higher energy d-orbital, such as the d_{x2-y2}, which does not directly communicate with the CO back bonding d-orbitals.

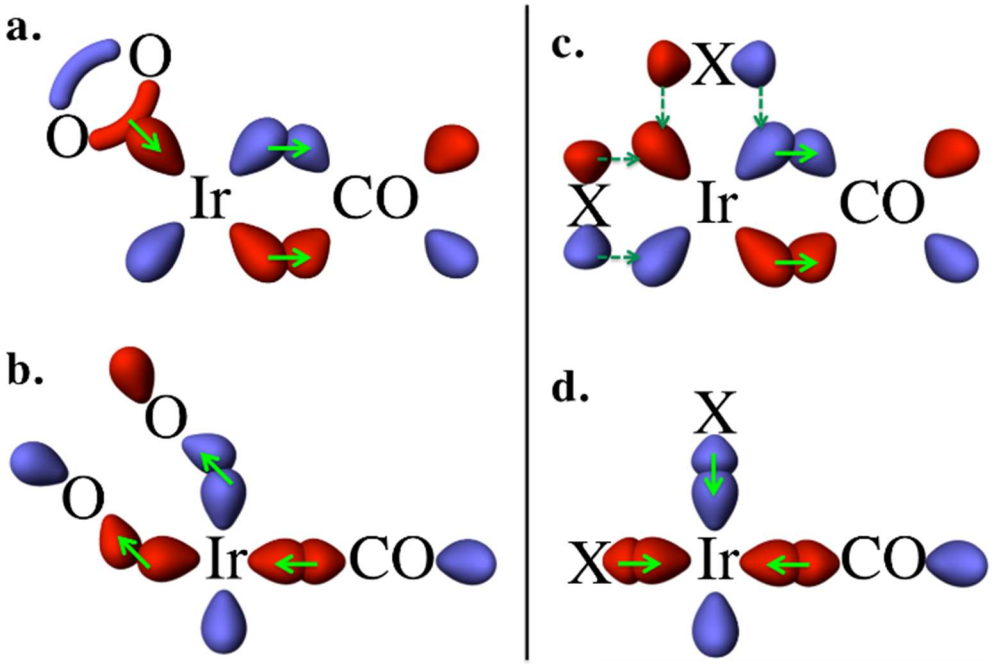

Figure 3.9. Orbital diagram showing binding of O_2 and CO to iridium by a) O_2 π-donation into the d_π orbital which back bonds into the CO π* orbital, and b) CO σ-donation into the d_{x2-y2} orbital that has the appropriate symmetry to back bond into the O_2 π* orbital. In contrast, the coordination of monatomic ligands (X = H, Br, I) proceeds by c) weak or no π interactions with the d_π orbital that back bonds to the CO π*, leaving only d) σ-donation by all ligands into and orbital with d_{x2-y2} symmetry.

The hypothesis that ligands transmit their solvent sensitivity to the trans CO ligand through interactions with the back bonding d_π orbitals can be further tested by measuring the solvatochromic shifts for a similar side-on binding ligand. At first glance, a likely candidate for this experiment is disulfur, however, these ligands are known to exist as several allotropes. The structure of the ligand bound to the VC and related compounds is ambiguous based on literature reports that it is either diatomic S_2,[151-154] or a polyatomic allotrope such as S_6.[132, 155] Hence, we label this adduct as VC-S_X. We carried out the spectroscopic measurements to determine ν_{CO} for many of the solvents used above, but found no clear trend in the data as a function of AN or any of the other solvent parameters tested for correlation (Section 3.6).

3.4: Conclusions

We have examined the vibrational solvatochromism for the carbonyl ligand on Vaska's complex and several of its adducts across a broad range of solvents. It is well-established that the ν_{CO} is a very sensitive reporter of the oxidation state of the iridium following oxidative addition to form VC adducts, but there is little reported on how the solvation shell interactions are reflected in the ν_{CO}. Surprisingly, we have shown that the ν_{CO} for VC and certain adducts is nearly insensitive to the surrounding solvent, which we interpret as a lack of specific strong solvent-solute interactions with any of the ligands, including the carbonyl itself. However, we show that the dioxygen ligand imparts a particular sensitivity to the electrophilicity of the solvent. A comparison of VC-O_2 to other octahedral hydride and electron-rich halide adducts suggests that the key to the solvent sensitivity depends not only on the electron density on a ligand, but also on the metal d-orbitals that are involved in coordination. DFT calculations using low and high acceptor number solvent continua were not able to accurately capture the blue-shifting of ν_{CO} in more electrophilic solvents, but the inclusion of specific hydrogen bonding interactions were able to induce these experimental trends. These calculations predicted that hydrogen bonding interactions were much more favorable with the O_2 ligand over the Br- ligands of VC-Br_2.

Modulation of the electronegativity of trans ligands in the DFT calculations resulted in larger ν_{CO} changes. The mechanism by which the O_2 ligand perturbs the frequency of the *trans* CO ligand appears to be by shifting electron density into and out of a metal d_π orbital that has the appropriate symmetry to back-bond into a π^* orbital on the CO. Unlike the monatomic ligands studied here, the side-on mode of ligation of dioxygen results in σ-

donation into the same metal orbital that back bonds into the π* orbital on the CO. In this manner, the interactions of the dioxygen ligand with the solvent are communicated to the orbital that dictates the vibrational frequency of the carbonyl.

3.5: Full FTIR Set

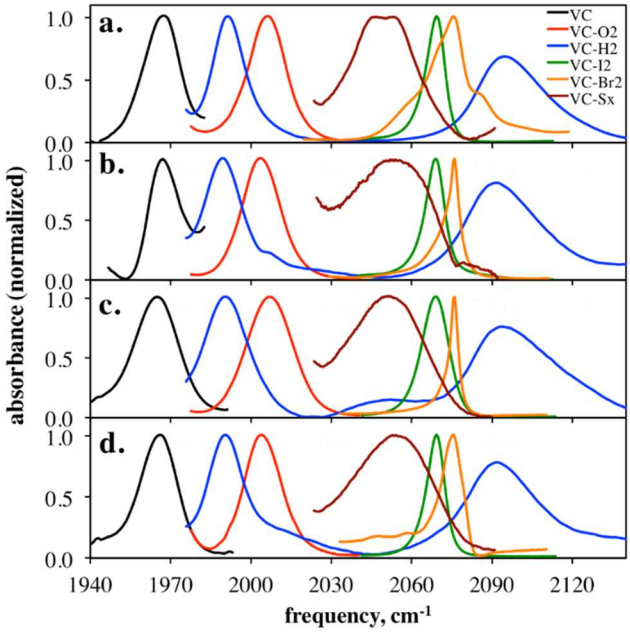

Figure 3.10. Solvent-subtracted, baseline, and normalized FTIR spectra showing the CO stretch (ν_{CO}) for VC, VC-O_2, VC-H_2, VC-Br_2, VC-I_2, and VC-S_X (colors coded as listed in legend) measured in a) THF (AN = 8), b) benzene (AN = 8.2), c) chlorobenzene (AN = 9), and d) toluene (AN = 10). The peak at ~2095 cm^{-1} is the Ir-H stretching mode (ν_{Ir-H}) for VC-H_2.

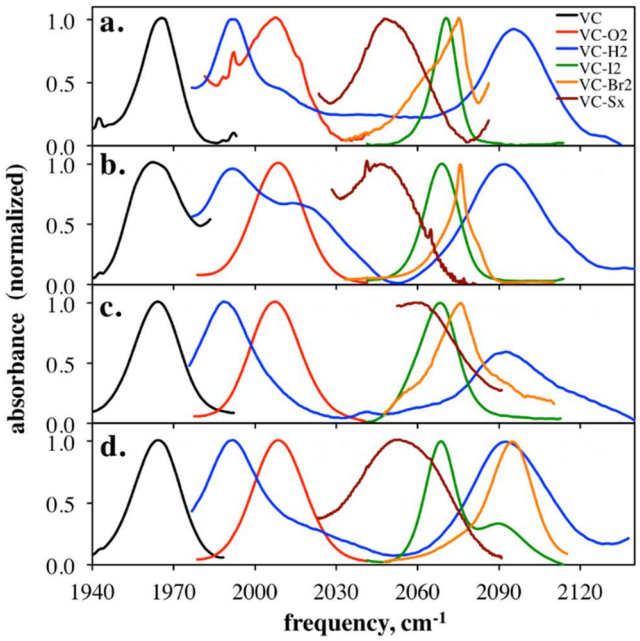

Figure 3.11. Solvent-subtracted, baseline, and normalized FTIR spectra showing the CO stretch (ν_{CO}) for VC, VC-O_2, VC-H_2, VC-Br_2, VC-I_2, and VC-S_X (colors coded as listed in legend) measured in a) acetone (AN = 12.5), b) *o*-dichlorobenzene (AN = 14.1), c) pyridine (AN = 14.2), and d) benzonitrile (AN = 15.5). The peak at ~2095 cm^{-1} is the Ir-H stretching mode (ν_{Ir-H}) for VC-H_2. The extra peak at ~2100 cm^{-1} for VC-Br_2 and VC-I_2 in benzonitrile is the CN stretching mode, presumably coordinated to the iridium.

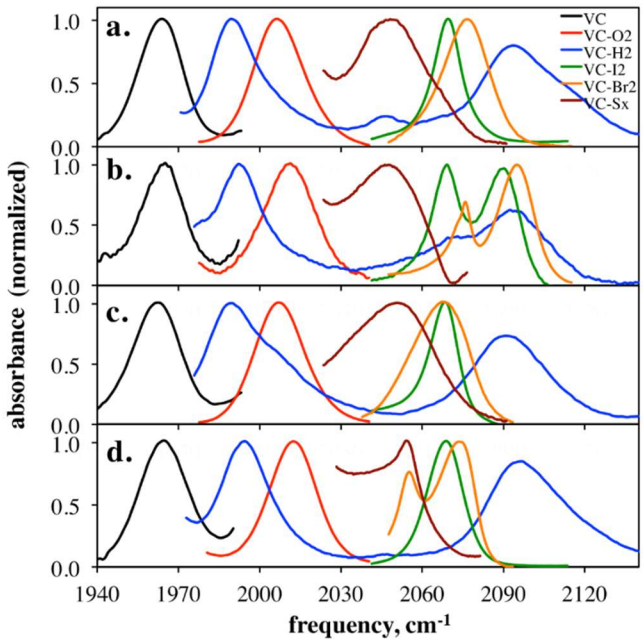

Figure 3.12. Solvent-subtracted, baseline, and normalized FTIR spectra showing the CO stretch (ν_{CO}) for VC, VC-O_2, VC-H_2, VC-Br_2, VC-I_2, and VC-S_X (colors coded as listed in legend) measured in a) DMF (AN = 16), b) acetonitrile (AN = 18.9), c) DMSO (AN = 19.3), and d) dichloromethane (AN = 20.4). The peak at ~2095 cm^{-1} is the Ir-H stretching mode (ν_{Ir-H}) for VC-H_2. The extra peak at ~2100 cm^{-1} for VC-Br_2 and VC-I_2 in acetonitrile is the CN stretching mode, presumably coordinated to the iridium.

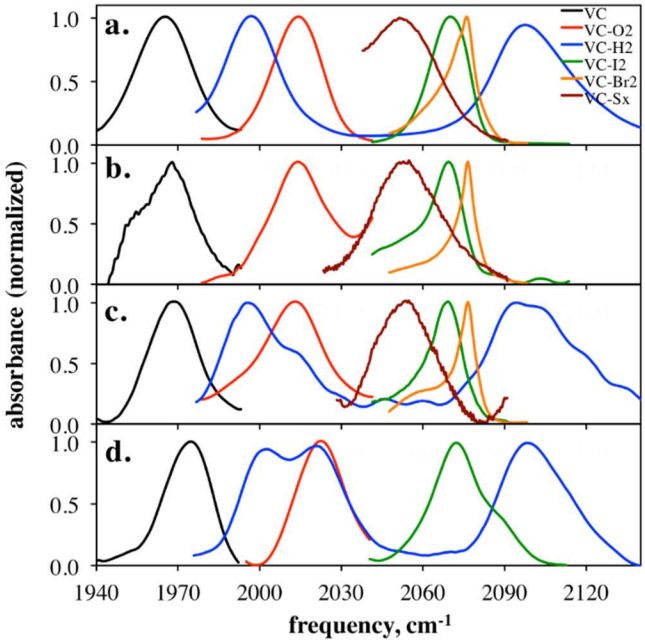

Figure 3.13. Solvent-subtracted, baseline, and normalized FTIR spectra showing the CO stretch (ν_{CO}) for VC, VC-O_2, VC-H_2, VC-Br_2, VC-I_2, and VC-S_X (colors coded as listed in legend) measured in a) chloroform (AN = 23.1), b) phenylethanol (AN = 33.8), c) benzyl alcohol (AN = 36.8), and d) *m*-cresol (AN = 50.4). The peak at ~2095 cm^{-1} is the Ir-H stretching mode (ν_{Ir-H}) for VC-H_2.

3.6: Uncorrelated Parameters

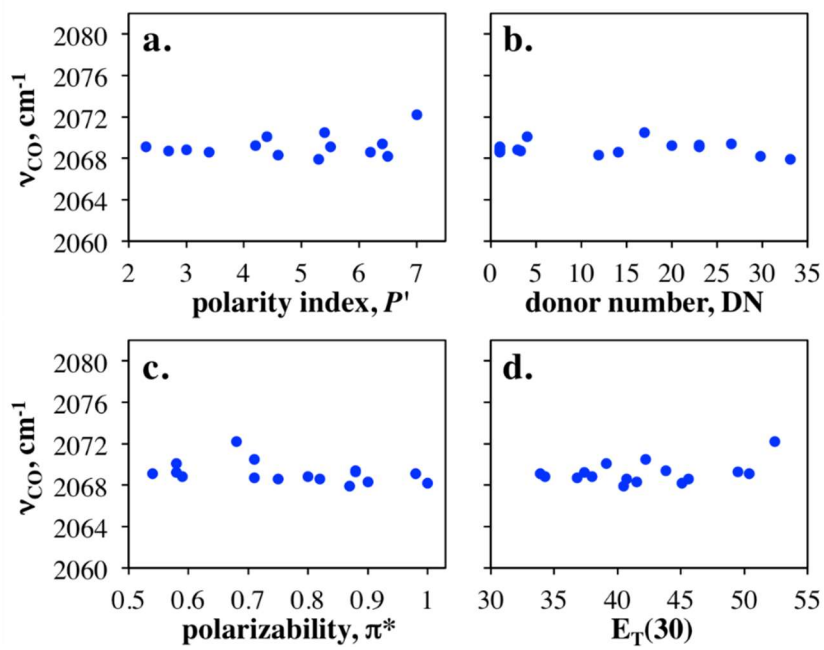

Figure 3.14. Center frequency of the CO stretch (ν_{CO}) for the I_2 adduct of Vaska's complex (VC-I_2) as a function of a) polarity index, b) donor number, c) polarizability, and d) $E_T(30)$

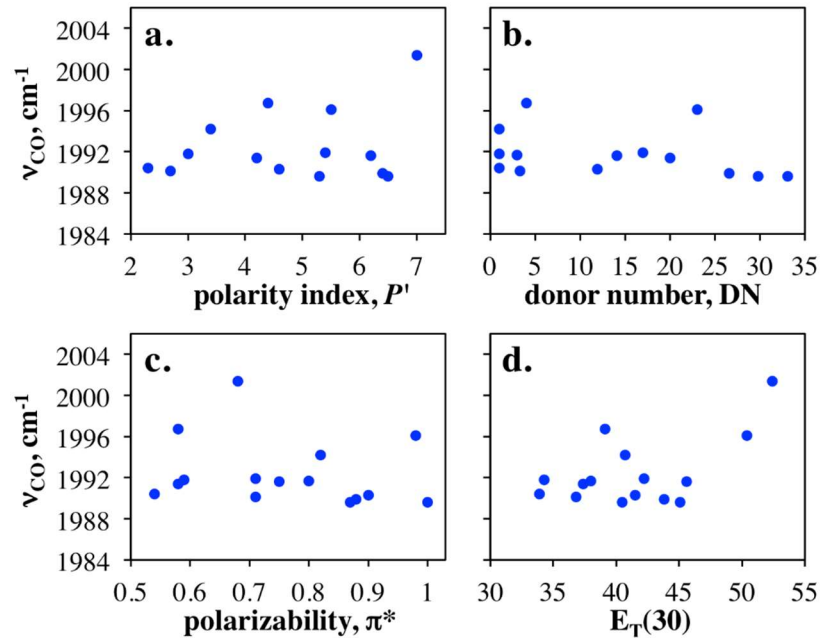

Figure 3.15. Center frequency of the CO stretch (ν_{CO}) for the H_2 adduct of Vaska's complex (VC-H_2) as a function of a) polarity index, b) donor number, c) polarizability, and d) $E_T(30)$.

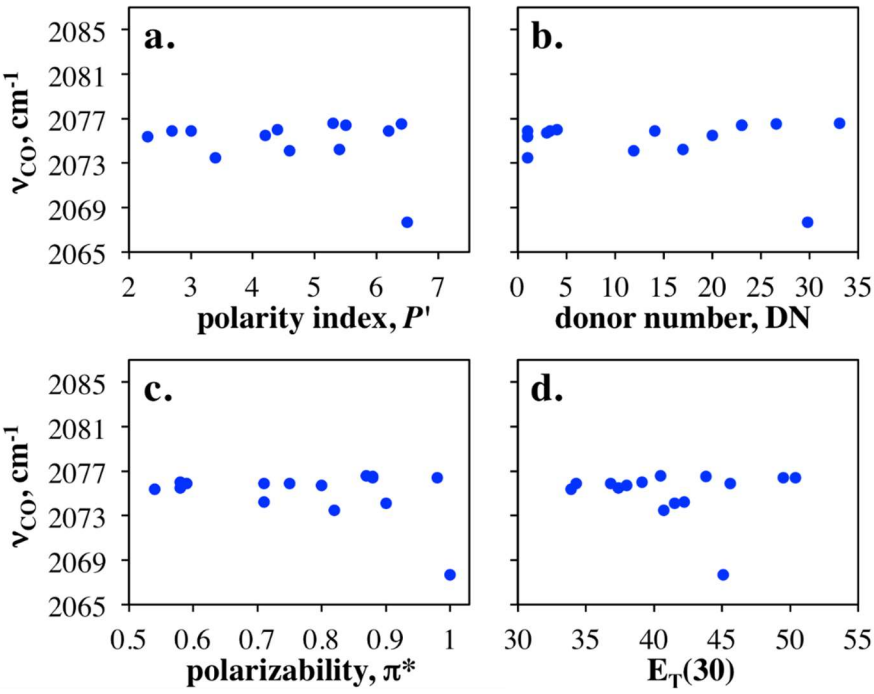

Figure 3.16. Center frequency of the CO stretch (ν_{CO}) for the Br_2 adduct of Vaska's complex (VC-Br_2) as a function of a) polarity index, b) donor number, c) polarizability, and d) $E_T(30)$.

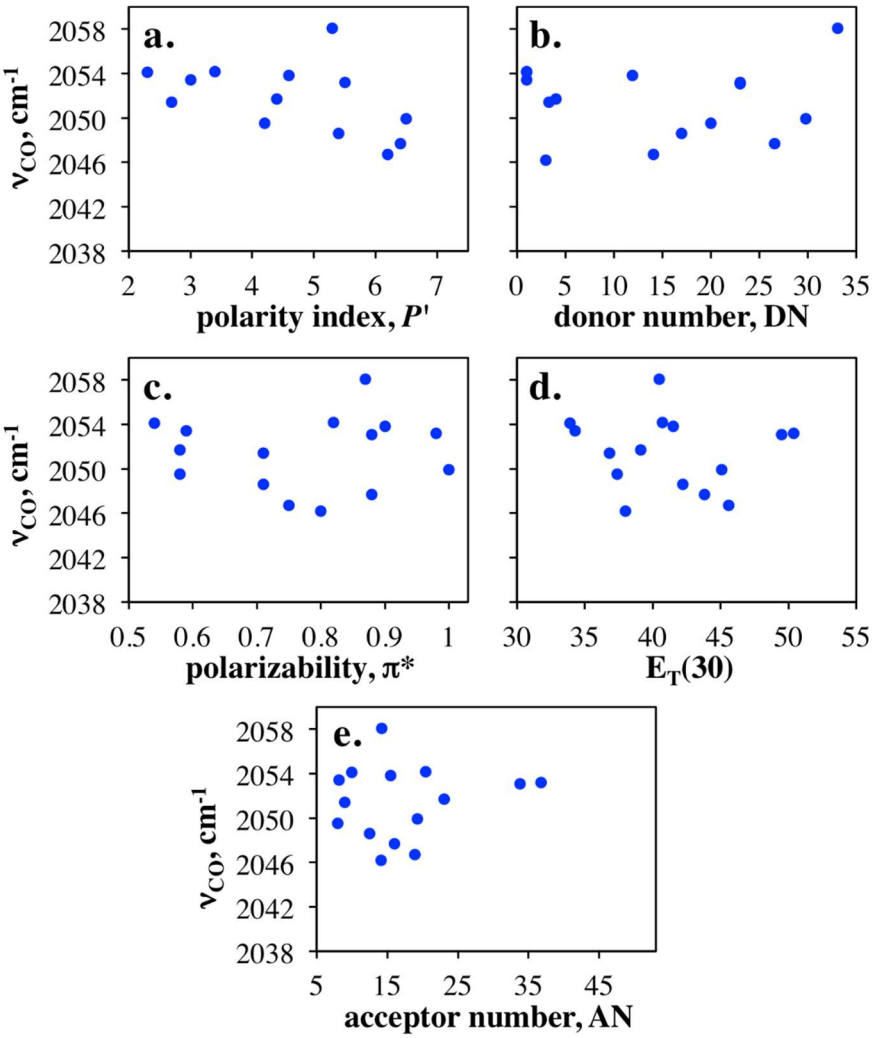

Figure 3.17. Center frequency of the CO stretch (ν_{CO}) for the sulfur allotrope adduct of Vaska's complex (VC-S_X) as a function of a) polarity index, b) donor number, c) polarizability, d) $E_T(30)$, and e) acceptor number.

Chapter 4: Characterizing Solvent Dynamics in Nanoscopic Silica Sol-Gel Glass Pores by 2D-IR Spectroscopy of an Intrinsic Vibrational Probe

ABSTRACT: Porous sol-gel matrices were synthesized with IR active Si-H vibrational chromophores integrated into the silica network. The Si-H vibrational mode was found to be highly accessible to solvents within the nanoscopic pores. Vibrational solvatochromism of the silane vibration was controlled largely by interactions between infiltrating solvents and the oxygen and hydroxide sites in the silica. Exchanging solvents in the silica matrices produced reversible solvatochromic shifts in some cases, but led to irreversible shifts when strongly interacting solvents were tested, suggesting that a layer of solvent was not exchangeable. 2D-IR spectroscopy was used to monitor spectral diffusion and extract the homogeneous linewidths of the Si-H mode for a range of infiltrating solvents, as well as solvent-free aerogel samples. It was demonstrated that the silane vibration is sensitive to the nature of the infiltrating solvent, making these vibrationally-active sol-gel films a general platform for solvent dynamics in nanoscopic confined volumes.

4.1: Introduction

The behavior of molecules in confined spaces is often distinct from their response in macroscopic volumes.[58, 60, 61, 80] This is due to the fact that the inter- and intramolecular interactions that dictate bulk properties are necessarily disrupted by the confining boundaries, thereby modifying the collective properties of molecules near interfaces. Understanding molecular dynamics in this boundary regime is important. For example, transport to, across, and through cell membranes involves fast, time dependent interactions between solutes, solvent, and lipids or proteins in the cell membrane.[156, 157] Similarly, practical techniques such as liquid chromatography utilize these dynamic interactions to achieve product selectivity in chemical separations.[20, 55, 56] Molecule-interface interactions can have a profound influence on chemical reactivity[57-61] and even on microscopic flow in microfluidic channels.[62]

The dichotomy of solvent behavior in the bulk and at interfaces within confined volumes has been studied most extensively for the case of water confined to reverse micelles.[37, 69-73, 158-160] For this particular case, a core-shell model has been proposed and tested for a number of spectroscopic observables.[69-73] Piletic and coworkers reported that the IR absorption spectrum and vibrational relaxation dynamics of water in reverse micelles could indeed be accurately modeled by core and shell populations.[69] In contrast, they showed that ultrafast spectral diffusion and reorientation dynamics of water in these nanoscopic pools were not captured by the core-shell model.[69] The collective (rather than binary) nature of certain properties of confined water has been corroborated by a number of recent experimental and computational studies, suggesting that the core-shell description can be qualitatively instructive but is quantitatively an oversimplification.[37, 158, 159, 161] The

behaviors of other solvents in nanoscopic volumes have chemical and technological implications that should also be explored. To a lesser extent than water, reverse micelles have been used to study confined non-aqueous solvents, and again the results are often interpreted within the construct of bulk-like and interfacial populations.[162-166] However, the thermodynamics of phase separation of amphiphiles and the interior and exterior solvents place limits on the generality of reverse micelles as a testing platform for solvent dynamics.

Porous silica is a useful alternative medium for studying confined solvent dynamics.[45-47, 74, 75, 78-80, 167, 168] Pore size, dispersity, surface area, and morphology are all properties that can be independently tuned by reaction conditions such as the solution pH,[81, 92-94] catalyst used,[169] water to precursor ratio,[95] and precursor itself.[170-172] Through advances in surfactant technology and templating methods, silica particles can be synthesized as small as 50 nm but still house 10 nm pores and surface areas as high as 1500 m^2/mg.[96, 97] Due to their large pores and low toxicity, these materials can potentially be utilized in drug delivery systems or in targeted therapeutic radiation.[86-88] Porous silica nanoparticles and sol-gel glasses have also been employed as scaffolding in the encapsulation of biomolecules such as enzymes and proteins.[82, 173-177] For these systems, the silica scaffolding provides structural support, resistance to heat and chemical denaturation, and at times improved activity.[178-187] Encapsulation can also affect the way that proteins fold[180, 181, 186] and even modulate their ultrafast structural dynamics.[54] Interestingly, Reategui and coworkers showed that some of the peculiar dynamical behaviors observed for biomacromolecules encapsulated in silica sol-gels are in fact driven by the kinetics and thermodynamics of the confined solvent.[177] Thus, in order to understand and potentially exploit the benefits of porous silica matrices for

biotechnological applications, one must come up with ways to characterize and tailor the behaviors of solvents in small spaces.

Seminal work by Fourkas and coworkers applied ultrafast optical Kerr effect (OKE) spectroscopy to a range of neat aqueous and non-aqueous solvents in silica sol-gels to characterize their ultrafast reorientational dynamics.[46, 47, 78-80] Although the observables in time-resolved IR and OKE spectroscopies are not directly comparable, these studies showed that the rich dynamical behavior observed in nanoscopic reverse micelles is also present in these porous glasses but with a greater flexibility of the types of solvents that can be interrogated. On the other hand, OKE spectroscopy probes the collective response of the confined liquid pool whereas IR spectroscopy monitors molecular vibrations that are sensitive to their immediate chemical environments.[121-128, 188, 189] Vibrational solvatochromism studies in binary solvent mixtures have shown that vibrations are particularly sensitive to the composition of the first solvent shell and can report on preferential solvation.[9, 190] Ideally, one would like to have the generality of the sol-gel platform for confining a wide range of liquids but the specificity of a local molecular mode to probe solvent dynamics. Unfortunately, studying a different solvent in the same confining matrix by IR spectroscopy typically means that a different vibrational mode will be monitored, which will have different couplings to its surroundings making comparative studies difficult.

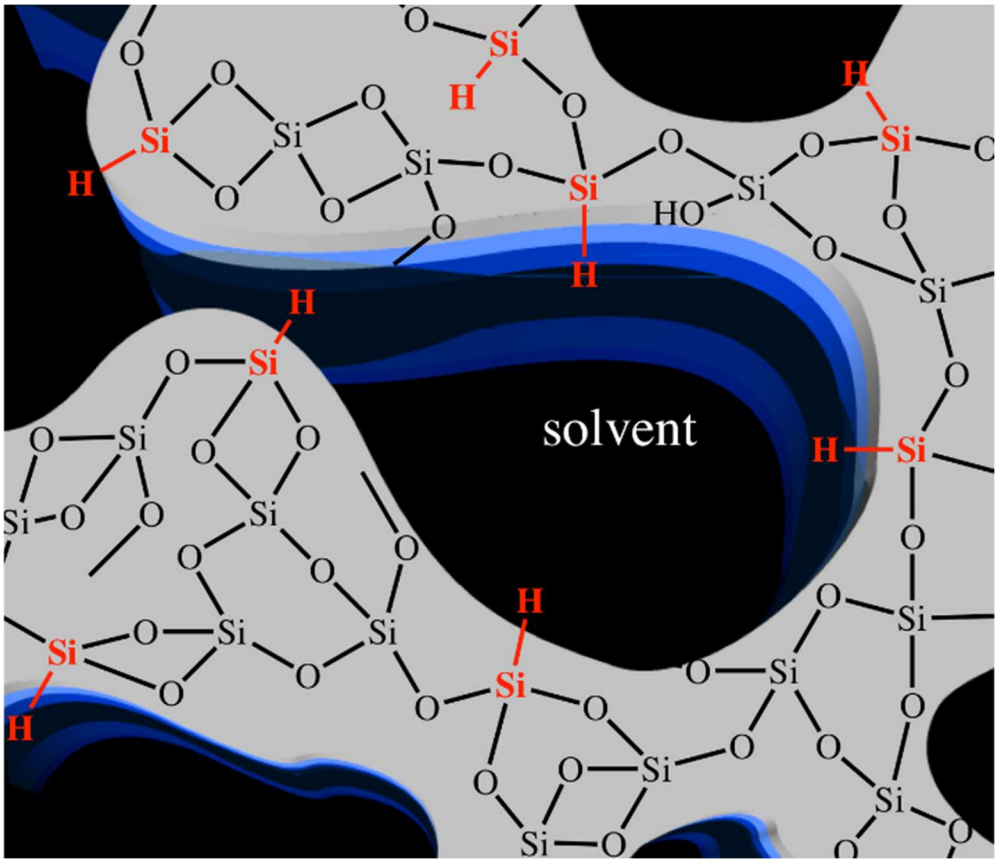

Figure 4.1. Schematic of porous silica matrix infiltrated with solvent and presenting internal and surface silane vibrational modes.

In the current study, a conventional silica sol-gel synthesis was adapted to incorporate strongly IR-active Si-H bonds into a porous silica matrix as shown schematically in Figure 4.1. This silane vibrational mode ($\nu_{Si\text{-}H}$) then served as an intrinsic vibrational dynamics probe of the solvent confined to the silica pore. In contrast to other confined dynamics studies, the probe is localized on the confining matrix rather than belonging to the solvent that fills the pores. The sensing platform is general and can be readily infiltrated with a broad range of solvents and solutes, regardless of the vibrational spectrum of the filling solution. Since the vibrational mode is localized to the silica interface, it is most sensitive to the interfacial solvent dynamics, potentially avoiding convolution of core and shell dynamics. Herein we demonstrate that the synthetic process

leads to nanoporous silica scaffolds that present a high concentration of silane vibrations on their surface. After characterizing the materials by steady-state methods, we apply ultrafast two-dimensional infrared spectroscopy (2D-IR) to determine the differences in interfacial solvent dynamics for four different solvents and in the absence of solvent.

4.2: Experimental Methods

Materials

Trimethoxysilane (TriMOS, 95% purity), triphenylsilane (97% purity), and chloroform were used as received from Sigma Aldrich. Tetramethyl orthosilicate (TMOS, 98% purity) was used as received from Fluka, isopropanol and hydrochloric acid were used as received from Macron, and N,N-dimethylformamide (DMF) and pentane were used as received from Fisher.

Silica samples studied in this work were either alcogels, xerogels, or aerogels. By definition, an alcogel is a sol-gel that remains soaked in a solvent whether it is the solvent that the gel forms in or another solvent in which the gel ages, leading to a silica matrix with solvent filled pores.[91] As the solvent in the alcogel evaporates, the surface tension of the leaving solvent collapses the pores in the gel, resulting in a low porosity xerogel. Alternatively, if the solvent is replaced by liquid CO_2 and the system is then brought to the CO_2 critical point and then into the gas phase, the "solvent" can then evacuated with the pores staying largely intact.[98]

Alcogel Synthesis

TriMOS (138 μL) was mixed with TMOS (782 μL), and HPLC grade H_2O (450 μL) to make an aqueous 15% TriMOS to TMOS (by volume) solution. An acid initiator,

0.04 M HCl (15 μL), was added to the mixture, the solution was briefly shaken, and subsequently sonicated for 15 minutes. The solution was allowed to react for 7 hours, and then an aliquot was sandwiched between two CaF_2 windows with a 50 micron Teflon spacer. A small section of the spacer was removed to allow for greater access to the gel for solvent exchange. The sample was held together with binder clips under ambient conditions until air bubbles in sample no longer moved when the sample was inverted. The gelled samples were then submerged in various neat solvents to remove reaction byproducts (alcohols) and, in some cases, exchange the pore solvent. The samples were allowed to soak in their respective solvents for at least three days before any measurements were made, although most samples soaked at least two weeks before any laser experiments were conducted. For samples in which the starting solvent was switched to a different solvent, the samples were soaked in the new solvent for at least three days before any experiments were conducted to ensure complete exchange. Solvent exchange was verified to be complete by FTIR spectroscopy as seen in Figure 4.2. Throughout this paper, these samples are simply referred to as alcogels. For some experiments, the prepared alcogels were placed under high vacuum to remove the pore solvent, leading to fractured xerogels that could be characterized by some methods but were not appropriate for 2D-IR measurements.

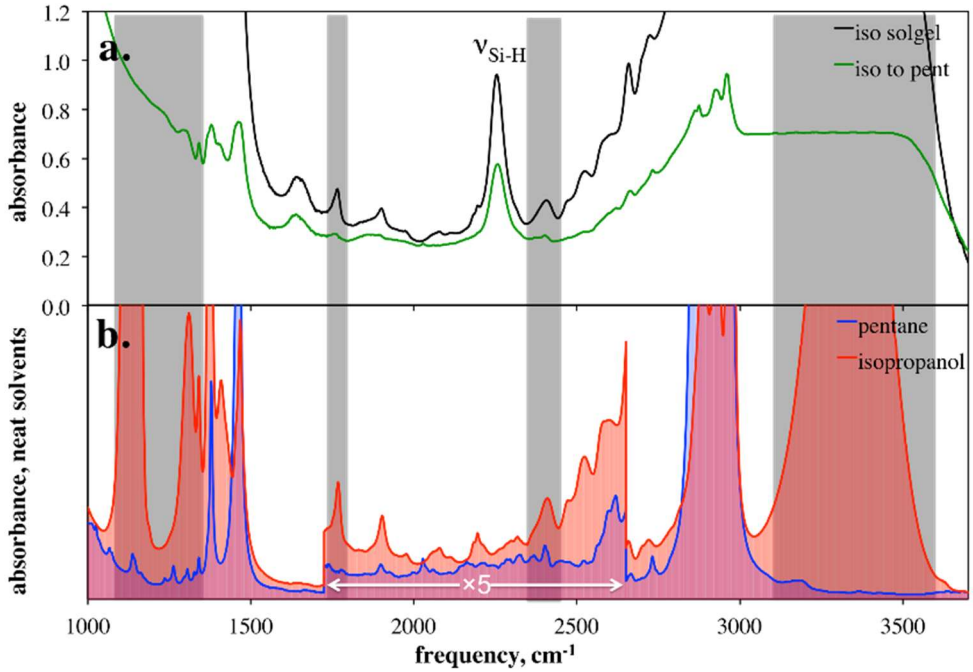

Figure 4.2. a) Raw FTIR spectra for a silica alcogel infiltrated with isopropanol (black) and then soaked in pentane for four days to exchange the solvent (green). b) Neat solvent spectra for isopropanol (red) and pentane (blue) are shown for reference. The middle section of this plot is scaled by a factor of five to clarify the smaller solvent peaks in this region.

Aerogel Synthesis

To produce aerogel samples, an isopropanol alcogel bound between two CaF_2 windows was placed in a critical point drier (Tousimis Automegasamdri 915B). The chamber was cooled down to 10 °C and purged with liquid CO_2 for 1.5 hours. The temperature of the chamber was raised to 38 °C while the pressure of the chamber increased to 1400 psi resulting in supercritical CO_2. As the pressure of the chamber was brought back to atmospheric pressure the CO_2 gas escaped the gel leaving empty uncollapsed pores, which was verified by FTIR as seen in Figure 4.3.[98]

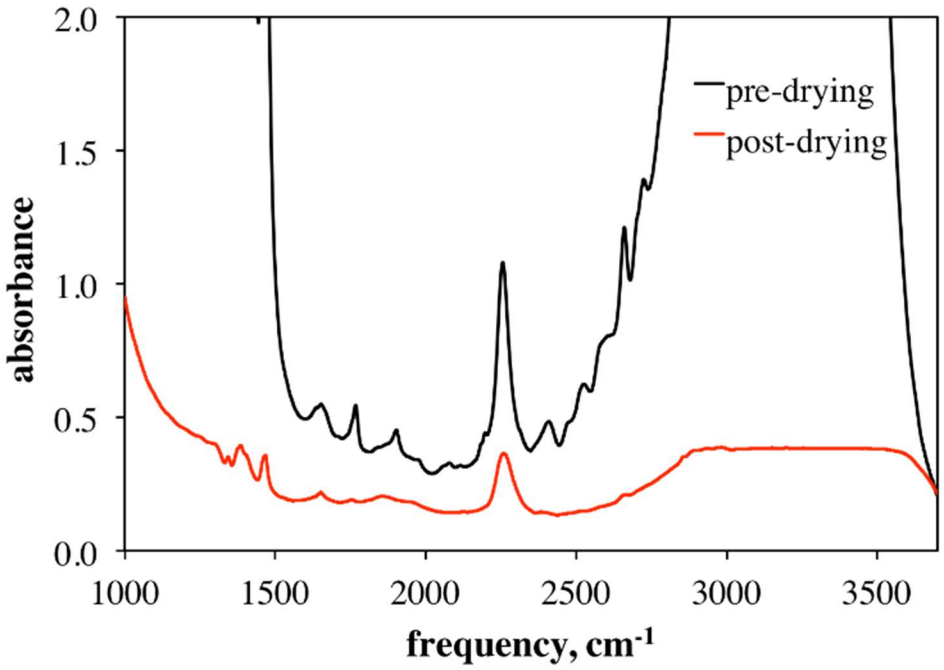

Figure 4.3. Raw FTIR spectra of an isopropanol alcogel before (black) and after supercritical CO_2 drying (red). Note that although there is a lot of persistent absorbance by the silica, the majority of the solvent peaks through the 1500 cm^{-1} to 2700 cm^{-1} range are absent after drying, indicating that the solvent has been removed.

Nonporous Xerogel Synthesis

To prepare nonporous silica xerogel films, TriMOS (360 µL) was mixed with TMOS (540 µL), and HPLC grade H_2O (450 µL) to make an aqueous 40% TriMOS to TMOS (by volume) solution. An acid initiator, 0.04 M HCl (15 µL), was added to the mixture, the solution was shaken until it was homogeneous, then a 250 µL aliquot of the solution was spin-coated onto a CaF_2 window at 150 rpm for 2.33 min, 1000 rpm for 15 sec, and 2000 rpm for 2 min, sequentially. The TriMOS:TMOS ratio was increased in these samples to account for the decrease in sample thickness resulting in roughly the same number of probes.

Material Characterization

Nitrogen adsorption-desorption isotherms were collected with a Micromeritics ASAP 2020 system at 77 K. Powdered samples of 50-100 mg were degassed at 90 °C until a pressure of 10 μm Hg was reached for 1 h and then at 120 °C for 6 h prior to measurement. BJH/KJS and BET models were used to calculate pore volume and surface area, respectively. Total pore volumes were calculated from the quantity of nitrogen adsorbed at relative pressure (P/P_0) of 0.99. Solid state ^{29}Si NMR (SSNMR) measurements were carried out on a VNMRJ 700MHz NMR spectrometer. All SSNMR experiments were performed at 25 °C on 700 MHz spectrometer using 3.2 mm BioMAS probe. About 20 mg of sample was packed into the rotor, and MAS (magic angle spinning) frequency was set to 10 kHz. Silicon spectra were recorded with a 90° pulse followed by 20 ms acquisition under proton decoupling. A recycle delay of 10 s and 6000 scans were used for acquiring each ^{29}Si spectra. Fourier transform infrared (FTIR) spectra were collected on a Nicolet 6700 FTIR spectrometer (Thermo Scientific) with at least 16 scans and a resolution of 2 cm^{-1}.

Laser Experiment setup

The laser system and experimental setups used for 2D-IR and pump-probe spectroscopy have been described previously in section 2.4.1 of this thesis.

4.3: Results and Discussion

In this study, we sought to compare the vibrational dynamics experienced by a Si-H mode bound to a porous silica scaffold in the presence of a range of solvents (alcogels), and in the absence of solvent (aerogel). Alcogel samples used in 2D-IR measurements had their pore volumes filled with DMF, isopropanol, chloroform, or pentane to provide a diverse set of solvent properties. Before describing the ultrafast dynamical results, a thorough characterization of the silica material is presented. In order for this system to measure confined dynamics effectively the silica gel must possess pores large enough for solvent infiltration, and these cavities should present Si-H probes on their surfaces that are sensitive to the dynamical differences between solvents.

To establish the porosities of the silica materials used in this study, nitrogen physisorption isotherms were measured for spin-cast nonporous, vacuum-dried alcogel (xerogel), and aerogel samples (Figure 4.4). As expected, the spin-coated sample had a relatively low porosity as illustrated by the flat isotherm in Figure 4.4, whereas the xerogel and aerogel samples both exhibited significantly higher adsorptions. Figure 4.4 also illustrates that the aerogel sample adsorbed almost double the nitrogen volume of the xerogel sample due to morphological changes in the xerogel during drying. When these isotherms were fit through BET calculations the xerogel and aerogel samples were found to have surface areas of 299 ± 7 m²/g and 470 ± 7 m²/g, respectively. The isotherm shapes in Figure 4.4 are indicative of type 1 adsorption to a microporous material with pore sizes that are less than 1.5 nm on average.

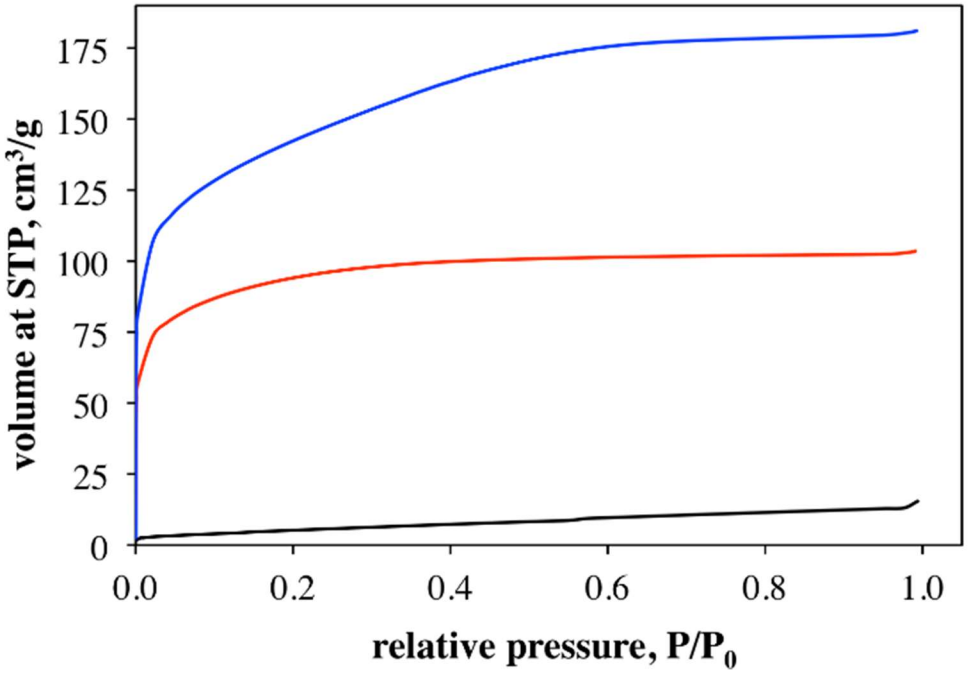

Figure 4.4. N_2 adsorption isotherms for representative spin-cast nonporous (black), vacuum dried alcogel (xerogel) (red), and aerogel (blue) samples.

With the porosity of the materials verified, experiments were needed to establish the accessibility of the vibrational probes to the solvent. One way to test the exposure of surface silane groups to the bathing solvent is to react them chemically and monitor their disappearance by IR spectroscopy. The Si-H bond is labile in the presence of weak bases such as pyridine. An FTIR spectrum was collected of an alcogel that was synthesized in THF and then soaked in pyridine for four days allowing for solvent exchange. The sample was then placed back into the original solution for three days ensuring that the solvent was exchanged back to THF. A comparison of the FTIR spectra of the silane vibration collected before (solid lines) and after (dashed lines) pyridine exposure is shown in Figure 4.5 for a spin-cast nonporous sample (red lines) and an alcogel (black lines).

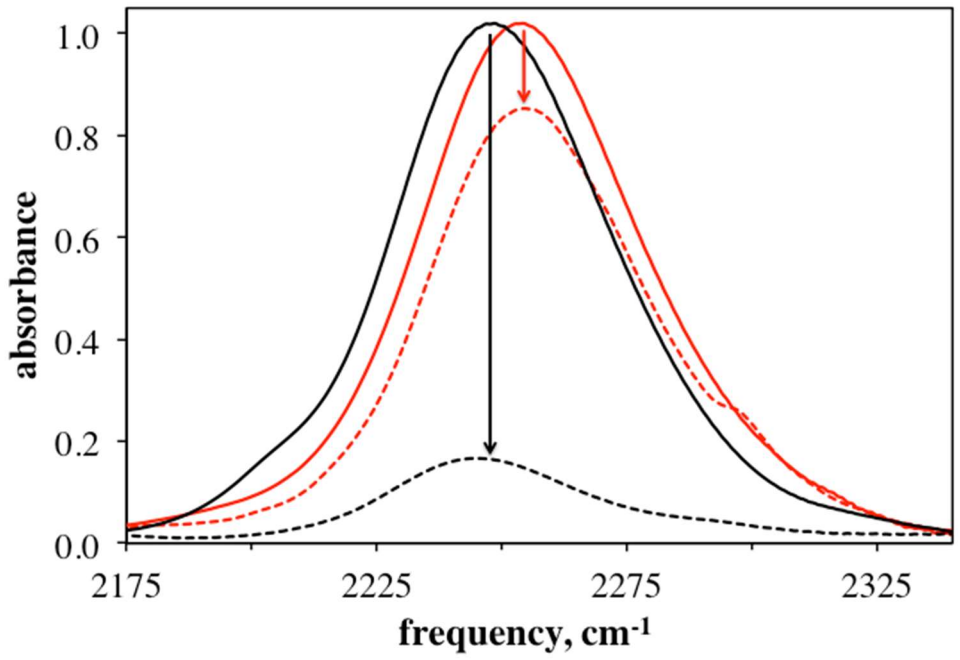

Figure 4.5. Baselined and normalized FTIR spectra of the Si-H vibration in nonporous spin-cast silica (red) and alcogel samples (black) before (solid lines) and after (dashed lines) exposure to pyridine for three days.

The peaks in Figure 4.5 were integrated to reveal that only ~12% of the silane bonds remained after four days of soaking in pyridine for the alcogel sample, whereas ~82% of the Si-H bonds remain in the non-porous spin-cast xerogel samples after the same treatment. It is clear that there is a greater accessibility of the silane vibrations in the alcogels. This is consistent with the higher porosity observed by nitrogen adsorption analysis in Figure 4.5 but also proves that a large fraction of the Si-H vibrational probes are on the surface of the pores and are directly accessible to the infiltrating solvent molecules for the alcogel samples.

In order to be an effective solvation probe, the solvent accessible silane vibrations also need to be spectroscopically sensitive to different solvents. For small molecule silanes, the Si-H vibrational frequency has been shown to be dependent on the inductive

effect of the other three substituents.[191-195] Smith and coworkers have constructed a model that shows correlation between the sum of the electronegativity of the nearest neighbors and Si-H frequency.[192] That model subsequently incorporates the contribution of next nearest neighbors as the second term in a series, however this second term showed little to no influence on $\nu_{Si\text{-}H}$. Recognizing the role that the inductive effect has on the Si-H vibration, the extent of crosslinking in silica sol-gels during the condensation reaction will affect the average $\nu_{Si\text{-}H}$.

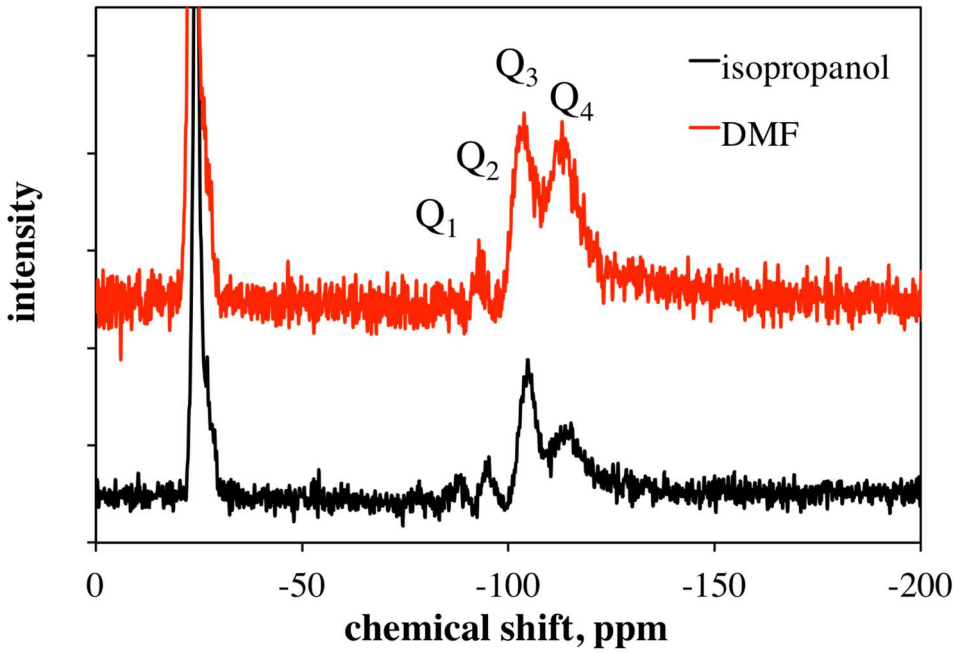

Figure 4.6. Solid-state Si^{29} NMR spectra of xerogel samples (vacuum dried alcogels) that were synthesized with isopropanol (black) and DMF (red) as the infiltrating solvents. The peaks at -86, -95, -104, and -112 ppm are assigned as the Q_1, Q_2, Q_3, and Q_4 peaks, respectively.[196-198] These peaks correspond to $(SiO)Si(OR)_3$, $(SiO)_2Si(OR)_2$, $(SiO)_3Si(OR)$, and $(SiO)_4Si$, respectively, where R is either H or CH_3.[196-198] We do not see evidence for the Q_0 peak. The silicon atoms in sol-gels infiltrated with both solvents are mostly tertiary and quaternary coordinated and highly cross-linked. The integrated peak areas are: (isopropanol) Q0 = 3.7%, Q_1 = 6.5%, Q_2 = 8.3%, Q_3 = 38.7%, Q_4 = 42.8%; and (DMF) Q_1 = 4.5%, Q_2 = 6.5%, Q_3 = 36.7%, Q_4 = 52.2%.

Figure 4.6 displays Si^{29} SSNMR spectra of xerogel samples that were aged in isopropanol and DMF, and subsequently vacuum dried prior to data collection. The data show that the alcogels aged in both solvents have 90-95% of the silicon atoms with at least secondary coordination to the silica matrix. Examining the numbers more closely, the DMF aged sample has almost 10% more quartenary crosslinking. In the absence of solvent, this would inductively blue shift the DMF peak in relation to the isopropanol peak, however, the FTIR spectra of DMF alcogel samples indicate the opposite. This result speaks even more to the effect that the solvent has on the Si-H frequency.

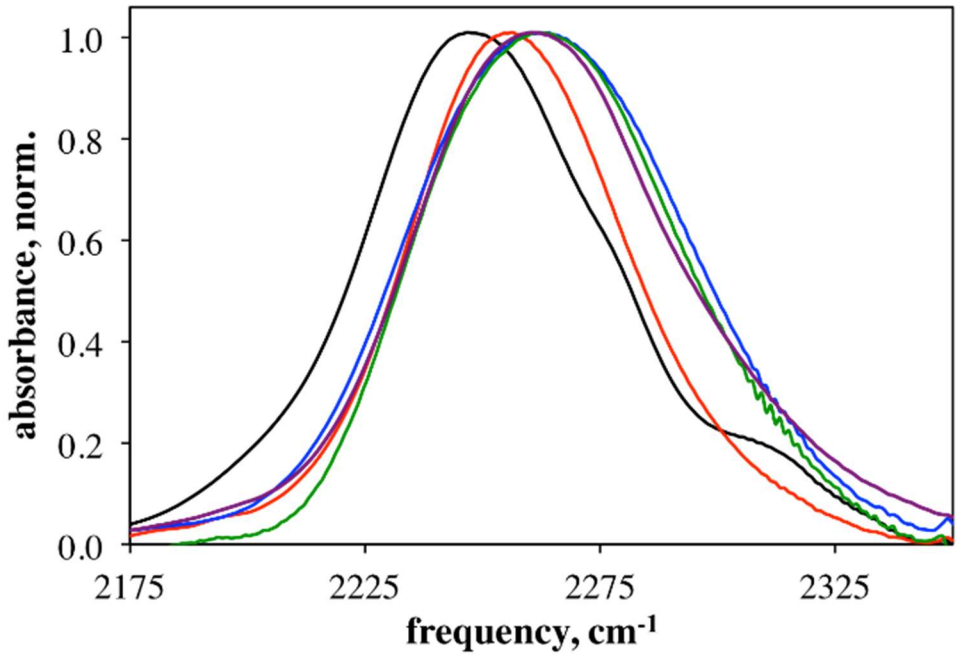

Figure 4.7. Solvent-subtracted, baselined, and normalized FTIR spectra of the Si-H vibration (ν_{Si-H}) for alcogels infiltrated with DMF (black), isopropanol (red), chloroform (blue), and pentane (green). Also overlaid is the Si-H spectrum for a solvent-free aerogel (purple).

Focusing attention on the Si-H vibration, Figure 4.7 shows the FTIR spectra for the ν_{Si-H} in TriMOS alcogel samples filled with DMF, isopropanol, chloroform, and pentane, as well as the spectrum from a solvent-free aerogel. FTIR spectra were recorded in a total

of 14 different solvents, and these four are presented here as they are the solvents studied by 2D-IR later in this paper. The apparent blue shoulder peak on the DMF spectrum is an artifact due to solvent subtraction. FTIR spectra of the ν_{Si-H} in all solvents are provided at the end of this chapter. The first observation is that both the peak centers and widths are solvent dependent. The mean frequencies and FWHMs for the Si-H in all solvents studied are tabulated in Table 4.3 at the end of the chapter. The center frequency shifts from 2244 cm^{-1} to as high as 2262 cm^{-1}, while the FWHM varies from 42 cm^{-1} to nearly 70 cm^{-1} wide. There is no correlation between the peak centers and their corresponding widths across the solvents examined, however we do find some correlation between the center frequency and the solvent properties. The solvatochromism of this mode indicates how the solvent interacts with the silane vibration and the pore surface. The fact that the mode is readily perturbed by changing the solvent in the pores corroborates our assertion that the majority of the silanes are at the silica surface. Referring to the schematic in Figure 4.1, the solvent may interact directly with the Si-H vibration or inductively through the silica matrix, which in turn affects the ν_{Si-H}. It has been shown that the Si-H vibration is inductively sensitive to chemical changes to whatever groups are bound to the neighboring oxygen atoms but are indifferent to any subsequent bonds.[192-195] Hence, the most relevant indirect interaction with the porous silica is between the solvent and the oxygen atoms bound to the silicon involved in the silane vibration.

Some insight into the nature of the solvent-solute interactions can be gleaned through analysis of the linear solvation energy relations (LSER) developed by Kamlet and coworkers.[23] Tabulated values for solvent hydrogen bond donating (α) and accepting (β) strengths, polarizabilities (π^*) and polarizability corrections (δ) are available in the

literature.[19, 23-25] Qualitatively, the Si-H center frequencies across the 14 solvents examined were well-correlated with solvent hydrogen bond accepting strength implying that this is the dominant contribution to solvatochromism. A more quantitative analysis was obtained by plotting the $\nu_{Si\text{-}H}$ values as a function of a solvent parameter (S), which was defined as a weighted linear combination of the solvent parameters, as in Equation 4.1.[23]

$$S = S_0 + a\alpha + b\beta + c(\pi^* + d\delta) \quad (4.1)$$

In this way, the relative contributions of the solvent parameters could be determined by iteratively adjusting the frequency offset (S_0) and coefficients (a, b, c, and d) to optimize the linear correlation between S and the experimental $\nu_{Si\text{-}H}$ values. The correlation plot obtained by this method is shown in Figures 4.8a-c.

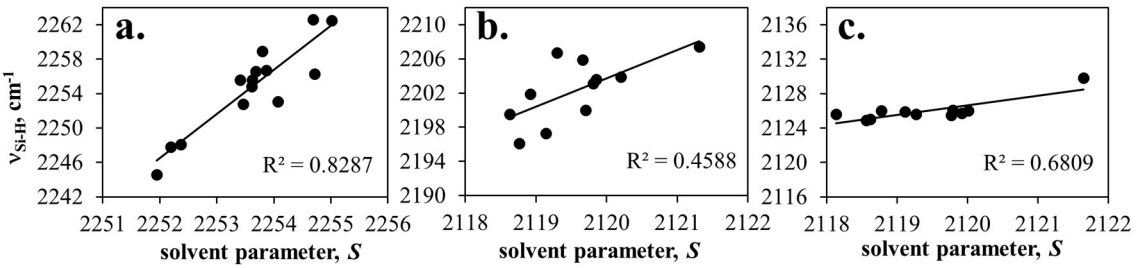

Figure 4.8a-c. LSER plot for the silane vibrational frequency in 14 different solvents as a function of the optimized solvent parameter defined in Equation 4.1 for a) alcogels a) triphenylsilane (TriPS) and b) TriMOS precursor. The y-axis scales are all 22 cm^{-1} facilitating an easy comparison of the extent of solvatochromism for each sample.

In this case, the strongest correlation was obtained using the solvent parameters tabulated by Marcus[24] but replacing the alcohol values with those reported by Carr.[19] However, we note that the Marcus parameters alone can give very strong correlations when the alcohol and non-alcohols are treated separately (Figures 4.9a-b). This seems to suggest that the Marcus solvation parameters are self-consistent among the alcohol and non-alcohol

groups, but fail to fully capture the contributions to the $\nu_{Si\text{-}H}$ across all solvents. This is not overly surprising as solvation parameters obtained by different methods are generally not perfectly correlated.[22] As discussed above, the extent of reaction is similar but may not be identical for all of the alcogel samples. Thus the extent of reaction should also be considered as an additional variable that might affect the LSER fit and not be correlated to any given solvent parameter. The solvent parameters used in this work are also provided in Table 4.3. After replacing the Marcus alcohol values with those of Carr, we obtained a squared correlation coefficient (R^2) of 83% for the plot in Figure 4.8a. As expected, the strongest influence on the silane frequency is the hydrogen bond accepting strength of the solvent (β), but the analysis also reveals that the hydrogen bond donating strength (α) has a major influence, perturbing the frequency in the opposite direction. Relatively small contributions to the solvatochromic shift were obtained from the solvent polarizability.

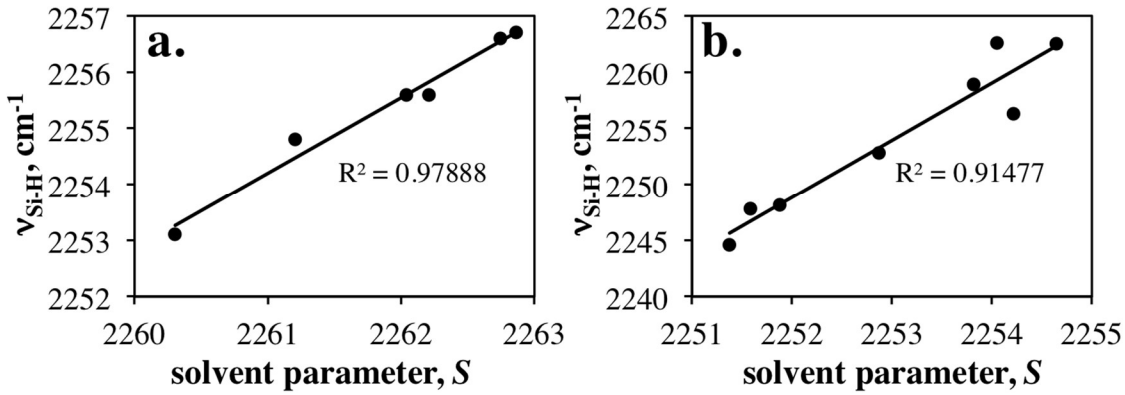

Figure 4.9a-b. LSER analysis of solvatochromic shifts of the $\nu_{Si\text{-}H}$ treating separately the a) alcohols and b) non-alcohols using Marcus' parameters for both correlation plots (not Carr alcohols).[19, 24] The high correlation obtained when separating these solvent types demonstrates that Marcus parameters do capture the correlation between solvent properties and spectral shifts, but are not internally consistent for these solvent categories.

The contribution of α to the frequency shift indicates that the solvent interaction with a hydrogen bond accepting site on the silica perturbs the frequency in one direction, which could only be facilitated by the oxygens in the Si-O-Si network. The opposing

influence of β suggests an interaction with a silica hydrogen bond donating group, which could be directly to the Si-H or indirectly to uncondensed OH groups on the sol-gel framework. In order to test for solvatochromism of the Si-H vibration with the absence of oxygen atoms bound to the silicon, a solvatochromic study was carried out with the TriMOS precursor molecule in the neat solvents and found that solvatochromism was present but to a lesser degree than for the silica alcogels (Figure 4.8b). This demonstrates that a more extensive silica network enhances the sensitivity of $\nu_{Si\text{-}H}$ to the surrounding solvent, presumably through inductive effects with next-nearest neighbor silicon and oxygen atoms. A similar study was performed on triphenylsilane in the same 14 solvents, and showed that the $\nu_{Si\text{-}H}$ was nearly insensitive to the solvent, thereby ruling out the direct interactions with the Si-H mode as the primary mechanism of solvatochromism. (Figure 4.8c). We conclude that solvent interactions with oxygen atoms in the silica have the most substantial influence on $\nu_{Si\text{-}H}$, and may be viewed as the sensing elements of the matrix while the silane vibration serves as a reporter of these surface interactions.

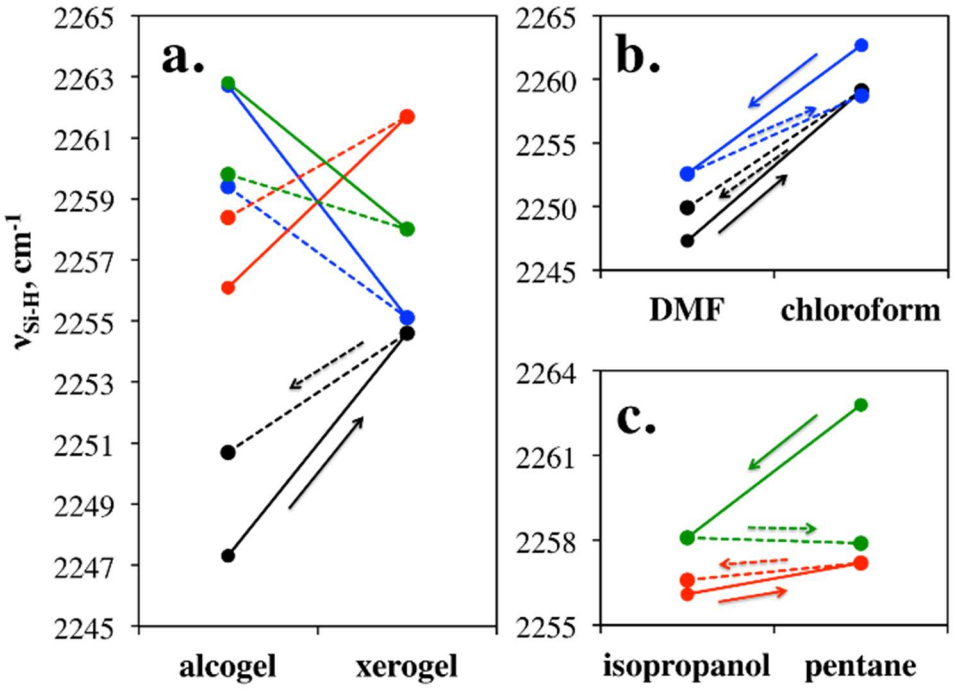

Figure 4.10a-c. Dynamic response of ν_{Si-H} to changes in the surrounding solvation environment when a) transferring from DMF (black), isopropanol (red), chloroform (blue), or pentane (green) alcogels to solvent-free xerogels (solid lines) and back (dashed lines); or solvent exchange from b) DMF to chloroform (black) or chloroform to DMF (red); or c) isopropanol to pentane (red) or pentane to isopropanol (green). In all frames, solid lines are the forward change and dashed lines are the return; arrows also indicate the direction of change.

The ν_{Si-H} responds dynamically to changes in the surrounding solvent shell. For example, Figure 4.10a illustrates the peak shifts measured when alcogel samples with various solvents were converted to xerogels by removing the solvent under high vacuum. It can be seen that there is a general narrowing of the range of frequencies among the xerogel samples relative to the alcogels, and the frequencies tend to converge towards the ν_{Si-H} for the aerogel sample. As noted above, xerogel formation leads to pore collapse and severe fracturing of the sample into a coarse powder, however, re-exposure of these resulting materials to their original solvents leads to partial recovery of the starting ν_{Si-H}. It can be seen in Figure 4.10a that the silane vibrational frequencies in all four samples move back towards their original values when solvent is reintroduced. The incomplete

reversibility is presumably due to morphological changes that accompany the solvent exchange. This hysteresis is small compared to the overall frequency shifts due to solvent switching. Yet, even when the pores collapse and fracture, the silane vibrational probes respond to solvation as before. Furthermore, Figures 4.10b and 4.10c show that the Si-H peak responds to exchanging the solvents in alcogels without first creating a solvent-free xerogel or aerogel. Figure 4.10b shows that not only do the silane peaks shift accordingly when the solvent is exchanged between chloroform and DMF, but that this shift is mostly reversible when the sol-gel glass is soaked in the original solvent. An interesting case is observed in Figure 4.10c in which the $\nu_{Si\text{-}H}$ in isopropanol shows very little change upon solvent exchange with pentane. Conversely, an alcogel that starts in pentane shows a highly irreversible $\nu_{Si\text{-}H}$ shift upon exchange with isopropanol. This preferential solvation in combination with absence of isopropanol solvent peaks after exchange in the FTIR spectra (Figure 4.2) highlights the fact that the first solvation shell at the silica interface primarily dictates the solvatochromism of the silane mode. This shell may be preferentially enriched in a solvent with a particularly high affinity for the silica surface. When isopropanol infiltrates the gel, it displaces the pentane solvent molecules and dominates the solvent-matrix interactions. Alternatively when the sample formed in isopropanol is exchanged into pentane a minimal blue shift is seen. This shift is mostly reversible upon exchanging back to the original solvent. These changes are indicative of preferential solvation of the surface by isopropanol. Even though the majority of the pore volume is pentane, which is evident by monitoring the solvent peaks through FTIR (Figure 4.2), the interfacial isopropanol molecules must not readily exchange.

The center frequency of the Si-H vibration gives some indication of the average chemical environment of the oscillator, however, there is also information in the vibrational peak widths. The peak widths for the silane mode are generally broad (see Table 4.3 at the end of the chapter), and we find no obvious trends in peak widths as a function of the solvent properties. Even when the solvent is removed to prepare xerogel and aerogel samples, the $\nu_{Si\text{-}H}$ remains broad suggesting that the majority of its width is due to the heterogeneity of the gel itself. These lineshapes are a convolution of the range of chemical environments that are present in sol-gel glasses with the time-dependent processes that lead to vibrational relaxation and time-dependent solvent shell rearrangements. Unfortunately, in a sample that is as heterogeneous as a microporous glass, the observed spectral response is dominated by the inhomogeneity of the system, rather than the more interesting solvent dynamics. Linear spectroscopies are not able to separate these dynamics, but nonlinear techniques such as 2D-IR spectroscopy can characterize solvent shell dynamics from within heterogeneous environments. Within these spectrally hidden details are the chemical interactions that determine the behavior of solvents and solutes at the aforementioned biologically and technologically relevant material interfaces.

Figure 4.11 shows representative 2D-IR spectra of $\nu_{Si\text{-}H}$ in an alcogel infiltrated with DMF and an aerogel at two T_ws (0.3 ps and 15 ps). All 2D-IR spectra collected for all samples studied in this work are provided at the end of the chapter (114 spectra total). In each frame in Figure 4.11, the upper, positive-going peak corresponds to the v = 0-1 transition and the lower negative-going peak is the anharmonically shifted v = 1-2 transition. The x-axis represents the frequency at which the oscillator ensembles are initially excited and the y-axis is the frequency where they reside at the end of the 2D-IR

pulse sequence. The elongation of the peaks in the diagonal direction illustrates inhomogeneity of the Si-H peak as discussed earlier for the FTIR peak widths.

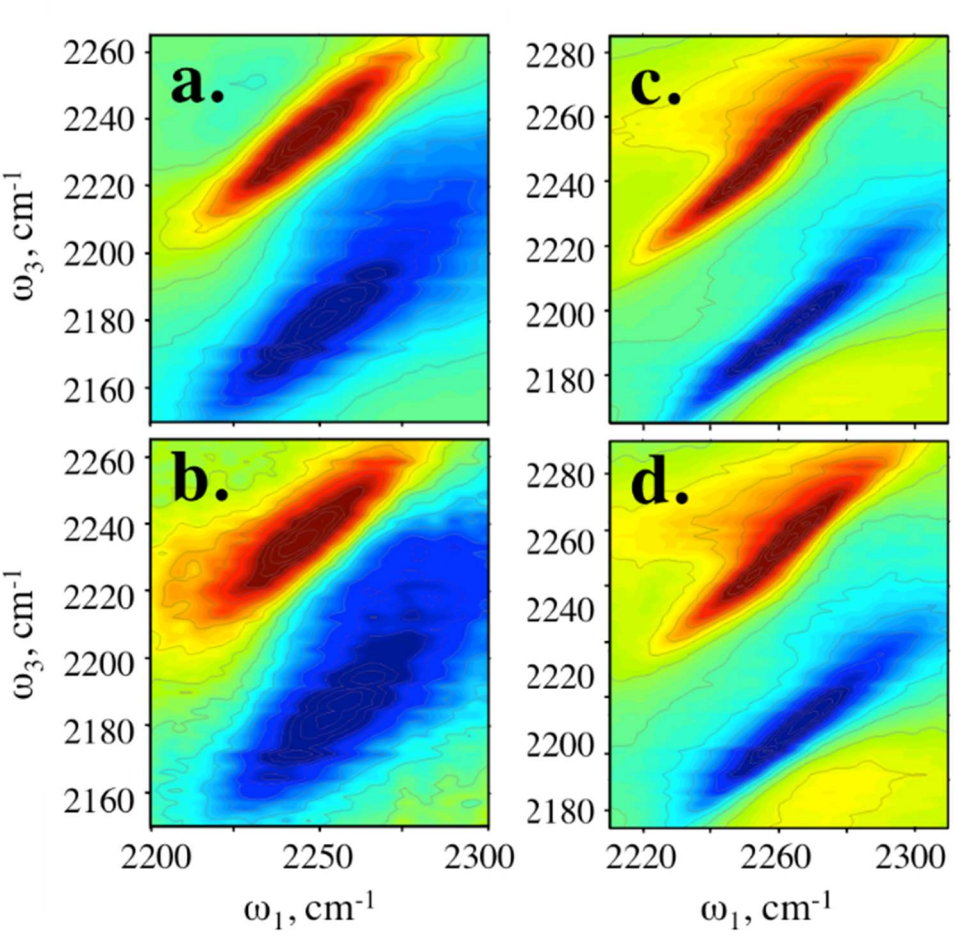

Figure 4.11. 2D-IR spectra of the $\nu_{Si\text{-}H}$ in an alcogel infiltrated with DMF (left column) and an aerogel (right column) collected at (a and c) T_w = 0.3 ps and (b and d) T_w = 15 ps.

At a short waiting time (T_w = 0.3 ps, top row) the peak width along the antidiagonal direction is due to homogeneous broadening of a subensemble of silane chromophores centered at that frequency, as well as spectral diffusion that is too fast to resolve with our pulse durations. For this work, we did not have sufficient signal to noise to determine whether the signal amplitude off-diagonal in this plot is evidence of mode coupling, and we choose to focus on the on-diagonal dynamics herein. These two samples represent the

most and least dynamic cases that were studied in this work, respectively, and it can be seen that the presence of DMF in the alcogel pores introduces additional width along the antidiagonal at $T_w = 0.3$ ps. Increasing the T_w to 15 ps allows the $\nu_{Si\text{-}H}$ to explore additional silica-solvent configurations, leading to spectral diffusion and a broadening along the antidiagonal dimension. Figure 4.11b shows evidence of spectral diffusion for the alcogel infiltrated with DMF, but the aerogel spectrum in Figure 4.11d is qualitatively unchanged. For both samples, the 2D-IR peaks remain somewhat elongated diagonally even at longer waiting times indicating that the $\nu_{Si\text{-}H}$ do not experience significant interconversion on the time scale of our measurement. Hence, a silane in a particular silica environment is not able to sample all of the possible silica-solvent configurations before relaxation of the mode is complete. IR pump-probe measurements indicated that the vibrational lifetimes (T_1) of these Si-H chromophores were also somewhat insensitive to the infiltrating solvent, exhibiting relaxation times of ~12 ps which is consistent with intramolecular relaxation. (T_1 values tabulated in Table 4.1). Nonetheless, the spectral diffusion that is observed between Figures 4.11a and 4.11b demonstrates that there are some frequency fluctuations experienced by the $\nu_{Si\text{-}H}$ in the presence of DMF that are not present in the absence of solvent. These are driven by the time dependent dynamics of the proximal solvent layer within the silica pores. A similar trend was observed for all four solvent-filled alcogels, although the broadening in pentane was notably minimal (see the spectra at the end of the chapter and analysis below).

Quantifying dynamics in a system where the 2D-IR peak shapes show minor variations with T_w can be difficult. In fact, the changes in the antidiagonal linewidths for the Si-H vibration in these sol-gel samples are not abnormally small, rather they are

overshadowed by the inhomogeneity along the diagonal in the 2D-IR plots. Many methods have been used to tease out dynamics from 2D-IR plots, each with its own merits and shortcomings.[4, 5, 110, 111, 199-201] Two of these methods, the center line slope (CLS)[5, 199] and ellipticity,[4, 110, 111] have been particularly popular due to providing a direct relation to the normalized frequency-frequency correlation function, $\bar{C}(t)$. The $\bar{C}(t)$ characterizes the time dependent frequency fluctuations of the $\nu_{Si\text{-}H}$ in the silica matrix and, in conjunction with the FTIR lineshape, can be used to obtain the full frequency-frequency correlation function, $C(t)$.[5, 202] An accurate $C(t)$ characterizes all possible homogeneous and inhomogeneous contributions to the lineshape for a given mode. This provides an experimental function that can also be directly calculated from molecular dynamics simulations to connect the macroscopic observables to the microscopic behavior of molecules.[5, 43, 199, 203]

In principle, for a measurement with ideal signal-to-noise and no uncertainty (due to systematic errors and data processing/phasing) the CLS and ellipticity metrics should provide the $\bar{C}(t)$ with equal fidelity. In practice, we find that for systems that are highly inhomogeneous and exhibit limited spectral diffusion, that the ellipticity does a better job of capturing the spectral changes. The peak ellipticity compares the diagonal and anti-diagonal widths of a 2D-IR peak.[4, 110, 111]

$$E = \frac{(\Delta\omega_{diag})^2 - (\Delta\omega_{antidiag})^2}{(\Delta\omega_{diag})^2 + (\Delta\omega_{antidiag})^2} \tag{4.2}$$

The $\Delta\omega$ values can be given by the diagonal and antidiagonal full widths at half max for a given T_w.[4, 110, 111] The $\bar{C}(t)$ is often described by a sum of exponential terms, each of which reflects the characteristic amplitude, Δ, and time constant, τ, for a particular

facet of the solvation dynamics. A static offset, $\tau_i = \infty$, is sometimes included to capture dynamics that are long enough to be effectively constant on the ultrafast time scale.

$$E(T_w) = \bar{C}(t) = \sum_i \Delta_i{}^2 \exp\left(\frac{-t}{\tau_i}\right) \tag{4.3}$$

The 2D-IR data were also fit with the CLS method and yielded similar trends but with generally lower signal-to-noise.

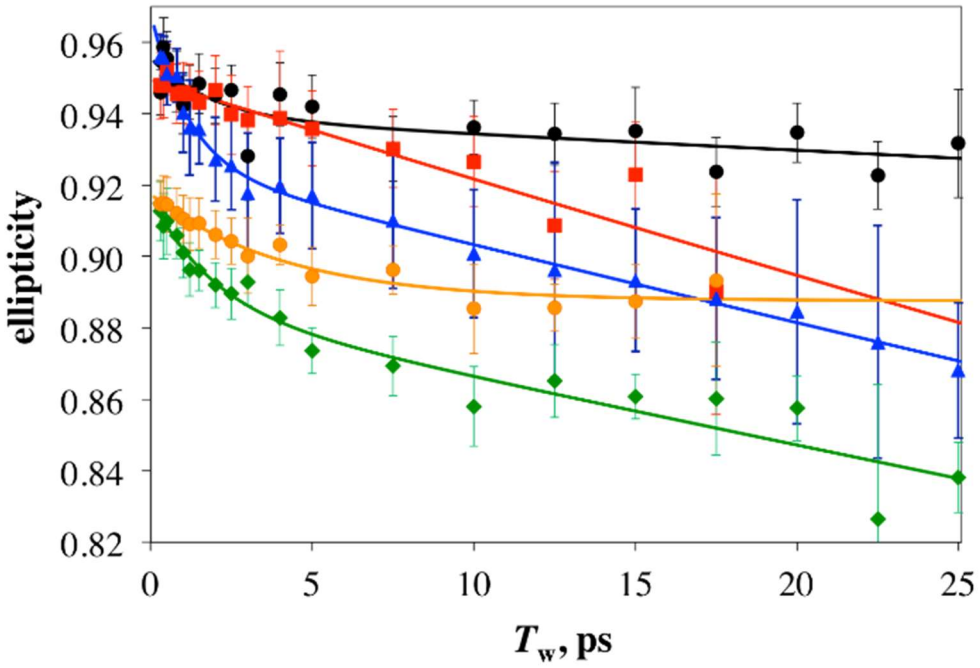

Figure 4.12. Ellipticities as a function of T_w for the v = 0-1 transition in 2D-IR spectra for the $\nu_{Si\text{-}H}$ in an aerogel (black circles), and alcogels infiltrated with pentane (red squares), chloroform (blue triangles), isopropanol (green diamonds), and DMF (orange circles). Overlaid solid lines are multiexponential fits to the data. Error bar calculation described in the Experimental Section.

Figure 4.12 shows the ellipticity values of the 0-1 peak as function of waiting time for the aerogel (black circles) and alcogels containing four different solvents. As expected, the silane vibrations in the aerogel sample exhibit minimal dynamics on the time scale of our measurements. In the absence of solvent in the silica pores, the peak ellipticity only decays by a few percent over a time period of 25 ps. However, once solvent is introduced,

the $\bar{C}(t)$ for each solvent shows a measurable decay that is solvent dependent. These decays were quantified by fitting to Equation 4.3 and the resulting parameters are given in Table 4.1.

Table 4.1. Vibrational lifetimes and exponential fit parameters to ellipticity decays for aerogel and alcogels. [a]

sample	T_1, (ps)	A_1	τ_1 (ps)	A_2	τ_2 (ps)	y-intercept
aerogel	14.4 (+/-0.4)	0.017 (0.007)	1.9 (2.0)	0.939 (0.007)	2060 (1820)	0.956
pentane	12 (+/-0.7)	---	---	0.950 (0.002)	337 (34)	0.950
chloroform	13.9 (+/-0.7)	0.043 (0.003)	1.2 (0.2)	0.926 (0.002)	408 (25)	0.968
DMF	10.7 (+/-0.6)	0.030 (0.002)	4.1 (1.0)	0.888 (0.002)	---	0.918
isopropanol	11.6 (+/-0.3)	0.886 (0.008)	449 (100)	0.031 (0.008)	1.9 (1.2)	0.917

a. Errors shown in parentheses represent the standard error of the fit.

The normalized $\bar{C}(t)$ obtained in this way assumes the short time approximation, which states that dephasing during the coherence periods of the 2D-IR pulse sequence has a negligible contribution to the correlation function,[4, 204] and therefore does not explicitly give the homogeneous lineshapes that bely the linear spectrum. However, following the procedure of Kwak and coworkers, the normalized $\bar{C}(t)$ can be used to reproduce the FTIR spectrum while iteratively adjusting the homogeneous dephasing time, T_2, and, in some cases, the Δ_i amplitudes of each spectral diffusion component, thereby determining the full $C(t)$ in the form of Equation 4.4.[5]

$$C(t) = \frac{\delta(t)}{T_2} + \sum_i {\Delta_i}^2 \exp\left(\frac{-t}{\tau_i}\right) \quad (4.4)$$

The resulting $C(t)$ parameters from this analysis are shown in Table 4.2 for the aerogel and four alcogel samples. Also included in the table are the corresponding homogeneous linewidths that are obtained from $\Gamma = 1/\pi T_2$. Focusing on this metric, the analysis shows that the homogeneous linewidths for the $\nu_{Si\text{-}H}$ subensembles are all significantly thinner than the linear lineshapes obtained by FTIR. These widths could not have been extracted without the use of nonlinear spectroscopy. Some of the samples have very narrow Γs of less than 1 cm^{-1} (chloroform and pentane) while others reach up to a few cm^{-1}. One immediate observation from these data is that Γ is solvent dependent. This is an important result for this study since we seek to demonstrate that the silane vibration intrinsic to the silica matrix is sensitive to the nature of the solvent rather than simply reporting the dynamics of the silica network itself. Table 4.2 shows that Γ does not track in any obvious way with the strength of solvent interactions described by the LSER parameters. For example, the aerogel sample should represent the case of α, β, and π* contributions of zero – air has minimal hydrogen bond donating or accepting strength or polarizability – but has a homogeneous linewidth that falls between those of DMF and isopropanol, the two solvents with the strongest interactions and solvatochromism. The Γ values for pentane and chloroform are nearly described by just the T_1 relaxation times, which shows that pure dephasing in these solvents is minimal. This is an intuitive result for pentane due to its nonpolarity and non-specific solvent-silica interactions, but is surprising for chloroform, which is polar and a weak hydrogen bond donor.

Table 4.2. Complete $C(t)$ parameters from ellipticity decays and iterative fitting of the linear lineshape.

sample	T_2 (ps) [a]	Γ (cm^{-1}) [a]	Δ_1 (cm^{-1}) [a]	τ_1 (ps) [b]	Δ_2 (cm^{-1}) [a]	τ_2 (ps) [b]
aerogel	3.8 (+2.0/-0.7)	2.8 (+1.5/-0.6)	3.6 (+/-1.1)	1.9 (+/-2.0)	26.7 (+/-0.2)	2060 (+/-1820)
pentane	22.2 (+2.7/-12.6)	0.5 (+0.1/-0.3)	------	-------	27.2 (+/-0.2)	337 (+/-34)
chloroform	24.8 (+3.6/-14.1)	0.4 (+0.1/-0.2)	6.1 (+/-1.2)	1.2 (+/-0.2)	28.6 (+/-0.2)	408 (+/-25)
DMF	2.9 (+1.1/-0.6)	3.7 (+1.4/-0.8)	4.7 (+/-0.5)	4.1 (+/-1.0)	25.5 (+/-0.1)	------
isopropanol	7.0 (+3.1/-1.7)	1.5 (+0.7/-0.4)	4.1 (+/-0.5)	1.9 (+/-1.2)	22.1 (+/-0.1)	449 (+/-100)
isopropanol to pentane	2.8 (+0.6/-0.4)	3.7 (+0.8/-0.6)	3.9 (+/-0.3)	2.7 (+/-2.4)	23.6 (+/-19.4)	373 (+/-91)

a. Error values in parentheses for T_2, Γ, Δ_1, and Δ_2 represent iteratively determined parameter limits that allow 99% of the best-fit chi-squared value to be recovered by floating all other parameters.
b. Error values for τ_1 and τ_2 represent the standard error of the exponential fit to the ellipticity decay data.

Transitioning to the Δ and τ parameters in Table 4.2 that describe spectral diffusion, we can divide the dynamics results into faster and slower categories characterized by Δ_1 and τ_1 or Δ_2 and τ_2, respectively. This categorization is somewhat artificial and does not reflect the entire range of solvent-silica fluctuations, rather it captures the dynamics that are most strongly coupled to the $\nu_{Si\text{-}H}$. We find that in the solvent-free aerogel and all four alcogels there is a significant contribution to the correlation function that is very slow or effectively static (Δ_2). This category describes frequency fluctuations that are very slow on the time scales of our measurements and appear as inhomogeneous broadening in the spectrum, although in the cases of pentane and chloroform there is a measurably slow decay

to the ellipticity that might contribute to mild dynamic line broadening for an oscillator with a longer T_1 relaxation time. Treating these components as inhomogeneity, it can be seen by comparison to the FWHM values from the FTIR spectra in Table 4.2 that the Δ_2 values track almost linearly (Figure 4.13). This is further evidence that the linear lineshape is dominated by inhomogeneous broadening and contains no extractable dynamic information for this system.

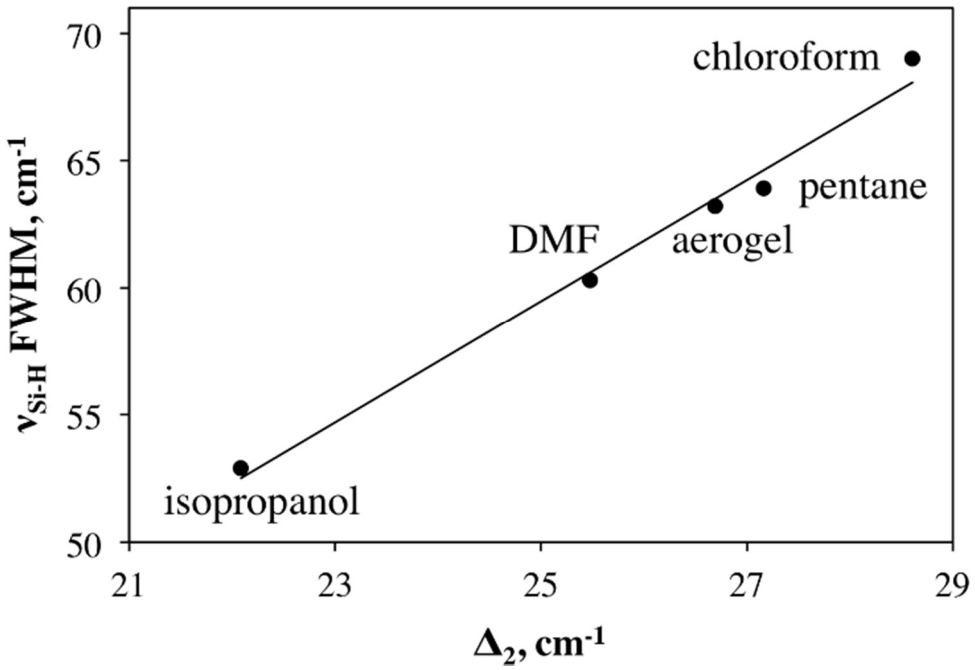

Figure 4.13. FWHM of the FTIR lineshapes of the ν_{Si-H} in the four alcogels and aerogel as a function of the static (or pseudo static) amplitude (Δ_2) in the complete $C(t)$. The fact that there is a linear correspondence shows that the variations in the linear linewidth are due to increases in inhomogeneity, not dynamical differences.

The remaining dynamics to discuss are those of faster spectral diffusion (Δ_1 and τ_1). In these parameters, the error bars are more comparable to the values themselves, making it difficult to differentiate between the amplitudes and time constants of the frequency fluctuations during the T_w period. Comparing the four alcogels, we note that the pentane lacks these dynamics in its correlation function, which might be anticipated due to its low polarity compared to the other three. Using the model that the frequency

fluctuations experienced by a vibrational oscillator are driven by time-dependent changes in the net electric field projected onto the transition dipole moment as a time dependent Stark effect, structural fluctuations of polar solvents in the vicinity of the $\nu_{Si\text{-}H}$ would induce larger amplitude frequency perturbations. Comparing the time constants for these three alcogels, DMF is slower, which could be a reflection of its higher viscosity, but this is only conjecture and is not conclusive from the data presented here. Comparing the faster dynamics of the three alcogels to the aerogel, we see that the time constants are very similar but that the relative contribution is smaller for the aerogel. This is consistent with the qualitative observation of the ellipticity decay in Figure 4.12, which showed that the aerogel 2D-IR lineshape changes were characterized by some very fast loss of correlation followed by a long inhomogeneous plateau. The additional contributions of few-ps dynamics for chloroform, DMF, and isopropanol were clearly visible in that figure, and are now quantified in Table 4.3.

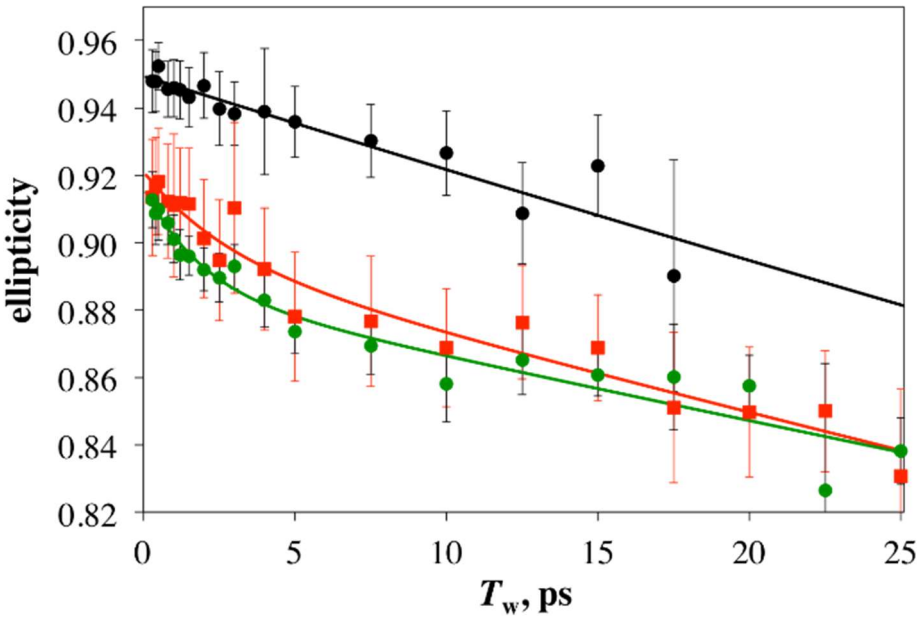

Figure 4.14. 2D-IR ellipticities as a function of T_w for the $\nu_{Si\text{-}H}$ in alcogels infiltrated with pentane (black circles), isopropanol (green circles), and isopropanol replaced with pentane (red squares). Overlaid solid lines are multiexponential fits to the data. Error bar calculation described in the Experimental Section.

Figures 4.14b examined the reversibility of the solvatochromism of these materials by monitoring $\nu_{Si\text{-}H}$. The chloroform-DMF solvent exchange was reversible whereas the pentane-isopropanol was irreversible. Isopropanol appears to have robust interactions with the surface of the pore, which limit its ability to exchange with the weaker interacting pentane molecules. To explore this phenomenon further, 2D-IR measurements were made on an isopropanol-to-pentane exchanged sample. Figure 4.14 shows a plot of the ellipticity decay for an exchanged sample along with the decay of the same sample before the exchange and another in neat pentane for reference. The isopropanol sample exchanged to pentane (red squares) exhibits dynamics very similar to its pre-exchange dynamics. For comparison, the pentane ellipticity decay is also shown and is clearly dissimilar to the exchanged sample. This result is consistent with the hypothesis that a layer of isopropanol molecules is not exchanged for pentane. Even though the majority of the pore volume is occupied by pentane, the frequency fluctuations are dominated by the behavior of isopropanol at the silica interface. The complete $C(t)$ parameters were determined as described above and are provided in Table 4.2. The fitted parameters of the solvent exchanged samples confirm the qualitative comparisons drawn above from Figure 4.14. The isopropanol-to-pentane sample was fit best with both slow and fast components resulting in parameters that, within error, are almost equivalent to the isopropanol sample.

4.4: Conclusions

Understanding not only the static structures but also the dynamic behavior of molecules at the material interfaces is important to a variety of fields. This work focused on measuring the dynamics of solvent adjacent to the surface of a confined volume, a pore within a microporous silica gel. To accomplish this, an intrinsic Si-H probe was inserted into a silica network, offering a scaffolding system that is sensitive primarily to the solvent dynamics near the surface of the pore wall. The system presents superficial probes that are highly accessible to solvent and sensitive to the solvation of the silica surface. 2D-IR spectroscopy was performed on this system in four different solvents and in the absence of solvent, and the spectral diffusion dynamics were also solvent dependent. Highly polar solvents such as isopropanol have stronger interactions with the amphiphilic silica surface in this system and are reluctant to exchange with nonpolar solvents such as pentane. As a result, FTIR and 2D-IR measurements report static and dynamic information that reflects the interfacial species, even when a large fraction of the pore volume is occupied by the nonpolar solvent.

Previous studies in reverse micelles and sol-gel films have been successful at elucidating the underlying molecular dynamics in confined liquids by monitoring an observable of the solvent or solute itself. The current work is unique in that the sensing element is the matrix itself rather than the infiltrating solvent. The sensitivity that this scaffolding system provides offers a unique perspective on solvent-surface interactions with minimal interference from molecules in the pore interior. Future work will seek to quantify the surface selectivity of this mode on the surface of the pore. In addition, to the best of our knowledge, this is the first 2D-IR study that has used Si-H as the probe

vibration, opening the door to a variety of applications that are both relevant in similar silica sol-gel studies but also in various inorganic applications.

4.5 Table of Solvent Parameters

Table 4.3. Solvent parameters and corresponding silane vibrational mode characteristics.

solvent	ν_{Si-H} (cm^{-1})[c]	FWHM (cm^{-1})	α[a]	β[a]	π*[a]	δ
DMSO	2244.6	51.8	0	0.76	1	0
DMF	2247.8	60.3	0	0.69	0.88	0
THF	2248.1	49.2	0	0.55	0.58	1
acetone	2252.8	50.8	0.08	0.43	0.71	0
methanol	2253.1	58.6	0.98[a] 0.35[b]	0.66[a] 0.46[b]	0.60[a] 0.35[b]	0
ethanol	2254.8	42.3	0.86[a] 0.29[b]	0.75[a] 0.52[b]	0.54[a] 0.29[b]	0
t-butanol	2255.6	49.3	0.42[a] 0.31[b]	0.93[a] 0.52[b]	0.41[a] 0.30[b]	0
isopropanol	2255.6	52.9	0.76[a] 0.29[b]	0.84[a] 0.51[b]	0.48[a] 0.21[b]	0
octane	2256.3	49.8	0	0	0.01	0
n-butanol	2256.6	48.8	0.84[a] 0.84[b]	0.84[a] 0.84[b]	0.47[a] 0.47[b]	0
1-octanol	2256.7	61.6	0.77[a] 0.35[b]	0.81[a] 0.51[b]	0.40[a] 0.36[b]	0
acetic anhydride	2258.9	59.6	0	0.29	0.76	0
chloroform	2262.5	69.0	0.2	0.1	0.58	0.5
pentane	2262.6	63.9	0	0	-0.08	0

a) Values from reference [24], unless otherwise noted.

b) Values from reference [19].

c) The FTIR spectra in each solvent were carried out in triplicate and the errors in FWHW and peak centers for each solvent were always within the resolution of the FTIR, see Experimental Section.

4.6 Full Set of FTIR Spectra

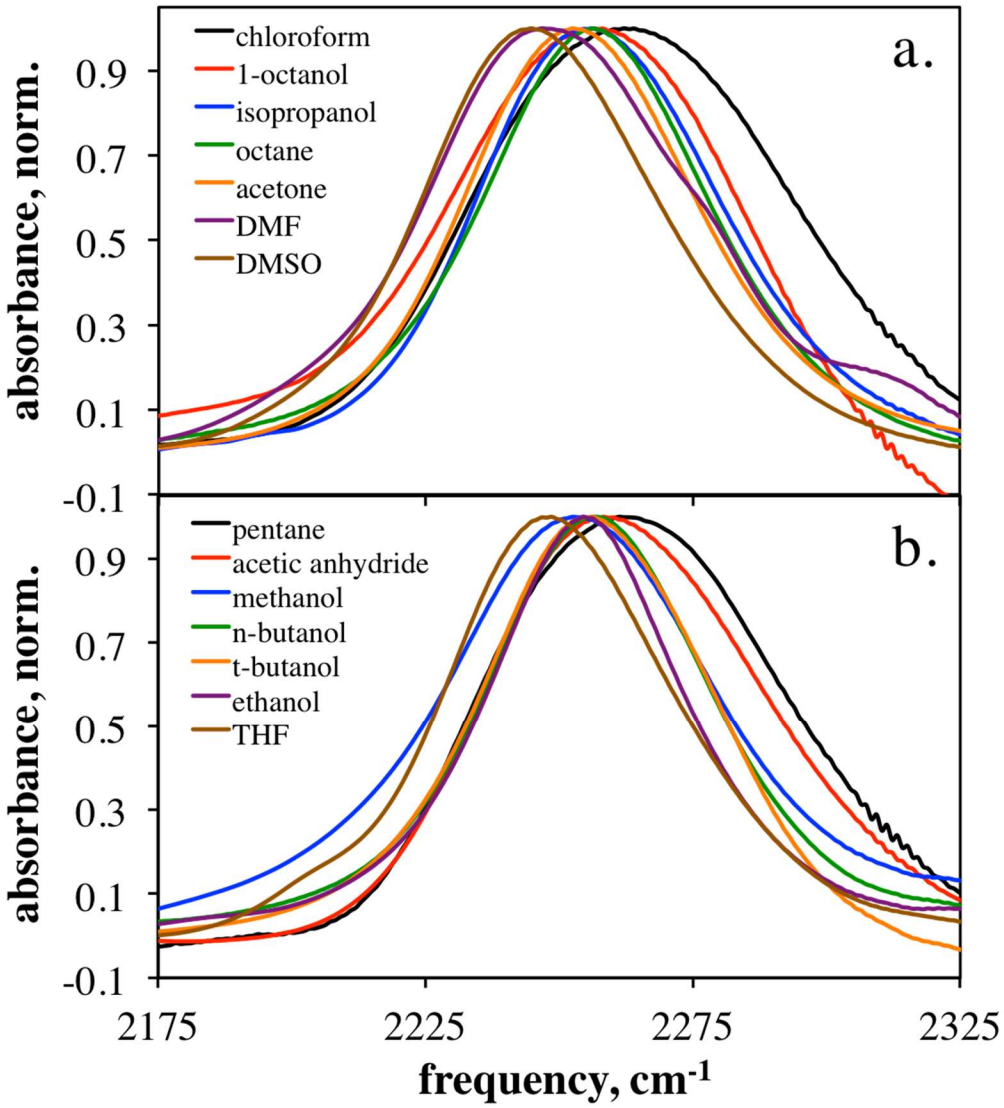

Figure 4.15. Baselined, solvent subtracted, and normalized FTIR spectra of the $\nu_{Si\text{-}H}$ region for silica alcogels infiltrated with all solvents examined in this study. Frames a) and b) show two groups of samples arbitrarily separated for clarity. These spectra were analyzed to produce the $\nu_{Si\text{-}H}$ values in Figures 4.8a-c and 4.9a-b as well as the center $\nu_{Si\text{-}H}$ and FWHMs in Table 4.3.

4.7 Full Set of 2D-IR Spectra

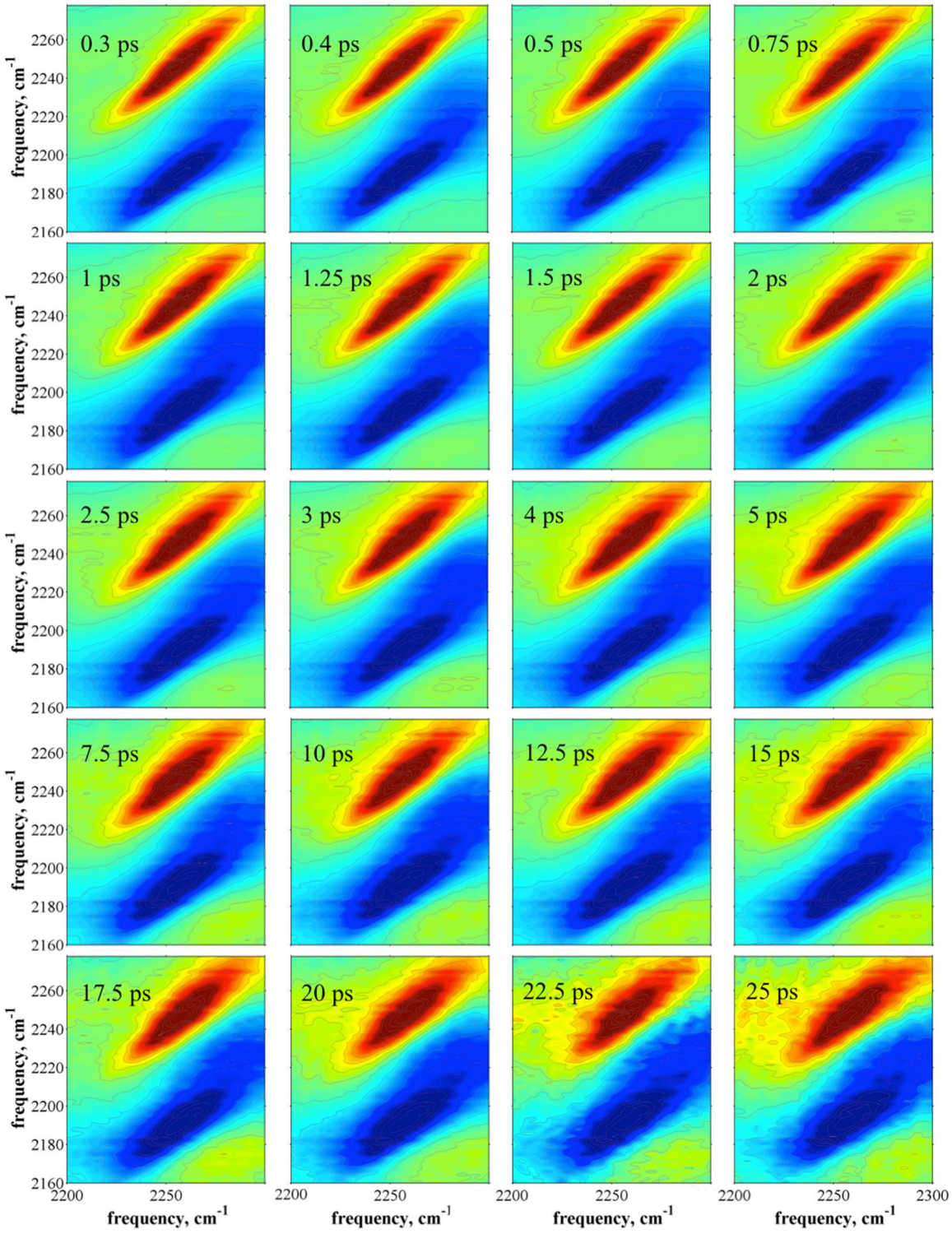

Figure 4.16. 2D-IR spectra for isopropanol infiltrated alcogel.

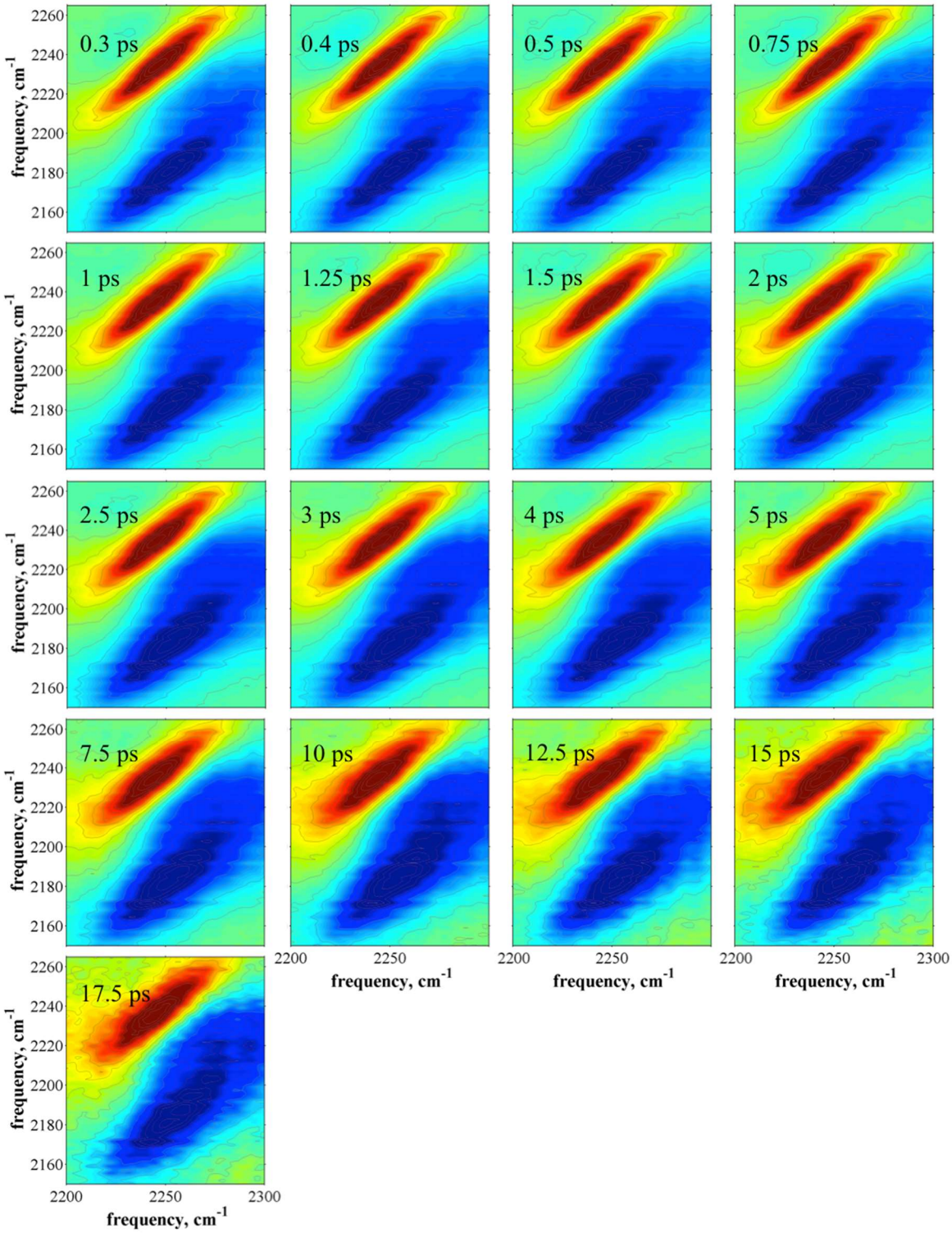

Figure 4.17. 2D-IR spectra for DMF infiltrated alcogel.

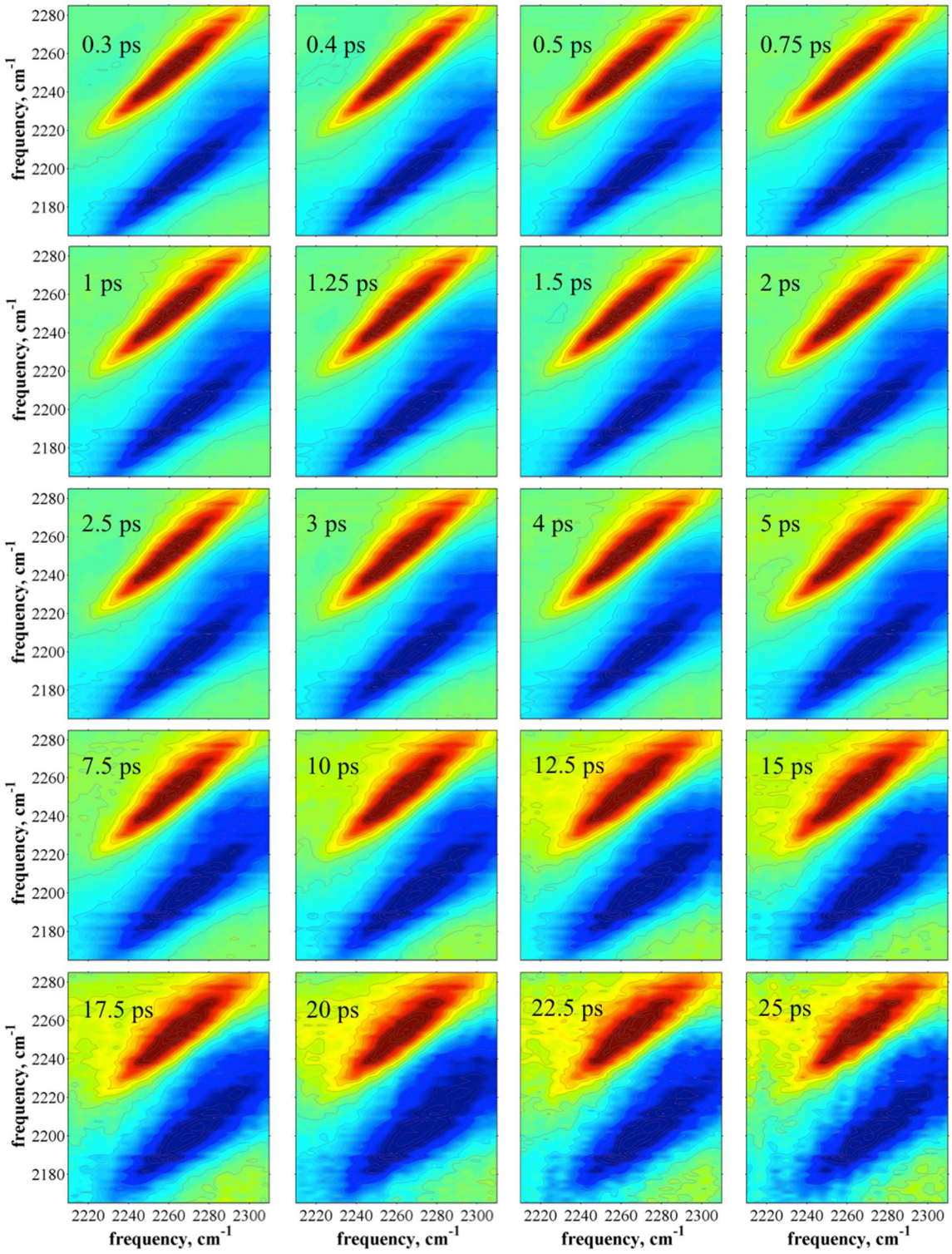

Figure 4.18. 2D-IR spectra for chloroform infiltrated alcogel.

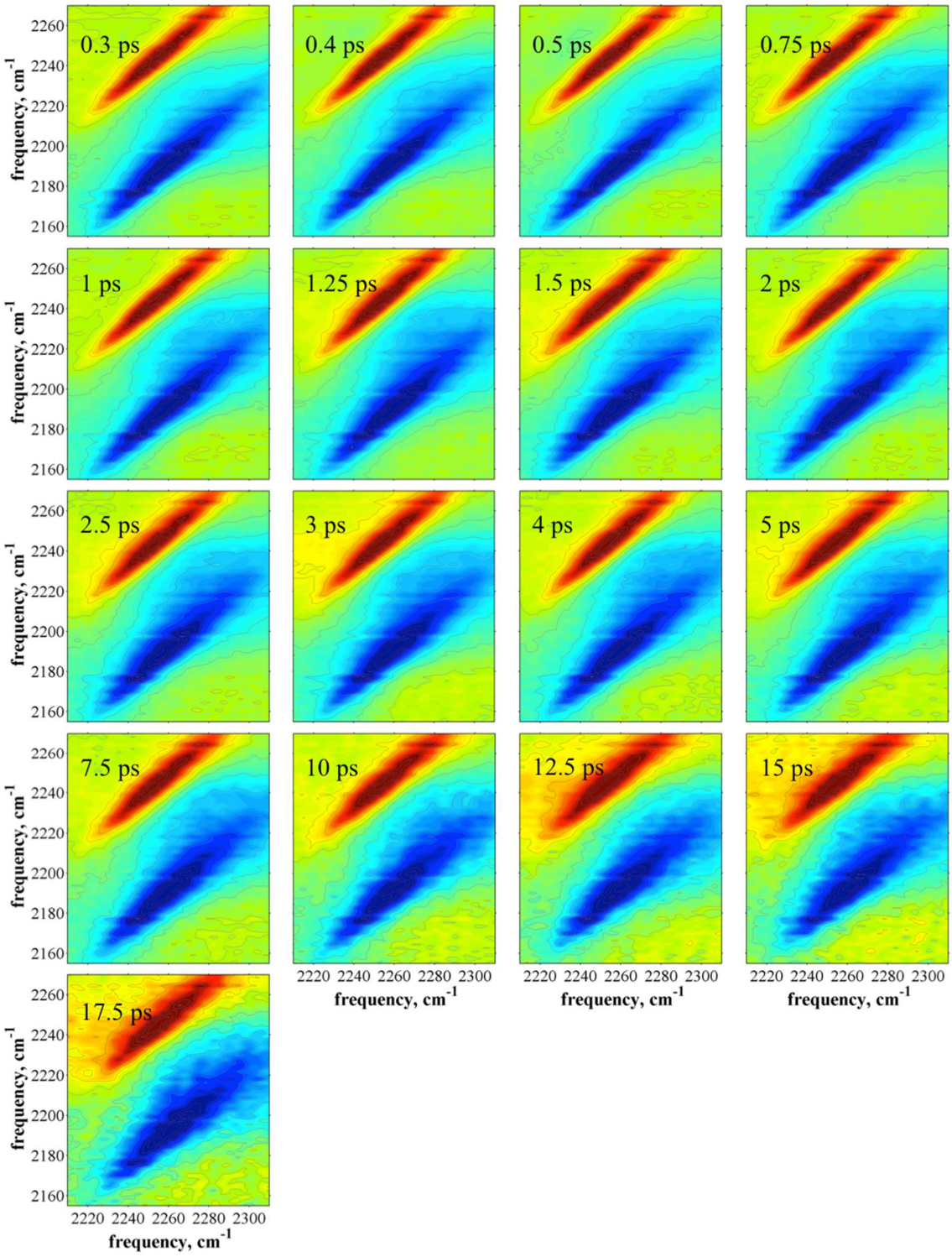

Figure 4.19. 2D-IR spectra for pentane infiltrated alcogel.

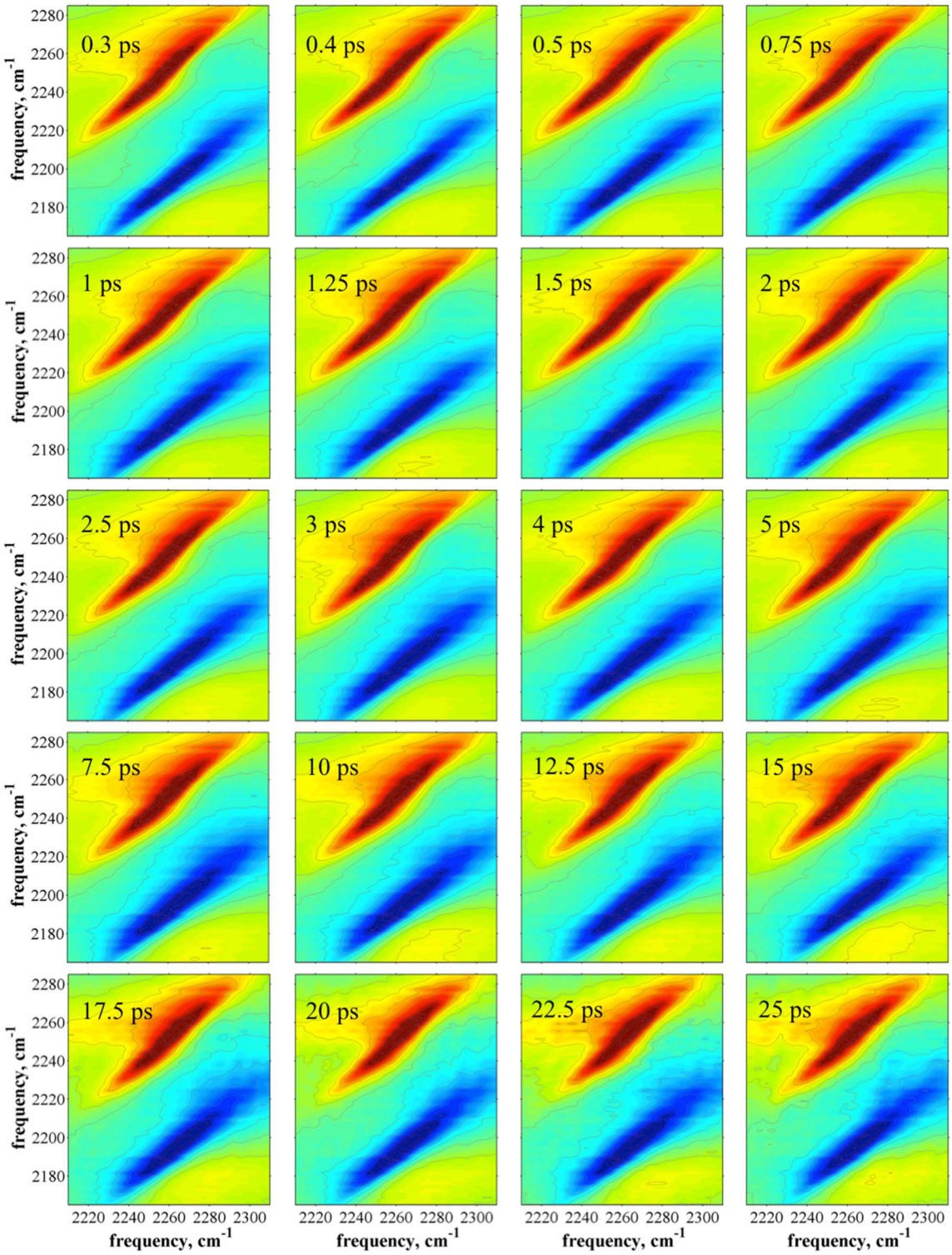

Figure 4.20. 2D-IR spectra for silica aerogel.

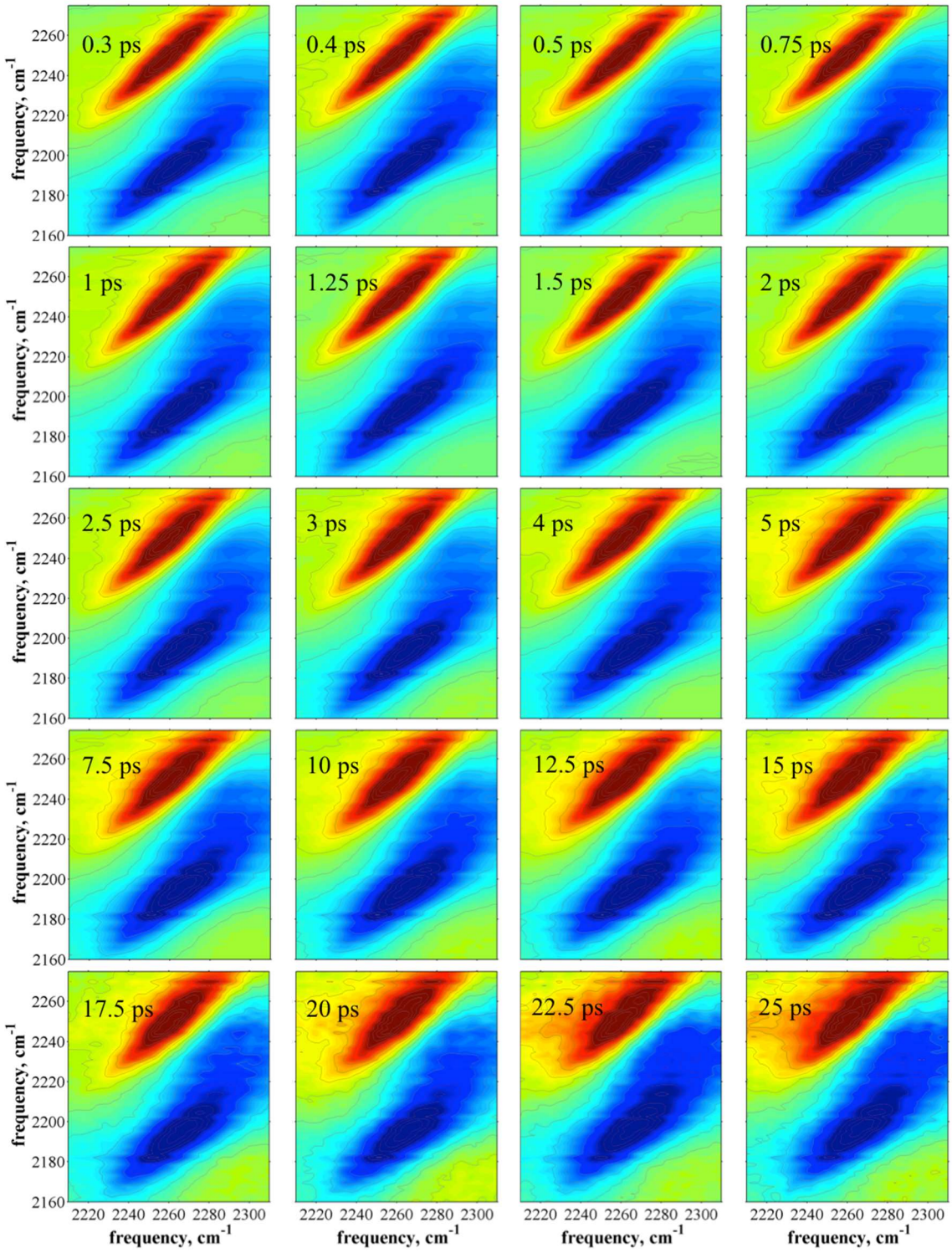

Figure 4.21. 2D-IR spectra for alcogel synthesized in isopropanol then switched to pentane.

Chapter 5: 2D-IR Spectroscopy of Porous Silica Nanoparticles: Measuring the Distance Sensitivity of Spectral Diffusion

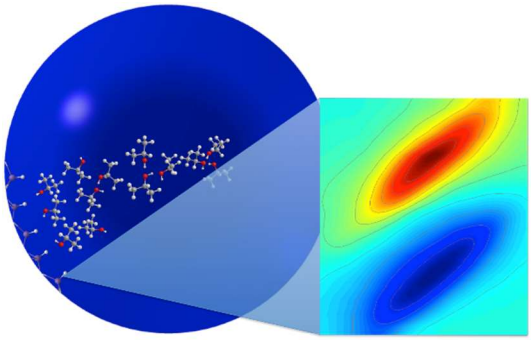

ABSTRACT Two-dimensional infrared spectroscopy (2D-IR) was used to investigate the sensitivity of a vibrational mode to spectral diffusion on the nanometer length scale. A confined volume within a porous silica nanoparticle was used as the model system. Utilizing a novel grafting technique, silane probes were covalently secured to the pore surface for a series of templated mesoporous silica nanoparticles with variable pore sizes. 2D-IR measurements determined that isopropanol exhibited two dominant times scales of ultrafast motions within the pores with time scales of a few picoseconds and tens of picoseconds. The unique perspective of the probe on a surface revealed that the vibrational dynamics of the reporting mode were perturbed by molecules up to ~5 nm away. The data were modeled well by a $1/d^2$ distance dependence for the coupling of solvent dynamics to frequency fluctuations, and a logistic radial distribution of fast and slow dynamic populations.

5.1: Introduction

Two-dimensional infrared spectroscopy (2D-IR) is an excellent technique for elucidating ultrafast dynamics in a variety of solvents.[1, 102, 205] In these measurements, a collection of vibrational oscillators is manipulated coherently by an ultrafast IR pulse sequence. The oscillators are vibrationally excited and then allowed to experience their surroundings for a coherence period, τ, and a population period, T_w, which are experimentally controlled by subsequent pulse interactions. The time dependent rearrangements of proximal atoms (either in the solvent or on the solute itself) induce time dependent frequency fluctuations that enable the oscillators to diffuse spectrally. The width along the diagonal dimension of a 2D-IR peak shape reflects the chemical heterogeneity experienced by that vibrational mode – this is the full range of possible frequencies that the oscillators can obtain. The antidiagonal width shows the portion of the diagonal frequency range that has been sampled through spectral diffusion and homogeneous dynamics. A 2D-IR peak that is diagonally elongated indicates that the oscillators have not yet sampled the full range of possible frequencies at that T_w. At the other extreme, a round peak shape with an antidiagonal width that is the same as its diagonal width shows that perturbations from the surrounding environment enabled all of the oscillators to experience all of the possible solvent/solute configurations, and therefore obtain all frequencies during the T_w period. The time scales of spectral diffusion obtained by 2D-IR quantify the transition between these two cases over the T_w time period and characterize an important facet of ultrafast solvent dynamics.

Ultimately, one seeks to relate the time scales of structural motions that are obtained from these macroscopic measurements back to their microscopic origins. This can be

achieved to some extent by pairing 2D-IR measurements with molecular dynamics (MD) simulations, as long as the modeling accurately reproduces the measured observable.[36, 37, 43, 203] In this context, an important but elusive question is: how far away can structural motions be from the reporting mode and still contribute to the vibrational frequency fluctuations that lead to spectral diffusion? The prevailing thought is that the majority of dynamics sensed in 2D-IR originate in the proximal solvent shell,[34, 109, 206-209] but it is difficult to differentiate dynamics from molecules adjacent to the probe from those that occur a few nanometers away. Understanding the distance sensitivity of spectral diffusion ultimately makes the technique more powerful and broadly applicable to new systems.

Conceptually, one could envision measuring the dynamics from a vibrational probe while progressively increasing the thickness of the bathing solvent layer. In the process, it must be appreciated that solvent molecules in the first solvation shell around a solute behave differently than they do at longer distances,[34, 109, 206-209] and, similarly, the dynamics of solvent molecules are altered by the presence of an interface.[63, 65, 67] Depending on the strength of the solvent-solute or solvent-surface interactions, the solvent will generally organize into more densely packed regions at their junction.[63-68] Molecular dynamics near a surface often become hindered due to an increase of order near the interface.[63, 65, 67] Of particular relevance to the current study, MD simulations by Tarmyshov and coworkers showed that isopropanol molecules exhibited slower dynamics and layered ordering out to three nm from a platinum surface, regardless of the net charge on the metal.[66] Likewise, MD simulations from Youngs and coworkers showed that isopropanol exhibited lamellar structure out to two nm from an alumina surface indicating that surface chemistry plays a role in the solvent structure near an interface.[67]

Moving beyond the proximal solvent shells, force field calculations predict that solvent shell structure varies continuously, as a function of distance.[63-68] Experimentally, mapping out the molecular dynamics over this coordinate is challenging. The archetypal systems to investigate solvent-surface interactions are confined volumes, such as reverse micelles,[69-73] porous silica,[47, 74, 75] and zeolites.[76] 2D-IR studies of water in reverse micelles have shown, conclusively, that spectral diffusion varies continuously with the volume of the solvent pool and is not well described as a core of bulk-like solvent independent of a shell of surface-like solvent.[37, 69, 158, 159] However, these measurements invariably probe a vibrational mode on the solvent molecules, which captures spectral diffusion from molecules in all possible environments within the pore rather than providing the information as a function of distance from the wall.

In the current study, silanes grafted onto the surfaces of mesoporous nanoparticles served as vibrational probes of pore solvent dynamics. Unlike the aforementioned confined volume measurements in which the vibrational reporter was on the solvent molecules themselves, this work monitors the impact of an adjustable solvent volume on spectral diffusion of a surface-localized mode. The confined volume is observed from the perspective of the surface, emphasizing the dynamic behavior of solvent molecules near the silica interface. By employing a templated silica nanoparticle synthesis,[84, 210] we systematically varied the average pore diameters to characterize the distance sensitivity of 2D-IR spectroscopy.

5.2: Experimental Methods

Materials

All reagents were used as received without further purification. Trimethoxysilane (TriMOS, 95% purity), hexadecyltrimethylammonium bromide (CTAB, 99%), N,N-dimethylhexadecyl amine (DMHA, >95%), and tetraethylorthosilicate (TEOS, 98%) were purchased from Sigma-Aldrich. Aqueous ammonium hydroxide (NH_4OH, 28-30%) was purchased from Macron Fine Chemicals. Isopropanol and ethanol were purchased from Decon Labs, Inc. The water used in these experiments was purified by a Millipore Milli-Q system equipped with a 0.22 μm Milli-pak filter.

Mesoporous Silica Nanoparticle (MSNP) syntheses

MSNPs with four different pore-sizes were synthesized by nearly identical procedures but using different proportions of starting materials as listed in Table 5.1. For each particle type, once the appropriate reactant proportions were combined, the flask was sealed with Parafilm and stirred vigorously for 1 h at 50 ºC. After stirring, the solutions containing DMHA were ultrasonicated for 1 h followed by 20 min of additional stirring; the 3 nm reaction mixture was used without ultrasonication. To each mixture, 2.5 mL of 0.88 M TEOS in ethanol were pipetted drop-wise and the solution was stirred for 1 h. The solution was transferred to beakers and was aged for 24 h at 50 ºC. After aging, each solution was purified by dialysis using glacial acetic acid, ultrapure deionized water, and ethanol. 30 mL of glacial acetic acid were added to a 3:1 water-ethanol mixture and dialysis was repeated two more times using increasing amounts of ethanol with 1:1 and 1:3 mixtures, respectively. Dialysis was completed over 72 h.

Table 5.1. Proportions of reactants used to prepare templates for MSNP syntheses.

pore diameter	CTAB (g)	DMHA (μL)	0.256 M NH_4OH (aq) (g)
3	0.29	0	150
6	0.145	67	150
9	0.145	134	150
12	0.145	200	150

Grafting Si-H to MSNP surfaces

The particles were dispersed in absolute ethanol, centrifuged for 45 min at 20,000 rpm at 4 ºC, and redispersed in toluene. This was followed by two additional toluene washes, where washing entails forming a nanoparticle pellet via centrifugation and then redispersing in the specified solvent. After centrifugation, the particles were dispersed in 10 mL of toluene and 0.75 mL of TriMOS were added to the solution. The particles were stirred for 24 h at 70 ºC. After stirring, the nanoparticle suspension was purified by two washes with toluene, as well as five washes with isopropanol; supernatant FTIR studies confirmed that free TriMOS in solution, as well as residual toluene, were largely removed via centrifugation washes. After purification, the suspensions were filtered with a 1 μm Millipore glass microfiber filter.

MSNP Characterization

Nitrogen adsorption-desorption isotherms were collected with a Micromeritics ASAP 2020 system at 77 K. Powdered samples of 50-100 mg were degassed at 90 °C until a pressure of 10 μm Hg was reached for 1 h and then at 120 °C for 6 h prior to measurement. Barrett-Joyner-Halenda/Kruk-Jaroniec-Sayari (BJH/KJS) and density function theory (DFT) modeling were used to calculate pore volumes, and the Brunauer, Emmett, and

Teller (BET) model was used to calculate surface areas. Total pore volumes were calculated from the quantity of gas adsorbed at relative pressure (P/P_0) of 0.99.

Dynamic light scattering (DLS) measurements were performed with a Brookhaven Instruments Zeta PALS system at 25 °C. Purified nanoparticle samples were measured at a concentration of 1 mg/mL.

Transmission electron microscopy (TEM) images were collected on a FEI Tecnai T12 electron microscope operating at 120 kV. TEM samples were prepared by dipping a copper grid coated with carbon and formvar (200 mesh, Ted Pella Inc.) into ethanolic particle suspensions and air drying. Diameter measurements were collected manually with Image J (NIH) and are reported as the average of 500 particles.

2D small angle x-ray scattering (2DSAXS) measurements were collected on the University of Minnesota small angle scattering line using a Rigaku RU-200 rotating anode generator with a fine-focus copper point source, conditioned with totally reflective cross-coupled Frank mirrors, and a Bruker-AXS Hi-Star multi-wire two-dimensional area detector. Data were collected with a line distance of 70 cm for 2 min X-ray exposures (40 kV and 60 mA). GADDS (generalized area detector diffraction system) software with step size of 0.005 degrees was used to integrate the whole diffraction pattern after background subtraction of the sample holder.

Spectroscopic studies were performed on solutions sandwiched between two 3 mm CaF_2 windows with a 50 μm Teflon spacer to define the sample path length. Fourier transform infrared (FTIR) spectra were collected on a Nicolet 6700 FTIR spectrometer (Thermo Scientific) with at least 16 scans and a resolution of 2 cm^{-1}. A background spectrum of the particles without Si-H modes in isopropanol was subtracted from the

particle spectra presented below, while an isopropanol background was subtracted from the TriMOS scan.

The 2D-IR instrument and experimental setup has been described in Section 2.3.

5.3: Results and Discussion

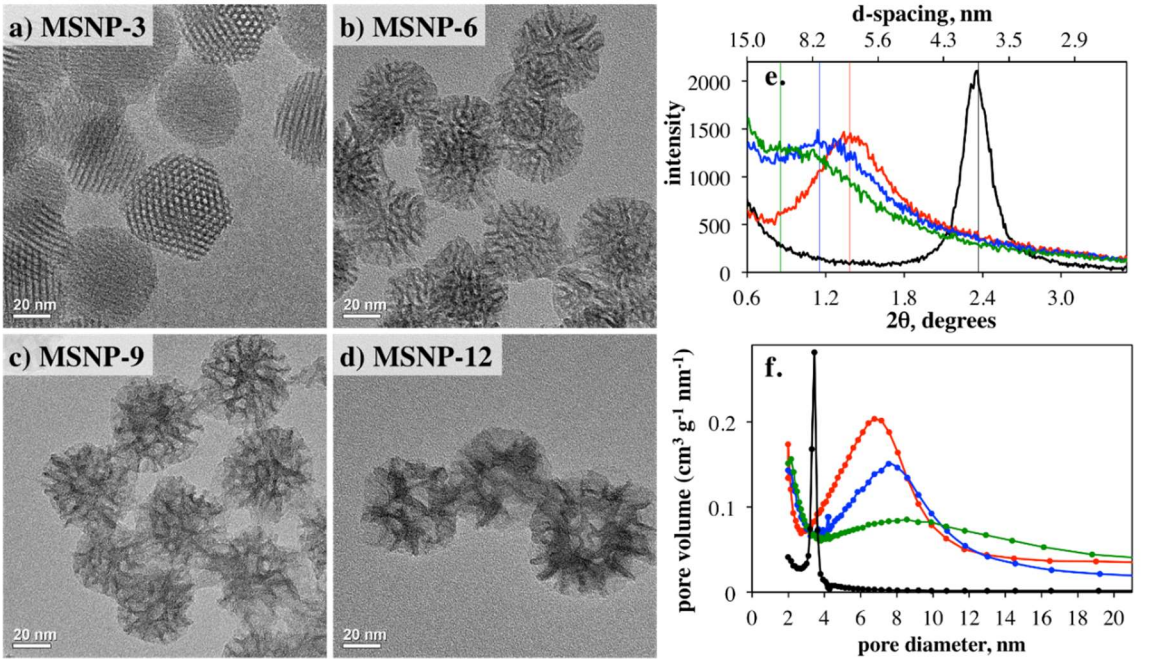

Figure 5.1. TEM images of a) MSNP-3, b) MSNP-6, c) MSNP-9, and d) MSNP-12 particles. e) 2DSAXS scattering intensities for MSNP-3 (black), MSNP-6 (red), MSNP-9 (blue) and MSNP-12 (green) particles demonstrating the systematic variation of pore sizes. f) Pore size distributions as determined from N_2 adsorption isotherms using BJH analysis and plotted with the same color scheme as (e).

Figures 5.1a-5.1d show representative transmission electron micrographs of the MSNPs used in this study. The characterization of these particles herein indicates that their pore sizes are roughly 3, 6, 9, and 12 nm, and they will be referred to for the rest of this work as MSNP-3, MSNP-6, MSNP-9, and MSNP-12, respectively. Figure 5.1a illustrates the traditional hexagonally ordered pore network observed in the MSNP-3 particles.[211] Comparison to MSNP-6 in Figure 5.1b demonstrates that the particle morphologies change when co-surfactants such as DMHA are used in the templating process. Inclusion of a small amount of DMHA resulted in larger (~6 nm) but more disordered pores. Increasing the amount of DMHA used in the micelle templating process further expanded the pores and decreased their ordering, transitioning to a "worm-like" morphology by MSNP-9 (Figure 5.1c).[212] Using the maximum amount of DMHA resulted in MSNP-12 particles

with large pore diameters that were a significant fraction of the nanoparticle itself. 2DSAXS measurements (Figure 5.1e) corroborated the TEM pore size variations, as MSNP-3, MSNP-6, MSNP-9, MSNP-12 had average d-spacings of 3.8, 6.6, 7.8, and 10.5 nm, respectively. The ordered, faceted nature of MSNP-3 was lost as DMHA was incorporated in the micelle templates for MSNP 6-12. The singly resolved SAXS peaks are in agreement with previous work describing mesoporous silica films.[213] Nitrogen physisorption isotherms further confirmed the TEM and 2DSAXS data, showing increased porosity from MSNP-3 to MSNP-12 (Figure 5.2).

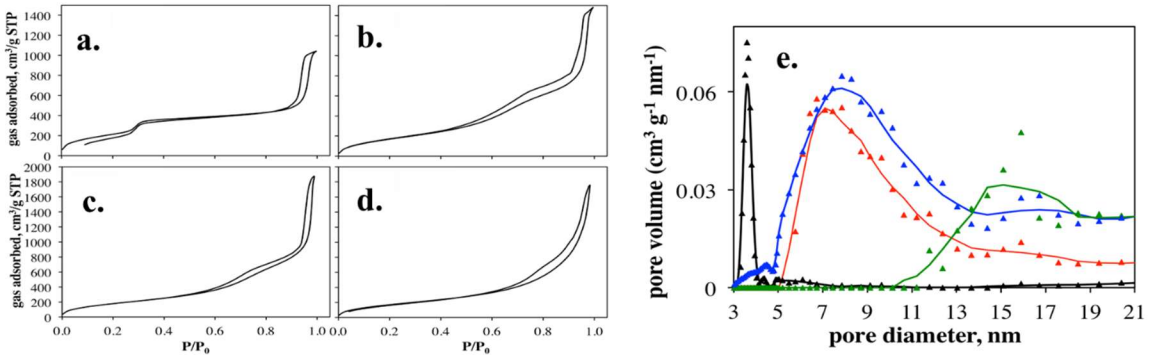

Figure 5.2. Nitrogen adsorption isotherms for a) MSNP-3, b) MSNP-6, c) MSNP-9, and d) MSNP-12, collected as described in the text. e) DFT pore distribution analysis from nitrogen adsorption isotherms. Maxima for MSNP-3, -6, -9, and -12 are 3.8, 6.6, 7.8 and 10.5 nm based on fitting the top of each curve to a Gaussian peak.

From Figure 5.2 we see that the MSNP-3 isotherm had traditional MCM-41 type IV isotherm features with a capillary condensation inflection at P/P_0 ~0.35.[211] MSNP-6, MSNP-9, and MSNP-12 have their major capillary condensation inflections shifted to higher P/P_0 values of 0.60, 0.75, and 0.85, respectively. These changes in capillary condensation resulted in the BJH pore distribution plots in Figure 5.1f. In agreement with TEM and 2DSAXS, BJH pore distributions show increases in both the pore diameters and pore distribution polydispersities as more DMHA was used to template the particles via TEOS condensation. It has been noted that modeling of larger pores, as in MSNP-9 and MSNP-12, is more accurate when treated by DFT.[214] This analysis produced somewhat

different pore size distributions (Table 5.2). As expected, there is strong agreement between the two methods for the smaller pore-diameter particles, but divergence from the BJH values by MSNP-12. The pore diameters for both analyses are tabulated in the Table 5.2, and the averaged values are 3.5, 6.9, 7.8, and 12.1 nm, in close agreement with the 2DSAXS results. BET surface area calculations revealed that the surface areas of all MSNPs in this work ranged from 676-928 $m^2 g^{-1}$ after grafting the Si-H moiety to the silica surfaces. The majority of this surface area is inside the pores themselves rather than on the exterior of the particles, and we expect a similar number of grafted molecules on all four sample types.

Table 5.2. Characterization results for MSNP-3, -6, -9, and -12 and TriMOS. T_1 values were recorded with particles and TriMOS in isopropanol.

particles	pore diameter (nm)				BET surface area (m^2/g)	DLS mean particle size (nm) [b]	T_1 (ps)[c]
	2DSAXS	N_2 adsorption					
		BJH KJS[a]	DFT[a]	average			
MSNP-3	3.8	3.42 (0.11)	3.62 (0.16)	3.52	928	159 (9.1)	9.6 (0.6)
MSNP-6	6.6	6.75 (1.77)	7.06 (2.89)	6.91	680	221 (0.6)	10.7 (0.5)
MSNP-9	7.8	7.64 (2.05)	8.03 (2.04)	7.84	702	194 (6.4)	10.2 (0.5)
MSNP-12	10.5	9.07 (3.80)	15.3 (1.1)	12.17	676	214 (24)	8.1 (0.4)
TriMOS	---	---	---	---	---	---	6.1 (0.1)

a. parentheses for N_2 adsorption pore distributions represent the standard deviation of the best fit Gaussian peak shape.
b. Parentheses for DLS indicate the standard deviations of three measurements. Note that these sizes are a few times larger than the TEM sizing histograms in Figure 5.3, which indicates that there is some degree of agglomeration of the re-suspended particles.
c. parentheses for T_1 represent the standard error of the exponential fit.

Even though porosity was varied across the samples (MSNP 3-12) in a controlled fashion, no major changes in the primary particle size (~50 nm) were observed via TEM (Figure 5.3) or DLS characterization (Table 5.2).

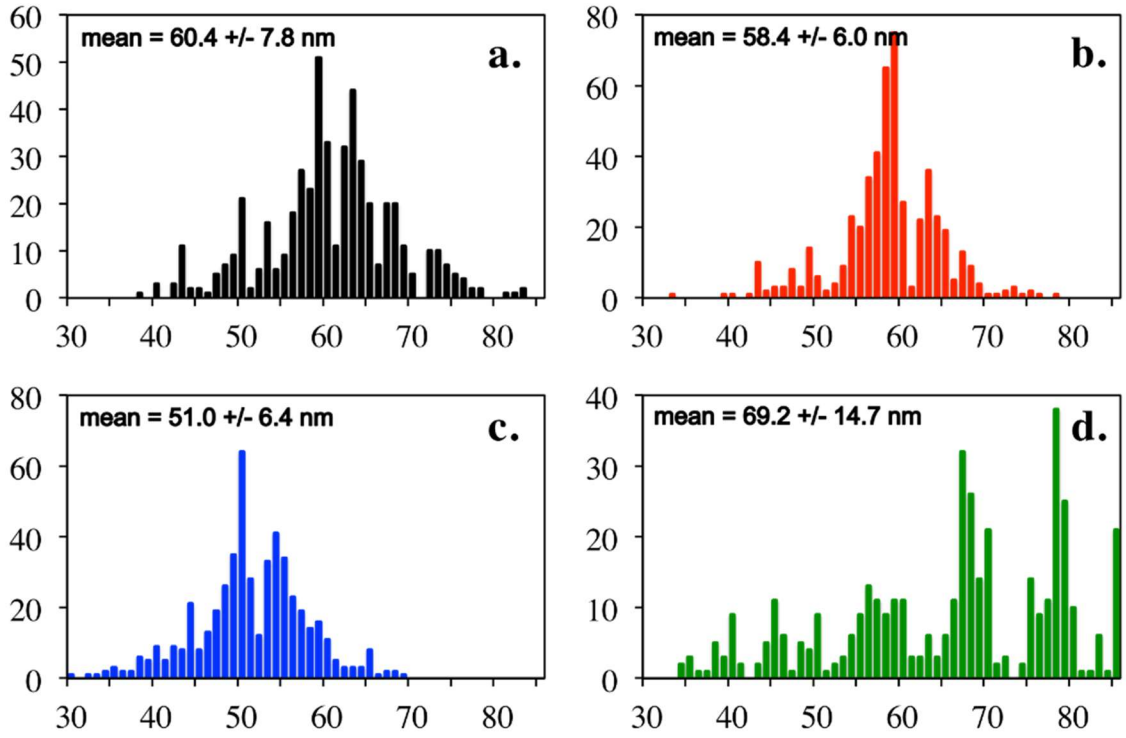

Figure 5.3. Particle size distributions from TEM analysis of 500 particles of a) MSNP-3, b) MSNP-6, c) MSNP-9, and d) MSNP-12. The mean and standard deviation of each distribution is given in the corresponding legend.

Figure 5.4 shows FTIR spectra of the Si-H vibrational mode (ν_{Si-H}) for the unreacted TriMOS precursor (ν_{Si-H} = 2197 cm^{-1}) dissolved in isopropanol and grafted to the four different MSNPs suspended in isopropanol. The silane vibrational frequency reports on the level of condensation within the silica matrix through the inductive effect.[191-195]

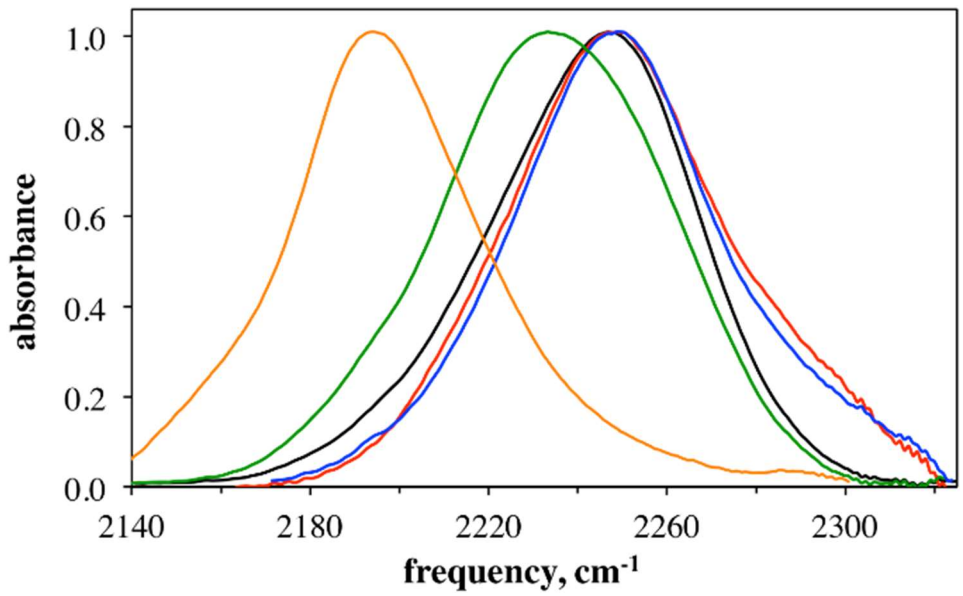

Figure 5.4. Solvent subtracted, baselined, and normalized FTIR spectra in the Si-H stretching region for uncondensed TriMOS in isopropanol (orange), and MSNP-3 (black), MSNP-6 (red), MSNP-9 (blue), and MSNP-12 (green) particles suspended in isopropanol.

In this study, the silica particles were fully formed at the time of grafting, so any differences in $\nu_{Si\text{-}H}$ are due to the degree of condensation of TriMOS on the nanoparticle surface. The blue-shifted Si-H peaks in Figure 5.4 illustrate the success of the TriMOS grafting technique, which, to our knowledge, is the first report of grafting of Si-H groups to a silica nanoparticle surface. The $\nu_{Si\text{-}H}$ for MSNP-3, -6, and -9 are all peaked at approximately 2248 cm^{-1}, which is about 8 cm^{-1} less than was observed in our previous work for a fully condensed sol-gel glass infiltrated with isopropanol.[7] This shows that the surface-bound silanes are not as completely condensed on the smaller nanoparticle pore surfaces as they were in silica sol-gel glasses.[210] The $\nu_{Si\text{-}H}$ for 12 nm particles is red-shifted to 2233 cm^{-1}, indicating less condensation on the largest pore surfaces. This could be due to the low curvature of the larger pore surfaces making it difficult to have multiple site coordination. Regardless of this difference, the large blue-shift for all MSNP spectra from

the unreacted TriMOS frequency clearly demonstrates that the silane is covalently attached to the surfaces of the silica nanoparticles.

At this point, we have established that the templating and grafting methodology results in average pore diameters that are systematically controlled and $\nu_{Si\text{-}H}$ modes that are attached to silica surfaces primarily inside of the MSNP pores. The $\nu_{Si\text{-}H}$ modes on the surface of the MSNP-3 through 12 particles are exposed to progressively larger pool volumes of isopropanol. By measuring 2D-IR spectra on this series, we can characterize the time scales and distance sensitivity of spectral diffusion.

Figure 5.5 shows early and late 2D-IR spectra for MSNP-3, MSNP-12, and TriMOS precursor in isopropanol. All 2D-IR spectra at all T_ws are available at the end of this chapter. The horizontal frequency axis in these spectra is obtained by Fourier transform of the time period between the first and last pulses in the 2D-IR sequence. The vertical axis is the Fourier transform of the time period after the third pulse obtained by spectrally resolving the signal in a monochromator. The positive-going red peaks are the v=0-1 fundamental transitions and the negative-going blue peaks are the v=1-2 transitions. Conceptually, one can interpret the x-coordinate as the frequency at which a subensemble of Si-H oscillators is excited by the first IR pulse, and the y-coordinate as the range of frequencies that this collection of oscillators exhibits after sampling its surroundings for a specified waiting time, T_w.

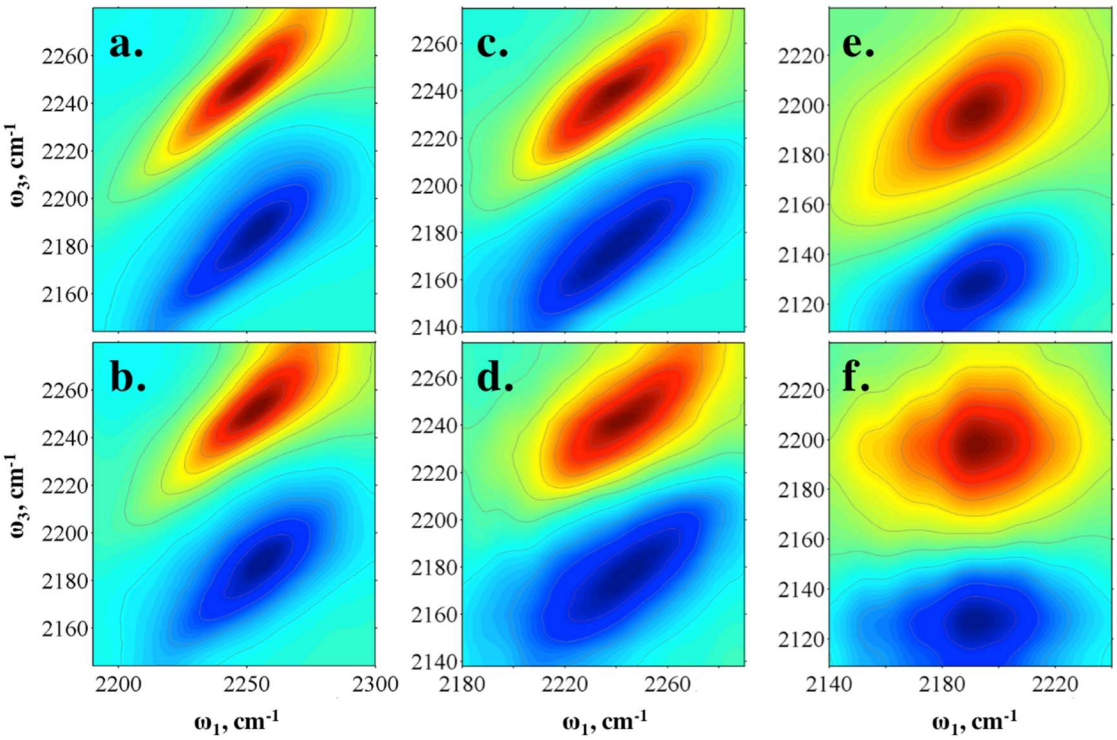

Figure 5.5. 2D-IR spectra of the ν_{Si-H} mode on MSNP-3 a) T_w = 0.3 ps and b) T_w = 10 ps; in MSNP-12 at c) T_w = 0.3 ps and d) T_w = 10 ps; and for TriMOS precursor in isopropanol at e) T_w = 0.3 ps and f) T_w = 7.5 ps. Contour lines mark 10% amplitude increments.

Going from MSNP-3 to MSNP-12 to TriMOS in isopropanol, there is a small increase in the antidiagonal peak width at the shortest T_w (comparing Figures 5.5a, 5.5c. and 5.5e). Since the diagonal widths are similar, this trend indicates a general increase in the solvent dynamics that cause frequency fluctuations on the time scale of a few hundred fs as the surrounding solvent goes from a nanoscopic pool to a bulk liquid. Qualitatively, the smaller pore nanoparticles show very little spectral diffusion (Figures 5.5a and 5.5b) as seen in our previous work with porous silica,[7] but the 12 nm pore sample shows some increased broadening along the antidiagonal dimension (Figures 5.5c and 5.5d). The TriMOS precursor in isopropanol clearly exhibits faster dynamics (broader peak shape) at early times (Figure 5.5e) and significant broadening at the longer T_w (Figure 5.5f). The

ν_{Si-H} 2D-IR peak shapes can be characterized by the peak ellipticity, which is a quantitative measure of the normalized frequency-frequency correlation function (FFCF).[110, 111, 200] Knowing the FFCF enables all linear and nonlinear spectroscopic observables to be calculated, and facilitates direct comparison to atomistic simulations.

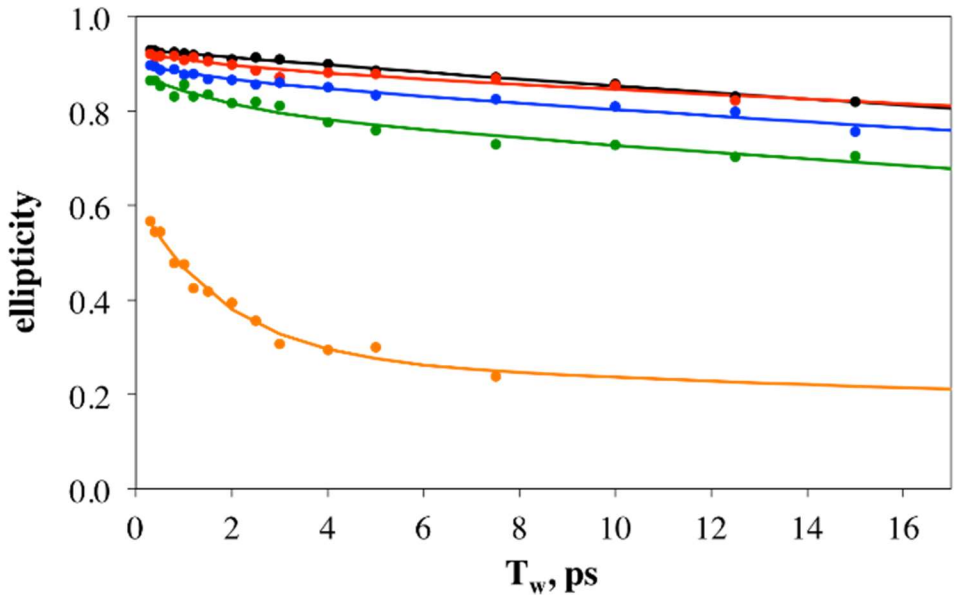

Figure 5.6. Peak ellipticity of the ν_{Si-H} 2D-IR peak shape (v=0-1 transition) as a function of T_w for MSNP-3 (black), MSNP-6 (red), MSNP-9 (blue), and MSNP-12 (green) infiltrated with isopropanol, as well as TriMOS precursor in isopropanol (orange). Overlaid solid lines show a global multi-exponential fit to the data as described in the text

Figure 5.6 shows the ellipticity values for the five samples as a function of T_w. The ellipticity decays for the ν_{Si-H} 2D-IR peak on the MSNPs show that the amount of spectral diffusion increases with the pore diameter, approaching that of the TriMOS precursor in isopropanol, which we view as a "very large pore" limit. As the pore sizes increase, the y-intercepts for the decays start out at lower ellipticity values, showing that there are progressively more dynamics occurring on a time scale faster than a few hundred fs. These could be homogeneous dynamics or very fast spectral diffusion.[202] In addition, the decays become more multi-exponential, indicating that the ν_{Si-H} probes on the surface of the pores

are sensitive to the dynamic characteristics of the augmented solvent core up to several nanometers away. By the time the TriMOS precursor is reached, the ellipticity decay begins near 0.6 and decays significantly over the 15 ps window (even though data were limited to 7.5 ps by the shorter vibrational lifetime of the $\nu_{Si\text{-}H}$ on this molecule). The lifetimes for all of the samples can be found in Table 5.2 and detailed discussion can be found in Appendix B.

The ellipticity decay for MSNP-3 decreases measurably and a slow dynamical component needs to be included in order to accurately characterize the FFCF. We expect that there should be some dynamical contribution in the 2D-IR data from the 3 nm pools of isopropanol and also from the silica matrix itself. We previously measured the silica dynamics for the $\nu_{Si\text{-}H}$ in solvent-free silica aerogels to be effectively constant.[7] Considering the radius of the pore and the lamellar structure predicted by Youngs and coworkers, it seems likely that the MSNP-3 pores are only large enough for 3-4 interfacial isopropanol layers.[67] With this in mind, we hypothesized that the limited dynamics reported by the surface-bound $\nu_{Si\text{-}H}$ on MSNP-3 might require two terms to capture the ellipticity changes: a slow exponential decay for the interfacial isopropanol and an effectively static term for the silica dynamics. At the "very large pore" limit (TriMOS), the ellipticity decays required a biexponential fit with few ps and tens of ps time constants. With the limiting cases in mind, we can think of the increasing pore size as effectively adding more bulk-like molecules into the core volume. If a core-shell model applies to this system, then the slow dynamics due to surface-like isopropanol in the vicinity of a $\nu_{Si\text{-}H}$ mode would remain constant as the pore diameter increases.

To test this model, we carried out a global fit in which a biexponential plus a constant offset was used to simultaneously fit all five of the ellipticity decays. The exponential time constants were shared among the five datasets while the amplitudes floated independently. The resulting fit matches the data remarkably well, and the curves are overlaid as solid lines on the data in Figure 5.6. The resulting time constants from this treatment were 1.6 and 33 ps. The amplitudes from the global fit reproduced the normalized FFCF, but we ideally want to model the full FFCF. Using the method described by Kwak and coworkers, the ellipticity decay parameters were used to reproduce the FTIR spectrum while iteratively adjusting the homogeneous dephasing time, T_2, and, in some cases, the amplitudes of each spectral diffusion component.[5, 202] This procedure yielded the full FFCF parameters in Table 5.3. The time constants, τ_i, in the FFCF give the time scales of the dynamics to which the $\nu_{Si\text{-}H}$ is sensitive. The Δ_i values are interpreted as the magnitudes of frequency fluctuations induced by the surroundings, and, when squared as in Equation 5.1, weight the contribution of a particular dynamical process in the FFCF.

$$FFCF(t) = \frac{\delta(t)}{T_2} + \sum_i {\Delta_i}^2 \exp\left(\frac{-t}{\tau_i}\right) \tag{5.1}$$

Table 5.3. Full FFCF parameters based on global fit to all data.

Sample	Δ_1 (cm^{-1})	τ_1 (ps)	Δ_2 (cm^{-1})	τ_2 (ps)	Δ_3 (cm^{-1})	Γ (cm^{-1})	FTIR FWHM
MSNP-3	0		12.9 (±0.1)		18.7 (±0.1)	11.5 (±0.4)	53.5
MSNP-6	1.23 (±0.15)		12.4 (±0.15)		20.2 (±0.15)	3.74 (±0.46)	56.9
MSNP-9	3.40 (±0.15)	1.6 (±0.3)	12.6 (±0.14)	33 (±36)	17.9 (±0.14)	2.76 (±0.39)	52.6
MSNP-12	7.01 (±0.15)		16.3 (±0.13)		19.1 (±0.15)	8.46 (±0.48)	60.8
TriMOS	13.4 (±0.15)		13.3 (±0.15)		0 (±0.02)	1.79 (±0.44)	47.3

The measured dynamics are the result of frequency perturbations induced by structural motions of the silica matrix and isopropanol dynamics in the pores. Our conjecture that the effectively constant component in the FFCF originates from the silica matrix is supported by the fact that the Δ_3 values are similar for all MNSP samples. As expected, the TriMOS sample does not require the Δ_3 term. The magnitudes of 1.6 ps dynamics (Δ_1) show an increase with the pore diameter to a maximum in the TriMOS sample. These fluctuations are communicated to the $\nu_{Si\text{-}H}$ from the isopropanol that is not interacting with the silica surface. We also note that the homogeneous linewidth, Γ, trends to narrower values from MSNP-3 to TriMOS. An outlier among these values is the MSNP-12, which perhaps shows some differences due to a different degree of condensation to the silica, as noted in the FTIR analysis above. Although the homogeneous dynamics are not the focus of this study, the FFCFs clearly show that the majority of the FTIR linewidth for the silane vibration is due to inhomogeneous broadening (dynamic and effectively static).

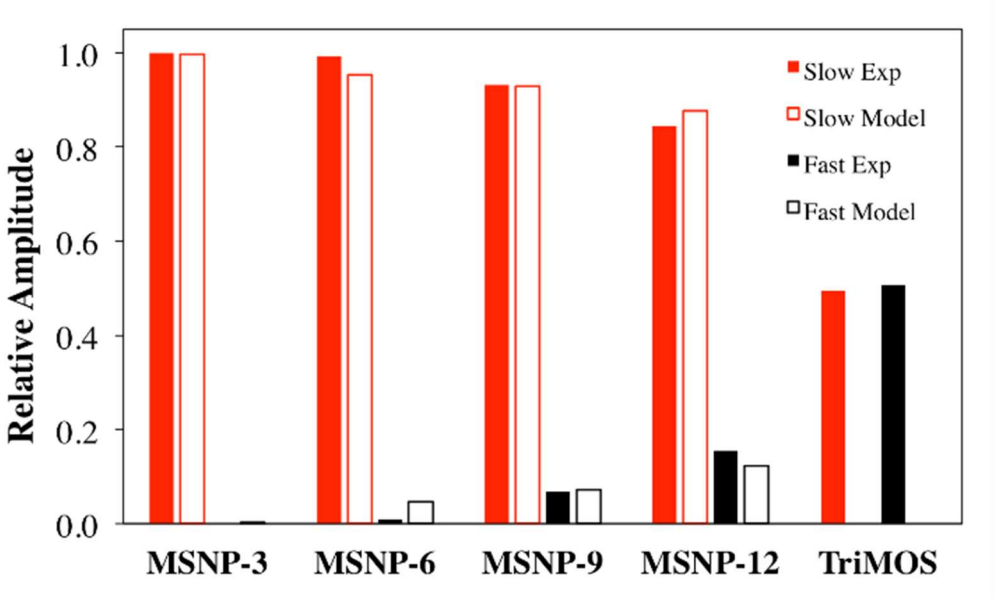

Figure 5.7. Proportional contributions of the fast Δ_1^2 (solid black) and slow Δ_2^2 (solid red) dynamics in the full FFCF. The results from the model are also shown for the fast (hollow black) and for the slow (hollow red) dynamics.

Figure 5.7 shows how the spectral diffusion amplitudes (Δ_1^2 and Δ_2^2) evolve as the pores are systematically varied. The amplitude for each component (Δ_i^2) was divided by the total dynamic amplitude ($\Delta_1^2 + \Delta_2^2$), giving its relative contribution to the spectral diffusion. Figure 5.7 illustrates that the bulk-like solvent dynamics (Δ_1, τ_1) become a larger fraction of the total spectral diffusion as the volume of the pore is increased. Conversely, as the pores become smaller, the dynamics of the average solvent molecule are dominated by the slow component (Δ_2, τ_2). For example, MSNP-3 exhibits almost no frequency fluctuations on the time scale of a few ps.

It is surprising that the Si-H vibrations at the pore surface are sensitive to dynamics at these relatively large distances. Spectral diffusion for water in reverse micelles showed continuous changes in spectral diffusion with pore diameter, but in those cases the 2D-IR signal was emitted from the solvent in the pores – increasing the volume of solvent changed the populations of the vibrational chromophores in different dynamical environments.[37, 69,

[158, 159] Here the ν_{Si-H} mode is only at the pore walls while the isopropanol volume is changing. If the frequency fluctuations of ν_{Si-H} were only affected by the immediate layer of solvent molecules then we would predict that the relative proportion of fast dynamics would be small and constant, but that is clearly not the case. Increasing the pore diameter from 3 to 12 nm leads to a monotonic increase in the fast dynamics reported by the FFCF of the surface-bound silane. Spectral diffusion must be influenced by solvent dynamics that originate several nm away from the reporter mode.

There are two explanations for the empirical data presented in Figure 5.7. Either the probe on the surface is directly sensing dynamics multiple nanometers away or the probe is only measuring the dynamics of the first few solvent layers which are affected by the presence of bulk-like isopropanol in the center of the pore. If the latter (indirect) mechanism were true, the dynamics as a function of distance from the pore surface would be dependent on the size of the pore whereas the former would be independent of the pore size.

Building on the global FFCF fit of the 2D-IR data above, we developed a model to predict the dynamic behavior of a solvent molecule in the pore based on its contribution to the spectral diffusion experienced by a mode on the pore surface. To model the spectral diffusion sensed by a vibrational mode attached to a pore surface, we must consider the dynamical behavior of a solvent molecule anywhere in the pore and the distance sensitivity of the reporting mode to solvent fluctuations. The pores were represented by spheres with radii (R_{pore}) that were determined by the 2DSAXS characterization. A single vibrational probe was envisioned on the pore surface under the assumption that the dipole had no effect on the organization of the solvent near the surface. We know from the global fit that there

are two solvent dynamic components that contribute to spectral diffusion. We can also infer that the dynamics near the surface favor the slow component, whereas dynamics in the center demonstrate both components equally. The distribution of slow dynamics was described as a radial function of the distance from the pore center, R_D, using a logistic functional form.

$$F(R_D) = \frac{A_1}{1+A_2 e^{k(R_D - R_{pore})}} + y \tag{5.2}$$

A_1, A_2, k, and y are fitting parameters that were adjusted to define the fraction of slow solvent dynamics at a given distance from the center of the pore. In this equation, A_1 is the slow amplitude at large distances from the pore center (i.e. near the pore wall), A_2 controls the midpoint of the function, k is the slope of the gradient, and y is an offset to the distribution. It is important to realize that Equation 5.2 is not explicitly a function of distance from the pore surface. The dynamic distribution as a function of distance from the surface is further complicated by an angular dependence. In fact, a molecule within a pore is actually influenced by the surface in every direction. The radial distance from the pore center in Equation 5.2 avoids the angular dependence but is still relevant to the planar surfaces typically modeled in MD simulations.

Not all dynamic motions contribute equally to spectral diffusion. Molecular motions closer to the probe will have a greater influence on the local electric field fluctuations and spectral diffusion. The electric field of the solvent inside the pore was treated as a collection of point charges rather than using explicit solvent molecules or dipoles, and we consider their time dependence to produce frequency fluctuations through the vibrational Stark effect.[203, 215] In the model, d was the distance between the transition dipole and the change in electric field. A $1/d^2$ dependence is characteristic for the electrostatic interaction between a dipole and a point charge. It should be noted that many functions of the form $1/d^n$ were tried but only when n=2 did the

model come close to recreating the proportionalities displayed in Figure 5.7 while also being physically reasonable. An illustration of d, R_{pore}, and R_D can be found in Figure 5.8. Together, Equation 5.2 and $1/d^2$ weigh the contribution of a point in the pore volume to spectral diffusion.

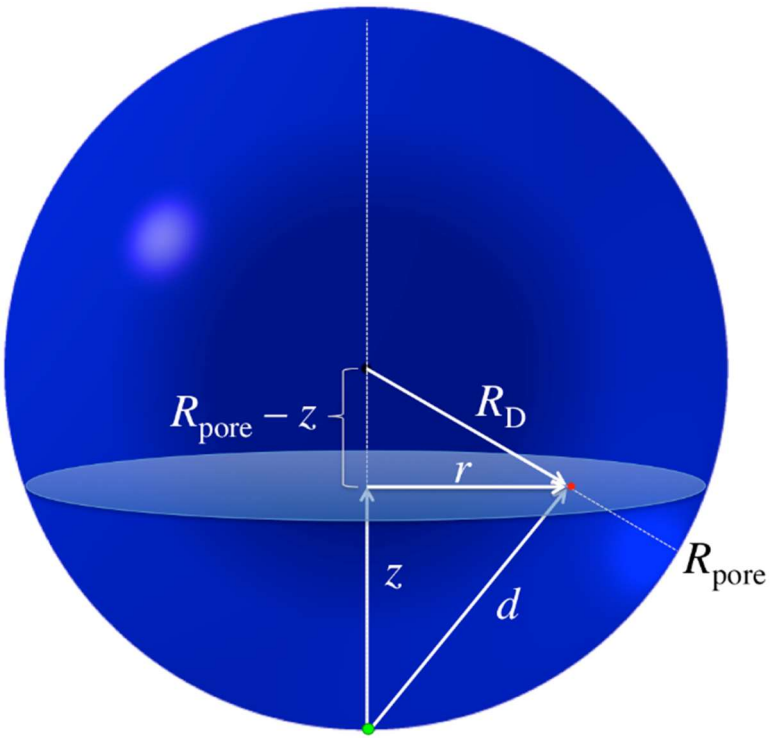

Figure 5.8. Diagram of the pore model and the relevant geometrical factors.

In order to calculate the contribution of the slow dynamics to the FFCF for each R_{pore} size, a sphere was numerically integrated as infinitesimally thin disks with maximum radii given by the equation of a circle that intersections the sphere horizontally at a given height, z, from the vibrational mode (green dot at the bottom of the pore in Figure 5.8). Figure 5.8 shows a single cross section through the pore volume with the corresponding geometrical distances for the model. The contribution of a given point (red dot) to spectral diffusion of the mode located at the bottom of the sphere (green dot) depends on the $1/d^2$ distance dependence of the interaction potential, and the radial dependence of the dynamic gradient given by the logistic function above. For the distance dependence, d at a given point is geometrically related to z and r as: $d = \sqrt{r^2 + z^2}$. For the radial dependence at that same point, R_D is related by: $R_D =$

$\sqrt{r^2 - \left(R_{pore} - z\right)^2}$. Equation 5.3 shows the integral used to calculate the proportional amplitude of the slow dynamics in the FFCF for each R_{pore}.

$$X_{slow} = \frac{\int_{0.1\text{Å}}^{2R_{pore}} \int_0^{r_{max}} 2\pi r \cdot \left(\frac{1}{d^2}\right) \cdot \left(\frac{A_1}{1 + A_2 e^{k(R_D - R_{pore})}} + y\right) dr dz}{\int_{0.1\text{Å}}^{2R_{pore}} \int_0^{r_{max}} 2\pi r \cdot \left(\frac{1}{d^2}\right) dr dz} \tag{5.3}$$

The lower integration limit on z is set to 0.1 Å to prevent the function from diverging due to the $1/d^2$ dependence. The radius of each disk is limited by the dimensions of the sphere with the maximum radius given by $r_{max} = \sqrt{R_{pore}^2 - \left(R_{pore} - z\right)^2}$. After substituting the geometric relationships in the paragraph above, Equation 5.3 was simplified to only three distance variables, R_{pore}, z, and r:

$$X_{slow} = \frac{\int_{0.1\text{Å}}^{2R_{pore}} \int_0^{\sqrt{R_{pore}^2 - (R_{pore} - z)^2}} \left(\frac{2\pi r}{r^2 + z^2}\right) \left(\frac{A_1}{1 + A_2 exp\left[k\left(\sqrt{r^2 - (R_{pore} - z)^2} - R_{pore}\right)\right]} + y\right) dr dz}{\int_{0.1\text{Å}}^{2R_{pore}} \int_0^{\sqrt{R_{pore}^2 - (R_{pore} - z)^2}} \left(\frac{2\pi r}{r^2 + z^2}\right) dr dz} \tag{5.4}$$

The total contributions from both components were calculated and summed over the entire pore volume, and the adjustable parameters from Equation 5.2 were floated to match the fractions of fast and slow solvent dynamics in the experimentally determined FFCFs. The ratio of the slow dynamics was found by dividing Equation 5.4 by the integral without the logistic function, that is, with a flat radial distribution. For the direct spectral diffusion model, on set of A_1, A_2, k, and y parameters of the logistic function were floated in an iterative fitting routine with the limitations that the logistic function could never exceed one (the slow dynamics cannot contribute over 100% of the dynamics) and that the slow dynamics contribute ~49.5% of the total solvent dynamics in the center of an infinitely large pore. This limiting value was selected as it is the proportional amplitude of the slow

dynamics for TriMOS in isopropanol, which we are treating as the "very large pore" limit. The calculated ratio for each nanoparticle was then compared to the empirical ratios, defined by the amplitude of the slow dynamics in the FFCF (Δ_2^2 since the amplitude of a particular component is the Δ squared) to the total solvent FFCF amplitude ($\Delta_1^2 + \Delta_2^2$). Residuals were calculated by comparing the theoretical values to the empirical values given in Table 5.4. The parameters that resulted in the best fit were A_1 = -0.5035, A_2 = 5*10^5, k = 7.9, and y = 1. The logistic function and theoretical ratios are found in Figure 5.7 and Table 5.4 respectively.

Table 5.4. Measured and calculated fractions of fast and slow spectral diffusion contributions.

particles	measured X_{fast}	measured X_{slow}	calculated X_{fast}	calculated X_{slow}
MSNP-3	0.000	1.000	0.020	0.999
MSNP-6	0.008	0.992	0.054	0.960
MSNP-9	0.068	0.932	0.094	0.897
MSNP-12	0.155	0.845	0.134	0.846
TriMOS	0.507	0.494	---	---

Figure 5.7 displays the predicted dynamical fractions for each MSNP pore size using a common distribution function (Equation 5.2). The predicted proportions of fast and slow dynamics match very well with the measured fractions from the globally fitted FFCFs of the MSNPs indicating that dynamics in each pore can be described by a single radial function. This supports the direct mechanism of communicating solvent dynamics to the surface mode, but it does not rule out the indirect mechanism. Unfortunately, allowing the dynamic distribution functions to be unique for each pore size creates an underdetermined scenario. The data from Figure 5.7 could also be readily reproduced using four different radial functions but the fitted functions are not unique. Nonetheless, this illustrates the plausibility of the indirect effect bulk-like isopropanol molecules may have on the measured spectral diffusion.

Figure 5.9 plots of the radial dynamic distribution function used to model the empirical data for each MSNP as a function of orthogonal distance from the pore surface to the center of the pore ($R_{pore} - R_D$). The functions displayed repeat radially from any other point on the pore surface to the center of the pore. The solid orange line represents the fraction of slow dynamics measured in bulk isopropanol and the dotted black line shows the common distribution function used to model direct spectral diffusion. What is clear from using a global function is that the increased spectral diffusion in the MSNP-9 and MSNP-12 stems from the inclusion of larger bulk-like pool. As the pores become larger, the composition of the dynamics in the first 1.5 nm is unaltered, but the volume of the bulk-like core increases.

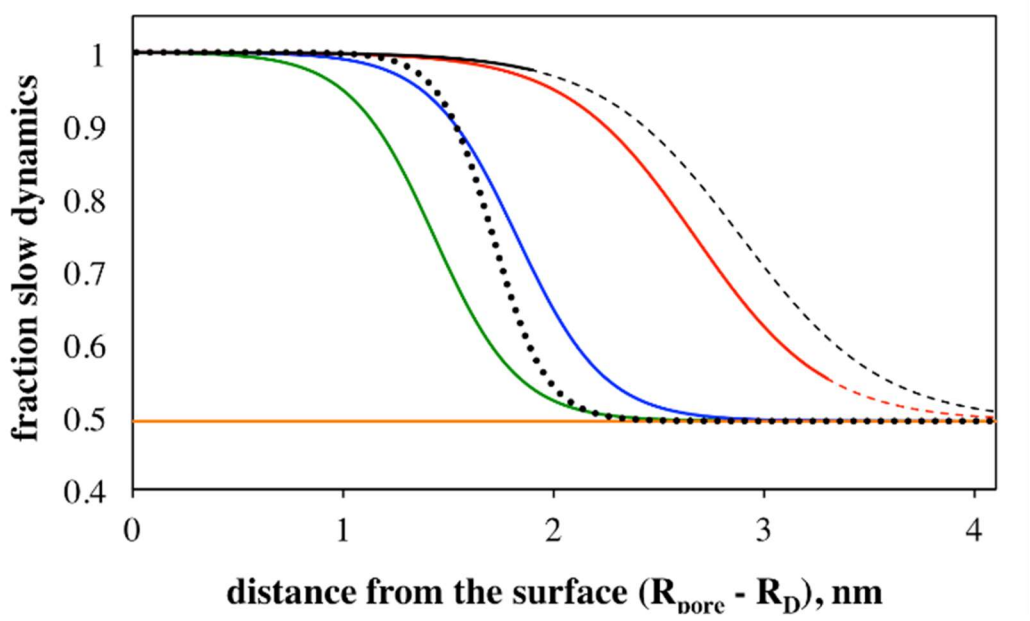

Figure 5.9. Fraction of slow dynamics predicted from the radial dynamics distribution function using a global fit to all pore sizes (black dotted) or independent distributions for MSNP-3 (black solid), MSNP-6 (red solid), MSNP-9 (blue solid), and MSNP-12 (green solid). The orange solid line indicates the fraction of slow dynamics in TriMOS in isopropanol. Dashed lines extrapolate the distributions beyond the pore radius for MSNP-3 and MSNP-6.

The shape of the dynamic distribution function for direct spectral diffusion seen in Figure 5.9 indicates a very quick change in solvent structure at around 1.4 nm from the pore surface, corresponding to edge of the fourth solvent shell. This sudden change corroborates multiple confined volume MD simulations,[67] including remarkable agreement with simulations of isopropanol at an alumina surface in which it was predicted that slower dynamics dominate out to 1.5 nm from the surface.[67] The colored lines overlaid in Figure 5.9 represent one possible series of radial functions used to model the case of indirect spectral diffusion. The solid lines stop when the function reaches the center of the respective pore, but continue with dashed lines continue to highlight the differences between their shapes. The parameters for these particular functions can be found in Table 5.5. In this model, increased spectral diffusion arises from changes in solvent dynamics approximately 1 nm away from the surface induced by the presence of the additional volume, as well as the increased bulk-like core. It is interesting that even though the shape of this function changed with pore diameter, the structure of the first 1-2 molecular layers did not.

Table 5.5. Fit Parameters from Equation 5.2 for the indirect spectral diffusion model.

particles	A_1	A_2	k	y
MSNP-3	-0.5035	1000	5.00	1.00
MSNP-6	-0.5035	5000	4.80	1.00
MSNP-9	-0.5035	5000	3.25	1.00
MSNP-12	-0.5035	5000	3.00	1.00

5.4: Conclusions

Mesoporous silica nanoparticles with tailored pore volumes were used to study the distance sensitivity of 2D-IR spectroscopy. In a departure from typical confined volume measurements, the vibrational mode was localized on the silica pore surface rather than being on the solvent molecules themselves. The dynamics near the surface-bound probe dominated spectral diffusion for pore diameters up to 10.5 nm and were notably slower than the solvent dynamics for a silane precursor in solution. The solvent structure near pore surfaces inhibited fast dynamics whereas the bulk solution had equal proportions of fast and slow spectral diffusion. A surprising observation in this work was that the FFCFs for the surface modes were sensitive to solvent dynamics several nanometers from the surface bound probe. Leveraging the systematic variation of pore diameters in MSNPs, we developed a model that found that the vibrational probes could have direct sensitivity to distant dynamic motions communicated through-space, but we could not rule out the indirect effect of solvent-solvent interactions. Regardless of whether the dynamic distribution changes with pore volume, a $1/d^2$ distance dependence was needed to reproduce the FFCF trends. The presence or absence of solvent restructuring will be further examined by repeating the current study using a weakly self-interacting solvent.

5.5 Full Set of 2D-IR Spectra

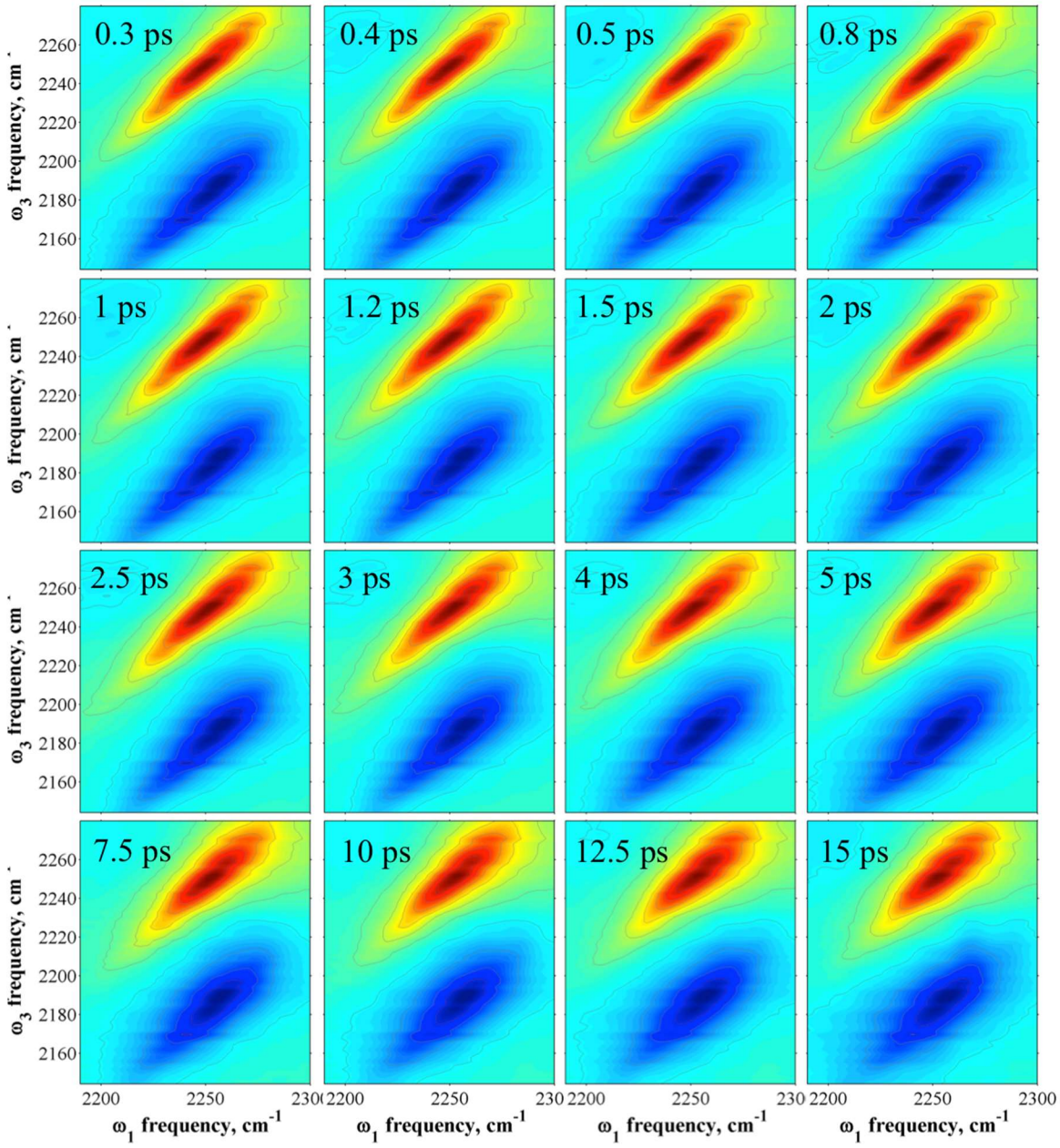

Figure 5.10. 2D-IR spectra at all T_ws collected for MSNP-3 infiltrated with isopropanol.

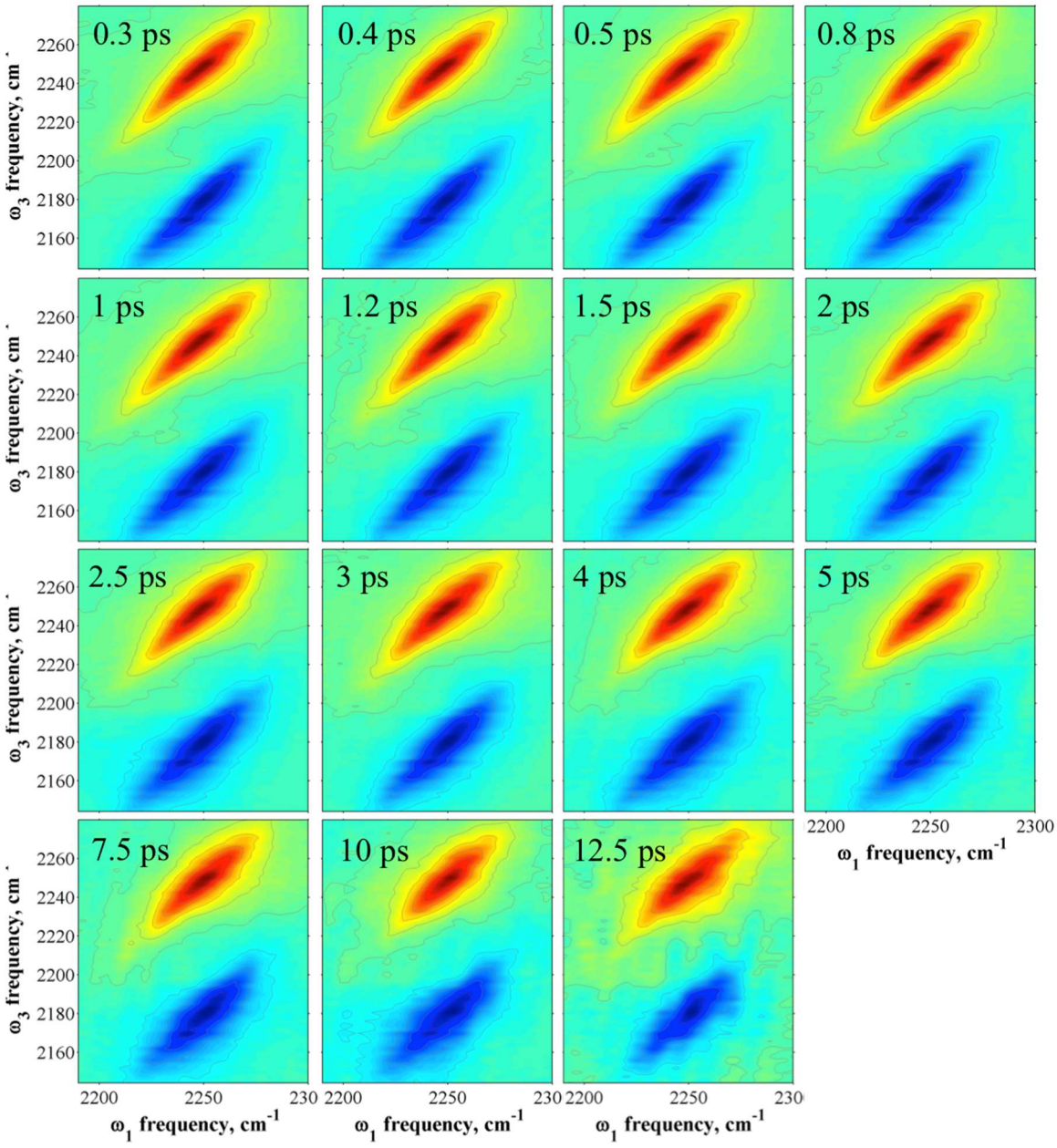

Figure 5.11. 2D-IR spectra at all T_ws collected for MSNP-6 infiltrated with isopropanol.

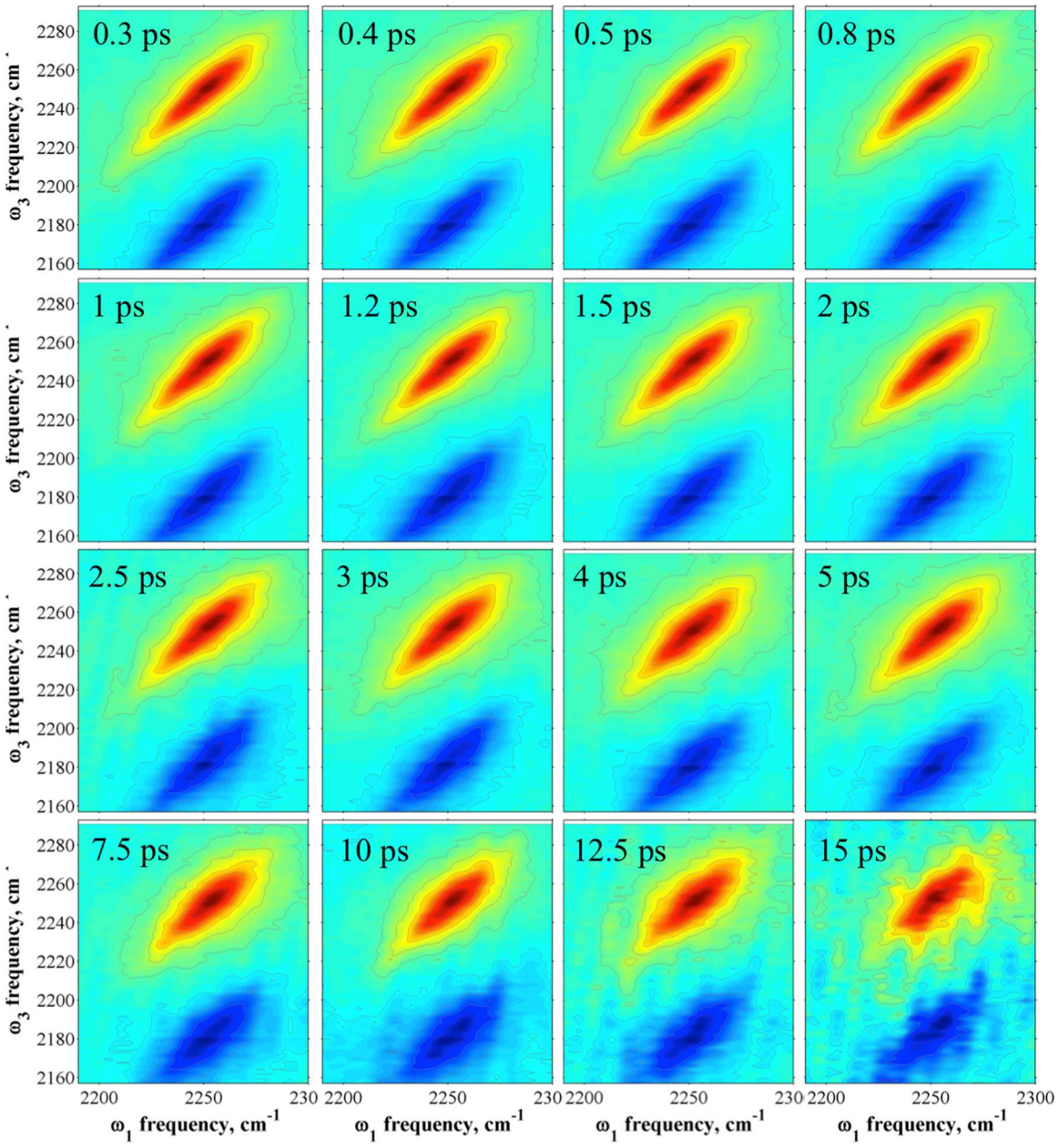

Figure 5.12. 2D-IR spectra at all T_ws collected for MSNP-9 infiltrated with isopropanol.

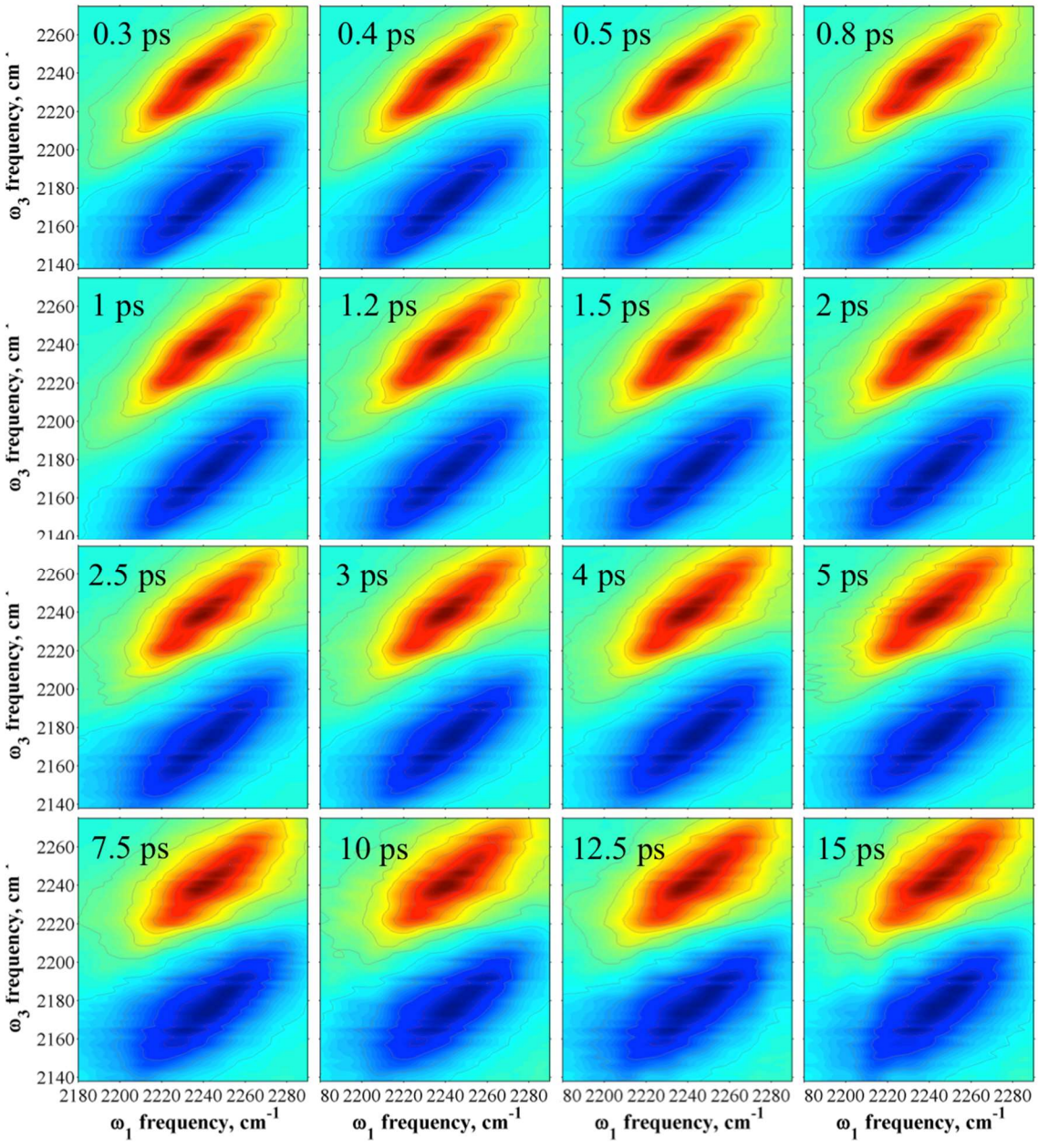

Figure 5.13. 2D-IR spectra at all T_ws collected for MSNP-12 infiltrated with isopropanol.

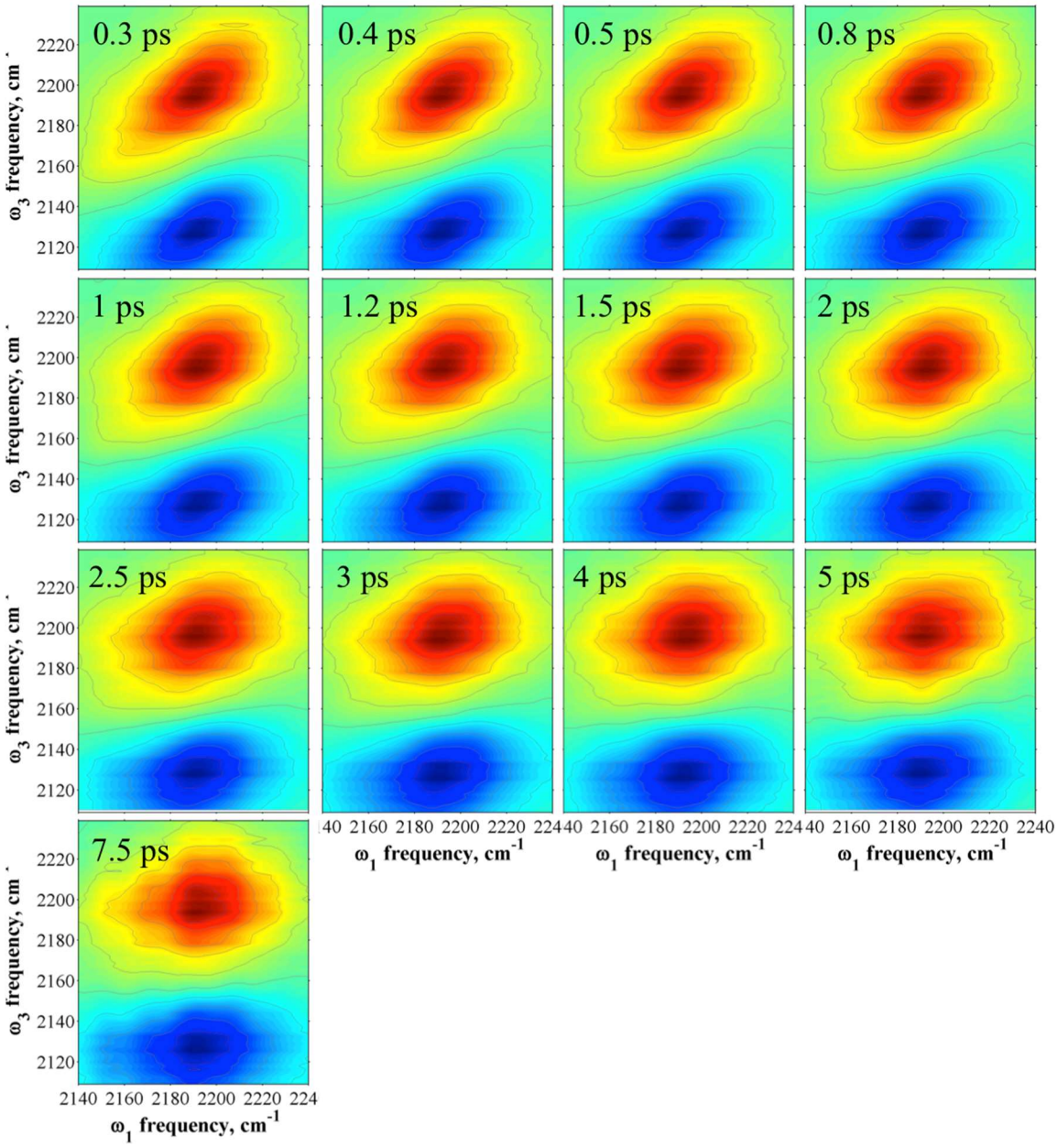

Figure 5.14. 2D-IR spectra at all T_ws collected for TriMOS dissolved in isopropanol.

Chapter 6: New Frontiers in 2D-IR Spectroscopy Non-equilibria Dynamics of Gel Aging

ABSTRACT: Two-dimensional infrared spectroscopy (2D-IR) was used to investigate the structural dynamics of an evolving silica material over the course of a silica sol-gel reaction. In a novel approach, 2D-IR scans were taken systematically providing quantifiable dynamic information for any point in the reaction. The measurements were primarily sensitive to the dynamics during gel aging, demonstrating a slowing of structural motions as the silica matrix continues to condense. Supplementary measurements were used to contextualize the immense number of 2D-IR scans. Si^{29} NMR and FTIR were used to find both quantitative and qualitative information of the time-dependent chemical composition of the sample. Rheological measurements were used to measure the viscosity of the material over time as well as to quantify the gel transition. In the end, we sought out to form a correlation between the dynamics observed via 2D-IR spectroscopy and the viscosity of an evolving silica sol-gel, but ultimately found minimal correlation. Strong correlation was found between the measured dynamics and the degree of condensation suggesting that the scales of the measurements in a silica sol-gel dictate any possible correlations.

6.1: Introduction

Two dimensional infrared (2D-IR) spectroscopy provides insight into the structural dynamics of condensed phase systems.[7, 216-218] It has been used to correlate solution dynamics and catalytic reactivity,[34, 209, 218] measure the rate coefficients for chemical exchange reactions,[100, 219] and provide mechanistic information pertaining to protein folding.[2] However, it is important to recognize that the spectral diffusion and homogeneous dephasing measured by this technique are only sensitive to a subset of the total system dynamics to which the vibrational probe is strongly coupled. In essence, the total spectrum of solvent and solute dynamics is filtered through the lens of the IR chromophore that generates the 2D-IR signal. We often wish to relate the dynamical quantities to some macroscopic behavior of the system, but the inherent bias of these measurements means that the measured dynamics may or may not be relevant to that behavior.

An example that has been previously explored is the relationship between ultrafast dynamics and solvent viscosity.[31, 220] Viscosity is often described as a measurement of a solution's internal friction, a catch-all term for a solution's resistance to flow due to intermolecular interactions.[31] As such, viscosity is an ensemble average of all of the interactions within a solution. In order for spectral diffusion and viscosity to correlate, spectral diffusion must capture specific dynamics that are constrained by the same intermolecular forces that largely impact the solution's ability to flow. This is easier said than done, but the most successful attempts have been able to control as many variables affecting intermolecular interactions as possible.

Kim and coworkers changed the viscosity of a protein solution by varying the concentration of a water:Guanidinium HCl binary solution but found little to no correlation between the protein dynamics and the solution viscosity.[221] In contrast, a similar study Finkelstein and coworkers found that protein dynamics were highly correlated to the solvent viscosity.[220] One of the more definitive links between the two was reported by King and coworkers, who discovered a strong correlation between the spectral diffusion sensed by a $Mn_2(CO)_{10}$ complex and the viscosity of alcohols with differing alkyl chain lengths.[109] While the correlation was strong, the variation of the solvent viscosity was less than an order of magnitude. In this work we present a system with a wide viscosity range and a limited range of chemical properties to measure a correlation between the structural dynamics and the materials viscosity. The system chosen for this study is silica sol-gel materials.

Sol-gel syntheses gained popularity decades ago as cheap, easy, resource inexpensive process for synthesizing porous metal alkoxide materials.[81, 91, 222] These highly customizable, one-pot reactions produce metal oxide materials that are used in applications such as coatings and optics.[85, 91, 223] Pore sizes, dispersities, surface areas, and morphologies can be independently tuned by controlling the reaction conditions, such as pH,[81, 92-94] catalyst used,[169] water to precursor[95] ratio, size of the container, and precursor itself.[170-172, 224]

Figure 6.1 shows a typical silica sol-gel reaction scheme using tetramethoxysilane (TMOS) as the monomer precursor. Polymerization of the monomers occurs in two steps, first is the hydrolysis of an alkoxy group on the monomer resulting in a silanol group. The second step involves the condensation of two silanol groups, crosslinking the two Si centers

together. The specific growth mechanism of the silica network is rarely known due to the convoluted nature of the kinetics itself. Not only are the kinetics highly dependent on the starting conditions but they are continuously evolving throughout the reaction. For instance, it is widely known that the reactivities of alkoxy/silanol groups are dependent on whether adjacent alkoxy/silanol groups have reacted.[89-91, 222] Hydrolysis and subsequent condensation continue as an extensive silica network is formed. As the network extends across the solution, different polymer groups will aggregate and polycondensation will occur, culminating in the gelation of the material. After gelation the silica network continues to condense further through a process called gel aging.[91, 93]

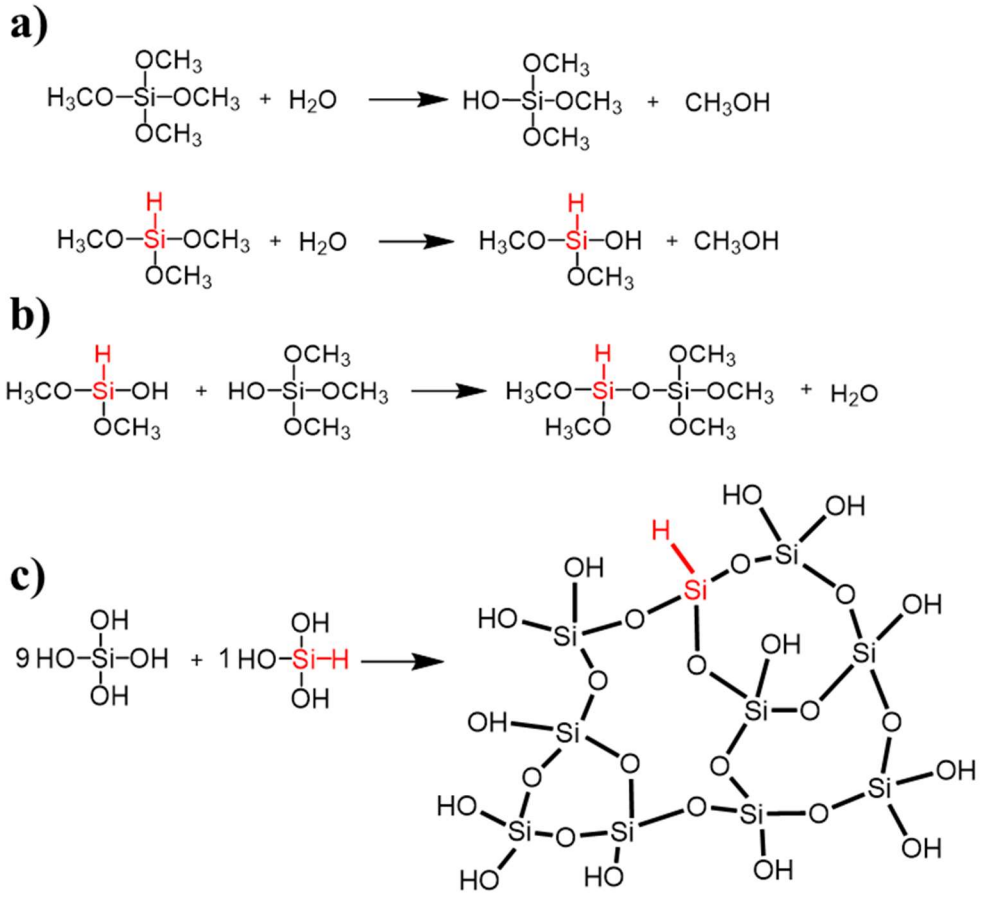

Figure 6.1 The reaction schemes for the a) hydrolysis of both TriMOS and TMOS precursors, b) the condensation of silinol groups, and c) the cross linking or polymerization of multiple monomers

In Chapter 4, a typical sol-gel synthesis was modified by our group to include a Si-H vibrational mode (ν_{Si-H}) covalently bound to the silica network, providing an intrinsic probe that exhibited sensitivity to the surrounding dynamics.[7] The vibrational frequency of the silane mode is known to be highly sensitive to the electronegativity of the other substituents bonded to the Si atom via the inductive effect. This inductive effect imparts sensitivity to the degree of condensation in silica sol-gel materials and even the solvation of adjacent siloxide bonds.[7] In this study, the previously adapted silica sol-gel synthesis was used in a non-equilibria 2D-IR study to monitor the molecular dynamics as a function of reaction time. While the shape of the ν_{Si-H} 2D-IR peak provided the dynamic information, the peak frequency gave information on the chemistry of the material. Additional chemical composition information was provided through a time lapse ^{29}Si NMR study and rheological measurements provided the viscosity of the sol during the reaction up to gel formation. The end result of this study is a direct comparison between viscosity and molecular/structural dynamics as a function of reaction time.

6.2: Experimental Methods

Materials

Trimethoxysilane (TriMOS, 95% purity) and chloroform were used as received from Sigma Aldrich. Tetramethyl orthosilicate (TMOS, 98% purity) was used as received from Fluka hydrochloric acid were used as received from Macron.

Synthesis

A 6:0.6:3.2:0.1 mixture of TriMOS:TMOS:HPLC grade H_2O:0.04 M HCl was prepared, briefly shaken, and subsequently sonicated for 15 minutes. The reaction time

was started once all the reactants were added, prior to the 15 minutes of sonication. An aliquot was sandwiched between two CaF_2 windows with a spacer of an appropriate thickness, typically 50 μm s. Most of the samples were characterized approximately 30-50 mins after the solutions were mixed. The exact times were noted and appropriately applied to the data listed below.

FTIR Spectroscopy

Fourier transform infrared (FTIR) spectra were collected on a Nicolet 6700 FTIR spectrometer (Thermo Scientific) with a resolution of 2 cm^{-1} under a constant flow of N_2 gas. Time lapse spectra were collected in two ways. Both methods used 50 to 250 μm path length cells constructed from two CaF_2 windows sandwiched around a Teflon spacer gasket. In the first approach, the sol-gel reaction mixture was prepared as described above and then allowed to react in the sample cell. Spectra were collected every 8.57 min over a period of 1250 minutes (242 sequential spectra). The second method prepared the sol-gel reaction mixture in a larger vial. Aliquots were drawn from the mixture while it reacted and were quickly assembled into a 50 μm path length sandwich cell. The number of scans was lowered to 16 (2 cm^{-1} resolution), the chamber was not purged with N_2, and spectra were acquired as frequently as possible New background spectra were collected prior to making each sample, to account for changes in the atmospheric composition.

NMR Spectroscopy

The Si^{29} NMR measurements were performed on a Bruker Avance 500 MHz NMR spectrometer. The probe was tuned to the Si^{29} signal at 99.4 MHz.

Rheology

The rheology measurements were performed on an AR-G2 Rheometer (TA instruments) using a Couette concentric cylinders geometry. Once the reaction mixture was added to the cell, a loose cap was placed over the well, carefully, to hinder evaporation. Time sweeps were conducted at 25.0 °C with a constant angular frequency of 1.00 rad/s. The percent strain was allowed float to apply a constant torque (7.690 μN·m). The experiments were stopped 5 minutes after the measured gel point to prevent the drying of silica on the aluminum surfaces of the bob and well.

2D-IR Spectroscopy

The laser system used for 2D-IR and pump-probe spectroscopy was described in the previous Chapters.[42, 190] Particular to this experiment, successive scans were collected at the same T_w (time delay between pulses 2 and 3) for approximately 24 hours or until the scatter produced by the aging and cracking sample made the spectra unusable. In order to expedite the 2D-IR spectra the number of shots per scan was lowered to 500, resulting in 24.7 minute scans. Scatter grew in during some runs as the samples gelled and aged. These scans were typically discarded due to the distortion of the peak shape. A fresh sample was then prepared and a new T_w was measured until the sample failed. The resulting data plots were then analyzed using the peak ellipticity[4, 110, 200, 201] metric in order to extract the frequency-frequency correlation function (FFCF) from the 2D-IR data directly.

IR Pump-Probe Spectroscopy

IR pump probe spectroscopy was performed using the same laser system as the 2D-IR measurements above, as described in previous chapters. The data were fit from 1 ps to 75 ps to determine the population relaxation times (lifetime, T_1) for the v=0-1 and 1-2

transitions. The vibrational relaxation times for these two transitions consistently showed similar trends and the 0-1 values were used in any data analyses.

6.3 Results and Discussion

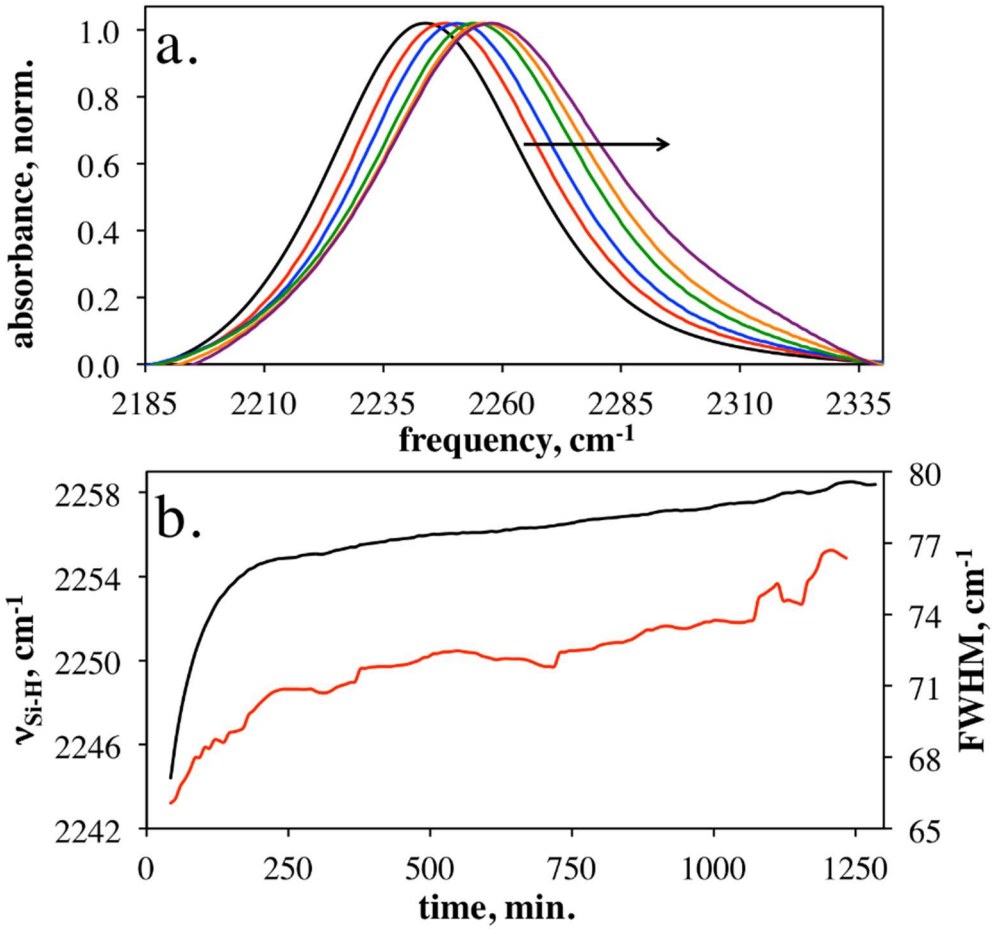

Figure 6.2 The results of the time lapse FTIR study of the sol-gel reaction including, a) a collection of normalized and baselined FTIR spectra of the Si-H peak over the course of the reaction, and b) a plot of both the Si-H peak center and FWHM as a function of reaction time.

Figure 6.2a shows selected FTIR spectra of the ν_{Si-H} collected over the course of the sol-gel reaction. As the reaction progresses the Si-H peak blue shifts significantly (~14 cm^{-1}) due to the progressive crosslinking of the silica matrix to which the mode is covalently bonded. It has been shown that the vibrational frequency of the Si-H mode is highly sensitive to the chemistry of the other silane substituents through the inductive effect and is therefore a metric of the degree of condensation in the sol-gel.[192] The center frequency in each FTIR spectrum is plotted as a function of reaction time in Figure 6.2b,

showing qualitatively the kinetics of the reaction. The sample reacts very quickly in the first hundred minutes and then slows down significantly, showing only a 4 cm^{-1} blue shift over the last 1000 minutes of the reaction. A plot of the FWHM is overlaid in Figure 6.2b showing that the width of the FTIR peak evolves similarly to the peak centers. This shows that the range of chemical environments and/or the structural dynamics are influenced by the same chemical processes that lead to a shift in the mean frequency of the silane vibration.

^{29}Si-NMR spectroscopy is a common technique to monitor the degree of condensation before, during, or after a sol-gel synthesis.[225-227] The silicon atom experiences different amounts of magnetic field shielding depending on the electron withdrawing nature of its substituents. Since carbon is more electronegative than silicon, a Si-O-C network will have a more deshielded Si atom than a Si-O-Si network. The result is less condensed Si centers are found upfield from their more condensed counterparts. Therefore ^{29}Si-NMR can be used as a metric for the degree of condensation of sol-gel materials. Figure 6.3a shows stacked ^{29}Si-NMR spectra for four different time points in the sol-gel reaction. There are groups of peak mulitplets found in each segment of the spectrum signifying different degrees of hydrolysis within a specific degree of condensation.[225] The completely uncondensed monomer (Q_0) extends from -72 ppm to -76 ppm, primary condensed Si centers (Q_1) extend from -81 ppm to -86 ppm, secondary condensed Si centers (Q_2) extend from -90 ppm to -94 ppm, and tertiary condensed centers (Q_3) extend from -100 ppm to -104 ppm. Quaternary condensed Si atoms did not show any resolvable peaks within the window of the experiment. Each peak within a region was integrated and

their areas were summed. The sum from each region was divided by the integration of all the peaks, providing a relative degree of condensation for each spectrum.

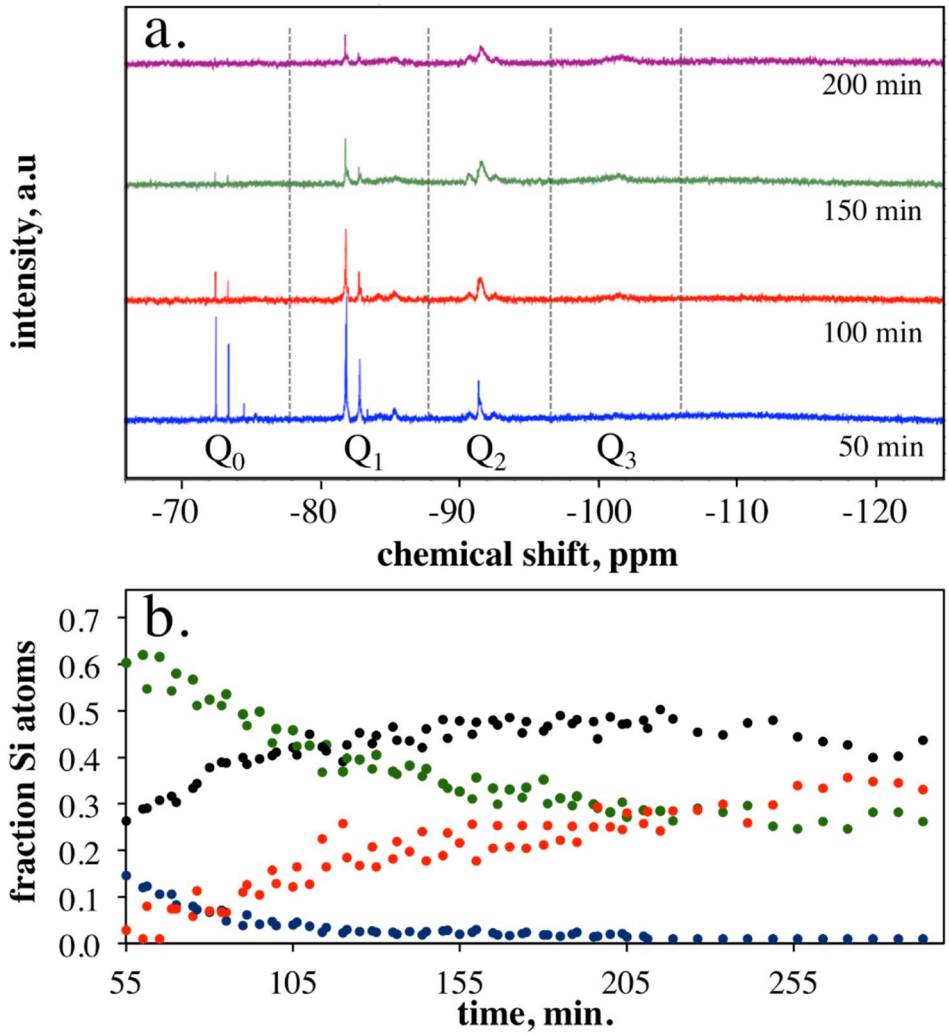

Figure 6.3 The results of the time lapse ^{29}Si NMR study including, a) example spectra at various points in the reaction and, b) the results of the integration of the peaks within each region indicated in Figure 6.3a.

Figure 6.3b is a plot of the fraction of silicon centers with each degree of condensation as a function of reaction time. This measurement enables us to quantify the proportions of differently condensed silicon atoms that could not be resolved in the FTIR time lapse above. The ^{29}Si-NMR analysis shows that nearly 15% of the silicon atoms at the beginning of the measurement belong to uncondensed monomers, while primary and

secondary condensed centers make up 60% and 25% of the Si atoms respectively. The uncondensed monomers decay quickly, which is immediately seen as a spike in the Q_1 population, but in turn quickly convert into Q_2 atoms. Both the Q_2 and the Q_3 populations steadily increase through the first 100 minutes of the reaction when the former eventually levels off illustrating conversion to more Q_3 atoms. Unfortunately as the sol forms a gel, the peaks become broader and unresolvable after ~300 minutes. In Chapter 4, solid-state Si^{29} NMR spectra were taken of older silica sol-gel samples with 15% TriMOS.[7] These samples, which were prepared with a similar synthesis but aged for 3-4 weeks in isopropanol, were found to have 90% of the Si atoms populating Q_2, Q_3, or Q_4 43% of the atoms populating Q_4. While the comparison is not exact, we conclude that the 10% TriMOS samples in this work will continue to condense significantly after the gel point. Previous work in Chapter 4 with covalently bound Si-H modes showed that the peak frequency is quite sensitive to interfacial solvation in addition to the degree of condensation which will change throughout the reaction, hindering any numerical interpretation of degree of condensation from the FTIR peak.[7]

During the NMR process, a disparity was observed between the time scales of gelation for the FTIR and NMR samples. The FTIR samples sandwiched between two CaF_2 windows with a 50 μm Teflon spacer observably gelled between 50-100 minutes, whereas the same solution took ~7 hours to gel in an NMR tube or a vial. The gelling process is dependent on the dimensions of the container. A container size dependency of the gel time has been observed and modeled for base catalyzed and neutral silica sol-gel materials.[228-230] Anglaret and coworkers found that base catalyzed sol-gel syntheses exhibited longer gel times as the size of the container increased whereas gel times in neutral

syntheses were nearly dimensionally independent.[230] Monte Carlo simulations corroborated their experimental findings and pointed to bond flexibility as the major influence in the aggregation mechanism. The container size dependence of acid catalyzed silica sol-gel syntheses has not been previously reported, but we found this to be the case for our synthesis.

To resolve this issue, we collected FTIR spectra of sol-gel samples that reacted in a range of container sizes for comparison to rheological measurements performed in the Couette cell. Figure 6.4a shows the center peak frequencies as a function of time for 50 μm and 125 μm thick samples. The same solution preparation was used for each of the samples seen in Figure 6.4a. There is a stark difference in the kinetics exhibited by the two curves in Figure 6.4a. It remains unclear from these two runs alone, whether the dimensional dependence extends past 125 μm. Unfortunately, the thickness of the FTIR samples was limited by Beer's law. In order to circumvent thickness limitations, the aliquot method, described in the experimental procedures was used to continuously probe the chemical makeup of the solution in a large dimension vial. In this method, fresh aliquots were sandwiched with a 50 μm spacer and FTIR spectra were taken quickly. The speed of the sample preparation and subsequent spectroscopy will be assumed to minimally perturb the results. The frequency curve from these aliquots (light blue) in Figure 6.4a is distinct from the curves of the other samples. The kinetics of this reaction shows a clear non-linear dimension dependence which suggests that the NMR data collected cannot be directly compared to the data in Figure 6.2. Instead, the more apt comparison would be to the frequency curve from the aliquot method.

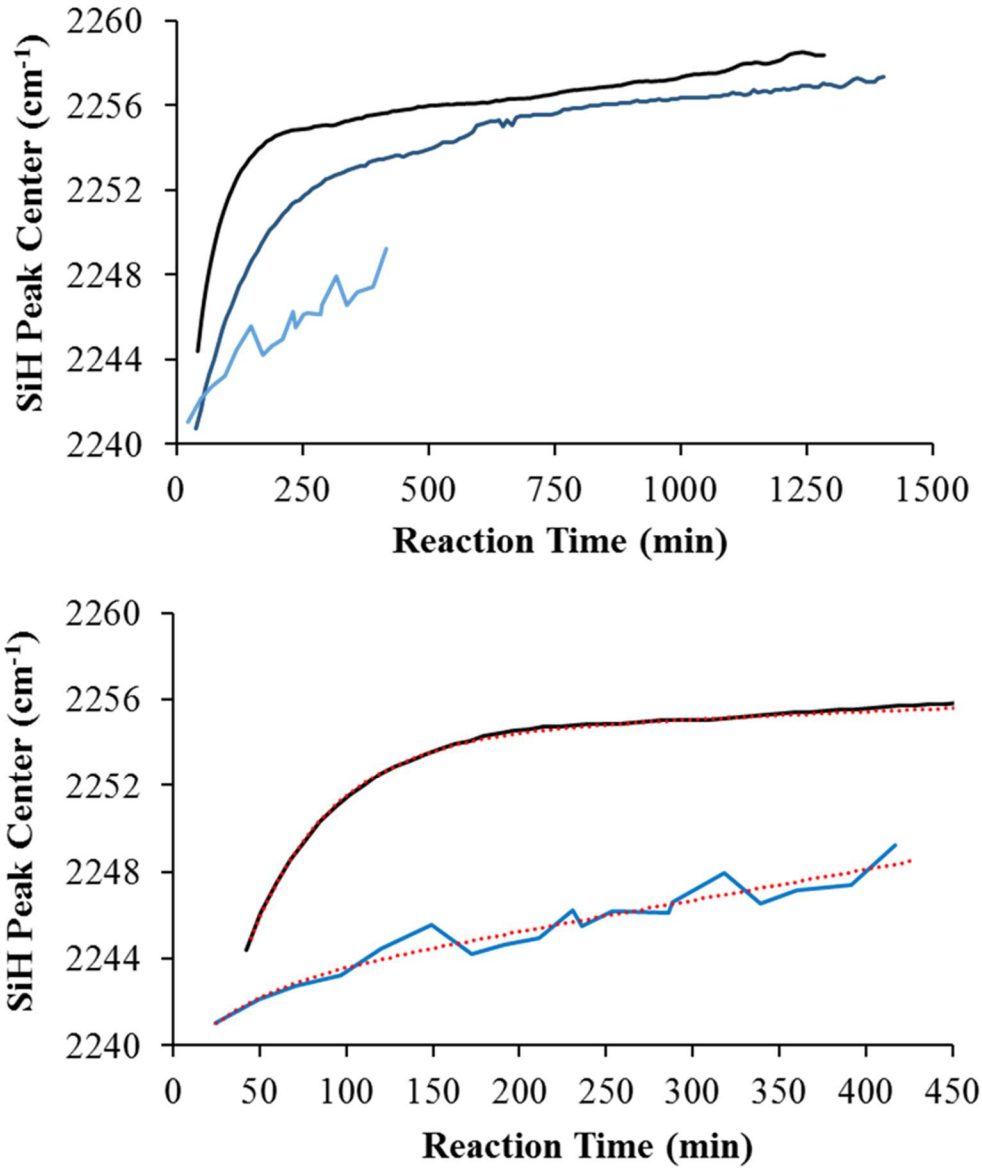

Figure 6.4 FTIR spectra were taken as function of reaction time for three different size containers, 50 μm (black), 125 μm (blue), and 3 dram vial (light blue). The top figure shows the Si-H peak centers over the course of the reactions. The bottom figure illustrates how the FTIR curves can be used to convert the time scales for each container.

The FTIR comparison in Figure 6.4b is the key for comparing the timescales of any properties of the sol-gel sample with macroscopic dimensions (NMR, Rheology) and dynamical properties and energetics elucidated from the ultrafast spectroscopy. Since both sample preps use the same starting solutions, identical FTIR spectra should have the same

chemical composition regardless of the kinetics. Specifically, the center frequency of the Si-H peak will be used as a metric of chemical composition or reaction progress. The time axis of the macroscopic reaction will be mapped onto the 50 μm reaction by comparing Si-H frequencies. Figure 6.4b illustrates this mapping process. Both the 50 μm and aliquot curves were fit to improve the translation process by providing interpolation of time points and averaging of the erratic aliquot curve. Using this method, the start of the 50 μm FTIR time lapse study, 42.3 minutes, translates to approximately 145 minutes into the NMR study, suggesting that these samples do not contain any uncondensed precursor by the time the 50 μm samples are made. Using this translation it is understood that the entire NMR time lapse experiment in Figure 6.3 takes place by the time the third 2D-IR scan is finished, while the fastest kinetics occur before the first FTIR scan is taken. This also shows that significant condensation must occur after the solution NMR window is closed, as the solid state NMR measurements in Chapter 4 suggest.

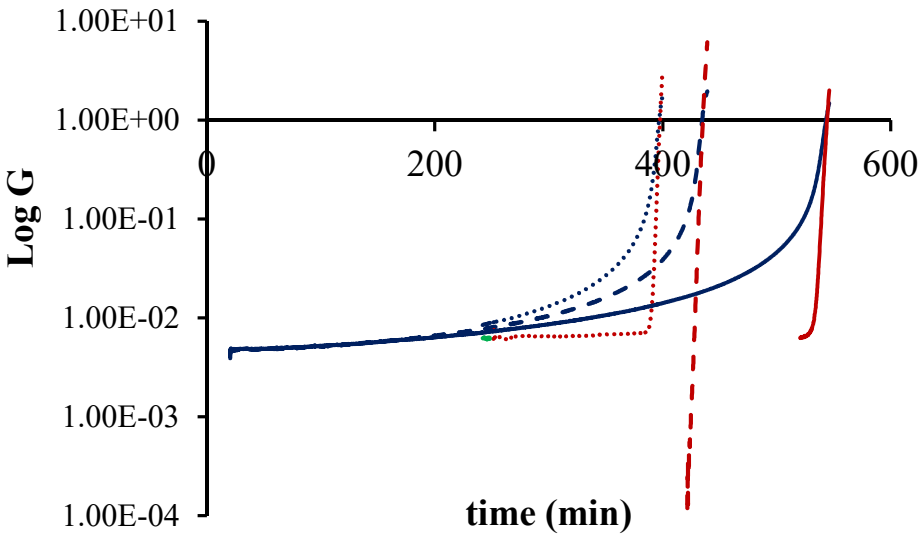

Figure 6.5 Displays rheological data collected over the course of the reaction. In each run, the blue curve represents the loss modulous (viscous behavior) and the red curve represents the storage modulous (elastic behavior).

Rheology is a technique used to measure the viscoelastic properties of a material. In this study rheology was used to monitor the viscosity as a function of time as well as finding the gel point of the sample. Figure 6.5 displays the plots of the raw rheological data. From these plots, the gel point is determined to be where the storage modulus, a measure of the elasticity of the material, becomes larger than the loss modulus, a measure of the viscosity of the material. The rheology scans were taken just past the point of gelation in all three trials, avoiding irreparable damage to both the well and bob due to dried silica. Running the rheology scans in triplicate, the gel point for this sol-gel material was 458 ± 62 minutes. The average point seems to match empirical observations of the gel point in a vial, an indication that the dimensions in these experiments is macroscopic for this reaction. The data from the three trials were interpolated and averaged. Figure 6.6 shows the time dependence of the viscosity during the reaction. By the start of the rheology experiment, the solution already has a viscosity of 40.67 cP, a viscosity similar to that of SAE-10 motor oil. The gap for the concentric cylinders was chosen to be 1.5 mm, a macroscopic scale similar to the width of an NMR tube.

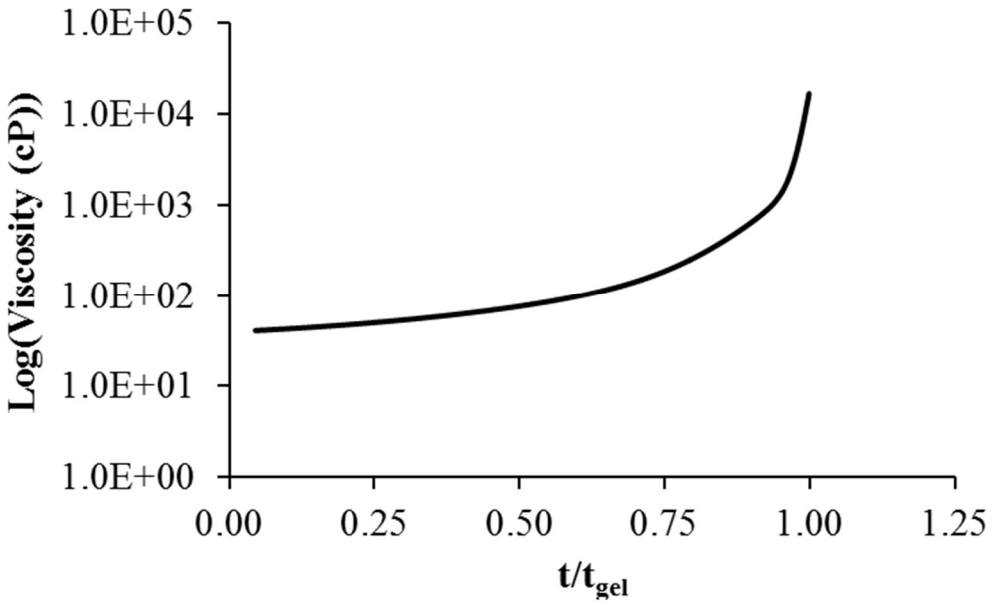

Figure 6.6 Displays the dynamic viscosity as a function of the gel time equivalence.

Translating the rheology gel time using Figure 6.4, the gel time for the 50 μm sample is $71\ +8.0/-6.5$ min. It should be noted that the microscale gap translated gel time matches well with previous physical observations for these samples.[7] From this point forward we consider any point of the reaction prior to 71 min as part of the gel formation and any point after, part of the gel aging process.

For clarity, a new dimension-independent timing convention will be introduced, called the gel time equivalence (t/t_{gel}). The gel time equivalence compares the reaction time to the gel time of that sample, allowing for direct comparison between measurements on both the macro- and microscales. While t/t_{gel} is rather exact for the macroscale samples, it is only approximate for the microscale samples suffering from the limitations described above.

2D-IR spectra were collected at a given T_w consecutively over the course of 24 hours. This procedure was deemed to be the most comprehensive way of looking at the dynamics as data points were collected every 24.7 minutes (t/t_{gel} = 0.35). This data

collection process was repeated for 9 different T_ws, with duplicate runs, resulting in approximately 700 2D-IR scans. Each scan was phased per the procedure in the experimental section. Figures 6.7a-i shows nine spectra taken at various Tws and points in the reaction. Figure 6.7a is a spectrum of the sol-gel after 100 minutes at a short T_w. The peak is highly correlated but has a significant antidiagonal width. The plots in Figure 6.7 are organized vertically by increasing T_w and horizontally by increasing reaction time. The T_w of the spectra increases moving from top to bottom (Figure 6.7a to 6.7g) down a vertical column as per a typical 2D-IR experiment indicating the dynamics at a particular point in the reaction. Analyzing the 0-1 peak shapes, spectral diffusion is evident as the peaks inhomogeneously broaden at longer T_ws, although it is clear that a completely inhomogeneously broadened peak is unlikely within restraints of the vibrational lifetime. The reaction time increases moving from left to right across a row in Figure 6.7 (i.e. from Figures 6.7a to 6c) illustrating the correlation at a specific T_w as the sample gels and ages. Once again analyzing the 0-1 peak, the dynamics appear to slow down as peaks become more correlated at later reaction times. Notice the effect condensation has on the 0-1 peak as it clearly blue shifts along the diagonal as a function of reaction time. Looking at the peak shapes as function of T_w (down a column) at the three different reaction times indicates how the dynamics are changing as the reaction progresses. From Figures 6.7, the dynamics appear to slow as the reaction proceeds. This decrease in spectral diffusion is consistent with a sample that transitions from a liquid to a solid.

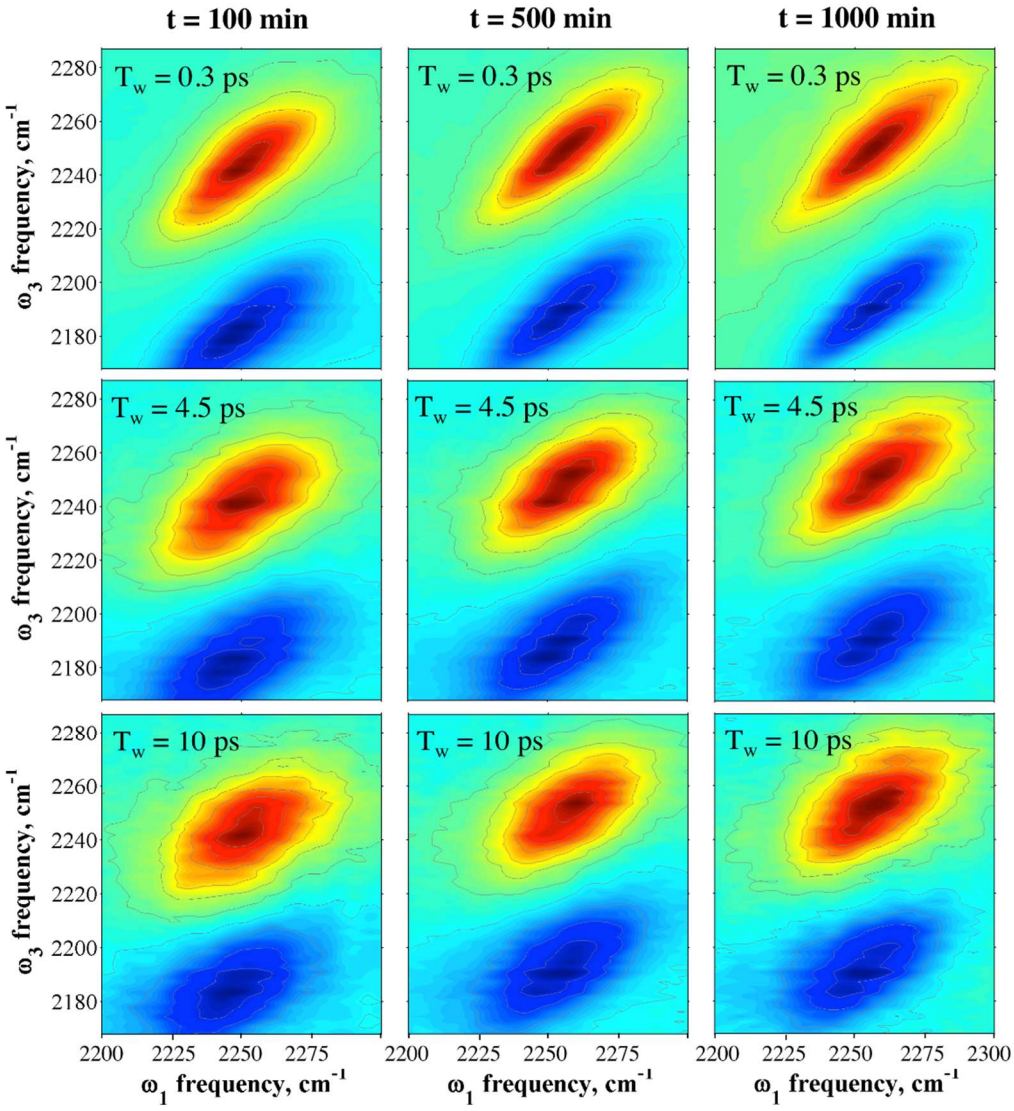

Figure 6.7 Displays nine 2D-IR spectra for different T_w at different points in the reaction. The T_w increases moving down a column and the reaction time increases moving across a row.

The 2D-IR peak shapes were analyzed via the ellipticity method, as detailed in Chapter 2. The ellipticity method is ideal for this system due to its relative simplicity and its direct relationship to the normalized frequency-frequency correlation function (FFCF). Figures 6.8 is a plot of the ellipticity as a function of reaction time for each T_w. This plot shows that as a sample reacts, the ellipticity of the 0-1 peak increases, demonstrating the observed trend from Figure 6.7. As the sample condenses the silica matrix has fewer

degrees of freedom to move and thus the dynamics become inhibited. Each T_w run from Figures 6.8a was fit with a curve with an equation of the form $y = -a_1 e^{-\frac{t}{b_1}} + c_1 t + d_1$ to interpolate the raw data. The fits to the duplicate runs were averaged, which are displayed in Figures 6.8b. The data and the fits for each T_w can be found at the end of the chapter.

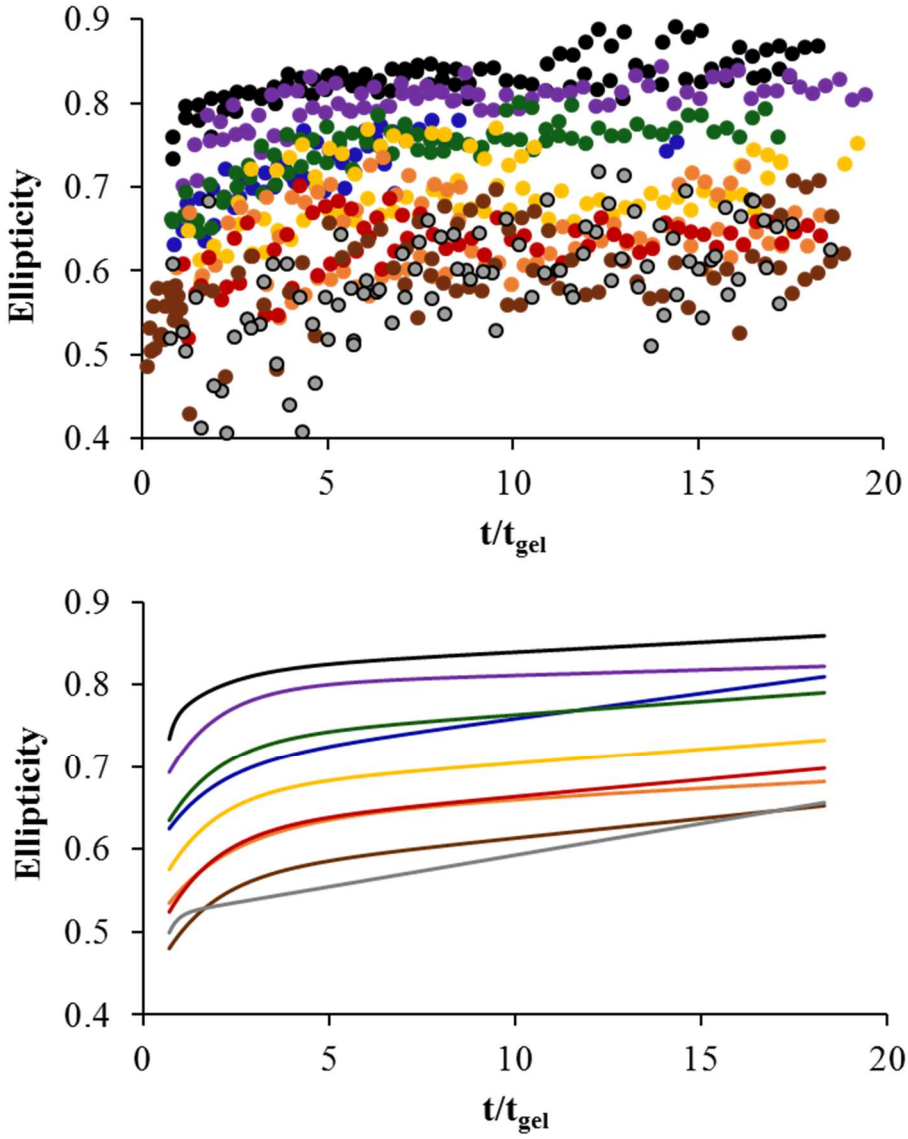

Figure 6.8 Displays the Ellipticity values for each 2D-IR scan taken during this study. Each color corresponds to a different T_w (0.3 ps-black, 1.0 ps-purple, 2.0 ps-blue, 3.0 ps-green, 4.5 ps-yellow, 6.0 ps-orange, 8.0 ps-red, 10.0 ps-brown, 15.0 ps-gray) The data points (left) were fit providing the curves (right).

Fitting the raw data to a functional form allows for the analysis of the normalized FFCF at any point in the reaction, even at later times, where scatter prevented data collection during some runs. Ellipticity decays at specific points in the reaction were found by taking vertical slices through the fits in Figures 6.8b. Figure 6.9 shows the decays as a function of reaction time. As stated earlier, the normalized FFCF is proportional to ellipticity decays as a function of T_w. FFCFs provide a link between the empirical 2D-IR peak shapes and physical processes occurring in the sample. Specifically the FFCF can be modeled as a series of exponential functions whose time constants represent time scales of the dynamics measured. The ellipticity decays in this study were fit with a single exponential decay with a static offset, illustrating two different dynamic motions, one fast component on the time scale of 6 ps and a very slow component with a time scale that is not resolvable in this experiment. A table with the parameters for the fit can be found at the end of the chapter.

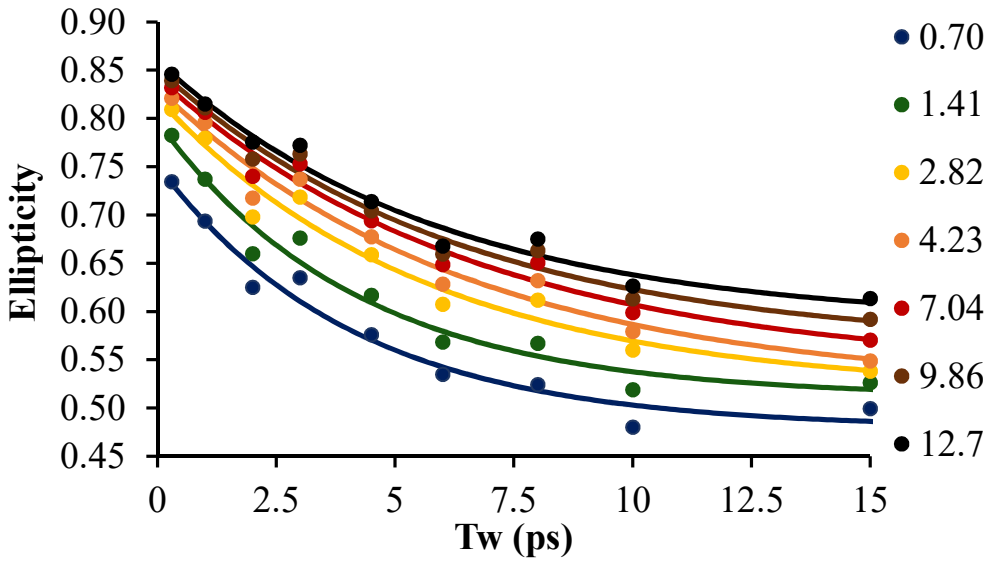

Figures 6.9 Displays Ellipticity decays for different points in the reaction. The points are slices through the fit data (Figure 6.8b) at different reaction times. The decays were then fit with a single exponential with an offset.

The normalized FFCF provides cursory information on the spectral diffusion evident in the 2D-IR scans but fails to provide meaningful information on the amplitudes of the dynamics as well as the homogeneous lineshape. Fortunately Kwak and coworkers have derived a method to calculate the full FFCF from the normalized FFCF and the corresponding FTIR. Using slices taken at meaningful points in the reaction and the closest FTIR taken to those points, full FFCF parameters were calculated. Figures 9a-c are plots of the calculated parameters from the full FFCF. Figure 9a is a plot of the Δ_i for both the fast and static components of the full FFCF. The error in the amplitudes is negligible compared to the magnitude of the amplitudes. Figure 9b is a plot of the time constant, τ_1 for the single exponential as a function of t/t_{gel}. Figures 6.10c is a plot of the homogeneous linewidth as a function of t/t_{gel}. Looking closely at Figures 6.10a, the amplitude of the fast component does not change significantly during the course of gel formation ($t/t_{gel} < 1$) but begins to increase after the gel is formed ($t/t_{gel} > 1$). The increase is however, not monotonic as the amplitude decreases over the course of gel aging. The static offset gradually increases over the course of the reaction in a linear fashion (R^2 ~ 96%). In Figures 6.10b, the single exponential time constant, τ_1, does not change substantially throughout gel formation but increases almost immediately after the gel forms. During gel aging, τ_1 continues to increase coinciding with an increase in the amplitude for the fast component, Δ_1. The amplitude shows very similar behavior to τ_1 as a function of reaction time as exhibited by Figures 6.10d, clearly demonstrating the importance of the gel point on the spectral diffusion measured in this study. The fact that both the amplitude and the time constant of the fast component increase during gel aging combined with the steady increase in the static offset, confirms that the dynamics of the

system are indeed becoming slower as the reaction proceeds. The homogeneous lineshape (Figures 6.10c) shows negligible time dependence and is seeming insensitive to the gel point. As described in Chapter 2, the homogeneous lineshape in systems such as a forming gel, is comprised of vibration lifetime, T_1, and a pure dephasing, T_2^*, component. Even though Γ is indifferent to the reaction, by studying the vibrational lifetime we can deduce a vague understanding of each components contribution to the stagnant parameter.

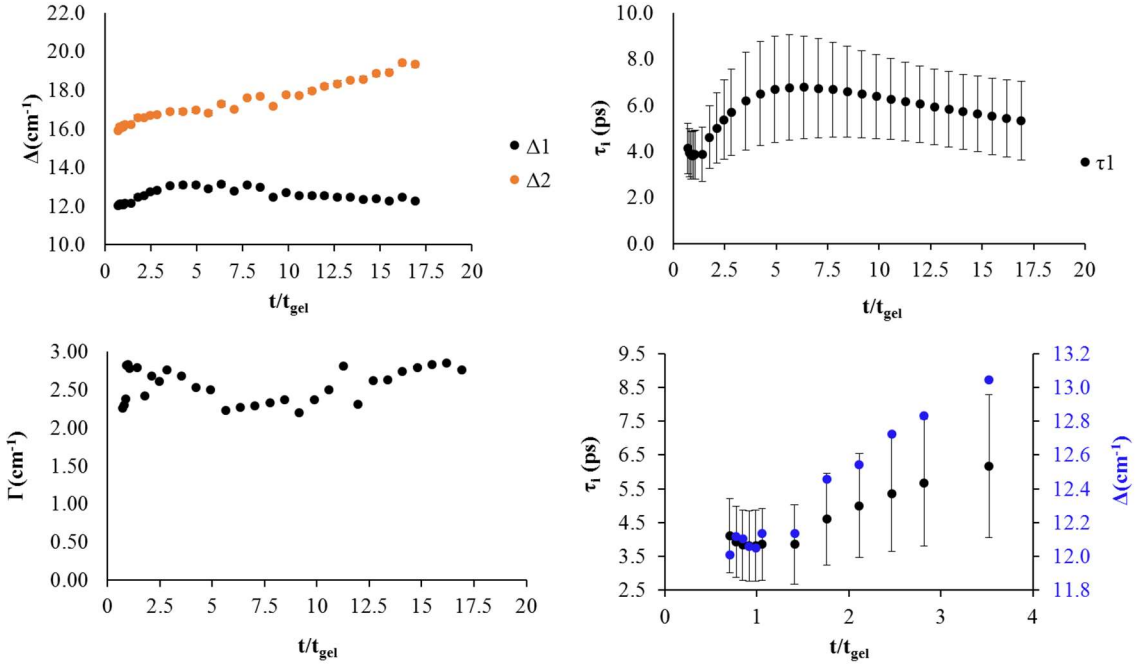

Figure 6.10 a-d Displays the parameters for the full FFCF at different points in the reaction. The decays from Figure 6.9 provide the a) amplitudes, b) time constant, c)homogeneous linewidth for the FFCF. Additionally the shape of the time constant and amplitude to the fast component is compared in d), demonstrating the difference in dynamics pre and post gelation.

A time lapse plot of the Si-H vibrational lifetime as a function of reaction time, measured by pump probe spectroscopy, is found in Figure 6.11. The time lapse plot shows that the 1-2 and 0-1 peaks decay with different lifetimes and exhibit different behavior as a function of reaction time. The lifetime of the 0-1 peak is consistently longer than the 1-2 peak and shows limited t/t_{gel} dependence whereas the lifetime of the 1-2 peak becomes longer as

the reaction proceeds. The difference in evolution of these two lifetimes could indicate a possible intramolecular vibration relaxation mechanism, however further investigation is needed. Since the homogeneous linewidth was found for the 0-1 2D-IR peak, it follows that only the 0-1 lifetime will contribute to the broadening. The reaction independence of the 0-1 lifetime coincides with the relative reaction independence of Γ, suggesting that the pure dephasing must also be reaction independent as well. Pure dephasing is typically highly dependent on the solvent and the probe within the system. The fact that the pure dephasing does not seemingly change over the course of the reaction suggests that the metric is not influenced by the inductive effect and that the proximal solvent shell does not change considerably throughout the course of the reaction.

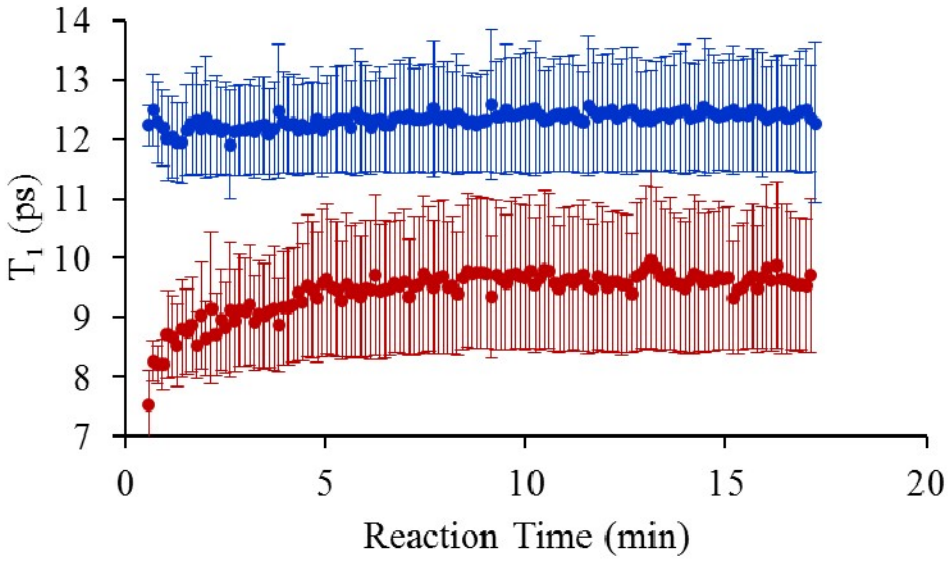

Figure 6.11 Displays the vibrational lifetimes of the 0-1 (blue) and 1-2 (red) peaks as a function of reaction time.

With the dynamic behavior observed, it is worth revisiting the broadening of the FTIR peak as the reaction proceeds. The width of a linear peak shape is dependent on both dynamic and static mechanisms. Since the peak broadens as the reaction proceeds it would

indicate that either the system is becoming more heterogeneous, or the system is becoming more dynamic, typically observed through faster or more prevalent spectral diffusion and/or broader homogeneous linewidths. The overall stagnant behavior of the homogeneous linewidths combined with the slowing of dynamics points to an increase in the heterogeneity of the silica matrix, as to be expected. Essentially the subensembles underneath the linear peak shape are becoming even more isolated and chemically diverse as the silica matrix continues to evolve.

The purpose of this study was to investigate any possible correlation between the localized dynamics and the macroscopic visco-elastic properties of the sample. Comparing the parameters for the dynamics in Figures 6.10 to the viscosity in Figure 6.6, there is a glaring disconnect between the dynamics and the rapid increase in viscosity pre and post gelation. Unfortunately, there are not enough 2D-IR data points during gel formation to reasonably interpret the dynamics during this time period. Predictively, the dynamics are becoming slower over the course of the gel aging process as both amplitudes and the time constant of the fast component increase after the gel is formed. However, the increase in all three is quite gradual after the gel point. The amplitude of the fast component, Δ_1, increases 8% after 180 minutes past the gel point and the static offset only increases 20% after 1100 minutes, both of which pale in comparison to the 15% increase in viscosity in the *first minute* after the gel is formed. Even the time constant of the fast component, which increases 20% after 55 minutes, shows minimal correlation to the viscosity of the sample. While the rheology data collected after the gel point is very limited, the general disconnect between the dynamics and the viscosity is evident. Up to this point, we have only discussed the silica polymer matrix within these sol-gel materials, ignoring the reaction byproducts.

Pockets of methanol and water molecules are known to form during silica sol-gel syntheses and are responsible for the genesis of the pores within these materials.[81, 91] In this context, the lack of correlation between 2D-IR and rheological observables is understandable as the viscosity is an ensemble measurement of both the polymer chains and the bathing solution. We believe in this system, that the viscosity is most likely measuring the friction between the polymer chains, while the 2D-IR measurements would be sensitive primarily to the intra-chain motions as well as the localized solvent motions.

The intra-chain motions, if observable in this experiment, would most certainly be slow and should be closely linked to the degree of condensation. As such, a more apt comparison would be between the parameters from the FFCF in Figures 6.10 and the qualitative degree of condensation found in the FTIR time lapse in Figure 6.2b. While there is little to no correlation between the dynamics and the Si-H frequency during gel formation, there seems to be significant correlation after the sample begins to age. Immediately after gel formation both ν_{SiH} and the parameters of the fast component experience significant change, as Δ_1, τ_1, and ν_{SiH} experience 36%, 40%, and 30% of their total change within the first 80 minutes of the gel aging, respectively. As the sample continues to age the static offset, Δ_2 begins to correlate to ν_{SiH} as both parameters continue to gradually increase.

The correlation between the FTIR and 2D-IR observables and lack thereof between the rheology and 2D-IR observables paints a picture of the physical mechanisms of gelation and gel aging and ultimately, the prohibitive factor in this study. Acid initiated silica sol-gel syntheses are known proceed in a primarily linear growth mechanism as hydrolysis is favored in acidic conditions.[81, 89, 91, 230] The time lapse NMR data in Figure 6.3 indicate

that secondary condensed Si atoms are prevalent during the gel formation process corroborating the linear growth mechanism. The increasing fraction of tertiary condensed atoms, along with interchain interactions, seemingly bring about the gelation of the material. From FTIR we know that the sample continues to condense throughout the gel aging process, seemingly producing a high fraction of tertiary and quartenary Si centers. This higher degree of crosslinking must elicit a slowing of the dynamics. The viscosity, as a macroscopic measurement, is seemingly dictated by interchain friction originating from low degrees of crosslinking and interchain interactions, whereas the localized dynamics are dictated by intrachain flexibility, which depends on high degrees of crosslinking.

6.4 Conclusions

In this study, an evolving silica sol-gel material was used as a model system to search for any possible correlations between structural dynamics and viscosity. In a novel approach, 2D-IR scans were taken systematically over the course of the reaction providing quantifiable dynamic information for any point in the reaction. A variety of supplementary measurements were used to contextualize the immense number of 2D-IR scans. Si^{29} NMR and FTIR were used to find both quantitative and qualitative information of the time-dependent chemical composition of the sample and rheology was used to measure the viscosity of the material over time as well as to quantify the gel transition. In the end, we sought out to form a correlation between the dynamics observed via 2D-IR spectroscopy and the viscosity of an evolving silica sol-gel, but ultimately found little to no correlation. We believe that while a system with a covalently bound Si-H probe is optimal for the proposed study, the scales of the measurements in a silica sol-gel prohibits such correlations. The low degree of crosslinking early in the reaction, characteristic of an acid

initiated linear growth mechanism, is enough for gelation to occur but does not significantly affect the localized dynamics. Once higher degrees of crosslinking begin to stiffen the silica polymer chains, the localized dynamics begin to slow. Ultimately the viscosity and dynamics are sensitive to slightly different metrics of gel synthesis.

Our ability to connect the dynamics measured to a physical mechanism for the gelation process is limited, however, we suggest that the linear growth mechanism plays a role in both the lack of significant correlation between macroscopic viscosity and localized dynamics and the container size dependence in these samples. The dimensional dependence of the gel formation begs for continual study. It seems likely that the dimensions of the container dictate the growth mechanism of the material. Acid catalyzed sol-gel reactions tend to evolve through a linear growth mechanism with the eventual activation of a branched growth mechanism. As the container becomes smaller the extent of a linear growth mechanism becomes hindered and the prevalence of a branched mechanism increases, leading to a more rapid increase in degree of condensation and thus an earlier gel time. A second time lapse study with a thicker sample while unwieldy, is compelling, and may lead to a great deal of fundamental understanding of the growth mechanisms in these materials.

6.5 Additional Figures

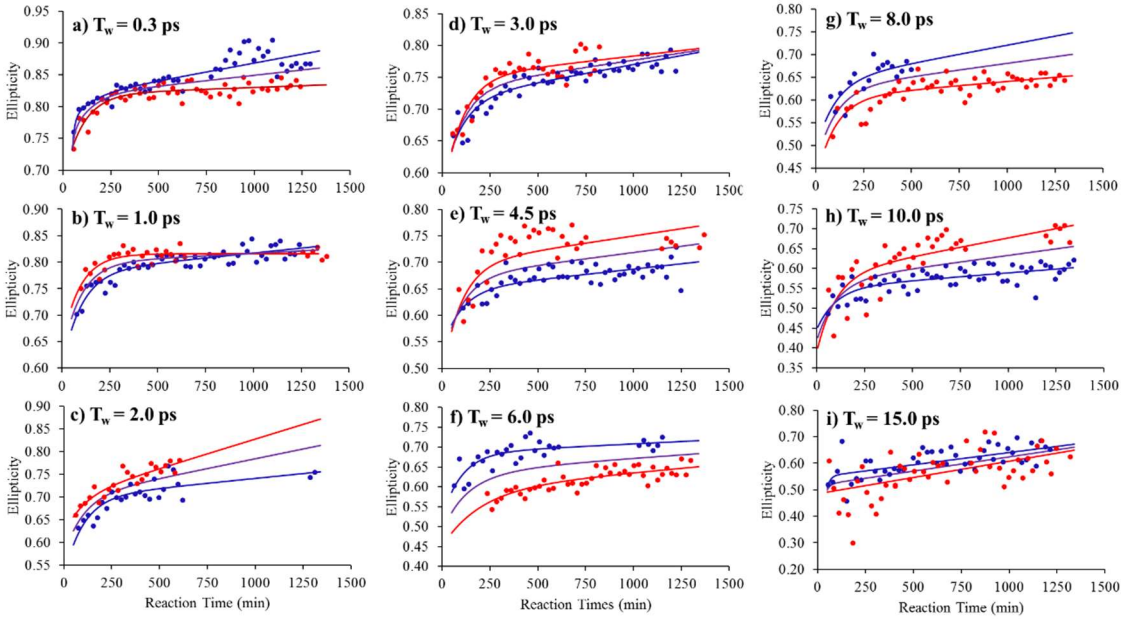

Figure 6.12 Displays the fits for the Ellipticity curves at each T_w

Bibliography

1. P. Hamm, M. H. Lim and R. M. Hochstrasser, *J. Phys. Chem. B*, 1998, **102**, 6123-6138.
2. S. H. Shim, D. B. Strasfeld, Y. L. Ling and M. T. Zanni, *Proc. Nat. Acad. Soc. USA*, 2007, **104**, 14197-14202.
3. C. R. Baiz, D. Schach and A. Tokmakoff, *Opt. Express*, 2014, **22**, 18724-18735.
4. S. T. Roberts, J. J. Loparo and A. Tokmakoff, *J. Chem. Phys.*, 2006, **125**, 084502.
5. K. Kwak, S. Park, I. J. Finkelstein and M. D. Fayer, *J. Chem. Phys.*, 2007, **127**, 124503.
6. H. S. Tan, I. R. Piletic and M. D. Fayer, *J. Chem. Phys.*, 2005, **122**, 057405.
7. C. J. Huber and A. M. Massari, *The Journal of Physical Chemistry C*, 2014, **118**, 25567-25578.
8. G. A. Krestov, *Thermodynamics of Solvation: Solution and Dissolution, Ions and Solvents, Structure and Energetics*, Ellis Horwood, 1991.
9. B. H. Jones, C. J. Huber and A. M. Massari, *J. Phys. Chem. A*, 2013, **117**, 6150-6157.
10. J. T. King, J. M. Anna and K. J. Kubarych, *Phys. Chem. Chem. Phys.*, 2011, **13**, 5579-5583.
11. P. Hamm, M. Lim and R. M. Hochstrasser, *J. Chem. Phys.*, 1997, **107**, 10523-10531.
12. C. P. Casey, S. E. Beetner and J. B. Johnson, *J. Am. Chem. Soc.*, 2008, **130**, 2285-2295.
13. M. H. M. Olsson and A. Warshel, *J. Am. Chem. Soc.*, 2004, **126**, 15167-15179.
14. E. D. Hermes, G. R. Jenness and J. R. Schmidt, *Mol. Simul.*, 2015, **41**, 123-133.
15. C. Reichardt, *Solvents and Solvent Effects in Organic Chemistry,*, VCH, Weinheim, 2nd edn., 1988.
16. D. G. Truhlar, W. L. Hase and J. T. Hynes, *J. Phys. Chem.*, 1983, **87**, 2664-2682.
17. B. M. Ladanyi and J. T. Hynes, *J. Am. Chem. Soc.*, 1986, **108**, 585-593.
18. D. E. Leahy, J. J. Morris, P. J. Taylor and A. R. Wait, *J. Chem. Soc.-Perkin Trans. 2*, 1992, DOI: 10.1039/p29920000705, 705-722.
19. J. Li, Y. Zhang and P. W. Carr, *Anal. Chem.*, 1992, **64**, 210-218.
20. P. C. Sadek, P. W. Carr, R. M. Doherty, M. J. Kamlet, R. W. Taft and M. H. Abraham, *Anal. Chem.*, 1985, **57**, 2971-2978.
21. L. R. Snyder, P. W. Carr and S. C. Rutan, *J. Chromatogr. A*, 1993, **656**, 537-547.
22. R. W. Taft, N. J. Pienta, M. J. Kamlet and E. M. Arnett, *J. Org. Chem.*, 1981, **46**, 661-667.
23. M. J. Kamlet, J. L. M. Abboud, M. H. Abraham and R. W. Taft, *J. Org. Chem.*, 1983, **48**, 2877-2887.
24. Y. Marcus, *Chem. Soc. Rev.*, 1993, **22**, 409-416.
25. L. R. Snyder, *J. Chromatogr. Sci.*, 1978, **16**, 223-234.
26. H. Schneider, Y. Badrieh, Y. Migron and Y. Marcus, *Zeitschrift Fur Physikalische Chemie-International Journal of Research in Physical Chemistry & Chemical Physics*, 1992, **177**, 143-156.
27. G. A. Neyhart, C. J. Timpson, W. D. Bates and T. J. Meyer, *J. Am. Chem. Soc.*, 1996, **118**, 3730-3737.
28. J. Marti, A. Lledos, J. Bertran and M. Duran, *J. Comput. Chem.*, 1992, **13**, 821-829.
29. D. M. Bishop, *J. Chem. Phys.*, 1993, **98**, 3179-3184.
30. S. N. Timasheff, *Annu. Rev. Biophys. Biomol. Struct.*, 1993, **22**, 67-97.
31. A. Ansari, C. M. Jones, E. R. Henry, J. Hofrichter and W. A. Eaton, *Science*, 1992, **256**, 1796-1798.
32. K. D. Rector, J. W. Jiang, M. A. Berg and M. D. Fayer, *J. Phys. Chem. B*, 2001, **105**, 1081-1092.
33. A. M. Massari, I. J. Finkelstein, B. L. McClain, A. Goj, X. Wen, K. L. Bren, R. F. Loring and M. D. Fayer, *J. Am. Chem. Soc.*, 2005, **127**, 14279-14289.
34. L. M. Kiefer and K. J. Kubarych, *J. Phys. Chem. A*, 2015, **119**, 959-965.
35. J. T. Hynes, *Annu. Rev. Phys. Chem.*, 1985, **36**, 573-597.

36. G. R. Medders and F. Paesani, *Journal of Physical Chemistry Letters*, 2014, **5**, 2897-2902.
37. P. A. Pieniazek, Y. S. Lin, J. Chowdhary, B. M. Ladanyi and J. L. Skinner, *J. Phys. Chem. B*, 2009, **113**, 15017-15028.
38. W. G. Rothschild, *Mol. Phys.*, 2007, **105**, 1003-1011.
39. J. Marti, J. A. Padro and E. Guardia, *J. Chem. Phys.*, 1996, **105**, 639-649.
40. J. B. Asbury, T. Steinel, C. Stromberg, S. A. Corcelli, C. P. Lawrence, J. L. Skinner and M. D. Fayer, *J. Phys. Chem. A*, 2004, **108**, 1107-1119.
41. B. H. Jones and A. M. Massari, *J. Phys. Chem. B*, 2013, **117**, 15741-15749.
42. B. H. Jones, C. J. Huber and A. M. Massari, *J. Phys. Chem. C*, 2011, **115**, 24813-24822.
43. A. A. Bakulin, C. Liang, T. L. Jansen, D. A. Wiersma, H. J. Bakker and M. S. Pshenichnikov, *Acc. Chem. Res.*, 2009, **42**, 1229-1238.
44. S. Park, K. Kwak and M. D. Fayer, *Laser Phys. Lett.*, 2007, **4**, 704-718.
45. A. A. Jaye, N. T. Hunt and S. R. Meech, *J. Chem. Phys.*, 2006, **124**, 024506.
46. Q. Zhong and J. T. Fourkas, *J. Phys. Chem. B*, 2008, **112**, 15529-15539.
47. R. A. Farrer and J. T. Fourkas, *Acc. Chem. Res.*, 2003, **36**, 605-612.
48. N. A. Smith, S. J. Lin, S. R. Meech, H. Shirota and K. Yoshihara, *J. Phys. Chem. A*, 1997, **101**, 9578-9586.
49. G. Giraud, C. M. Gordon, I. R. Dunkin and K. Wynne, *J. Chem. Phys.*, 2003, **119**, 464-477.
50. A. Tokmakoff and M. D. Fayer, *J. Chem. Phys.*, 1995, **103**, 2810-2826.
51. A. Tokmakoff and M. D. Fayer, *Acc. Chem. Res.*, 1995, **28**, 437-445.
52. C. W. Rella, K. D. Rector, A. S. Kwok, J. R. Hill, H. A. Schwettman, D. D. Dlott and M. D. Fayer, *J. Phys. Chem.*, 1996, **100**, 15620.
53. C. W. Rella, A. Kwok, K. D. Rector, J. R. Hill, H. A. Schwettmann, D. D. Dlott and M. D. Fayer, *Phys. Rev. Lett.*, 1996, **77**, 1648.
54. A. M. Massari, I. J. Finkelstein and M. D. Fayer, *J. Am. Chem. Soc.*, 2006, **128**, 3990-3997.
55. A. Martin and R. Synge, *Biochem. J*, 1941, **35**, 1358-1368.
56. A. Martin and R. Synge, *Biochem. J*, 1941, **35**, 91-121.
57. R. K. Mitra, S. S. Sinha, P. K. Verma and S. K. Pal, *J. Phys. Chem. B*, 2008, **112**, 12946-12953.
58. U. Raviv, P. Laurat and J. Klein, *Nature*, 2001, **413**, 51-54.
59. W. H. Thompson, *J. Phys. Chem. B*, 2005, **109**, 18201-18208.
60. H. J. Wang, X. K. Xi, A. Kleinhammes and Y. Wu, *Science*, 2008, **322**, 80-83.
61. R. A. Schoonheydt and B. M. Weckhuysen, *PCCP*, 2009, **11**, 2794-2798.
62. D. J. Beebe, G. A. Mensing and G. M. Walker, *Annu. Rev. Biomed. Eng.*, 2002, **4**, 261-286.
63. K. Gkionis, J. T. Obodo, C. Cucinotta, S. Sanvito and U. Schwingenschloegl, *Journal of Materials Chemistry A*, 2014, **2**, 16498-16506.
64. Z. Hu and J. D. Weeks, *J. Phys. Chem. C*, 2010, **114**, 10202-10211.
65. K. Johnston and V. Harmandaris, *J. Phys. Chem. C*, 2011, **115**, 14707-14717.
66. K. B. Tarmyshov and F. Mueller-Plathe, *J. Chem. Phys.*, 2007, **126**, 074702.
67. T. G. A. Youngs, D. Weber, L. F. Gladden and C. Hardacre, *J. Phys. Chem. C*, 2009, **113**, 21342-21352.
68. T. S. Gulmen and W. H. Thompson, *Langmuir*, 2009, **25**, 1103-1111.
69. I. R. Piletic, D. E. Moilanen, D. B. Spry, N. E. Levinger and M. D. Fayer, *J. Phys. Chem. A*, 2006, **110**, 4985-4999.
70. D. Cringus, A. Bakulin, J. Lindner, P. Vohringer, M. S. Pshenichnikov and D. A. Wiersma, *J. Phys. Chem. B*, 2007, **111**, 14193-14207.
71. D. Cringus, J. Lindner, M. T. W. Milder, M. S. Pshenichnikov, P. Vohringer and D. A. Wiersma, *Chem. Phys. Lett.*, 2005, **408**, 162-168.

72. A. M. Dokter, S. Woutersen and H. J. Bakker, *Proc. Nat. Acad. Soc. USA*, 2006, **103**, 15355-15358.
73. D. E. Moilanen, E. E. Fenn, D. Wong and M. D. Fayer, *J. Phys. Chem. B*, 2009, **113**, 8560-8568.
74. P. Dutta and K. Bhattacharyya, *Journal of Chemical Sciences*, 2004, **116**, 5-16.
75. N. T. Hunt, A. A. Jaye and S. R. Meech, *PCCP*, 2007, **9**, 2167-2180.
76. J. Sivaguru, A. Natarajan, L. S. Kaanumalle, J. Shailaja, S. Uppili, A. Joy and V. Ramamurthy, *Acc. Chem. Res.*, 2003, **36**, 509-521.
77. A. Planchais, S. Devautour-Vinot, F. Salles, F. Ragon, T. Devic, C. Serre and G. Maurin, *J. Phys. Chem. C*, 2014, **118**, 14441-14448.
78. B. J. Loughnane, R. A. Farrer, A. Scodinu, T. Reilly and J. T. Fourkas, *J. Phys. Chem. B*, 2000, **104**, 5421-5429.
79. A. Scodinu and J. T. Fourkas, in *Dynamics and Friction in Submicrometer Confining Systems*, eds. Y. Braiman, J. M. Drake, F. Family and J. Klafter, 2004, vol. 882, pp. 193-204.
80. X. Zhu, R. A. Farrer and J. T. Fourkas, *J. Phys. Chem. B*, 2005, **109**, 12724-12730.
81. C. J. Brinker and G. W. Sherer, *Sol-Gel Science: The Physics and Chemistry of Sol-Gel Processing*, Academic Press, Boston, MA, 1st edn., 1990.
82. L. M. Ellerby, C. R. Nishida, F. Nishida, S. A. Yamanaka, B. Dunn, J. S. Valentine and J. I. Zink, *Science*, 1992, **255**, 1113-1115.
83. S. C. Warren, M. R. Perkins, A. M. Adams, M. Kamperman, A. A. Burns, H. Arora, E. Herz, T. Suteewong, H. Sai, Z. H. Li, J. Werner, J. H. Song, U. Werner-Zwanziger, J. W. Zwanziger, M. Gratzel, F. J. DiSalvo and U. Wiesner, *Nature Materials*, 2012, **11**, 460-467.
84. S. M. Egger, K. R. Hurley, A. Datt, G. Swindlehurst and C. L. Haynes, *Chem. Mater.*, 2015, **27**, 3193-3196.
85. Y. Wan and D. Zhao, *Chem. Rev.*, 2007, **107**, 2821-2860.
86. J. F. Chen, H. M. Ding, J. X. Wang and L. Shao, *Biomaterials*, 2004, **25**, 723-727.
87. M. Liong, J. Lu, M. Kovochich, T. Xia, S. G. Ruehm, A. E. Nel, F. Tamanoi and J. I. Zink, *Acs Nano*, 2008, **2**, 889-896.
88. J. Kim, J. E. Lee, J. Lee, J. H. Yu, B. C. Kim, K. An, Y. Hwang, C. H. Shin, J. G. Park and T. Hyeon, *J. Am. Chem. Soc.*, 2006, **128**, 688-689.
89. G. Orcel, L. L. Hench, I. Artaki, J. Jonas and T. W. Zerda, *J. Non-Cryst. Solids*, 1988, **105**, 223-231.
90. G. Orcel and L. Hench, *J. Non-Cryst. Solids*, 1986, **79**, 177-194.
91. L. L. Hench and J. K. West, *Chem. Rev.*, 1990, **90**, 33-72.
92. M. Stolarski, J. Walendziewski and M. S. B. Pniak, *Applied Catalysis a-General*, 1999, **177**, 139-148.
93. M. K. Titulaer, W. K. Kegel, J. B. H. Jansen and J. W. Geus, *J. Non-Cryst. Solids*, 1994, **170**, 128-133.
94. U. Schubert and N. Husing, *Synthesis of Inorganic Materials*, Wiley-VCH, Weinheim, Germany, 2005.
95. M. A. B. Meador, L. A. Capadona, L. McCorkle, D. S. Papadopoulos and N. Leventis, *Chem. Mater.*, 2007, **19**, 2247-2260.
96. C. T. Kresge, M. E. Leonowicz, W. J. Roth, J. C. Vartuli and J. S. Beck, *Nature*, 1992, **359**, 710-712.
97. Y. Wan and D. Y. Zhao, *Chem. Rev.*, 2007, **107**, 2821-2860.
98. M. J. Vanbommel and A. B. Dehaan, *J. Non-Cryst. Solids*, 1995, **186**, 78-82.
99. D. Zimdars, A. Tokmakoff, S. Chen, S. R. Greenfield, M. D. Fayer, T. I. Smith and H. A. Schwettman, *Phys. Rev. Lett.*, 1993, **70**, 2718-2721.
100. Y. S. Kim and R. M. Hochstrasser, *Proc. Nat. Acad. Soc. USA*, 2005, **102**, 11185-11190.

101. C. R. Baiz, P. L. McRobbie, J. M. Anna, E. Geva and K. J. Kubarych, *Acc. Chem. Res.*, 2009, **42**, 1395-1404.
102. P. Hamm and M. T. Zanni, *Concepts and Methods of 2D Infrared Spectroscopy*, Cambridge University Press, Cambridge, 2011.
103. K. D. Rector, M. D. Fayer, P. Hamm and R. M. Hochstrasser, *Ultrafast Infrared and Raman Spectroscopy*, Marcel Dekker, Inc., New York, 2001.
104. I. C. Spector, C. M. Olson, C. J. Huber and A. M. Massari, *Opt. Lett.*, 2015, **40**, 1850-1852.
105. J. B. Asbury, T. Steinel, K. Kwak, S. A. Corcelli, C. P. Lawrence, J. L. Skinner and M. D. Fayer, *J. Chem. Phys.*, 2004, **121**, 12431-12446.
106. D. M. Jonas, *Annu. Rev. Phys. Chem.*, 2003, **54**, 425-463.
107. I. J. Finkelstein, H. Ishikawa, S. Kim, A. M. Massari and M. D. Fayer, *Proc. Nat. Acad. Soc. USA*, 2007, **104**, 2637-2642.
108. S. Woutersen, Y. Mu, G. Stock and P. Hamm, *Chem. Phys.*, 2001, **266**, 137-147.
109. J. T. King, C. R. Baiz and K. J. Kubarych, *J. Phys. Chem. A*, 2010, **114**, 10590-10604.
110. K. Lazonder, M. S. Pshenichnikov and D. A. Wiersma, *Opt. Lett.*, 2006, **31**, 3354-3356.
111. S. Roy, M. S. Pshenichnikov and T. L. C. Jansen, *J. Phys. Chem. B*, 2011, **115**, 5431-5440.
112. R. M. Stratt, *The Molecular Mechanisms Behind the Vibrational Population Relaxation of Small Molecules in Liquids*, Marcel Dekker, Inc., New York, 2001.
113. E. Heilweil, *Applications of Broadband Transient Infrared Spectroscopy*, Marcel Dekker, Inc., New York, Fayer, M. D. edn., 2001.
114. P. F. Barbara, T. J. Meyer and M. A. Ratner, *J. Phys. Chem.*, 1996, **100**, 13148-13168.
115. O. H. Kwon, T. H. Yoo, C. M. Othona, J. A. Van Deventer, D. A. Tirrell and A. H. Zewail, *Proc. Nat. Acad. Soc. USA*, 2010, **107**, 17101-17106.
116. L. Rohrschneider, *Anal. Chem.*, 1973, **45**, 1241-1247.
117. C. Reichardt, *Chem. Rev.*, 1994, **94**, 2319-2358.
118. R. Papadakis, I. Deligkiozi and A. Tsolomitis, *Analytical and Bioanalytical Chemistry*, 2010, **397**, 2253-2259.
119. V. Gutmann, *Electrochim. Acta*, 1976, **21**, 661-670.
120. U. Mayer, V. Gutmann and W. Gerger, *Monatsh. Chem.*, 1975, **106**, 1235-1257.
121. P. Bacelon, J. Corset and C. Deloze, *J. Solution Chem.*, 1983, **12**, 23-31.
122. J. Engberts, G. R. Famini, A. Perjessy and L. Y. Wilson, *J. Phys. Org. Chem.*, 1998, **11**, 261-272.
123. D. J. Parker, *Spectrochimica Acta Part a-Molecular and Biomolecular Spectroscopy*, 1983, **39**, 463-476.
124. R. D. Pensack, K. M. Banyas and J. B. Asbury, *PCCP*, 2010, **12**, 14144-14152.
125. M. C. R. Symons, G. Eaton, T. A. Shippey and J. M. Harvey, *Chem. Phys. Lett.*, 1980, **69**, 344-347.
126. D. A. Estrin, L. M. Baraldo, L. D. Slep, B. C. Barja, J. A. Olabe, L. Paglieri and G. Corongiu, *Inorg. Chem.*, 1996, **35**, 3897-3903.
127. D. A. Friesen, R. E. Nashiem and W. L. Waltz, *Inorg. Chem.*, 2007, **46**, 7982-7991.
128. R. S. Czernuszewicz, V. Mody, A. A. Zareba, M. B. Zaczek, M. Galezowski, V. Sashuk, K. Grela and D. T. Gryko, *Inorg. Chem.*, 2007, **46**, 5616-5624.
129. K. Dimroth, C. Reichardt, T. Siepmann and F. Bohlmann, *Liebigs. Ann. Clreni.*, 1966, **661**, 1.
130. E. M. Kosower, *J. Am. Chem. Soc.*, 1958, **80**, 3253-3260.
131. C. G. Swain, M. S. Swain, A. L. Powell and S. Alunni, *J. Am. Chem. Soc.*, 1983, **105**, 502-513.
132. F. A. Cotton, *Advanced Inorganic Chemistry*, Wiley-Interscience, Inc., New York, 5th edn., 1988.
133. G. B. Ray, X. Y. Li, J. A. Ibers, J. L. Sessler and T. G. Spiro, *J. Am. Chem. Soc.*, 1994, **116**, 162-176.

134. Y. Zhao and D. G. Truhlar, *J. Chem. Phys.*, 2006, **125**, 194101.
135. W. J. Hehre, L. Radom, P. v. R. Schleyer and J. A. Pople, *Ab Initio Molecular Orbital Theory*, Wiley, New York, 1986.
136. J. M. L. Martin and A. Sundermann, *J. Chem. Phys.*, 2001, **114**, 3408-3420.
137. A. V. Marenich, C. J. Cramer and D. G. Truhlar, *J. Phys. Chem. B*, 2009, **113**, 6378-6396.
138. M. J. T. Frisch, G. W.; Schlegel, H. B.; Scuseria, G. E.; Robb, M. A.; Cheeseman, J. R.; Scalmani, G.; Barone, V.; Mennucci, B.; Petersson, G. A.; Nakatsuji, H.; Caricato, M.; Li, X.; Hratchian, H. P.; Izmaylov, A. F.; Bloino, J.; Zheng, G.; Sonnenberg, J. L.; Hada, M.; Ehara, M.; Toyota, K.; Fukuda, R.; Hasegawa, J.; Ishida, M.; Nakajima, T.; Honda, Y.; Kitao, O.; Nakai, H.; Vreven, T.; Montgomery, J. A., Jr.; Peralta, J. E.; Ogliaro, F.; Bearpark, M.; Heyd, J. J.; Brothers, E.; Kudin, K. N.; Staroverov, V. N.; Kobayashi, R.; Normand, J.; Raghavachari, K.; Rendell, A.; Burant, J. C.; Iyengar, S. S.; Tomasi, J.; Cossi, M.; Rega, N.; Millam, N. J.; Klene, M.; Knox, J. E.; Cross, J. B.; Bakken, V.; Adamo, C.; Jaramillo, J.; Gomperts, R.; Stratmann, R. E.; Yazyev, O.; Austin, A. J.; Cammi, R.; Pomelli, C.; Ochterski, J. W.; Martin, R. L.; Morokuma, K.; Zakrzewski, V. G.; Voth, G. A.; Salvador, P.; Dannenberg, J. J.; Dapprich, S.; Daniels, A. D.; Farkas, Ö.; Foresman, J. B.; Ortiz, J. V.; Cioslowski, J.; Fox, D. J. , *Gaussian 09, revision A.02*, Wallington, CT, 2009.
139. S. G. Bratsch, *J. Chem. Educ.*, 1988, **65**, 34-41.
140. H. Hotop and W. C. Lineberger, *J. Phys. Chem. Ref. Data*, 1985, **14**, 731-750.
141. G. R. Desiraju, *J. Chem. Soc.-Dalton Trans.*, 2000, DOI: 10.1039/b003285i, 3745-3751.
142. P. B. Chock and J. Halpern, *J. Am. Chem. Soc.*, 1966, **88**, 3511-3514.
143. S. La Placa and J. Ibers, *J. Am. Chem. Soc.*, 1965, **87**, 2581-2586.
144. L. Vaska, L. Chen and C. Senoff, *Science*, 1971, **174**, 587-589.
145. J. S. Valentine, *Chem. Rev.*, 1973, **73**, 235-245.
146. L. Vaska and R. E. Rhodes, *J. Am. Chem. Soc.*, 1965, **87**, 4970-4971.
147. G. L. Geoffroy, G. S. Hammond and H. B. Gray, *J. Am. Chem. Soc.*, 1975, **97**, 3933-3936.
148. L. Vaska, *Acc. Chem. Res.*, 1968, **1**, 335-344.
149. M. A. Bennett, R. J. H. Clark and D. L. Milner, *Inorg. Chem.*, 1967, **6**, 1647-1652.
150. K. Fagnou and M. Lautens, *Angewandte Chemie-International Edition*, 2002, **41**, 26-47.
151. A. P. Ginsberg, J. H. Osborne and C. R. Sprinkle, *Inorg. Chem.*, 1983, **22**, 254-266.
152. T. Suzuki, N. Tsuji, K. Kashiwabara and K. Tatsumi, *Inorg. Chem.*, 2000, **39**, 3938-+.
153. W. D. Bonds and J. A. Ibers, *J. Am. Chem. Soc.*, 1972, **94**, 3413-3419.
154. R. Ugo, G. LaMonica, S. Cenini, A. Segre and F. Conti, *J. Chem. Soc. A*, 1971, 522-528.
155. A. P. Ginsberg, W. E. Lindsell, C. R. Sprinkle, K. W. West and R. L. Cohen, *Inorg. Chem.*, 1982, **21**, 3666-3681.
156. T. Ando and J. Skolnick, *Biophys. J.*, 2013, **104**, 96-105.
157. E. Yamamoto, T. Akimoto, M. Yasui and K. Yasuoka, *Scientific Reports*, 2014, **4**, 4720.
158. A. A. Bakulin, D. Cringus, P. A. Pieniazek, J. L. Skinner, T. L. C. Jansen and M. S. Pshenichnikov, *J. Phys. Chem. B*, 2013, **117**, 15545-15558.
159. R. Costard and T. Elsaesser, *J. Phys. Chem. B*, 2013, **117**, 15338-15345.
160. T. K. De and A. Maitra, *Adv. Colloid Interface Sci.*, 1995, **59**, 95-193.
161. J. Nishida and M. D. Fayer, *J. Chem. Phys.*, 2014, **140**, 144702.
162. D. Blach, J. J. Silber, N. M. Correa and R. D. Falcone, *PCCP*, 2013, **15**, 16746-16757.
163. N. M. Correa, J. J. Silber, R. E. Riter and N. E. Levinger, *Chem. Rev.*, 2012, **112**, 4569-4602.
164. R. Lu, R. X. Zhu, R. B. Zhong and A. C. Yu, *Journal of Photochemistry and Photobiology a-Chemistry*, 2013, **252**, 116-123.
165. A. Sengupta, K. Gavvala, R. K. Koninti, H. Chaudhuri and P. Hazra, *Chem. Phys. Lett.*, 2013, **584**, 67-73.
166. J. P. Wang, J. S. Chen and G. J. Zhao, *J. Colloid Interface Sci.*, 2014, **423**, 1-6.

167. B. Bagchi and B. Jana, *Chem. Soc. Rev.*, 2010, **39**, 1936-1954.
168. H. Shirota, *J. Chem. Phys.*, 2005, **122**, 44514.
169. F. Kirkbir, H. Murata, D. Meyers, S. R. Chaudhuri and A. Sarkar, *J. Sol-Gel Sci. Technol.*, 1996, **6**, 203-217.
170. P. B. Wagh, R. Begag, G. M. Pajonk, A. V. Rao and D. Haranath, *Mater. Chem. Phys.*, 1999, **57**, 214-218.
171. B. Cao and C. S. Zhu, *J. Non-Cryst. Solids*, 1999, **246**, 34-38.
172. J. H. Harreld, T. Ebina, N. Tsubo and G. Stucky, *J. Non-Cryst. Solids*, 2002, **298**, 241-251.
173. W. Jin and J. D. Brennan, *Anal. Chim. Acta*, 2002, **461**, 1-36.
174. I. Gill, *Chem. Mater.*, 2001, **13**, 3404-3421.
175. G. D. Yadav and S. R. Jadhav, *Microporous Mesoporous Mater.*, 2005, **86**, 215-222.
176. G. Yang, J. P. Wu, G. Xu and L. R. Yang, *Bioresour. Technol.*, 2009, **100**, 4311-4316.
177. E. Reategui and A. Aksan, *J. Phys. Chem. B*, 2009, **113**, 13048-13060.
178. K. E. Jaeger and M. T. Reetz, *Trends Biotechnol.*, 1998, **16**, 396-403.
179. M. T. Reetz, *Adv. Mater.*, 1997, **9**, 943-954.
180. S. Bruno, M. Bonaccio, S. Bettati, C. Rivetti, C. Viappiani, S. Abbruzzetti and A. Mozzarelli, *Protein Sci.*, 2001, **10**, 2401-2407.
181. T. K. Das, I. Khan, D. L. Rousseau and J. M. Friedman, *J. Am. Chem. Soc.*, 1998, **120**, 10268-10269.
182. D. K. Eggers and J. S. Valentine, *Protein Sci.*, 2001, **10**, 250-261.
183. E. H. Lan, B. C. Dave, J. M. Fukuto, B. Dunn, J. I. Zink and J. S. Valentine, *J. Mater. Chem.*, 1999, **9**, 45-53.
184. C. R. Lloyd and E. M. Eyring, *Langmuir*, 2000, **16**, 9092-9094.
185. J. M. Miller, B. Dunn, J. S. Valentine and J. I. Zink, *J. Non-Cryst. Sol.*, 1996, **202**, 279-289.
186. G. Ping, J. M. Yuan, Z. F. Sun and Y. Wei, *J. Molec. Recog.*, 2004, **17**, 433-440.
187. A. K. Williams and J. T. Hupp, *J. Am. Chem. Soc.*, 1998, **120**, 4366-4371.
188. C. J. Huber, T. C. Anglin, B. H. Jones, N. Muthu, C. J. Cramer and A. M. Massari, *J. Phys. Chem. A*, 2012, **116**, 9279-9286.
189. D. M. Walker, E. C. Hayes and L. J. Webb, *PCCP*, 2013, **15**, 12241-12252.
190. B. H. Jones and A. M. Massari, *J. Phys. Chem. B*, 2013, **ASAP online**, DOI: 10.1021/jp4064627.
191. M. I. Batuev, A. D. Petrov, V. A. Ponomarenko and A. D. Matveeva, *Bull. Acad. Sci. USSR*, 1956, **5**, 1269-1274.
192. A. L. Smith and N. C. Angelotti, *Spectrochim. Acta*, 1959, **15**, 412-420.
193. G. Lucovsky, *Solid State Commun.*, 1979, **29**, 571-576.
194. G. Lucovsky, R. J. Nemanich and J. C. Knights, *Physical Review B*, 1979, **19**, 2064-2073.
195. H. W. Thompson, *Spectrochim. Acta*, 1960, **16**, 238-241.
196. I. S. Chuang and G. E. Maciel, *J. Phys. Chem. B*, 1997, **101**, 3052-3064.
197. L. W. Kelts and N. J. Armstrong, *J. Mater. Res.*, 1989, **4**, 423-433.
198. A. Steel, S. W. Carr and M. W. Anderson, *Chem. Mater.*, 1995, **7**, 1829-1832.
199. K. Kwak, D. E. Rosenfeld and M. D. Fayer, *J. Chem. Phys.*, 2008, **128**, 204505.
200. K. Lewis, J. Myers, F. Fuller, P. Tekavec and J. Ogilvie, *Spectroscopy*, 2010, **24**, 393-397.
201. N. Demirdoven, M. Khalil and A. Tokmakoff, *Phys. Rev. Lett.*, 2002, **89**, 237401.
202. E. E. Fenn and M. D. Fayer, *J. Chem. Phys.*, 2011, **135**, 074502.
203. K. A. Merchant, W. G. Noid, R. Akiyama, I. J. Finkelstein, A. Goun, B. L. McClain, R. F. Loring and M. D. Fayer, *J. Am. Chem. Soc.*, 2003, **125**, 13804-13818.
204. G. R. Fleming and M. H. Cho, *Annu. Rev. Phys. Chem.*, 1996, **47**, 109-134.
205. M. D. Fayer, *Annu. Rev. Phys. Chem.*, 2009, **60**, 21-38.
206. E. W. Castner and M. Maroncelli, *J. Mol. Liq.*, 1998, **77**, 1-36.

207. T. H. Joo, Y. W. Jia, J. Y. Yu, M. J. Lang and G. R. Fleming, *J. Chem. Phys.*, 1996, **104**, 6089-6108.
208. R. M. Stratt and M. Maroncelli, *J. Phys. Chem.*, 1996, **100**, 12981-12996.
209. B. H. Jones, C. J. Huber, I. C. Spector, A. M. Tabet, R. L. Butler, Y. Hang and A. M. Massari, *The Journal of Chemical Physics*, 2015, **142**, 212441.
210. Y. S. Lin, N. Abadeer, K. R. Hurley and C. L. Haynes, *J. Am. Chem. Soc.*, 2011, **133**, 20444-20457.
211. P. J. Branton, P. G. Hall, K. S. W. Sing, H. Reichert, F. Schuth and K. K. Unger, *Journal of the Chemical Society-Faraday Transactions*, 1994, **90**, 2965-2967.
212. K. Zhang, L. L. Xu, J. G. Jiang, N. Calin, K. F. Lam, S. J. Zhang, H. H. Wu, G. D. Wu, B. Albela, L. Bonneviot and P. Wu, *J. Am. Chem. Soc.*, 2013, **135**, 2427-2430.
213. A. Sayari, Y. Yang, M. Kruk and M. Jaroniec, *J. Phys. Chem. B*, 1999, **103**, 3651-3658.
214. A. V. Neimark, P. I. Ravikovitch, S. C. O. Domhnaill, F. Schuth and K. K. Unger, *Theoretical and experimental studies of capillary hysteresis in MCM-41*, Kluwer Academic Publishers, Norwell, 1996.
215. C. R. Baiz and K. J. Kubarych, *J. Am. Chem. Soc.*, 2010, **132**, 12784-12785.
216. A. A. Eigner, T. C. Anglin and A. M. Massari, *J. Phys. Chem. C*, 2010, **114**, 12308-12315.
217. J. Nishida, A. Tamimi, H. Fei, S. Pullen, S. Ott, S. Cohen and M. Fayer, *Proceedings of the National Academy of Sciences*, 2014, **111**, 18442-18447.
218. D. E. Rosenfeld, Z. Gengeliczki, B. J. Smith, T. D. P. Stack and M. D. Fayer, *Science*, 2011, **334**, 634-639.
219. M. D. Fayer, in *Annu. Rev. Phys. Chem.*, 2009, vol. 60, pp. 21-38.
220. I. J. Finkelstein, A. M. Massari and M. D. Fayer, *Biophys. J.*, 2007, **92**, 3652-3662.
221. S. Kim, J. K. Chung, K. Kwak, S. E. J. Bowman, K. L. Bren, B. Bagchi and M. D. Fayer, *J. Phys. Chem. B*, 2008, **112**, 10054-10063.
222. C. J. Brinker, *J. Non-Cryst. Solids*, 1988, **100**, 31-50.
223. M. Faustini, L. Nicole, C. Boissiere, P. Innocenzi, C. Sanchez and D. Grosso, *Chem. Mater.*, 2010, **22**, 4406-4413.
224. G. C. Hoang, *Journal of the Korean Physical Society*, 1997, **31**, 227-230.
225. J. J. Vanbeek, D. Seykens and J. B. H. Jansen, *J. Non-Cryst. Solids*, 1992, **146**, 111-120.
226. G. Engelhardt, *Zeitschrift Fur Chemie*, 1975, **15**, 495-496.
227. G. Engelhardt, W. Altenburg, D. Hoebbel and W. Wieker, *Z. Anorg. Allg. Chem.*, 1977, **437**, 249-252.
228. R. Jullien, A. Hasmy and E. Anglaret, *J. Sol-Gel Sci. Technol.*, 1997, **8**, 819-824.
229. A. Hasmy, E. Anglaret, R. Thouy and R. Jullien, *J. Phys. I*, 1997, **7**, 521-542.
230. E. Anglaret, A. Hasmy and R. Jullien, *Phys. Rev. Lett.*, 1995, **75**, 4059-4062.
231. T. S. Coffey, *American Journal of Physics*, 2008, **76**, 551-557.
232. J. F. Eichler, H. Patrick, B. Harmon and J. Coonce, *J. Chem. Educ.*, 2007, **84**, 1120-1123.
233. A. Hobson, *American Journal of Physics*, 2009, **77**, 293-293.
234. B. H. McGuyer, J. M. Brown and H. B. Dang, *American Journal of Physics*, 2009, **77**, 677-677.
235. J. E. Baur and M. B. Baur, *J. Chem. Educ.*, 2006, **83**, 577-580.
236. A. L. Smith, *Spectrochim. Acta*, 1960, **16**, 87-105.
237. A. Tokmakoff, B. Sauter and M. D. Fayer, *J. Chem. Phys.*, 1994, **100**, 9035-9043.

Appendix A: Quantifying the Soda Geyser

Abstract

Although the science behind the soda geyser demonstration is well known, describing the microscopic origins of this dramatic and sticky demonstration can be difficult. In this experiment, an apparatus was designed to contain the reaction, thereby allowing for quantitative analysis of the amount of CO_2 released after dropping in various initiating objects. The exploratory studies were tested with a moderate sized group of 12-17 year old participants at a summer learning event, and their data confirmed that the difference in the surface area of the initiators was a primary factor for the release of dissolved gas. Additional studies were performed to relate the soda temperature to the amount of dissolved CO_2. In this laboratory experiment, students gained a greater understanding of surface area and its effect on gas nucleation and bubble formation, as well as gas solubility and its temperature dependence. The experimental approach provided a dramatic yet contained format for students to form and test their own hypotheses about the chemical processes behind this popular classroom demo.

A.1: Introduction

From viral videos to Mythbusters, millions of scientists and non-scientists have witnessed the eruption of a "soda geyser" after adding a mint candy to a freshly opened two-liter bottle of soda. For the unaware, the result is the rapid release of CO_2 gas and a blast of foamy soda that can shoot dozens of feet into the air under the right conditions. As described previously, what occurs is the nucleation of CO_2 gas to form bubbles on high surface area portions of the candy. Certain types of initiators, namely mint Mentos® and Lifesavers® candies, have been shown to produce the most dramatic geysers, and electron microscopic analysis of these objects confirms a highly textured surface for efficient bubble nucleation.[231] Eventually the formed bubbles become too large and are released, bumping into other bubbles and causing a massive release of effervescence. Although this demonstration is exciting to watch, it is hard to get quantitative information about individual trials for comparison. Some experiments have used the mass difference before and after the eruption to quantify the process[231] but this inadvertently measures the loss of both evolved gas and the foamy soda it propels. Other experiments have measured the height of the eruption,[232] however, the height does not necessarily represent the extent of the reaction for slower, less violent eruptions. From a pedagogical perspective, it is more desirable to measure the quantity of CO_2 gas released as a function of initiator properties without the added variable of the soda volume.

A.2: Experimental Overview

This experiment is appropriate for middle school, high school, and possibly early undergraduate students. The experiment was tested at a summer learning event with participants from grades 7 through 12. A later section will discuss how it can be incorporated into secondary education curricula. A student learning assessment after the event found the experiment to be popular and informative for the participants. Before the students used the controlled apparatuses, a demonstration of an untamed soda geyser was performed outdoors to illustrate the effect and make observations. After the excitement of the geyser, students were asked to provide hypotheses to explain their observations. Then our soda geyser apparatus was introduced and demonstrated by the instructor as a way to test some of the hypotheses. Once the students were trained to use the apparatus, minimal instruction was provided, allowing the students the opportunity to explore each of the initiators individually and in various combinations. Connections between their observations and the physical and chemical processes occurring in the experiment were emphasized, and the moles of gas released were calculated.

A.3: Experimental Details

The simple apparatus for quantifying the soda geyser in a laboratory setting is shown schematically in Figure A.1a. The containers, tubing, and hose connectors are available from Fisher Scientific, as well as many other lab supply companies. The lid of a 64 oz wide-mouth plastic jar was drilled and fitted with plastic NPT (National Pipe Thread) hose connectors on the inside and outside surfaces. O-rings were used to create an air-tight seal for the fittings to the lid surface. The 3/8” hose barb on one of the inner connectors

was carefully cut off with a razor blade, and this became the input opening for the jar. Two lengths of tubing (approximately 18") were attached to the connectors on top of the lid as the input and output tubes. Figure A.1b shows an expanded view of the caps and fittings on the soda bottle and water reservoir. The output tube was directed into a 1 L beaker for measuring the volume change of the soda geyser. A length of tubing long enough to reach the bottom of the jar was attached to the remaining barb on the interior side of the lid (the jar output). The 64 oz jar was filled with water and the lid assembly was tightened to achieve an air-tight seal. Parafilm can be used to improve the seal, but we did not find this to have a significant influence on the measurements. A two liter bottle cap was drilled and fitted with a 3/8" male tube connector using another o-ring for an air-tight seal. The hose barb was also removed on the inside of the cap with a razor blade, and this cap served as the connection to each soda bottle. For the following studies we used 12 oz soda bottles to minimize cost, waste, and mess. A 3-1/2" galvanized nail was used to hold all initiator objects out of the soda until we were ready to begin the experiment. It was found later that the roughness of the nail itself caused ~100 mL of water to be displaced when dropped into a freshly opened soda. Therefore, 3-1/2" smooth nails are recommended, but this could also be viewed as a variable for the students to discover and test on their own. Candies were threaded onto the nail and held by the nail head, whereas a small wire cage was hung from the nail head for more complicated objects, such as the sugar cubes. Once loaded with the initiator, the nail was slid into the soda cap connector from the inside and a Hoffman screw pinch clamp was tightened onto it to hold it while the cap was tightened onto each soda bottle. A cold 12 oz soda was opened gently, its cap was completely removed, and the bottle cap containing the nail and initiator was tightened onto it. In this

study, we used carbonated soft drinks with artificial sweetener, which we refer to throughout as “soda”.

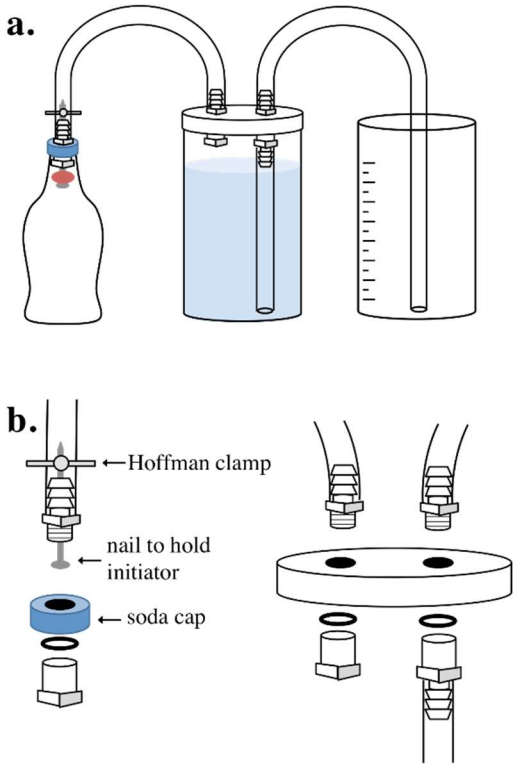

Figure A.1. a) Schematic of the controlled soda geyser apparatus, and b) an expanded view of the soda and water reservoir caps and their fittings.

When everything was secured, the hose clamp holding the nail was loosened, dropping the nail and initiator(s) into the soda. CO_2 and soda were forced through the tubing into the water-filled plastic jar. The CO_2 pressurized the headspace of the jar and forced the water (mixed with some soda) through the output tube into the measurement beaker. Once most of the CO_2 was released and the pressure in the headspace equaled atmospheric pressure, the volume of liquid pushed out into the measurement beaker was equal to the amount of headspace gained in both the soda bottle and the plastic jar, in other words, equal to the amount of CO_2 that was released. From this volume, the number of moles and molecules of CO_2 were calculated using the Ideal Gas Law.

A.4: Hazards

There are no chemical hazards associated with the materials used in this experiment, although there are certainly possibilities for messes that can lead to a disorderly lab space. Goggles should be worn to avoid soda sprays to the eyes. It should be made clear that the initiators are not to be dropped into the soda bottles and capped with the undrilled caps as this will create an unsafe explosion hazard. Also, threading the candies and chalk onto the nail can be dangerous for younger students, so 13/64" holes can be pre-drilled into the candies and chalk to make this process easier.

A.5: Testing the Experiment

The experiment was tested at a summer learning event ("University on the Prairie", U of MN Southwest Outreach Center, Lamberton, Minnesota, Summer 2012) with 54 students from grades 7 through 12. The participants were split up by age into three sessions with 16 to 20 students per session. Each session lasted 90 minutes. The students in each session were separated into groups of two or three people, and each group was given a controlled soda geyser apparatus and five different initiator samples to test. Mint Mentos®, fruit Mentos®, a disk of sidewalk chalk (approximately the same size as the candies), a sugar cube, and a ¼-20 steel nut were provided to drop into five cold unopened 12 oz Diet Coke® sodas. Before the students used the controlled apparatuses, a demonstration of an untamed soda geyser was performed outdoors to illustrate the effect and make observations. Students discussed and recorded hypotheses to explain their observations. At this point the contained geyser apparatus was introduced along with the possible

initiators to test. The instructor encouraged the students to study the design of the apparatus and discuss its operation to ensure an accurate understanding of the experiment. This discussion was useful for identifying possible sources of error after the experiment was completed. The instructor showed the students a trial run of how the apparatus should be assembled and used. Before the unopened soda bottles were handed out, it was stressed that CO_2 (carbonation) was being released and in order to obtain the most accurate results the soda should not be shaken or disturbed.

A.6: Results and Discussion

Table A.1 shows the volumes of gas measured from each sample along with the calculated number of moles and molecules of CO_2 released. A common hypothesis gathered from the students before testing commenced was that the mint flavoring of the candies contributed to the effervescence of the geyser, but the comparison of the mint to fruit flavored candies showed that this was not a significant contributor to the effect. Many expected that the sugar in the candy played a role in the process, which was partially borne out in the observation that a sugar cube led to a significant volume of CO_2 evolved. However, this conclusion was called into question by the piece of chalk, which evolved the greatest volume of gas. A discussion ensued in which the students compared the result of this initiator to that of the smooth steel nut, and a general consensus was reached that the roughness of the initiator was the variable of interest.

Table A.1. Quantities of liquids and gas evolved from the controlled soda geysers.

initiator	volume of water displaced (mL) [a]				Moles of CO_2	Molecules of CO_2 ($\times 10^{22}$)
	Group 1	Group 2	Group 3	weighted average[b]		
mint Mentos®	546 (74)	538 (38)	475 (158)	509 (110)	0.0208	1.25
fruit Mentos®	571 (160)	485 (49)	525 (103)	525 (118)	0.0215	1.29
chalk	726 (95)	649 (58)	691 (134)	699 (89)	0.0286	1.72
sugar cube	546 (178)	555 (160)	635 (145)	570 (163)	0.0233	1.40
¼-20 nut	230 (111)	290 (66)	275 (173)	255 (131)	0.0104	0.628

a. Values in parentheses represent the standard deviations of the measurements.
b. Averages weighted by the number of participants in each group.

An additional temperature dependence study was performed by the authors of this paper in order to establish whether this experimental setup could be used to teach students about the temperature dependence of gas solubility. The bottles of Diet Coke® were held at their respective temperatures for approximately four hours and the temperature of the remaining soda in the bottles was measured. All of the trials were performed with Mint Mentos® as the initiator. The CO_2 either exists dissolved in the solution or in the headspace of the soda. When the bottle is open the CO_2 in the headspace is released along with a small portion of the dissolved CO_2 due to a disruption in the system equilibrium. Any remaining CO_2 in the system must have been dissolved originally in the solution. Therefore a colder soda should release more CO_2 due to higher gas solubility at lower temperatures. Table A.2 contains the data collected after three trials at each temperature using mint Mentos®. The values in parenthesis indicate the standard deviations. Although the precision in the data could be improved, it can be seen that the 7 °C soda did indeed release

the most CO_2. At first glance, it appears that the data point at 60 °C contradicts the earlier logic. We noted that the 60 °C trials exhibited pressurization of the headspace of the jar prior to the burst, demonstrating that a portion of the collected volume is not due to nucleation of CO_2 on the substrate. One explanation for this observation is that the system at 60 °C is further from equilibrium after the pressure in the headspace is released. This would result in a more rapid release of CO_2 and possibly the higher evacuated volume than the room temperature system. A complex problem such as the temperature dependence can be an adaptation to the experiment for implementation into undergraduate curricula.

Table A.2. Temperature dependent volumes of gas evolved.

temperature	7°C	22°C	60°C
displaced volume (mL)[a]	633 (36)	485 (52)	522 (26)

a. Values in parentheses indicate the standard deviations of the measurements.

This experiment is versatile and appropriate for a broad age range of students. During the course in which it was tested, it was a standalone experiment with a limited amount of time. This required closer direction from the instructors to complete the tasks. The 90 minute period was enough time for the students to see the demonstration, listen to a five minute lecture, test each of the substrates, and record their data. The more advanced students even had enough time to test combinations of substrates and antacid tablets. In a classroom setting, the activities could be extended to cover a few 45 minute class periods. Junior high school and high school aged students could utilize one period to learn the procedure and construct the geyser apparatus. Given more time, a student led inquiry could

be utilized. Ideally the students would be given a box of items with a range of roughnesses and surface areas, including some red herring items such as mint extract. They could then compile their data and develop their own hypotheses.

Furthermore, the controlled soda geyser apparatus could be used to test a number of additional variables, such as the nature of the soda (diet vs. regular, different flavors). Some other initiators that may be interesting to try include iron filings,[233] and porous CO_2 producing materials such as AlkaSeltzer®. An interesting study that could be carried out with the latter is whether the method described in this paper is able to detect the CO_2 that is produced when the sodium bicarbonate in the antacid reacts with the acidic soda. Furthermore, with the availability of many at home carbonation systems, it is feasible to make a series of measurements of solubility versus headspace pressure, allowing for the determination of the Henry's Law constant. For a more dramatic experiment, it has also been reported that nucleation can be triggered by placing the plastic bottle into either a dewar of liquid nitrogen[234] or a sonicator,[235] which could be carried out using the apparatus detailed in this paper. With these activities in mind, an instructor could plan to incorporate the soda geyser into their curriculum during discussions of material phase changes or solubility, or even to teach the scientific method of developing and testing hypotheses.

A.7: Conclusion

By applying a controlled experimental setup to the well-known soda geyser demonstration, students in a summer course were able to quantify the volume of CO_2 released during the reaction. In practice, after trying various initiator objects a group of 12-17 year old students discovered that the surface area of a sample affects the extent of effervescence. Using the Ideal Gas Law, the students were able to calculate the moles of CO_2 that were released. A few of the students in the test group already knew the underlying physics of the geyser experiment, but were still notably engaged in the experimental process, which is visually exciting and reinforces pre-existing knowledge. We further demonstrated that temperature dependent solubility experiments could be conducted in a classroom setting to illustrate how temperature affects gas solubility in liquids. Although we acknowledge that the amount CO_2 measured is only a fraction of the gas originally in the bottle, this experiment is still a visually stimulating and semi-quantitative demonstration of many fundamental concepts of chemistry.

Appendix B: Vibrational Lifetime Study of Si-H modes

Author's Note

This appendix discusses some interesting observations involving the vibrational lifetime of the Si-H mode in chapters 4-6. The story that the data presents has not been fully developed and as such did not justify a full chapter. However, I felt that the observations in this appendix needed to be documented in my thesis in hopes of the continuation of this work in the future.

B.1: Experimental

The data presented in this appendix was gathered by pump-probe spectroscopy through procedures detailed in Section 2.4.3. The lifetimes were extracted by fitting the pump-probe decays over the entire spectrum. The lifetimes of the 0-1 and 1-2 peaks were averaged by selecting only the lifetimes of the frequencies that had intensities above (below) 85% of the maxima (minima). The error bars presented in this appendix are the standard deviations of the lifetimes over the same frequencies.

B.2: Results and Discussion

Figure B.1 presents the vibrational lifetimes of 0-1 and 1-2 transitions of the Si-H mode for the various systems discussed in Chapters 4-6. Figure B.1a displays the lifetimes, T_1, for the silica sol-gel samples presented in Chapter 4. Figure B.1b and B.1c display the T_1 for TriMOS and TriPS in chloroform, isopropanol, and pentane. Figure B.1d displays

the T_1 for the Si-H modes grafted onto the surface of the various mesoporous silica nanoparticles presented in Chapter 5. In Figure B.1a, the lifetimes of the mode in various solvents are overall similar with the exception of the chloroform and the 0-1 mode on pentane. In all solvents, the 0-1 vibration has a longer lifetime than the 1-2 vibration, suggesting that the lifetime could be dependent on the frequency of the transition. To further test this trend, the lifetimes of the Si-H mode on TriMOS and TriPS are compared in Figures B.1b and B.1c. The TriMOS data shows the same correlation for the lifetimes of the 0-1 and 1-2 peaks, whereas the TriPS data exhibits anti-correlated behavior. The MSNP data in Figure B.1d exhibits no correlation between the frequency of the transitions and the lifetimes.

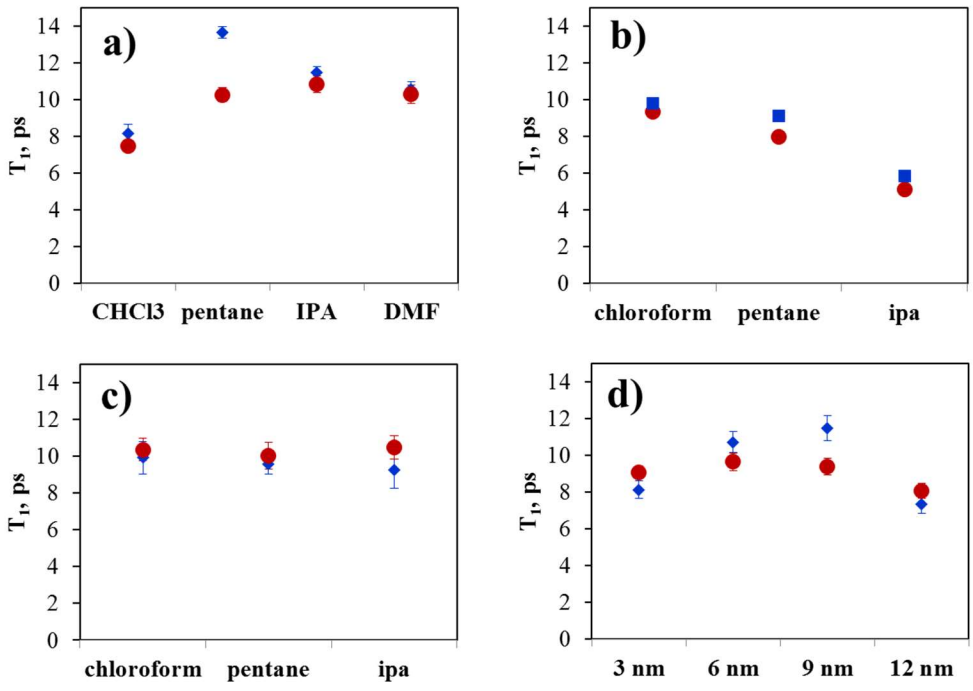

Figure B.1 Displays the vibrational lifetimes of the 0-1 (blue) and 1-2 (red) transitions for a) the silica sol-gel samples in Chapter 4, b) TriMOS dissolved in various solvents, c) TriPS dissolved in various solvents, d) the variable pore diameter mesoporous silica nanoparticles.

In Chapter 4, we discussed the inductive effect and how the Si-H frequency is sensitive to the electronegativity of the substituents bonded to the Si center. As a result of this inductive effect, the average frequencies of the Si-H mode in each system are different. Figure B.2 displays the average vibrational lifetime for each type of the sample in Figure B.1 as a function of the average Si-H peak frequency.

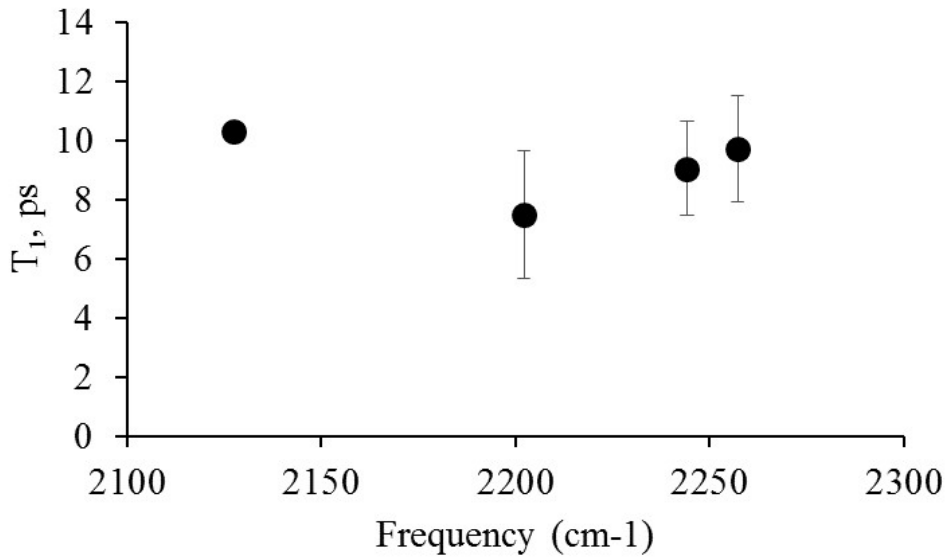

Figure B.2 plots the average lifetime vs. the average Si-H peak frequency for each of the plots in Figure B.1

Figure B.2 further illustrates the trend between lifetime and vibrational frequency. In this figure, the average ν_{SiH} for systems in Figure B.1 is plotted versus their average 1-2 vibrational lifetime. The error bars for each data point illustrates the variety of lifetimes for each system. Figure B.2 shows the unique behavior of the TriPS system. The TriPS system defies the near linear relationship exhibited by the other three systems, while further demonstrating a narrow range of lifetimes. The latter does not necessarily prove a lack of relationship between a Si-H mode's frequency and lifetime as TriPS does not exhibit strong

solvatochromism. The lack of correlation between the TriPS data and the other data sets suggests that the relaxation pathway may be different in this system.

A frequency dependence of vibrational relaxation is not unusual, depending on the mechanism of relaxation. Modes with vibrational lifetimes of a few to tens of the picoseconds typically exhibit internal vibrational relaxation (IVR). Since the lifetimes discussed in this appendix are sub 15 ps, it is safe to say that IVR is the primary relaxation mechanism. Thinking about the structure of the molecules studied thus far, TriPS is the only system where Si centers are not covalently bound to oxy groups. Si-OR bonds in most compounds have a frequency of 1000-1250 cm^{-1}, roughly half that of the Si-H vibration.[236] Tokmakoff and coworkers have shown that IVR of highly energetic modes can involve relaxation into multiple low energy modes.[237] For instance, the relaxation of the Si-H mode could be into two Si-O bonds, of which there are multiple in silica and also TriMOS. Figures B.3 a-c show the relevant sections of the FTIR spectra for this coupling discussion. Figure B.3a shows FTIR spectra in the range of 900-1200 cm^{-1} for TriMOS in IPA, chloroform, and pentane along with the neat solvents. In the TriMOS spectra, intense Si-OR peaks are found at 1040 cm^{-1}, 1096 cm^{-1}, and 1084 cm^{-1} for IPA, pentane, and chloroform respectively. Figure B.3b shows FTIR spectra in the same 900-1200 cm^{-1} range for TriPS in the same three solvents. Notice that the intense Si-OR peaks in these spectra are missing. Figure B.3c shows the FTIR of the Si-H peak for TriMOS in the three solvents along with shaded boxes simulating the frequency range of the frequency doubled Si-OR mode. This figure illustrates the importance of the Si-H frequency. The redder the Si-H peak the better coupling the mode will have into the Si-OR bonds. The Si-H peak in IPA does not overlap significantly with the frequency doubled box suggesting that the

intense IPA peaks from 1100-1200 cm^{-1} must play a role. Extrapolating this observation to the other systems, the Si-H modes in the silica materials exhibit longer lifetimes due to the blue shifting of the Si-H peak.

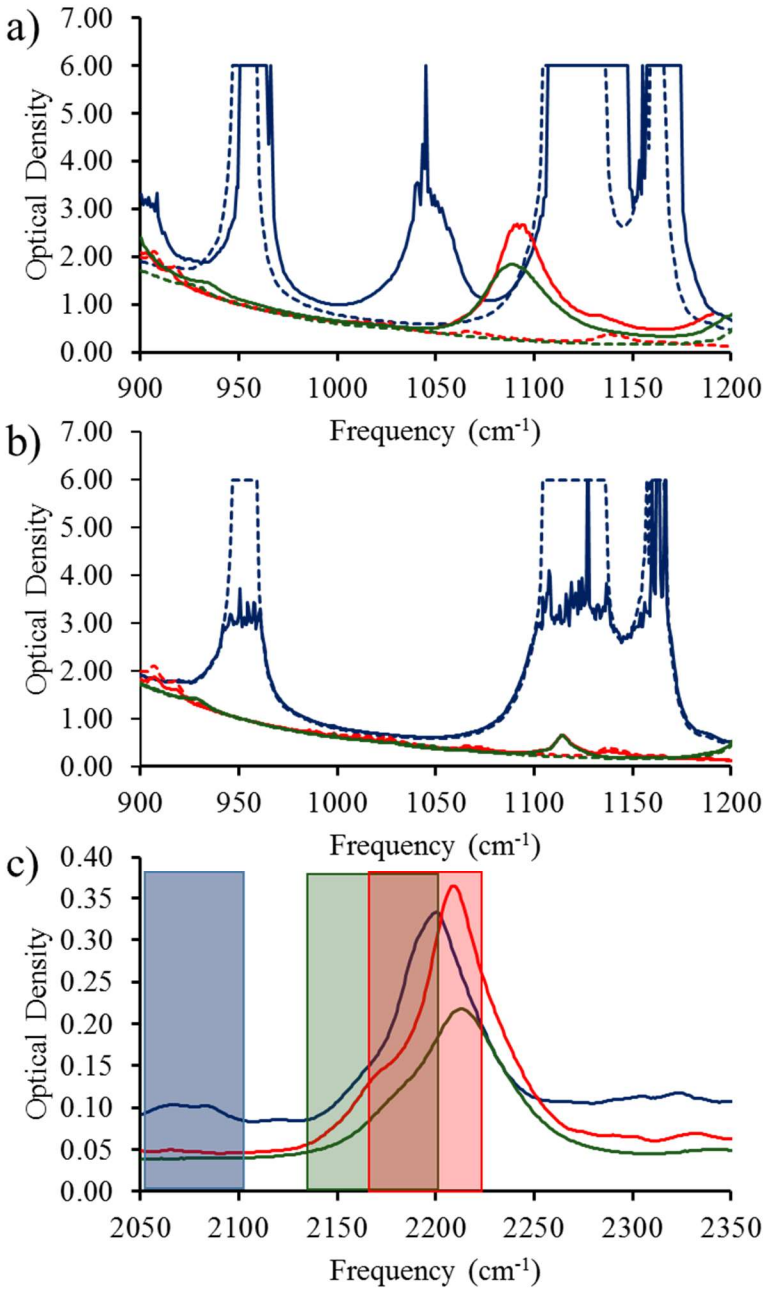

Figure B.3 Displays FTIR spectra for a) TriMOS and b) TriPS in IPA (blue), chloroform (green), and pentane (red) along with the neat solvent spectra. The Si-H peak of TriMOS is displayed, c), along with the frequency doubled Si-OR peak for each sample.

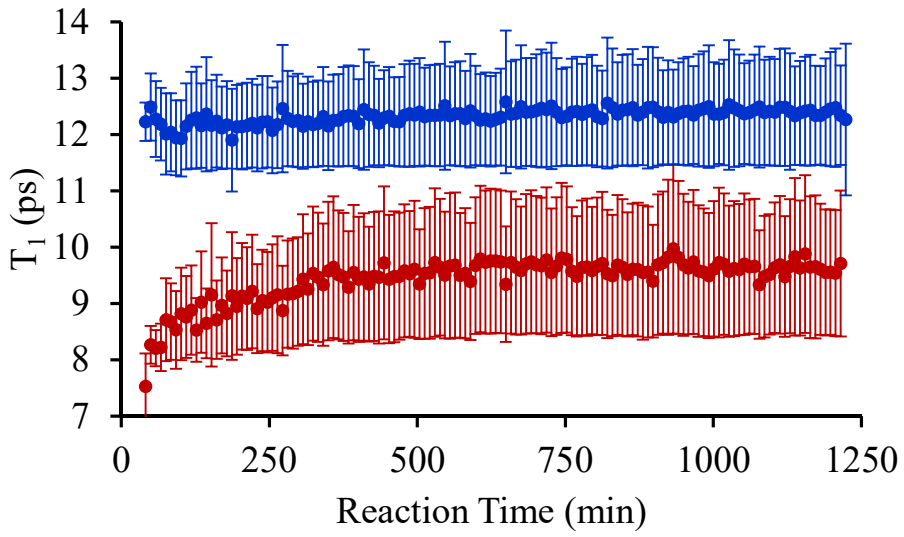

Figure B.4 Displays the vibrational lifetimes of the 0-1 (blue) and 1-2 (red) peaks as a function of reaction time.

The time lapse study in Chapter 6 provides the ultimate test of this IVR hypothesis. As we learned previously, the Si-H mode blue shifts as the silica matrix continues to condense throughout both the gel formation and gel aging processes. The time dependent lifetime of the Si-H peak in an evolving silica polymer was presented in Chapter 6, however for the sake of convenience it is presented once again in Figure B.4. In this figure, we see that the 1-2 vibrational lifetime is time dependent whereas the 0-1 lifetime is rather stagnant at ~ 12 ps. Once again we that the 1-2 vibrational lifetime is shorter than the 0-1 lifetime at any point in the reaction. Interestingly the 1-2 curve evolves similarly as the Si-H peak frequency as a function of time (Figure B.5), further evidence for the IVR mechanism described above. Essentially, the 1-2 peak blue shifts and therefore experiences weaker coupling to the Si-OR bonds. The insensitive behavior of the 0-1 peak may indicate that the 0-1 peak experiences very weak coupling to the Si-OR bonds initially and the coupling weakens as the 0-1 peak blue shifts.

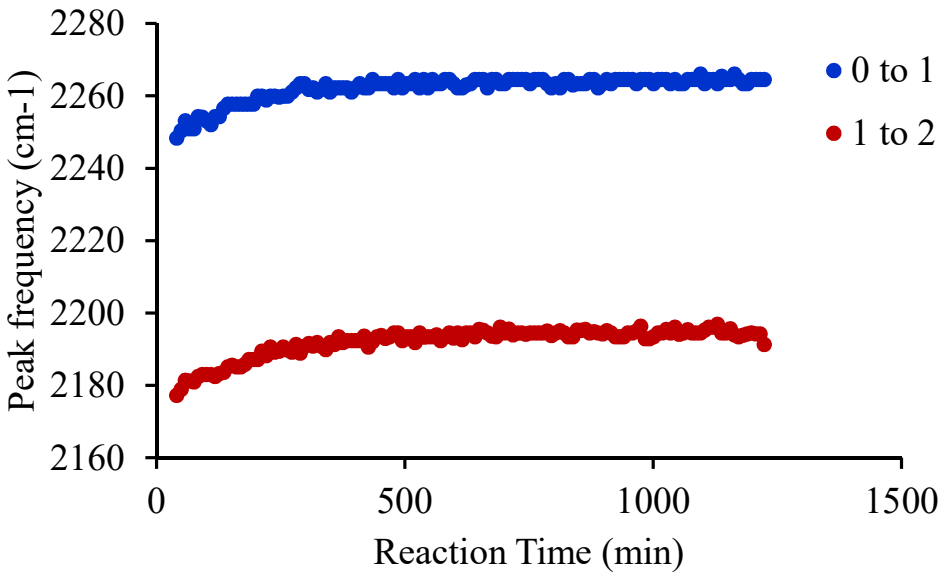

Figure B.5 Displays the peak centers for the 0-1 (blue) and 1-2 (red) transitions as a function of reaction time.

Figure B.6 tests the linear relationship between T_1 and the 1-2 peak center by plotting the two metrics together. The data in Figure B.6 shows a relatively strong linear correlation ($R^2 = 0.8281$) between vibrational frequency and lifetime. The time lapse data shows that the lifetime is certainly dependent on the frequency of the Si-H peak for a system where the solvent composition is fairly constant. However, Figure B.6 cannot rule out the importance the probe system composition plays into this correlation beyond inductive effects. In order to test whether the major factor is composition or simply frequency, the lifetimes for each sample for each system are plotted as a function of vibrational frequency (Figure B.7)

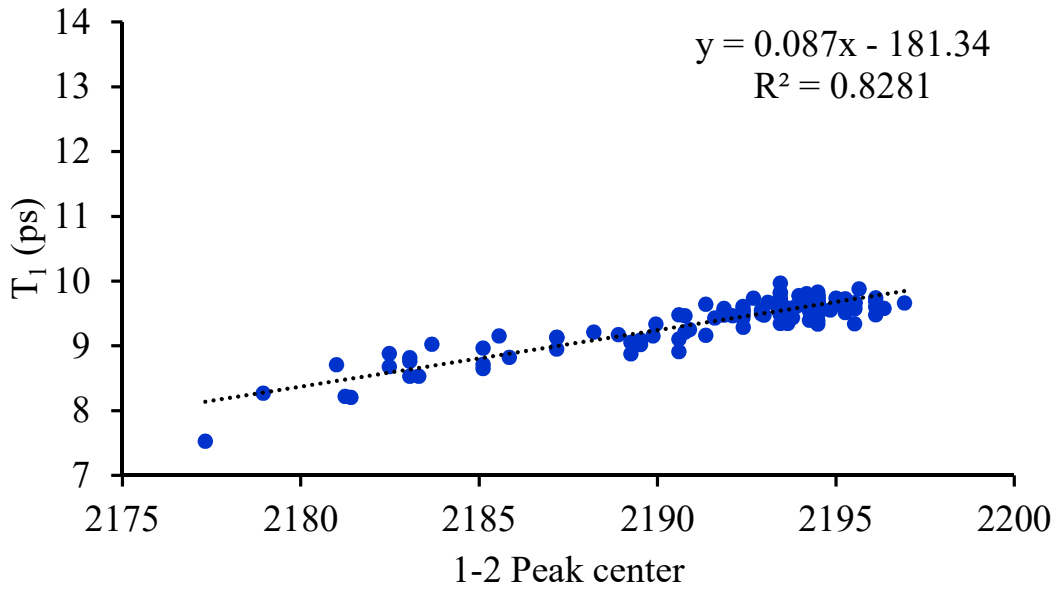

Figure B.6 Plots the lifetime of the 1-2 transition as a function of the 1-2 peak center.

From Figure B.7, we can see that three out of the five systems shows a linear relationship between ν_{SiH} and T_1, albeit with different slopes. Both the silica sol-gel system and the TriPS systems show no correlation. Among the three correlated systems are the aforementioned time lapse data, the variable pore sized silica nanoparticles, and the solvatochromic TriMOS samples. The fact that the TriMOS system has a linear relationship, even though there are only three data points, shows that the correlation between the two observables is impartial to the mechanism of the frequency shift. Therefore, the chemical composition of the probe system is primarily important due to inductive effects. The fact that the silica sol-gel samples are individually uncorrelated is perplexing and needs further investigation.

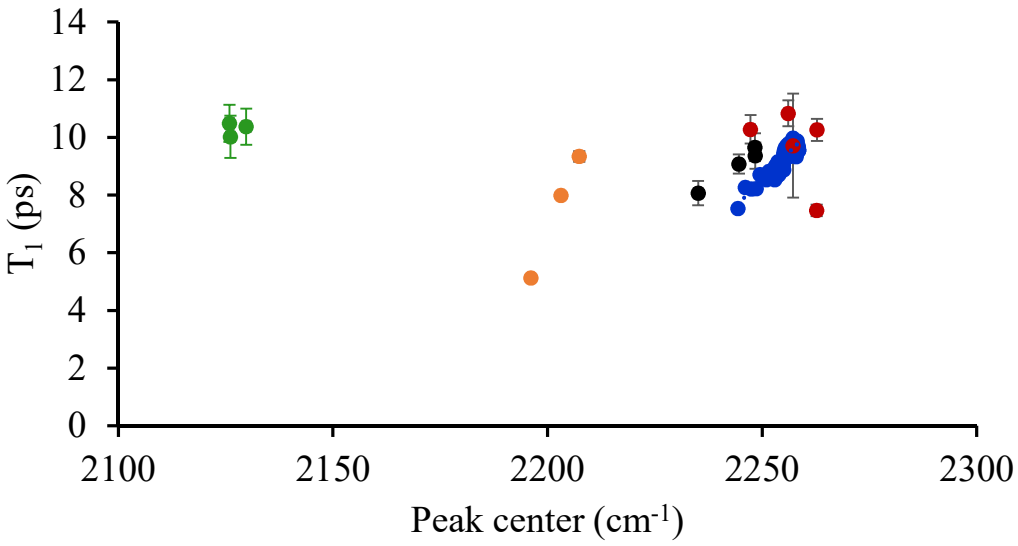

Figure B.7 Plots the 1-2 lifetime as a function of Si-H peak center for all the Si-H systems presented in this appendix.

Lastly as a proof of concept, the lifetime over the pump-probe spectrum is shown in Figure B.8. In this figure the lifetimes throughout the 1-2 and 0-1 peaks show the same trends as their averages do over time. In fact, the lifetimes used to find the average 1-2 lifetime are fit with essentially the same slope as in Figure B.6.

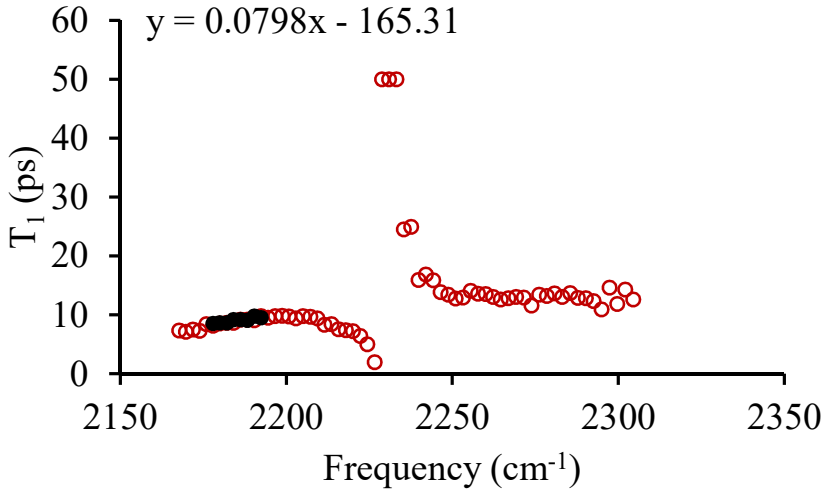

Figure B.8 Displays the lifetime as function of frequency for a given pump probe scan.